UNIVERSITÀ
DEGLI STUDI
DI PADOVA

Sede Amministrativa: Università degli Studi di Padova
Sede Consorziata: Università degli Studi di Udine

Dipartimento di PROCESSI CHIMICI DELL'INGEGNERIA

SCUOLA DI DOTTORATO DI RICERCA IN : INGENERIA INDUSTRIALE
INDIRIZZO: INGEGNERIA METALLURGICA
CICLO: XXIII

THIN ZrO_2-BASED SOL-GEL FILMS FOR THE PROTECTION OF ALUMINUM ALLOYS: BARRIER, ADHESION AND INHIBITION ABILITIES

Direttore della Scuola : Ch.mo Prof. PAOLO BARIANI
Coordinatore d'indirizzo: Ch.mo Prof. MAURIZIO MAGRINI
Supervisore :Ch.mo Prof. LORENZO FEDRIZZI

Dottorando : LUCA PAUSSA

Summary

Aluminum alloys are widely employed in several applications and industrial sectors: automotive industry, aircraft industry, food industry, package industry and construction industry are the most common fields where aluminum and its alloys are employed. The property which provides the added value to aluminum alloys is the advantageous strength-to-weight ratio. The mechanical properties of aluminum alloys can be improved by the precipitation of nanometric second-phase particles which are able to strengthen the aluminum microstructure. Large intermetallic particles generate a microstructure very susceptible to localized corrosion attack due to localized galvanic coupling with the aluminum matrix. Aluminum alloys are usually protected with a paint system consisting of conversion layers, primers and top coats. Chromium-based pre-treatments are extensively employed as conversion coatings because they provide very good adhesion for primers and top coats associated with good barrier properties. Chromate conversion coatings also exhibit self-healing abilities. Since Cr^{6+} is dangerous and not environmental friendly, the use of chromate conversion coatings is strongly restricted and alternative pre-treatments should be employed for the protection of aluminum alloys. The sol-gel technology enables to obtain inorganic or hybrid inorganic-organic systems at low temperatures. Sol-gel films are usually able to provide good adhesion and barrier properties improving the corrosion behaviour of metal substrates. Metal corrosion rates can be further decreased by the use of inhibitors.

The aim of this thesis is to develop ZrO_2 sol-gel coatings for the corrosion protection of aluminum substrates. Thin ZrO_2 films have been deposited from both organic and inorganic sols. By controlling the sol synthesis, sol-gel coatings containing inhibitor species were also produced. The investigation of the corrosion protection and the inhibition properties of ZrO_2 sol-gel films were carried out by means of electrochemical techniques. The study of the electrochemical behaviour was dealt with in two different approaches: the macro and the micro

investigations. The macro-electrochemical investigation employed open circuit potential and polarization measurements among the DC techniques. Electrochemical Impedance Spectroscopy was employed for the AC characterization. The micro-electrochemical investigation was performed by using the micro-cell technique as localized investigation tool.

ZrO_2 sol-gel coatings produced in this work were very thin. The strategy used was to deposit systems with an overall thickness of less than 200 nm. Systems thicker than 200 nm tend to crack and be widely defected. On the other hand, ZrO_2 sol-gel coatings with a thickness lower than 200 nm are able to provide an adequate protection due to their homogeneous structure. The thin ZrO_2 films are well adherent to the aluminum alloy substrates. The irregular surface shape produced by the etching of the aluminum surface is well covered even if the bottom of the surface cavities can be critical for sol-gel deposition.

ZrO_2 sol-gel coatings are not able to provide self-healing ability. The addition of inhibitor species into the starting sol is one of the possible routes to follow in order to supply self-healing ability to ZrO_2 sol-gel coatings. Inorganic and organic inhibitors have been added to the sol-gel protection systems. The macro-electrochemical evaluation of the corrosion inhibition provided by cerium nitrate salts in solution was carried out. The cerium compounds precipitate on the aluminum substrates following deposition mechanisms which are controlled by the chemical composition of the metal surfaces. The cerium precipitation occurs in a wide range of pHs limiting the corrosion activity of very reactive aluminum alloys like AA2024-T3.

The microstructure affects the corrosion behaviour of all types of alloys. It also influences the behaviour of inhibitor species. The second phase particles present in the AA2024-T3 microstructure were therefore investigated by means of the micro-cell technique. The investigation of the microstructure focused on two types of intermetallics containing aluminum-copper-magnesium or aluminum-copper-iron-manganese. The regions containing intermetallics with a high amount of magnesium are very reactive and their electrochemical behaviour is not stable. Localized corrosion attacks are generated by the galvanic coupling between the matrix and the intermetallics. The cerium salts are able to reduce the activity of the entire AA2024-T3 surface. The cerium inhibition action is evidenced by the shift to more noble values of the open circuit potential. The anodic and the cathodic behaviour are strongly affected by the cerium inhibition which is able to

homogenize the heterogeneous electrochemical behaviour of AA2024-T3. The regions containing magnesium-rich intermetallics are subjected to major alteration: they are the preferential sites for cerium deposition. This behaviour is most likely due to the magnesium dissolution which is as intense as the correlated reduction reactions.

In order to produce the inhibited ZrO_2 sol-gel coatings, the sol synthesis was modified taking into account the stability of the precursors. The amount of chelating ligands added to the sol was increased maintaining the viscosity in a good range for the sol-gel deposition by dipping or spraying techniques. The ZrO_2 sol-gel coatings inhibited with cerium nitrate salts exhibit the self-healing ability that non-inhibited ZrO_2 sol-gel systems are not able to provide.

The electrochemical characterization of thin sol-gel films is often problematic due to the difficulty to reach a steady state condition. The Electrochemical Impedance Spectroscopy is often employed for the coating characterization as a function of immersion time. The impedance measurements can be carried out under voltage and current controls. Measurements carried out under voltage control are not able to provide reliable results in the case of unstable systems. Measurements performed under current control are instead able to guarantee reliable results avoiding the sample damage due to the system polarization that might occur when the open circuit potential is not stable.

The demonstrators coated with ZrO_2 sol-gel coatings applied by means of a controlled air pressure industrial robot exhibit very good corrosion properties. The ZrO_2 sol-gel layers promote paint adhesion, limiting creepage and blister formation in the scratch area in industrial tests. ZrO_2 sol-gel coatings can be considered as an alternative to chromate-based pre-treatments for aluminum alloys.

Sommario

L'alluminio e le sue leghe sono notevolmente impiegati in molte applicazioni e settori industriali: l'industria automobilistica, l'industria aerospaziale, l'industria dell'imballaggio e l'industria delle costruzioni rappresentano i più comuni campi di impiego delle leghe di alluminio. Il loro ampio utilizzo è dovuto al favorevole rapporto tra la bassa densità dell'alluminio e le proprietà meccaniche ottenibili. Le caratteristiche meccaniche delle leghe di alluminio possono essere migliorate favorendo la precipitazione di particelle nanometriche in grado di rafforzare la matrice. I composti intermetallici sono i responsabili dello sviluppo degli attacchi localizzati a causa del loro diverso comportamento elettrochimico rispetto alla matrice. A causa di ciò, le leghe di alluminio sono generalmente protette da un sistema composto da diversi strati di conversione e da più layers di rivestimenti organici. I pre-trattamenti a base cromo sono molto utilizzati come strati di conversione perchè sono in grado di promuovere una buona adesione tra il substrato metallico e gli strati polimerici più esterni. Inoltre, le conversioni superficiali a base cromo sono in grado di ripristinare le proprietà barriera (effetto self-healing) che gradualmente tendono a diminuire. Purtroppo, il cromo esavalente (Cr^{6+}) è pericoloso e poco compatibile con molti degli aspetti ambientali. I rivestimenti a base cromo devono essere sostituiti da sistemi alternativi a basso impatto ambientale. La tecnologia sol-gel permette di ottenere a bassa temperatura sistemi inorganici o sistmi ibridi organici-inorganici. I rivestimenti prodotti con tecnologia sol-gel sono in grado di migliorare il comportamento a corrosione dei substrati metallici poichè garantiscono delle buone proprietà barriera promuovendo una migliore adesione dei rivestimenti organici. Il comportamento dei substrati metallici può essere anche migliorato utilizzando sostanze inibitrici della corrosione.

L'obbiettivo diquesta tesi è quello di sviluppare sistemi sol-gel a base ZrO_2 per la protezione delle leghe di alluminio contro la corrosione. Films sottili a

base ZrO_2 sono stati depositati partendo da sol inorganici e da sol organici. Il controllo della sintesi del sol permette di introdurre all'interno del rivestimento specie chimiche con proprietà inibitrici. In questa tesi, la caratterizzazione del comportamento a corrosione dei sistemi sol-gel a base ZrO_2 e la valutazione dell'effetto inibitore sono stati realizzati utilizzando alcune delle techniche elettrochimiche normalmente impiegate per questo scopo. Lo studio elettrochimico è stato suddiviso in due fasi comprendenti una macro analisi e una micro analisi. Per l'indagine su macro-scala sono state impiegate techniche elettrochimiche in corrente continua come la misura del potenziale di libera corrosione e le curve di polarizzazione potenziodinamiche. La spettroscopia di impedenza elettrochimica è stata utilizzata per la valutazione del comportamento relativo a lunghi tempi di immersione. Le misure localizzate di corrosione sono state eseguite impiegando la tecnica micro-cell che basa il suo principio di funzionamento sulla riduzione dell'area esposta all'elettrolita durante la misura.

I sistemi sol-gel a base ZrO_2 prodotti durante l'attività svolta sono molto sottili. L'obbiettivo di partenza consisteva nella produzione di rivestimenti con spessore non superiore ai 200 nm.Infatti, sistemi sol-gel con spessore superiore a 200 nm tendono a contenere un maggior numero di difetti mentre sistemi più sottili sono in grado di fornire una buona protezione dovuta alla loro struttura omogenea. I sistemi sol-gel a base ZrO_2 prodotti sono molto aderenti al substrato metallico. La superficie è ricoperta omogeneamente anche se la deposizione del rivestimento appare critica nelle regioni più irregolari che sono state prodotte dal processo di decapaggio.

I sistemi a base ZrO_2 non sono caratterizzati da capacità di autoriparazione (self-healing). L'introduzione di inibitori all'interno della soluzione di partenza può consentire di incorporare tale proprietà all'interno dei sistemi a base ZrO_2. In quest'ottica sono stati aggiunti inibitori organici ed inorganici concentrando lo studio del comportamento elettrochimico su sistemi inibiti con nitrato di cerio. Il meccansimo di protezione legato al cerio è dovuto alla precipitazione di composti contenenti cerio sulle aree attive del substrato. La precipitazione del cerio avviene in un ampio intervallo di pH limitando l'attività elettrochimica di leghe di alluminio molto reattive come la lega AA2024-T3.

La microstruttura di tutte le leghe metalliche, oltre ad influire notevolmente sul comportamento a corrosione, determina anche il modo in cui gli inibitori sono in grado di rallentare i processi elettrochimici. Il comportamento degli in-

termetallici presenti nella lega AA2024-T3 è stato investigato tramite la tecnica micro-cell. Le regioni contenenti intermetallici ricchi in magnesio sono molto reattive ed il loro comportamento elettrochimico è molto instabile. Morfologie di corrosione localizzata sono state identificate all'interfaccia tra la matrice e gli intermetallici esposti alla soluzione elettrolitica. L'introduzione del nitrato di cerio all'interno della soluzione aggressiva tende a ridurre l'attività elettrochimica della lega. L'azione inibitrice del cerio è evidenziata dalla variazione del potenziale di libera corrosione della lega AA2024-T3 che assume valori più nobili. I comportamenti anodico e catodico della lega AA2024-T3 sono fortemente influenzati dalla precipitazione di composti contenenti cerio che avviene in seguito all'interazione tra il metallo e l'inibitore. Le regioni contenenti una elevata quantità di intermetallici ricchi in magnesio rappresentano le zone in cui la precipitazione di cerio è più intensa. Tale evidenza è probabilmente correlata alla rapida dissoluzione del magnesio associata alle intense reazioni di riduzione che avvengono contemporaneamnte.

La sintesi del sol contenente come inibitore il nitrato di cerio è stata opportunamente modificata in modo tale da poter depositare rivestimenti sol-gel a base ZrO_2 altamente omogenei. Le quantità di inibitore e di agenti complessanti introdotti nel sol sono state modificate in modo tale da ottenere un sol con una viscosità compatibile con il processo di deposizione per immersione o per spruzzatura. I rivestimenti sol-gel a base ZrO_2 inibiti con nitrato di cerio hanno evidenziato proprietà autoriparatrici che i sistemi senza l'inibitore non sono stati in grado di offrire.

La caratterizzazione elettrochimica di film sottili prodotti con tecnica sol-gel è molto spesso problematica a causa dello sviluppo di condizioni fortemente non stazionarie (corrosione localizzata). La spettroscopia d'impedenza elettrochimica è spesso utilizzata per la valutazione del comportamento dei sistemi protettivi. Le misure d' impedenza possono essere realizzate applicando un seganle di ingresso in tensione o in corrente. Le misure d' impedenza effettuate utilizzando il controllo in tensione non sono in grado di fornire risultati attendibili quando il sitema elettrochimico è instabile. Le misure realizzate con il controllo in corrente sono invece in grado di garantire risultati più attendibili senza provocare il danneggiamento del sistema dovuto alla sua polarizzazione durante la misura.

Il comportamento a corrosione di substrati rivestiti con sistemi sol-gel a base ZrO_2 ed applicati tramite un processo di spruzzatura industriale è stato molto

simile a quello esibito da sistemi contenenti conversioni superficiali a base cromo. Il sistema sol-gel a base ZrO_2 promuove una buona adesione dei rivestimenti organici applicati su prototipi industriali. Lo sviluppo di blisters e di fenomeni di perdita di adesione osservati durante le prove industriali di corrosione è stato limitato. I sistemi sol-gel a base ZrO_2 possono essere quindi considerati come una possibile alternativa ai sistemi di conversione a base cromati impiegati nel campo della protezione delle leghe di alluminio contro la corrosione.

Contents

List of Figures

List of Tables

Chapter 1

Layout of the thesis

Corrosion science and engineering base one of their principles on the correct choice of the material to use by evaluating its electrochemical behaviour in each of the possible environments of employment. The choice of the material also depends on many other factors like the appearance, the fabricability, the cost, the mechanical and the physical properties. The corrosion rate of aluminum and its alloys can be reduced or sped down by applying a protective system. Protective coatings should guarantee three fundamental abilities. They should be able to provide a physical barrier against aggressive species. They should be able to improve the adhesion of organic primers and top coats. They should be able to provide self-healing ability when corrosion phenomena take place at the metal substrate.

This thesis seeks to investigate the behaviour of thin ZrO_2 sol-gel films as a replacement of chromium-based coatings for the corrosion protection of aluminum alloys. The synthesis and the deposition of the sol-gel coatings followed a route based on the production of active protective systems able to work and to evolve as a function of the corrosion step involved. The electrochemical techniques used for the coating characterization have been employed to obtain the feedbacks for the improvement of the entire production process. The thesis emphasizes practical fundamentals that make it possible to determine whether electrochemical techniques are useful for the sol-gel study, choose the correct electrochemical method and interpret the results.

Chapter 2 provides a general introduction to some corrosion aspects and the possible alternatives to improve the electrochemical behaviour of aluminum alloys. It also underlines some concepts of the sol-gel process including the synthesis and the characterization of sols. An overview on the electrochemical techniques

is presented at the end of the chapter. In Chapter 3, the materials and the experimental procedures have been generally described including the section relative to the instrumentations employed.
The section about results and discussion is divided in different parts. Chapter 4 and Chapter 5 report the electrochemical results of ZrO_2 sol-gel coatings produced from metal-organic and inorganic precursors. Chapter 6 includes the discussion on the macro-electrochemical behaviour of aluminum alloys immersed in aggressive solutions containing cerium nitrate species. Chapter 7 treats in detail the micro-electrochemical behaviour of the AA2024-T3 microstructure. This chapter focuses on the evaluation of the influence of the microstructure on the cerium precipitation mechanisms.
Chapter 8 presents the ability to recover and inhibit the electrochemical behaviour of ZrO_2 sol-gel films containing cerium nitrate as inhibitor species. Chapter 9 summarizes the critical aspects regarding the performing of correct electrochemical impedance measurements. In this chapter, an alternative experimental method based on current control is proposed. In Chapter 10, the results of industrial tests performed on ZrO_2 sol-gel coated aluminum alloys are finally reported. The conclusions of the PhD thesis are reported in Chapter 11, which summarizes the electrochemical behaviour of ZrO_2 sol-gel films developed for the replacement of chromium based conversion coatings.

Chapter 2

Introduction

The sol-gel process can be considered one of the most interesting technologies in the field of innovative pre-treatments for corrosion protection. The sol-gel technology enables to produce glass or ceramic materials at lower temperatures than those usually employed for the ordinary production process. This feature is a very important advantage because the deposition of ceramic or inorganic-organic hybrid films can be performed on metallic substrates susceptible to overaging. Aluminum alloys are considered as metallic substrates which can not undergo severe thermal treatments and are therefore excellent substrates for sol-gel film deposition. The corrosion behaviour of aluminum alloys coated with sol-gel films can be evaluated by means of several electrochemical techniques. In many cases, sol-gel films deposited on reactive substrates are characterized by a strong instability and it is very complex to perform the electrochemical investigation on these systems. For the characterization of pre-treated systems, Electrochemical Impedance Spectroscopy is often used as well as Potentiodynamic Polarization Measurements. The evaluation of the behaviour of macroscopic areas gives information about the overall electrochemical reactions occurring at the electrode while this approach is not able to give direct feedback to the microstructure of the alloys. In the cases where information on the microscopic electrochemical behaviour is needed, localized techniques have to be used. Micro-electrochemical techniques can be divided into two groups based on their operation mode: techniques based on the reduction of the electrochemical cell size and techniques based on the use of a scanning micro-electrode.

2.1 Aluminum alloys: corrosion and protection

Aluminum alloys are widely employed in many applications and industrial sectors: automotive industry, aircraft industry, food industry, package industry and construction industry are the most common fields where aluminum and its alloys are employed. The physical property which provides the added value to aluminum alloys is the low weight. Indeed, the aluminum density is only $2.7 Kgdm^{-3}$ which corresponds to $\frac{1}{3}$ of steel density, for instance. Moreover, aluminum alloys can be employed in contact with a wide range of foods because their resistance to several environment is rather good. Aluminum conducts electricity and heat easily, almost in the same way as copper [31]. Only a limited number of alloying elements can be added to aluminum to modify its property; they are chromium, copper, iron, magnesium, manganese, silicon, titanium and zinc. The solubility of these elements in aluminum is described by binary-diagrams and varies element by element.

2.1.1 Designation

Designation and compositions of aluminum alloys are defined by the American National Standards Institute (ANSI) and wrought products are identified by a four digit code with the first digit indicating the main alloying element. Table 2.1 shows the aluminum alloy groups defined by the ANSI designation.

Alloy series	**Main alloying element**
1xxx	aluminum greater than 99%
2xxx	copper
3xxx	manganese
4xxx	silicon
5xxx	magnesium
6xxx	magnesium and silicon
7xxx	zinc and magnesium
8xxx	silicon and iron

Table 2.1: Aluminum alloys designation

The second digit indicates some control of the impurities for 1xxx series while it is related to some alloy modification for the other series. The last two digits for

1xxx series indicate the minimum aluminum percentage considering the decimal part (1xxx series contains an aluminum amount grater than 99%). For the other series, the last two digits are employed for the identification of different alloys in the same group.

2.1.2 Corrosion of aluminum alloys

Corrosion is a phenomenon involving electrons transfer between metals and the surrounding environment. Metals start to corrode because they tend to electrochemically react involving oxygen, hydrogen or other environmental chemical species. The oxidation reaction identifies metal dissolution which is balanced by reduction reactions occurring at the cathodic sites. Typical examples of reactions occurring on aluminum surface are the aluminum dissolution reactions:

$$Al \rightarrow Al^{3+} + 3e^{-} \tag{2.1}$$

the oxygen reduction reaction in acid and base solution:

$$O_2 + 4H^{+} + 4e^{-} \rightarrow 2H_2O \tag{2.2}$$

$$O_2 + 2H_2O + 4e^{-} \rightarrow 4OH^{-} \tag{2.3}$$

the hydrogen evolution:

$$2H^{+} + 2e^{-} \rightarrow H_2 \tag{2.4}$$

Since electrochemical reactions occur, thermodynamic and kinetic conditions have to be satisfied. Indeed, an electrochemical reaction occurs when the Gibbs free energy is negative and the kinetics of the reaction is fast enough to promote an evolution of the system. One example of an electrochemical reaction satisfying the first condition (thermodynamic) but not the second one (kinetic) is constituted by the platinum oxidation reaction in Harrison solution (sodium chloride and ammonium sulfate). In that case, the kinetic is so slow that platinum can be considered inert in that environment. In certain environmental conditions, on several metals a natural oxide film able to increase the corrosion behaviour can grow. This phenomenon, known as metal passivity, is typical of aluminum alloys. Aluminum can react with oxygen forming Al_2O_3 which can be hydrated.

Although the natural oxide is very thin, ranging around 10 nm, it is however able to act as a physical barrier between the metal substrate and the environment. Despite the fact that natural oxide is stable under a wide range of conditions, it is possible that alumina film can dissolve becoming less protective. The stability range of aluminum oxide starts from pH 3 to pH 9. For pHs lower than 3 and higher than 9, the aluminum oxide is not stable and it is not able to protect the metal substrate.

Corrosion types of aluminum alloys

Aluminum alloys are mainly corroded by localized attack forms while uniform corrosion proceeds over a large area. Localized corrosion is due to some weak points of the metal microstructure where the electrochemical reactions can be sparked more easily than in other regions. Weak points consist in grains exposed on the metal surface, dislocation outcroppings and other types of local defects. By considering the previous definition, it is possible to identify the different forms of localized corrosion.

Pitting corrosion Metals corroded by pitting develop a corrosion morphology that looks like deep cavities with a circular shape. Pitting is one of the most destructive and insidious corrosion types because it grows in depth and for this reason it is very difficult to identify. It is very difficult to measure and compare different pits taking into account both depth and size. Moreover, pitting can not be predicted even at laboratory scale. The mechanism and the kinetic of pitting corrosion is based on the auto-catalytic nature of oxidation reactions which promotes the growth of the phenomenon in depth. Solutions responsible of pitting corrosion mainly contain chlorides or chlorine ions. Marine environments are practical examples.

Crevice corrosion Crevice corrosion is a form of attack occurring within fissures, cracks and other regions of metals surface particularly shielded. This attack is related to a stagnant volume of solution generated by holes, rubber gaskets, mechanical joints like rivets and screw heads, surface dirt, corrosion products, sand grains and so on. The mechanism and the growth of corrosion attack is related to the different concentration of species between anodic and cathodic regions. As in the case of pitting corrosion, corrosion reactions are auto-promoted

by the local chemical conditions which are worsened by chlorides.

Galvanic and Intergranular corrosion These kinds of corrosion attack are due to a different electrochemical potential between materials, phases or structures. Galvanic corrosion occurs between two metals immersed in an electrolytic solution having different electrochemical potentials. The less noble metal will tend to dissolve. The more noble metal acts as a cathode whereas the less noble acts as an anode. Intergranular corrosion is originated by the difference in the electrochemical potential between the grain boundaries and the center of the grain. This difference is due to the different energy and chemical stability of the grain and its boundary. Indeed, impurities or second phase particles can be present at the grain boundary, making the region more active and less stable

2.1.3 Chemical modification of the metal surface

The corrosion protection of components made of aluminum alloys is usually guaranteed by several coatings deposited layer by layer on the metal substrates. The chemical modification of the metal surface should be able to guarantee both, the corrosion protection and the improvement of the adhesion between the metal substrate and the outer organic coatings. The process producing the chemical modification of the surface is usually preceded by degreasing and pickling steps. These steps enable to remove oils and greases from the surface and are able to dissolve the thick oxide layer which grows during hot-working. Many electrochemical or chemical processes are nowadays employed for aluminum alloys surface modification like anodizing, chromate conversion based, fluo-titanation or fluo-zirconation systems and so on. Sol-gel process is now employed as an alternative route to modify the chemical composition and the surface properties of aluminum alloys.

Anodizing Anodizing is used to increase the thickness of the oxide growing on the aluminum surface. In this electrochemical process, the aluminum surface acts as anode because it is subjected to a potential difference. The film that grows during anodizing is well adherent to the substrate because it is the growth of the natural oxide initially covering the metal substrate. When the process is carried out correctly, the oxide covering the substrate is highly compact and

provides an efficient protection against corrosion. The aluminum oxide produced by anodizing is usually composed by an inner dense layer acting as physical barrier and an outer porous layer less dense and protective. The formulation of electrolytic baths can be composed of several acids but the most used is based on H_2SO_4. By changing the electrolyte, the flowing current densities or the temperature of the bath, it is possible to obtain oxide morphologies with distinct properties. Indeed, it is possible to obtain a kind of oxide very stable and not soluble in the electrolyte, with a low porosity level and low conductivity rather than oxides more soluble in the electrolyte and highly porous. The corrosion resistance of the oxide can be affected by both the porous size and the presence of harmful compounds, impurities and alloying elements. Copper is one of the most critical elements which strongly affects the corrosion properties of anodized oxide. The intermetallic phases containing copper and aluminum dissolve during the anodizing process producing a reduction of the density and of the thickness of the aluminum oxide [32]. Another inconvenience related to anodizing is due to possible gas formation. The gas formed can be O_2 and it is due to the oxidation of O^{2-} ions diffusing within the oxide layer. Since small gas bubbles with high internal pressure can be formed, they can blow up producing a severe damage of the surrounding areas and an inhibition of the further film growth [33]. In marine and high humidity applications, the employment of anodized substrates is suggested rather than the use of organic coatings which are preferentially attacked by filiform corrosion. For anodized film oxides, it was estimated in industrial environment that the rate dissolution is around $0.7 - 0.9\ mm$ [34].

Chromate based coatings The chemical conversion coating based on chromates is an electrochemical process used for the deposition of chromium oxide on aluminum substrates. The process is carried out under very acid conditions because the electrochemical baths contain chromic acid bringing the pH solutions to around 2. The deposition mechanism is based on the activation of anodic and cathodic areas on the aluminum surface where aluminum dissolution and reduction reactions occur in this order. Furthermore, hexavalent chromium (Cr^{6+}), which is a strong oxidant, is reduced to a trivalent oxidation state. In the cathodic regions where strong reduction reactions occur, the local pH tends to increase so that chromates precipitate on the surface. The main reactions involved are the dissolution of aluminum:

$$Al \rightarrow Al^{3+} + 3e^- \tag{2.5}$$

the hydrogen evolution:

$$3H^+ + 3e^- \rightarrow \frac{3}{2}H_2 \tag{2.6}$$

the reduction reaction of chromium from the hexavalent to the trivalent state:

$$CrO_4^{2-} + 8H^+ + 3e^- \rightarrow Cr^{3+} + 4H_2O \tag{2.7}$$

the precipitation of cerium compounds at the cathode:

$$Cr^{3+} + CrO_4^{2-} + H_2O \rightarrow Cr(OH)CrO_4 + H^+ \tag{2.8}$$

the precipitation of aluminum hydroxide at the cathode:

$$Al^{3+} + 2H_2O \rightarrow AlO(OH) + 3H^+ \tag{2.9}$$

At the end of the deposition process, the coating undergoes thermal treatment in order to achieve a greater density and the reduction of water content inside. The chromate based film is well adherent to the surface and it is able to guarantee a good protection against corrosion. Moreover, it promotes the improvement of the adhesion property between the metal substrate and the organic coating deposited as top coat. Chromate based coatings are widely employed for their self-healing ability. The Cr^{6+}/Cr^{3+} mix can re-arrange its oxidation state producing a further precipitation of chromium-containing compounds able to protect the uncovered metal substrate. For this reason, chromate based coating is often employed in industrial application requiring a strong corrosion resistance. By controlling the parameters of chromate chemical baths, coatings can be produced with a wide range of properties. For example, by reducing the pH solution down to 1.2, the oxide film growing on the aluminum surface is less dense and less thick [35]. Corrosion products formed within defects at pH 1.2 are able to protect the metal substrate better than corrosion products formed at higher pHs. Since at low pHs corrosion products inside defects are dense and compact, the corrosion behaviour of the chromate based coatings improves because a further corrosion attack is avoided [35]. The reduction of pH solution produces an increasing of the number of defects and porosity. The net effect of positive and negative aspects

leads to the decreasing of the corrosion behaviour of chromate conversion coatings. The chemical composition and the microstructure of chromate conversion coatings are strongly dependent on the preparation treatment that metal surface, as well as the heterogeneous aluminum microstructure, have undergone. Lunder et al. [36] proved that the nucleation and growth phases are affected by the shape of intermetallics in the matrix as well as their size. For AA6060-T6 aluminum alloy, it was found that the thickness of chromate based film deposited on intermetallics rich in iron and copper is much thinner than that formed on the matrix. That aspect has been correlated to the different electrochemical behaviour exhibited by grain boundaries and the center of grains. Since grain boundaries act as anodic sites with respect to the center of the grain, the oxide deposition on the center is supported by the anodic dissolution of the grain boundaries. This evidence was confirmed by other results which proved that on grain boundaries no oxide deposits could found. Although the deposition mechanism starts on intermetallics, the film grows faster on the matrix. For AA6060-T6 aluminum alloy, it was estimated that the oxide formed on intermetallics was 40 nm thick whereas it was 200 nm on matrix regions. Chromate process deposition carried out only for 10 seconds are able to reduce the cathodic activity of AA6060-T6 surface improving its corrosion behaviour [36].

Fluo-titanation and fluo-zirconation Conversion coatings based on fluo-titanation and fluo-zirconation are encompassed in the category of chromium-free treatments. The coatings produced by these processes appear color-less and for this reason it is not possible to recognize with the naked eye the presence of the film on the metal surface. Both, zirconium and titanium are able to form a very stable complex containing six fluorine atoms. However, zirconium and titanium as well as their oxide are easily soluble in HF producing the correlated acids. The following dissociation reaction 2.10 and the mechanism processes for zirconium are valid for titanium, as well:

$$ZrO_2 + 6HF \rightarrow H_2ZrF_6 + 2H_2O \tag{2.10}$$

The aluminum dissolution reaction 2.5 produces aluminum ions which are involved with the reaction product of 2.10:

$$Al^{3+} + ZrF_6^{2-} \rightarrow AlF_6^{3-} + Zr^{4+} \tag{2.11}$$

It was found that oxygen reduction and hydrogen evolution reactions occur on $\alpha - Al(Fe, Mn, Si)$ particles which behave cathodically with respect to the AA6060 aluminum matrix [37]. In these regions, the local increasing of the pH promotes zirconium oxide precipitation:

$$Zr^{4+} + 3H_2O \rightarrow ZrO_2 \cdot H_2O + 4H^+ \tag{2.12}$$

Besides that, a mixed insoluble oxide precipitates on the aluminum surface obeying the following reaction:

$$2Al + 4H^+ + 3ZrF_6^{2-} + 5H_2O \rightarrow 2AlOF_3ZrOF_2 + 12HF + H_2 \tag{2.13}$$

The mixed chemical composition of the oxide precipitated on aluminum surface is confirmed by GD-OES measurements [38]. The deposition mechanisms related to the formation of a mixed Zr/Ti oxide and a chromate conversion coating are substantially different. Zr/Ti oxide precipitation is promoted by the local pH variation while in the case of chromates, an increasing of pH leads to the reduction of Cr^{6+} to Cr^{3+} through red-ox reactions [38]. Chromium reduction reaction and hydrogen evolution are competitive reactions occurring on the same electrode. Cr^{6+} to Cr^{3+} is supported by the initial stage of the process while hydrogen evolution tends to occur more easily at the end of the conversion process. The Zr/Ti oxide film thickness is affected by the chemical composition of the metal substrate as well as in the case of chromates. The shape and the size of intermetallic particles strongly influence the film mechanism growth. By reducing the pH and stirring the solution, it is possible to modify the mechanism of deposition [38]. Zr/Ti oxide is able to guarantee a very good adhesion with organic coatings [39]. However, Zr/Ti oxide is not able to provide self-healing ability which chromate based coatings are able to provide.

Silanes Silanes are chemical compounds very similar to hydrocarbon alkyls in which the chain covalent bonds are formed between silicon atoms. The chemical formula of silanes is Si_nH_{2n+2}. Silanes are widely employed and they are used as coupling agent to increase the adhesion between metal substrates and organic coatings. The adhesion can be further improved by using modified silanes in which hydrogen atoms are substituted by complex groups. Chains are hydrolyzed in order to allow the formation of chemical bonds between the precursors. Not

hydrolyzed groups should guarantee the improvement on the adhesion properties. The process parameters controlling the bath features are the concentration of the solution, the reactive groups in the silane chain and the solution pH. Silanes industrially employed are based on either amines or ethoxy groups. Although the silane concentration is one of the parameters to take into account for the synthesis, Jenkins et al. [40] found that the adhesion energy is not strongly dependent on the amount of precursors used. Franquet et al. [41] obtained the same result. They even found that for silanes with CH_3 groups, the chain length strongly affects the adhesion property. The longer the chain length is, the better the adhesion is. Otherwise, the adhesion tends to be better for short silane chains containing CH_2 groups. Salt spray and pull-off tests showed that silanes can act as good adhesion promoters between aluminum alloys (5xxx series) and an epoxy-polyester organic coating [42]. The silane behaviour was compared with that one provided by aluminum substrate pre-treated with fluo-zirconation process. The behaviour provided by silanes after 1000 hours of salt fog test was very good and better than that provided by fluo-zirconate system. In order to further improve the adhesion of silanes, it is possible to mix precursors with several properties like hydrophobic behaviour, tendency to create bonds with a category of organic compounds, affinity to functional groups and so on [43].

Cerium Salts Cerium is a lanthanide element which is able to form insoluble oxide with a very low toxicity. These two properties have driven researchers to develop cerium compounds for corrosion protection of aluminum and its alloys. Cerium is able to protect metal substrates because a compact film consisting of cerium oxide/hydroxide can precipitate and substitute the natural aluminum oxide dissolved by aggressive species. Chemical conversion coatings based on cerium salts can be produced by using cerium chloride in aqueous solution. However, the spontaneous precipitation process takes a very long time, ranging from days to weeks and it is not compatible with the industrial scale-up. In order to reduce process time, it is possible to adopt various methods. The process time can be reduced by applying a cathodic current in order to promote, near the metal surface, local pH conditions favourable to cerium compounds precipitation, by increasing the bath temperature or by adding strong oxidant species to the electrolyte (i.e. H_2O_2). The cerium deposition mechanism of cerium compounds is well known in literature [44]. It states that intermetallics with cathodic be-

haviour play an important role in the overall mechanism of precipitation. The precipitation mechanism is divided in two different steps: in the first part, hydrogen evolution and oxygen reaction reduction leads to a local pH increase on cathodic intermetallics where cerium precipitation occurs. In the second part, the continuous dissolution of passive oxide is coupled with the further cerium precipitation. Small cathodic sites underneath the passive film become more active promoting cerium precipitation. A protective film 150 nm thick was obtained by dipping aluminum alloys in boiling water containing cerium salts [45]. By adding H_2O_2 to the initial cerium salt solution, a thicker coating with many cracks and defects, which tends to preferentially precipitate on intermetallic particles, was obtained [45, 46]. It is possible to speed up the deposition process by adding catalysts or increasing the solution pH [46]. Although the employment of catalysts promotes the reduction of process time, precipitates can contain not only cerium compounds but also a part of catalysts (usually containing copper). Therefore, the effect on the corrosion behaviour of cerium oxide/hydroxide film, based on catalysis processes, is strongly affected by this aspect. However, conversion coatings based on cerium salts enable to drastically reduce cathodic current because oxygen reduction reaction is shifted to lower potential [45]. The surface characterization of cerium conversion coatings deposited on AA5083 aluminum alloys [47], evidenced that a mixed layer was formed: it was found that cerium compounds grown via island-growth precipitated on cathodic intermetallic particles while an Al_2O_3 layer covered the aluminum matrix.

2.1.4 Corrosion inhibition

Corrosion phenomenon can slow down by several methods and the employment of inhibitors is one of the ways to improve the electrochemical behaviour of corroding systems. An inhibitor is a substance that, when added to the environment, is able to decrease the corrosion rate. There are numerous inhibitor types which can be divided in different groups in conformity with their mechanism of inhibition: the adsorption-type inhibitors are those able to be adsorbed on the metal surface reducing the metal dissolution and the reduction reactions. Another type is based on the control of the hydrogen evolution. This type is very effective in acid solution but in alkaline condition, where oxygen reduction governs the cathodic reactions, it is not able to reduce the corrosion rate. A third type founds its

ability by removing oxidant species from the solution. For example, sodium sulphide is able to remove dissolved oxygen from aqueous solution as indicated by the following equation:

$$2Na_2SO_3 + O_2 \rightarrow 2Na_2SO_4 \tag{2.14}$$

Also this type is not effective in acid conditions. Another type of inhibitors are the oxidizers which are substances, like chromates, nitrates, ferric salts, able to improve the corrosion behaviour of active-passive metals. They promote the formation of a passive film on metals exhibiting the active-passive transition. Inhibitors can be further classified by taking into account the controlled reaction (anodic or cathodic). Anodic inhibitors act as retarding catalyst of oxidation reactions decreasing the corrosion current. The scheme of the mechanism obeying the mixed-potential theory, is represented in Figure 2.1(a) and shown that anodic inhibitors shift the E_{corr} to more noble potentials. Otherwise, cathodic inhibitors tend to decrease the cathodic activity and the corrosion current as shown in Figure 2.1(b). They produce the E_{corr} shifting to less noble potentials.

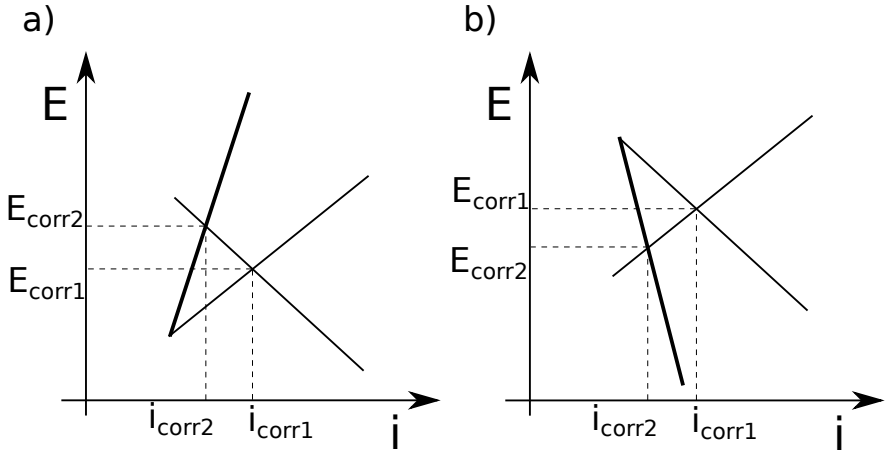

Figure 2.1: Corrosion inhibition mechanisms

2.2 Sol-gel technology

Sol-gel materials encompass a wide range of inorganic and inorganic-organic hybrid materials which are prepared following a common preparation strategy. They

are prepared from a starting precursor solution going through distinct steps involving the generation of colloidal suspensions (sol) which are subsequently converted to viscous gels and from there to solid materials [1]. Nowadays, the sol-gel process is one of the most used and studied techniques for the production of high quality glass-ceramic materials. The process is versatile and it is possible to easily control the entire evolution. The sol-gel technique is basically constituted by three steps: the preparation of the starting precursor solution, the conversion from sol to gel and the increasing of material density by means of thermal treatment. A sol is a dispersion of colloidal particles suspended in Brownian motion within a fluid matrix [2]. Colloids are suspensions of particles of linear dimensions between 1 nanometer to 1 micrometer. The stability of colloids can be checked measuring the solution viscosity which can be increased by the particles' agglomeration. Indeed, the stability of colloidal particles is related to their resistance to aggregation and in some cases it can be very high. A remarkable example is given by a few gold sols produced more than 150 years ago at the Royal Institution in London, which are still stable. They are still so stable that they are not useful for preparing solid materials ... Sols' stability can be improved increasing the ionic strength of the solution modifying the charge of the counter-ion [3]. Therefore, it is possible to control the sol-gel synthesis checking both the initial size of the colloidal particles and the chemical reactivity of sols. The size of initial colloid particles depends on the nucleation and growth steps. To obtain colloids, the nucleation rate has to be faster than the growth rate. Nucleation depends on the saturation limit which then controls the particle precipitation. Nucleation rates will be highest for substances with very low solubility. The growth rate of particles formed by the initial nucleation depends on several factors among which the amount of material available and the material diffusion rate from the solution to the growing particles are very important. The sol-gel process is composed of different stages which can be identified as the hydrolysis step, the condensation step, the gelation step, the ageing step, the drying step and the densification step. In some cases (*i.e.* silica-gel chemistry), the steps occur slow enough to allow detailed study for their identification. Otherwise (*i.e.* metal alkoxides), the chemical evolution of the starting solution is so fast that it is much more difficult to control and study the entire synthesis.

There are several advantages related to materials produced by means of sol-gel process:

- the temperatures used during the process are very low and are frequently close to room temperature;

- inorganic and organic precursors can be mixed together for the production of inorganic-organic hybrid materials;

- since high quality precursors are usually used, high-purity materials are produced;

- the chemical conditions are mild because extreme pH for hydrolysis and condensation steps can be avoided modifying the synthesis procedure;

- controlled porous materials can be produced;

- it is possible to cast ceramic materials in a range of complex shapes;

- materials with good optical properties can be produced;

- since the low temperature of sol-gel process is usually lower than the crystallization temperature for oxide materials, amorphous materials are usually produced.

On the other hand, the sol-gel process has some drawbacks which limit its application. The precursors are often expensive and sensitive to moisture, limiting the up-scaling at industrial level. Some syntheses require a long step for drying and densification, increasing the overall time of the process. Shrinkage, dimensional change and cracking can occur during densification and drying processes. These problems, although not insuperable, do require careful attention. Table 2.2 summarizes the stages related to sol-gel process:

2.2.1 Silica sol-gels reaction mechanisms

As mentioned in 2.2, since the evolution of silica gels is slower than the one of metal alkoxides, it is easier to identify separately the reaction mechanism related to the sol-gel steps. For this reason, this section will treat silica gel chemistry in order to give an overview on the reaction mechanisms correlated to a generic synthesis. It is important to point out that several stages of sol-gel processes occur simultaneously and they are treated separately for explanation convenience. In this section, sol-gel processes of metallorganic precursors will be discussed. The

Sol-gel stage	Description
Hydrolysis	$M(OR)_4 + nH_2O \rightarrow M(OR)_{4-n} + nROH$
Condensation	$X_3MOH + HOMX_3^{'}, X_3MOR + HOMX_3^{'} \rightarrow$ $X_3M-O-MX_3^{'} + H_2O, X_3M-O-MX_3^{'} + ROH$
Gelation	Formation of clusters related to the viscosity increasing
Ageing	Formation of a cross-linked structure associated to shrinkage and covalent links as substituted of non-bonded contacts. Changes in pore size and pore wall strength
Drying	Expulsion of the liquid (water, alcohol, volatile components) during shrinkage associated to the development of capillary stress which frequently leads to cracking
Densification	Thermal treatment for the formation of a dense ceramic or hybrid material

Table 2.2: Sol-gel stages description

processes are known as alkoxides methods. The structural formula of alkoxides is $M(OR)_n$, where R is an organic radical while M is the metal precursor. The solvent used is usually the alcohol corresponding to the initial alkoxide.

Hydrolysis The hydrolysis of alkoxides follows the reaction described in Table 2.2. Since the reaction rate can not be fast enough to guarantee the evolution to gel formation, the synthesis has to be carried out under catalysis. The hydrolysis can be accelerated by acid catalysed or base catalysed processes. The mechanism for both processes are shown in Figure 2.2.

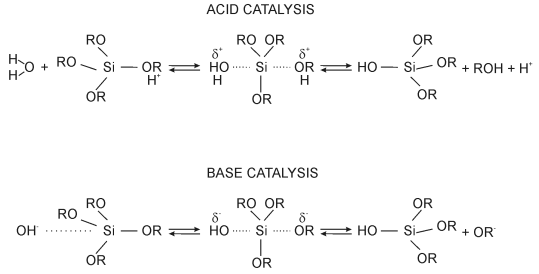

Figure 2.2: Hydrolysis: base and acid catalysis

The effect of catalysis is to speed up the hydrolysis reaction and it can be

evaluated by comparing the rate at different pH values. In the case of silica gel, the isoelectric point (where the net charge on the molecule is equal to zero) is at pH 2.2 [4]. It has been evaluated that the time to form a gel strongly depends on the solution pH. Figure 2.3 shows the time to form a gel (t_{gel}) as a function of pH for a silica gel.

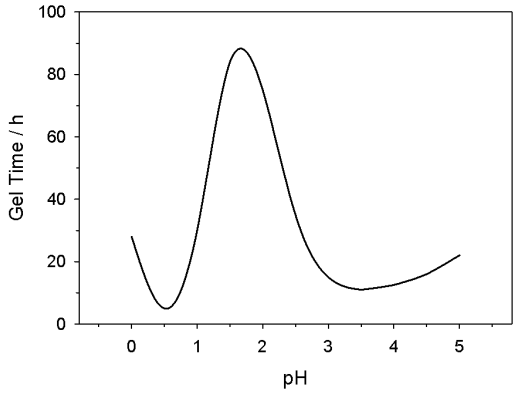

Figure 2.3: Gel time as a function of pH for HCl-catalysed process for TEOS

The gel time is longest in correspondence to the isoelectric point while it tends to decrease in acid or base conditions relative to the isoelectric pH point. The first organic radical is hydrolyzed faster than the second while the third one is hydrolyzed slower than the second in acid conditions. This is due to the electronic effect related to the organic radical substitution in acid conditions. Alkoxy groups are more electron donating than hydroxy groups. As more alkoxy groups are substituted by hydroxy groups, the rate of hydrolysis reaction tends to be reduced. Otherwise, in base conditions the mechanism is exactly the opposite. The length of the organic chain heavily affects the rates of hydrolysis. Larger alkoxy groups are more cumbersome and the steric hindrance slows down the hydrolysis rate. Another factor which must also be taken into account is the hydrophobic or hydrophilic character of the precursor. TEOS (tetraethoxy silane) and water are immiscible and it is necessary to add an organic co-solvent to achieve miscibility and better hydrolysis conditions. Many different co-solvents have been used, including alcohols, formamide, dimethylformamide and so on. The choice of co-solvents is important, since the use of a different alcohol from that generated by hydrolysis of the alkoxide can affect the reactions occurring in the bulk solution. The water-alkoxide ratio must be chosen in order to develop

optimum conditions for hydrolysis. If the amount of water is small, the hydrolysis rate slow down due to the reduced reactant concentration. If the water amount is high, the alkoxide is too diluted and gel times increase.

Condensation Condensation reactions can involve either water or alcohol formation. As in the case of hydrolysis, condensation reaction must be sped up by catalysed processes. The mechanisms are displayed in Figure 2.4.

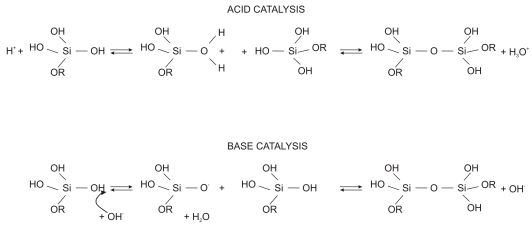

Figure 2.4: Condensation Mechanism

The condensation rate depends on the steric effect and the charge on the transition state. Condensation rate under the acid hydrolysis catalyzed process for $(RO)_3M(OH)$ is faster than for $(RO)_2M(OH)_2$, which condenses faster than $(RO)M(OH)_3$ and so on. This means that under acid catalysis, the first hydrolysis step is the fastest, and the product of this first step also undergoes the fastest condensation. Therefore, under acid conditions an open structure is initially obtained and followed by further hydrolysis and cross-condensation reactions. On the contrary, under base catalysis, the successive hydrolysis reactions occur faster and the fully hydrolyzed species undergo the fastest condensation reactions. As a consequence, under base catalysis a highly cross-linked large sol is initially obtained which eventually links to form gels with large pores between the interconnected particles as shown in Figure 2.5.

Gelation Gelation occurs when links formed between sol particles involve macroregions across the containing vessel. This is a generic definition because it is not possible to identify exactly the gel-point related to an established viscosity. However, at the gelation point, the mixture starts having a high viscosity but low elasticity [5, 6]. No exotherm or endotherm change occurs and a further crosslinking tends to increase the solution viscosity as shown in Figure 2.6.

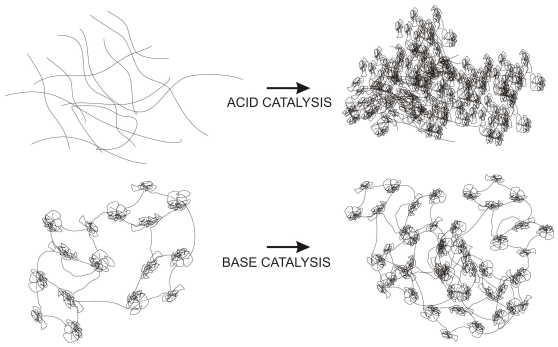

Figure 2.5: Gel structure for acid and base catalysed reactions

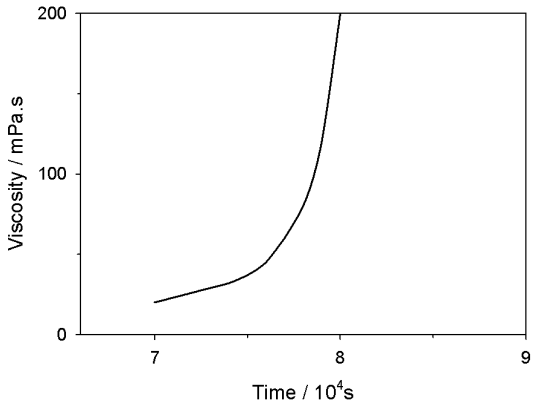

Figure 2.6: Viscosity changes

Ageing The chemical evolution of gelled samples was investigated with the NMR technique [7]. It has been found that a continuous increase in the number of Q_3 and Q_4 Si species (Si attached via oxygen links to other 3 or 4 other silicon atoms) is related to the condensation reactions of hydroxy groups. This evolution can continue for months if the samples are kept at room temperature. The net effect of the chemical evolution is a stiffening and shrinkage of the samples. Shrinkage is due to the formation of new bonds where former weak interactions between alkoxy and hydroxy groups were present. The shrinkage promotes the expulsion of the liquid contained into the porous gel (syneresis), so that the appearance becomes transparent. Another process related to the ageing stage is often refereed to as coarsening or ripening. In this process, material coming from the surface of large particles can precipitate on the initial narrow necks which join particles to each other. Figure 2.7 shows the scheme to explain the ripening

process.

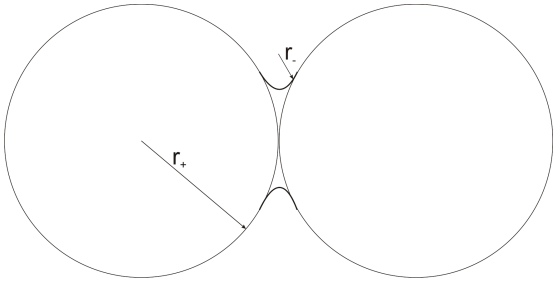

Figure 2.7: Curvature of particles and necks

The surface of a particle has a positive radius (r_+) whereas that of the neck between two particles is smaller and negative (r_-). As explained by the Kelvin equation [3], across a curved interface between two media, a pressure gradient can be determined. This is related to a different solubility of regions with a different radius of curvature. The solubility of a solid material with curved surface of radius r is related to the solubility of a flat surface S_0 by the following equation:

$$S = S_0^{\frac{2\gamma_{sl}V_m}{RTr}} \tag{2.15}$$

where V_m is the molar volume of the solid particle and T is the temperature. Small particles have high solubility whereas regions with negative curvature have small solubility. Therefore, materials tends to be accumulated at the necks with negative curvature. However, the ageing stage becomes very important when solutions have to be stored and the sol stability has to be guaranteed for long times.

Drying In the first part of this stage, gels shrink by an amount equal to the volume of water or liquid evaporated. As the gels dry and shrink, the compact structure and the additional cross-linking formed lead to the increase of the stiffness of the structure. At a critical point, the structure becomes stiff enough to resist further shrinkage as liquid continues to evaporate. At this point, the liquid begins to withdraw into the porous structure and, due to the surface tension and the small porous size, a very high gradient pressure across the curved surface of the liquid menisci in the pores is generated. Due to this critical stress, gels tend to crack at this point.

Densification There are many applications where sol-gel systems are prepared and dried at room temperature but in many other cases sol-gels have to undergo thermal treatment. The production of dense ceramic materials from gels requires the use of thermal treatments. From the discussion so far in this section, it is clear that controlling the hydrolysis, condensation, ageing and drying stages, materials with a wide range of characteristics can be obtained. Therefore, the effect of thermal treatment on the final structure depends on the former stages at low temperature. Three different regions can be observed during thermal treatment of silica gels and they are reported in Figure 2.8

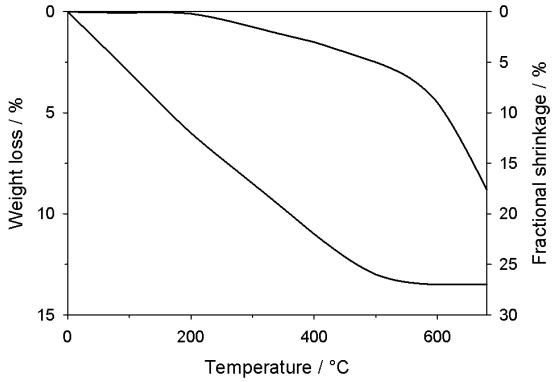

Figure 2.8: Stage of densification

The first stage can be identified at temperatures lower than 200 °C where weight loss occur and a little shrinkage takes place. At temperatures ranging from 200 °C to 700 °C, the sol-gel structure displays both weight loss and shrinkage. In this intermediate region, three processes occur simultaneously: loss of organic compounds (leading to weight loss but small shrinkage), further condensation (producing both, weight loss and shrinkage) and structural relaxation (giving shrinkage but no weight loss). The loss of organic compounds proves that at this stage the matrix is still porous. Indeed, the space occupied in the matrix by the former organic species, at this stage becomes porous (due to the organic compound loss) with the size of the organic compounds dimension. However, structural relaxation and further condensation gradually lead to the porosity reduction. At temperature above the upper limit of the intermediate region, a sharp increase in shrinkage can be observed whereas weight loss is negligible. The transition temperature is close to the glass transition temperature for the

material, above which there is a viscous flow leading to rapid densification.

2.2.2 Metal Oxide Gels

Metal oxides can be prepared via two different methods, depending on whether the precursor is a metal organic compound (as in the case of silica gel described in 2.2.1) or an aqueous solution of inorganic salts. In both cases, the chemistry is dominated by the high electropositive character of metal atoms relative to that of silicon. Table 2.3 shows the estimated partial positive charge on the central atom in a series of metal ethoxides [8].

Ethoxide	$Zr(OEt)_4$	$Ti(OEt)_4$	$Nb(OEt)_5$	$Ta(OEt)_5$
$\delta(M)$	+0.65	+0.63	+0.53	+0.49

Ethoxide	$VO(OEt)_3$	$W(OEt)_6$	$Si(OEt)_4$
$\delta(M)$	+0.46	+0.43	+0.32

Table 2.3: $\delta(M)$ partial positive charge

This means that the rate of the nucleophilic attack on the central metal atom is much faster than on silicon alkoxide precursors. The estimation of the hydrolysis rate at pH 7 for $Si(OEt)_4$ is around $5 \cdot 10^{-9} M^{-1} s^{-1}$ whereas it is $10^{-3} M^{-1} s^{-1}$ for $Ti(OEt)_4$. The several coordination numbers and the geometry of metals allow the metals to take on a wide range of permissible transition states in contrast to the limited reactions permitted to silicon state. Metal alkoxides are more versatile than silicon alkoxides but they are also more reactive, particularly with moisture. Therefore, it is necessary to be carefully when sols, based on metal alkoxides, are stored, handled and prepared [9, 10, 11, 12].

Reactions of Metal Oxide precursors The hydrolysis reaction occurs involving a nucleophilic attack of the metal alkoxide without acid or base catalysis. The reaction follows the proton transfer from a water molecule to the alkoxy group. The effect of the reactions is the hydrolysis of the alkoxide which leaves an alcohol molecule as shown in Figure 2.9:

This reaction is followed by the reaction between the product of the reaction in figure 2.9 with an alkoxide (alcoxolation), as displayed in Figure 2.10:

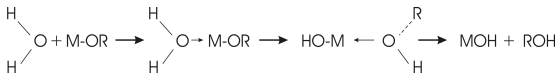

Figure 2.9: Metal alkoxide hydrolysis

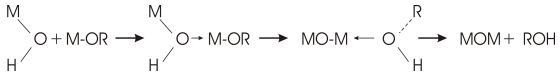

Figure 2.10: Metal alkoxide hydrolysis: alcoxolation

or with another hydrolyzed alkoxide (oxolation), shown in Figure 2.11:

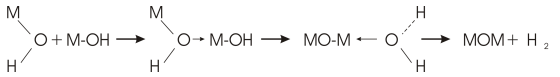

Figure 2.11: Metal alkoxide hydrolysis: oxolation

Many factors affect the thermodynamics and kinetics of metal alkoxide reactions: the partial negative charge of the incoming nucleophile, the partial positive charge of the electrophilic metal, the partial charge of the leaving group, the acid or base catalysis, the steric factors, the organic chain length and the solvent used. For example, when the precursor based on $Zr(OPr^n)_4$ is dissolved in n-propanol, the propanol associates with the propoxide species and hydrolysis rapidly leads to a precipitate while the same precursor is dissolved in cyclohexane, oligomeric metal alkoxide species are formed which hydrolyze more slowly leading to a gel rather than a precipitate. However, by controlling the hydrolysis and condensation reactions is possible to obtain metal oxide materials from metal alkoxides. The control of reactions can be made increasing the chain length of precursors, modifying the solvent or adding chelating ligands to the starting solution. Indeed, finer control is achievable via the use of chelating ligands which form mixed complexes with alkoxide ligands. Studies on the stabilization of tetra(i-propoxy)titanium(IV) with acetylacetone [13, 14] reveal that the structure formed hydrolyzes slower than the non stabilized precursor. However, care must be taken to ensure that all the chelating ligands are finally removed in the applications where pure oxides are required. Similar results have been obtained by treating metal alkoxides with acetic acid [13], which is able to form bridging carboxilate complexes as shown in Figure 2.12.

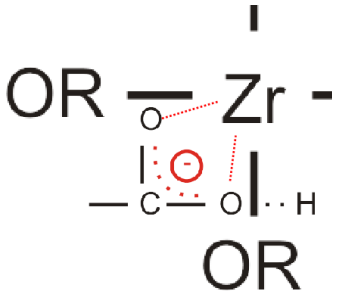

Figure 2.12: Hydrolysis control by acetic acid

2.2.3 Applications of sol-gel systems

Sol-gel technology enables us to produce ceramics and glasses with an alternative route at a low processing temperature. As fully discussed in the paragraph 2.2, films and bulk materials can be produced at low temperature with the adequate properties required by each application and depending on its shape. From the sol-gel method, it is furthermore possible to produce porous material applications where a controlled porous size is needed. The added value of the sol-gel approach is often the determining factor which allows to produce high quality materials. Optical materials, chemical sensors, electronic and catalytic materials are some examples of applications where a sol-gel process can be used. Nevertheless, the most interesting field where a sol-gel process would be very useful is the coating field. The sol-gel method enables to coat curved surfaces and large areas using simple deposition techniques and it allows to produce systems with a multilayer structure which can not be produced employing other methods. Sol-gel layers have been used for the production of passivation coatings, coatings with antireflection properties, adhesion promoters, biocompatible coatings, antisoiling coatings and so on [15, 16, 17]. Thin sol-gel layers can be deposited by dip or spin coating technology [18, 19]. Sol-gel coatings deposited by spin technology are less dense than those applied by dipping. The structure of films deposited by dipping is aligned along the withdrawal direction and the cross-linked structure can develop more easily. The density of sol-gel coatings deposited by spin or dip techniques depends on their thickness: thin layers are denser than thick films. Moreover, there are some general rules related to the sol-gel process: lower alkyl groups of alkoxides produce denser films with higher oxygen content, the pore size depending on the solvent. Higher water contents during hydrolysis produce

denser films, aggregation of particles prior to deposition leads to highly porous films.

2.3 Electrochemical Techniques

The electrochemical evaluation can be carried out following two distinct approaches. Electrochemical measurements can be performed applying an input perturbation which can be either time-depending or non time-depending. In the former case, the electrical parameters are periodic waves while in the latter case constant functions are employed to perform electrochemical measurements. Measurements performed with variable input waves belong to the Alternate Current (AC) methods while measurements involving non time-depending functions are encompassed in Direct Current methods (DC).

2.3.1 Direct Current methods

When a corrosion process proceeds following an electrochemical mechanism, anodic and cathodic reactions are coupled with an electronic current across the metal and an ionic current in the electrolyte [20, 21]. For the investigation of electrochemical reactions, DC methods can be used and they are able to give information about the determination of corrosion rates, the evaluation of corrosion mechanisms and the determination of critical potentials. By using DC methods, potential or current values can be measured. The Open Circuit Potential (OCP) of a corroding electrode is measured between this electrode and a stable reference electrode. OCP measurement enables to obtain information about the determination of the activity/ passivity of metals and the evolution of electrochemical systems in aggressive solutions while it is not able to quantify the rate of the corrosion process. Otherwise, it is possible to estimate the value of the rate of chemical consumption of metals by means of the measurements of the flow of electric current related to partial reactions (i.e Faraday's Law). However, the direct measurement of the corrosion current is difficult because the corroding electrode surface consists of many short-circuited corrosion cells, with corresponding currents. For this reason, current measurements are carried out in the electrolyte since the currents in the metal are equal to the current flowing in the electrolyte.

When the potential of a corroding metal surface is changed by applying an

external source, the metal will be polarized. Polarized measurements can be carried out near the corrosion potential or far away from the corrosion potential (greater than 100mV).

Measurements for the determination of the polarization resistance, the potentials and the currents of corrosion cells are included in the former. On the other hand, measurements carried out far from corrosion potential are used for the detection of total polarization curves in order to evaluate the electrochemical behaviour, to identify the pitting potential and to evaluate the passivation and the re-passivation potentials. Polarization measurements are therefore performed by applying an input δV or a δI signal with a scan rate depending on the kind of measurements to perform. The output signal is measured and the data acquired is displayed in a V-I diagram. The corrosion resistance R_p is defined as the slope of the current density- potential curve at the corrosion potential, as follows:

$$R_p = (\frac{dE}{di})_{E \to E_{corr}} \tag{2.16}$$

where R_p is inversely proportional to the corrosion rate. The anodic branch of a polarization curve depicts the oxidation reactions occurring on the electrode surface while reduction reactions are evaluated by the cathodic branch. In electrochemistry, anodic currents are defined as positive while the cathodic ones are negative [48].

2.3.2 Alternating Current methods

AC electrochemical methods are developments of the DC techniques that have been just discussed in 2.3.1. AC methods are time-depending because a periodic input signal is applied during measurements. Electrochemical Impedance Spectroscopy (EIS) is encompassed in this method group [22]. Electrochemical Impedance Spectroscopy (EIS) and in general AC methods have seen a tremendous increase in popularity in recent years. Initially applied to the determination of the double-layer capacitance [23] and in AC polarography [24, 25, 26], they are now applied to the characterization of electrode processes and complex interfaces. EIS studies the system response to the application of a periodic small amplitude AC signals. These measurements are carried out at different ac frequencies and, thus, the name impedance spectroscopy was later adopted. Analysis of the system response contains information about the interface, its structure and reactions

taking place there. EIS is now described in the general books of electrochemistry, specific books on EIS, and there are also numerous articles and reviews. It became very popular in the research and applied chemistry. The Chemical Abstract database shows 1,500 citations per year of the term impedance since 1993 and 1,200 in earlier years and 500 citations per year of electrochemical impedance. The approach used for EIS measurements results from the approach used for DC measurements. For example, the linear polarization technique (DC) is often carried out by applying a slow potential sweep of low magnitude about the corrosion potential and measuring the resulting net current. The net current is defined as the net anodic current ($I_{net} = I_{anodic} - I_{cathodic}$) which is considered positive. The use of a slow sweep potential and a small amplitude of the input perturbation is applied to guarantee the optimal conditions to perform electrochemical measurements. For small applied over-potentials η (where $\eta = E_{applied} - E_{corr}$) the net current is proportional to the over-potential, as follows:

$$I_{net} = \frac{\eta}{R_p} \tag{2.17}$$

where R_p is the polarization resistance. The R_p is the only component describing the behaviour of a corroding metal polarized by a DC input signal. Otherwise, for alternating methods, corroding systems are described by one more component, the capacitance C_{dl} of the surface [22]. Therefore, by applying a periodic input perturbation, a deeper and more useful electrochemical investigation can be performed. In the case of electrochemical measurements, a sine wave perturbation is generally used. Considering the input and the output signal as follows:

$$\begin{aligned} x(t) &= A\sin(\omega t) \rightarrow INPUT\ SIGNAL \\ y(t) &= B\sin(\omega t + \phi) \rightarrow OUTPUT\ SIGNAL \end{aligned} \tag{2.18}$$

considering the transfer function $H(\omega)$ as follows:

$$H(\omega) = |H(\omega)|e^{j\phi} = \frac{Output\ signal}{input\ signal} \tag{2.19}$$

it is possible to define the impedance function imposing the current and the potential perturbations as input signal and output signal, respectively:

$$Z(\omega) = |Z(\omega)|e^{j\phi} = \frac{V}{I}e^{j\phi} \tag{2.20}$$

which can be written as:

$$Z(\omega) = Re\{Z\} + jIm\{Z\} \tag{2.21}$$

Data acquired can be depicted by either Bode representation described by equation 2.20 or Nyquist 2.21 representation showing the real and the imaginary parts of the impedance function. An impedance measurement can be considered valid when it obeys three fundamental conditions:

Linearity A system is linear when its response to a sum of individual input signals is equal to the sum of the individual responses. This also implies that the system is described by a system of linear differential equations. When an electrochemical system is perturbed by an external power source, the charge flowing and the mass transport phenomena occur. These are due to two different aspects: the first is related to the electrochemical reactions which allow the charge flowing between metal and solution. The second is related instead to the electric and the chemical potential gradients which allow the transport of chemical species between the solution and the interface metal/solution. The laws governing the mass and the charge transport are basically non linear. For example, the Tafel's Law correlates the faradic current and the potential as follows:

$$i_F = i_0 e^{\frac{\alpha n F}{RT}\Delta V} \tag{2.22}$$

which is non linear. However, it has been seen that the behaviour of non linear systems can be explained by the sum of linear contributions. Therefore, local analysis of non linear systems can be solved in the field of the linear system theory. From an experimental point of view, the performing of electrochemical measurements by applying a small input perturbation, enables to maintain the analysis in the field of linear system theory. For the linear systems the response is independent of the amplitude. It is easy to verify the linearity of the system: if the obtained impedance is the same when the amplitude of the applied ac signal is halved then the system is linear.

Causality The response of the system must be entirely determined by the applied perturbation, that is the output depends only on the present and past

input values. The causal system cannot predict what its future input will be. Causal systems are also called physically realizable systems. If the system is at rest and a perturbation is applied at t = 0, the response must be zero for $t < 0$. In the complex plane the above criterion requires that, for $t < 0$, $\omega = 0$.

Stability The stability of a system is determined by its response to inputs. A stable system remains stable unless excited by an external source and it should return to its original state once the perturbation is removed and the system cannot supply power to the output without considering the input. The system is stable if its response to the impulse excitation approaches zero at long times or when every bounded input produces a bounded output. The impedance measurements must also be stationary, that is the measured impedance must not be time dependent. This condition may be easily checked by repetitive recording of the impedance spectra; then the obtained Bode or Nyquist plots should be identical.

Impedance measurements can be fitted using an electric circuit as a physical model. Data elaboration allows to calculate values related to the electrochemical system under study. Circuits can be composed of resistors, capacitors and other components. Since an impedance spectrum can be fitted by an infinite number of electric circuits, the chosen model must physically describe the electrochemical system. Therefore, electrical components can be associated to the electrochemical and chemical properties of corroding and coated electrodes. Electrical model are usually composed by:

R_s resistance of the electrolyte

R_{ct} charge transfer resistance related to the energy activation of chemical reactions. Considering a generic metal oxidation reaction $M \rightarrow M^{n+} + ne^-$, such reaction has to be over an opportune energy level

R_{coat} coating resistance due to the barrier provided by a protective layer

C_{dl} double layer capacitance related to charge separation (ions and electrons) at the interface between the metal and the electrolyte

C_{coat} coating capacitance related to the insulating properties of a protective layer

EIS fitted data enable to calculate the values of the electrical components and they are useful to determine the electrochemical behaviour of a corroding system as a function of immersion time. This can not be done with other techniques like polarization curves being destructive analytical methods. For example, EIS measurements are able to give information about R_{ct} (which is equal to R_p although it does not consider the diffusion contribution but only the activation) which is inversely proportional to the corrosion rate described by the equation 2.17. Figure 2.13 shows the Bode module, the Bode phase and the Nyquist diagrams of the impedance spectrum of an electrical circuit consisting of a parallel RC mesh connected in series with a resistor (Figure 2.13(a)). The circuit can be used to fit the impedance data for the evaluation of the R_{ct}, the R_{sol} and the C_{dl} values. The Bode module plot consists of a straight region where the angle between the curve (the impedance spectrum is acquired point by point but in this example a continuous curve is reported for explanation convenience) and the X-axis is equal to 45 °. In that region, the behaviour can be approximated to the behaviour of a pure capacitor. The impedance module of a pure capacitor is described as follows:

$$\begin{aligned} |Z_C| = \frac{1}{\omega C} \Rightarrow \log|Z_C| = \log\left(\frac{1}{\omega C}\right) = \log 1 - \log(\omega C) \\ \Rightarrow \log|Z_C| = -\log(\omega) - \log(C) \end{aligned} \tag{2.23}$$

The equation (2.23) explains the linear dependence between the $\log|Z|$ and the perturbation frequency (which is directly proportional to ω) in the middle region of the impedance spectrum reported as example in Figure 2.13.

2.3.3 The Microcell Technique

Large scale electrochemical measurements are able to provide information about the behaviour of regions in the centimeter-range. Therefore, OCP measurements, polarization curves and EIS measurements can not be used to study the local behaviour of corroding electrodes. The micro-cell technique has been developed for electrochemical studies in the scale ranging from micrometers to a few hundred nanometers [27, 28, 29]. The technique is based on the reduction of the electrochemical cell by using a glass micro-capillary. The working electrode is then defined by the inner size of the glass micro-capillary. In order to avoid solution

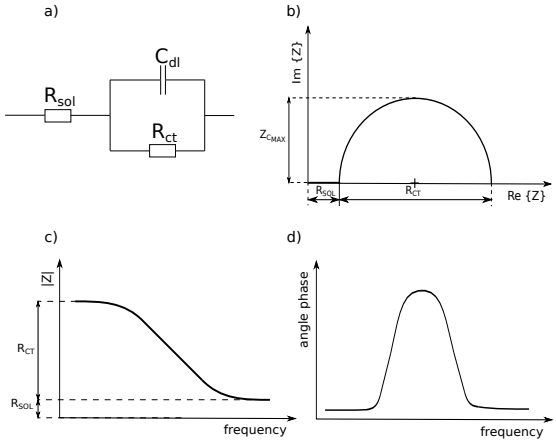

Figure 2.13: Example of Bode module, Bode phase and Nyquist diagrams

leakage at the interface between micro-capillary and the corroding electrode, the tip of the glass micro-capillary is covered by the application of a silicon rubber gasket. This expedient enables to configure the setup wetting only the region of the metal substrate where the measurement has to be performed. Figure 2.14 shows the glass micro-capillary tip after grinding.

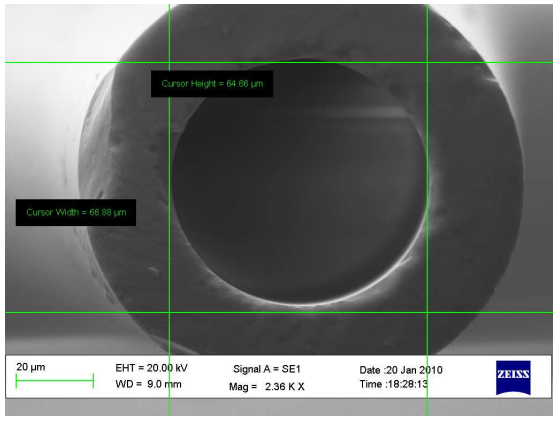

Figure 2.14: Glass micro-capillary with silicone sealant

By reducing the working electrode area, it is possible to investigate heterogeneous regions which can give different electrochemical responses. The size of the region which is possible to investigate is determined by both the micro-capillary size and the lower current resolution of the potentiostat [28]. In order to select the region of interest where measurements have to be performed, the micro-cell is mounted on the revolving nose-piece of an optical microscope. This set

up enables to point the measurements towards the region desired and observable by the optical microscope. The electrochemical behaviour of heterogeneous micro-structures of several metal alloys can be therefore investigated by using the micro-cell technique. The lateral resolution of this technique, which depends on the micro-capillary size, determines the micro-structure size to investigate. For example, by employing a glass micro-capillary with a 50 μm size, micro-structure phases which can be studied without interference of other intermetallics, have to be larger than the micro-capillary size. Otherwise, measurements carried out on phases smaller than the micro-capillary size are affected by the surrounding regions wetted by the electrolytic solution. However, the local evaluation of OCP rather than the anodic or cathodic behaviour can give information that the macro-electrochemical instrumentation setup is not able to provide. The micro-cell technique has been often used for the electrochemical investigation of the behaviour of aluminum alloys. Interesting results were obtained studying aluminum alloys of the 2xxx series [30]. It was found that breakdown potential of regions containing Al-Cu-Mg intermetallics is more negative than that of regions containing Al-Cu-Fe-Mn intermetallics. Moreover, the breakdown potential of the matrix is more positive than in any other region.

Bibliography

[1] C.J. Binder, G.W. Scherer, Sol-gel Science: The physic and chemistry of sol-gel processing, Academic Press: London, 1990

[2] D.J. Shaw, Colloid and Surface Chemistry, Butterworth, 4^{th} ed., 1992

[3] J.D. Wright, N.A.J.M. Sommerdijk Sol-gel Materials-Chemistry and Application, SCRIVERE EDITORE

[4] B.K. Coltrain, S.M. Melpolder, J.M. Salva, Proceeding 4th Int. Conf. Ultrastructure Processing and Composites, New York, 1989

[5] P.J. Flory Principles of Polymer Chemistry, CornellU.P: Ithaca, NY, 1953

[6] R. Zallen The Physics of Amorphous Solids, Wiley: New York, 1983

[7] A.J. Vega, G.W. Scherer J. Non-Cryst. Solids 111 (1989) 153

[8] J. Livage, M. Henry, C. Sanchez Prog. Solid St. Chem. 18 (1988) 259

[9] N. Bjerrum Z. Phys. Chem. 59 (1907) 336

[10] A. Werner Ber. 40 (1907) 272

[11] P. Pfeiffer Ber. 40 (1907) 4036

[12] L.G. Sillen Quart. Rev. 13 (1959) 146

[13] J. Livage, C. Sanchez, M. Henry, S. Doeuff Solid State Ionics 32 (1989) 633

[14] F. Babboneau, A. Leaustic, J. Livage Better Ceramics Through Chemistry III Mater.Res.Soc.Symp.Proc Pittsburgh (1988) p.317

[15] D.R. Gerritsen, A. Kros, J.A. Lutterman, R.J.M. Nolte, J.A. Jansen Biomaterials 32 (1989) 633

[16] D.R. Uhlmann, T. Suratwala, K. davidson, J.M. Boulton, G. Teowee J. Non-Cryst. Solids 218 (1997) 113

[17] D.R. Uhlmann, G.P. Rajendran SPIE Proc. 1328 (1990) 270

[18] C.J. Brinker, A.J. Hurd, P.R. Schunk, G.C. Frye, C.S. Ashley J. Non-Cryst. Solids 147 (1992) 424

[19] B.E. Yoldas J. Sol-Gel Sci. Technol. 1 (1993) 65

[20] P. Marcus, F. Mansfeld Analytical Methods in Corrosion Science and Engineering CRC press, 2006

[21] C. Wagner, W. Traud Z. Electrochem. 44 (1938) 391

[22] R. Cottis, S. Turgoose Electrochemical Impedance and Noise Houston, Texas, 1999

[23] D.M. Mohilner Electroanalytical Chemistry Ed., Dekker, New York, 1966, p.241

[24] B. Breyer, H.H. Bauer Alternating Current Polarography and Tensammetry Wiley-Interscience, New York, 1963

[25] D.E. Smith Electroanalytical Chemistry New York, Vol. 1, 1966, p.1

[26] A.M. Bond Modern Polarographic Techniques in Analytical Chemistry Dekker, New York, 1980

[27] H. Bohni, T. Suter, F. Assi Surf. Coat. Technol. 130 (2000) 80

[28] M.M. Lohrengel, A. Moehring, M. Pilanski Electrochim. Acta 47 (2001) 137

[29] M.M. Lohrengel, A. Moehring, M. Pilanski, J. Fresenius J. Anal. Chem. 367 (2000) 334

[30] T. Suter, C. Alkire J. Electrochem. Soc. 148 (2001) B36

[31] ASM HANDBOOK

[32] J. Konieczny, L.A. Dobrzanski, K. Labisz, J. Duszczyk J. Materials Processing Technology 157 (2004) 718

[33] E. Zhuravlyova, L. Iglesias-Rubianes, A. Pakes, P. Skeldon, G.E. Thompson, X. Zhou, T. Quance, M.J. Graham, H. Habazaki, K. Shimizu Corros. Sci. 44 (2002) 2153

[34] V. Lopez, J.A. Gonzalez, E. Otero, E. Escudero, M. Morcillo Surface and Coatings Technology 153 (2002) 235

[35] P. Campestrini, E.P.M. van Westing, A. Hovestad, J.H.W. de Wit Electrochimica Acta 47 (2002) 1098

[36] O. Lunder, J.C. Walmsley, P. Mack, K. Nisancioglu Corros. Sci. 47 (2005) 1604

[37] O. Lunder, C. Simensen, Y. Yu, K. Nisancioglu Surface and Coatings Technology 184 (2004) 278

[38] J.H. Nordlien, J.C. Walmsley, H. Osterberg, K. Nisancioglu Surface and Coatings Technology 153 (2002) 72

[39] L. Fedrizzi, F. Deforian, P.L. Bonora Electrochimica Acta 42 (1997) 969

[40] M.L. Jenkins, R.H. Dauskardt, J.C. Bravman J. Adhesion Sci. Technol. 13 (2004) 1497

[41] A. Franquet, C. Le Pen, H. Terryn, J. Vereecken Electrochimica Acta 48 (2003) 1245

[42] F. Deforian, S. Rossi, A. Cambruzzi, L. Fedrizzi ICEPAM Conference 2004 16-18 June, CD-ROM, Oslo

[43] A. Ramrus, J.C. Berg J. Adhesion Sci. Technol. 12 (2004) 1395

[44] A.E.W. Hughes, R.J. Taylor, B.R.W. Hinton, L. Wilson Surf. Interface Anal. 23 (1995) 540

[45] M. Dabala, L. Armelao, A. Buchberger, I. Calliari Applied Surface Science 172 (2001) 312

[46] A. Decroly, J.P. Petitjean Surface and Coatings Technology 2 (2005) 194

[47] M. Bethencourt, F.J. Botana, M.J. Cano, M. Marcos Applied Surface Science 189 (2002) 162

[48] M.G. Fontana Corrosion Engineering McGraw-Hill Book Company, 1986

Chapter 3

Materials and Experimental Procedure

The production and the characterization of sol-gel coatings deposited by dipping require several experimental steps. First of all, metal substrates have to be prepared for the sol-gel deposition. Metal substrates are modified by the degreasing and the pickling treatments in order to produce favourable surface conditions for the following coating deposition. Sols were prepared starting from precursors diluted in organic or inorganic solvents. The calculation of the precursor amount to add is necessary to predict the sol rheology and the coating properties. The addition of functional chemical species to the precursor solution can be done following a route that allows the control of hydrolysis and condensation reactions. Sol-gel coatings deposited on metal substrates have to be then analyzed by means of surface characterization and by electrochemical techniques. In this stage, by evaluating both the surface morphology and the corrosion properties of the coatings, it is possible to modify the synthesis parameters and the deposition procedure in order to find the optimal conditions for the production of sol-gel defect-free coatings. Synthesis and deposition stages are important as well as the characterization step, because feedbacks coming from the latter stage are necessary for the improvement of the former stages which are tightly related to the coating quality. In this chapter, a general discussion on materials, experimental procedures and characterization techniques has been carried out. An example of the sol-gel synthesis and a general information on the entire process are here reported. An exhaustive description of the experimental procedure is reported at the beginning of each one of the chapters in which results are discussed.

3.1 Materials

In this work, aluminum alloys were employed as metal substrates for sol-gel depositions. Three different categories of aluminum alloys were employed during the development of the project. AA2024 aluminum alloy was used for the optimization of zirconia based coatings while the AA6060 type was used for the study of the inhibition effect provided by zirconia based sol-gel films containing cerium nitrate. At a later stage of the research project, the coating deposition was carried out with a robot-controlled air pressure gun in spraying cabins, in order to evaluate industrial production of the ZrO_2 film. Three types of aluminum demonstrators were industrially produced: AA6013 panel with AA6061 stringers for aerospace industry application; AA7075 skin with holes for rivets in the aircraft industry application and AA3105 sheets for coil-coating application in the field of the domestic appliances industry. The alloys' compositions are given in Table 3.1.

	AA2024	**AA3105**	**AA6013**	**AA6060**	**AA6061**	**AA7075**
Si	0.5 max	0.6 max	1-1.5	0.3-0.6	0.4-0.8	0.4 max
Fe	0.5 max	0.7 max	0.5 max	0.1-0.3	0.7 max	0.5 max
Cu	3.8-4.9	0.3 max	0.2 max	0.1 max	0.15-0.4	1.2-2
Mn	0.3-0.9	0.3-0.8	0.2 max	0.1 max	0.15 max	0.3 max
Mg	1.2-1.8	0.2-0.8	0.2-0.5	0.35-0.6	0.8-1.2	2.1-2.9
Cr	0.1 max	0.2 max	0.1 max	0.05 max	0.04-0.35	0.18-0.28
Zn	0.25 max	0.4 max	0.2 max	0.15 max	0.25 max	5.1-6.1
Ti	0.15 max	0.1 max	0.15 max	0.1 max	0.15 max	0.2 max
Al	balance	balance	balance	balance	balance	balance

Table 3.1: Aluminum alloys chemical composition

3.2 Degreasing and Pickling Procedures

The surfaces of commercial metals and alloys vary as produced and fabricated. The degree of scaling or amounts of oxide varies and and also the content of other contaminants like oils and greases. Because of this situation, the cleaning of the metal surface is usually required. The dirt and oils elimination is carried out by

an alkaline cleaning process while the removal of scaling oxides is obtained by a pickling procedure. The surface preparation was performed according to a general procedure employed for aluminum and its alloys. This procedure was carefully fitted to every alloy category considered in the thesis. The alkaline cleaning bath is basically composed by surface-active agents able to roughly clean the metal substrates. The pickling procedure can be divided into two different steps: the alkaline etching and the acid etching. The former bath is constituted by an alkaline solution of a strong base like $NaOH$. The latter bath contains a diluted acid which can be a mixture of different acids in which the phosphoric acid plays an important role. The alkaline etching dissolves the aluminum oxide which however re-precipitates on the alloy surfaces and it is re-solubilized by the acid etching. The alkaline cleaning and the alkaline etch were carried out at 70 $^{\circ}C$ while the acid etch step was performed at 25 $^{\circ}C$. After every cleaning step, the aluminum alloy samples were immersed in distilled water in order to avoid the contamination of the baths. For example, in the usual procedure employed for AA2024 aluminum alloy, the alkaline cleaning step was carried out for 15 minutes, the alkaline etching for 2 minutes and the acid etching for 7 minutes. Since surface preparation according to the that procedure strongly increased the roughness of the alloy surface (holes and cavities), times of alkaline etching and acid etching were then varied with respect to the standard. Alkaline etching times of 1 minute and 3 minutes and acid etching times of 5 minutes and 10 minutes were then selected. Several attempts were made to produce a less rough surface to make the sol-gel deposition more easy to perform. The weaker surface preparations were not able to completely remove the contaminant species on the surface and it was decided to employ the standard procedure for the optimization of the sol-gel deposition process. The morphology obtained after the surface preparation will be shown and discussed in the chapter 4 and in the chapter 8.

3.3 Sol-gel Synthesis and Inhibitor aggregation

This section describes the general procedures employed for the synthesis of zirconia based sols. Soluble precursors in inorganic or organic solvents were used. Zirconium butoxide ($Zr(OBu^n)_4$) and zirconium propoxide ($Zr(OPr^n)_4$) were used as metal-organic precursors diluted in ethanol or butanol. Zirconyl nitrate was used as salt precursor for the development of water-based systems. The

present paragraph is focused on the sol preparation from metal-organic precursors. In the following part, the description of the sol preparation relative to the coating systems evaluated in chapter 8 is reported. These coatings are based on a multi-layer structure which is composed of three different layers. However, the discussion on the structure and the chemical composition of these systems is treated in more detail in chapter 8. The first step for sol preparations is to define the amount of precursors to add. Indeed, as discussed in the Introduction (see chapter 2), the sol concentration controls the structure and the thickness of sol-gel films. The synthesis considered as example, starts from the sol 0.1M ($Zr(OPr^n)_4$). The precursor amount to add in 1 Liter of alcohol (ethanol), is given by the following equation (3.1):

$$\begin{aligned} n^{\circ}mol_{Zr(OPr^n)_4} &= \frac{mass_{Zr(OPr^n)_4}}{Molecular\ Weight_{Zr(OPr^n)_4}} \\ &= 0.1 \cdot 327.548 = 32.7548\ g\ (for\ liter) \end{aligned} \tag{3.1}$$

Since the density of the compound containing the $Zr(OPr^n)_4$ precursor is $1.058 KgL^{-1}$ ($\rho_{precursor\ compound}$), it is possible to calculate the volume of the precursor compound to add for the preparation of 0.1M sol. In this work, the amount of the precursor compound was calculated as follows:

$$Volume_{precursor\ compound} = \frac{mass_{Zr(OPr^n)_4}}{\rho_{precursor\ compound}} = \frac{32.7548}{1.058} = 30.959\ mL \tag{3.2}$$

However, the precursor compound is not pure and it is necessary to calculate the exact volume containing 0.1M $Zr(OPr^n)_4$. Since the precursor is diluted 70% in volume, the total amount of precursor compound to add is given by the following equation (3.3):

$$Volume^*_{precursor\ compound} = \frac{Volume_{precursor\ compound}}{0.7} = 44.2274\ mL \tag{3.3}$$

which corresponds to the mass:

$$\begin{aligned} mass_{precursor\ compound} &= Volume^*_{precursor\ compound} \cdot \rho_{precursor\ compound} \\ &= 44.274 \cdot 1.058 = 46.79258\ gL^{-1} \end{aligned} \tag{3.4}$$

As described in the Introduction (chapter 2), metal oxide gels need to be stabilized by adding chelating ligands. In the synthesis carried out in this project, acetic acid (AcH) was used for this purpose. Different $\frac{[AcH]}{[Zr]}$ molar ratios were proposed for the sol synthesis. After the evaluation of the sols stability, it was established that the $\frac{[AcH]}{[Zr]}$ molar ratio equal to 1, allows to produce stable sols.

$$\frac{[AcH]}{[Zr(OPr^n)_4]} = 1 \;\Rightarrow\; n^\circ mol_{AcH} = 0.1 \cdot n^\circ mol_{Zr(OPr^n)_4} = 0.1\ mol \tag{3.5}$$

which corresponds to the mass:

$$mass_{AcH} = n^\circ mol_{AcH} \cdot Molecular\ Weight_{AcH} = 0.1 \cdot 60.048 = 6.0048\ g \tag{3.6}$$

corresponding to the acetic acid volume:

$$Volume_{AcH} = \frac{mass_{AcH}}{\rho_{AcH}} = \frac{6.0048}{1.06} = 5.6649\ mL \tag{3.7}$$

The hydrolysis of precursors needs to be promoted by adding distilled water. In the case of metal oxide gels, hydrolysis reaction can occur without the addition of water because the precursors can easily react with the atmospheric humidity. However, the synthesis was initially carried out by adding the calculated water amount considering a $\frac{[H_2O]}{[Zr]}$ molar ratio equal to 1.

$$\frac{[H_2O]}{[Zr(OPr^n)_4]} = 1 \;\Rightarrow\; n^\circ mol_{H_2O} = 0.1\ mol \tag{3.8}$$

which corresponds to the mass:

$$mass_{H_2O} = n^\circ mol_{H_2O} \cdot Molecular\ Weight_{H_2O} = 0.1 \cdot 18 = 1.8\ g \tag{3.9}$$

Sol syntheses are usually carried out under acid conditions. In our case, the sol pH was reduced by adding nitric acid HNO_3. To reduce the sol pH, 0.1M HNO_3 acid solution was added . It was calculated that for 1 L of solution, a volume of nitric acid equal to 6.3 mL had to be added. However, with this acidification it was not possible to obtain stable solutions because the hydrolysis and the condensation reaction rates had increased too much. The sol viscosity became higher than 8 $mPa \cdot s$ in a very limited length of time leading to rheological properties

incompatible with the deposition of defect-free sol-gel coatings. For this reason, the synthesis was carried out without the addition of nitric acid and in a following step without the addition of distilled water. Therefore, the final precursor solution was consisting of $Zr(OPr^n)_4$ (eq. 3.3) and acetic acid (eq. 3.7) both diluted in 1 L of ethanol. The synthesis procedure brought to the production of zirconia based coatings, the structure of which should be composed by zirconium-oxygen covalent bonds. Nevertheless, the strategy of the project was to develop sol-gel systems able to provide self-healing ability. Since ZrO_2 films ca not provide self-healing ability, the addition of chemical species able to offer an active protection against corrosion was made. The inhibition action related to cerium compounds (chapters 6 and 7) induced us to modify the sol synthesis in order to produce zirconia sol-gel coatings containing cerium compounds as inhibitor species. The new synthesis approach considered the addition of cerium nitrate directly into the sol. The syntheses the solutions containing the precursor and the inhibitor were carried out separately. In one vessel, the metal-organic precursor with the chelating ligands were diluted in alcohol. The remaining amount of alcohol was used for the dilution of the inhibitor compound and of distilled water. The two solutions were stirred separately for 30 minutes. At the end of this first step, the two solutions were mixed together and stirred for another hour to homogenize precursor and inhibitor molecules. Therefore, the final solution was ready for coatings deposition. Figure 3.1 shows the scheme of the synthesis procedure employed for the production of zirconia sols containing cerium nitrate as inhibitor species.

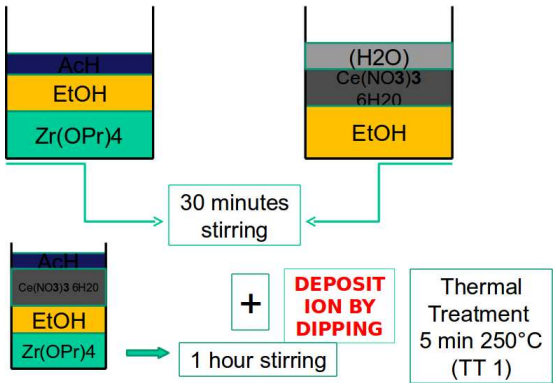

Figure 3.1: Synthesis scheme for zirconia sol containing cerium nitrate

The amount of cerium nitrate added was calculated taking into account the

initial concentration of the precursor. Inhibited solutions with three distinct precursor/inhibitor molar ratios were produced. The solution with the lowest cerium concentration was synthesized considering $\frac{[Zr]}{[Ce]} = \frac{[90]}{[10]}$. A molar ratio equal to $\frac{[Zr]}{[Ce]} = \frac{[70]}{[30]}$ was used for the production of the solution containing the highest amount of cerium while a third solution was produced with a molar ratio $\frac{Zr}{Ce} = \frac{[80]}{[20]}$.
As an example, in this chapter, the calculus for the production of the inhibited solution with $\frac{[Zr(OPr^n)_4]}{[Ce(NO_3)_3 \cdot 6H_2O]} = \frac{[70]}{[30]}$ has been considered. The precursor concentration corresponded to the same value used for the calculation of pure zirconia systems which is equal to 0.1M $Zr(OPr^n)_4$. The amount of cerium nitrate can be calculated by the equation 3.10, as follows:

$$n^\circ mol_{Ce(NO_3)_3 \cdot 6H_2O} = n^\circ mol_{Zr(OPr^n)_4} \cdot \frac{30}{70} = 0.04285 \; mol \tag{3.10}$$

which corresponds to the mass:

$$\begin{aligned} mass_{Ce(NO_3)_3 \cdot 6H_2O} &= n^\circ mol_{Ce(NO_3)_3 \cdot 6H_2O} \cdot Molecular\ Weight_{Ce(NO_3)_3 \cdot 6H_2O} \\ &= 0.04285 \cdot 434.202 = 18.6055 \; g \end{aligned} \tag{3.11}$$

For inhibited systems, the amount of chelating ligands has to be calculated proportionally to the sum of cerium nitrate and zirconium propoxide amounts. This corresponds to:

$$\frac{[AcH]}{[Zr + Ce]} = 2 \Rightarrow n^\circ mol_{AcH} = n^\circ mol_{(Zr+Ce)} = 2 \cdot (0.04285 + 0.1) = 0.2857 \; mol \tag{3.12}$$

which corresponds to the acid acetic mass:

$$mass_{AcH} = n^\circ mol_{AcH} \cdot Molecular\ Weight_{AcH} = 0.2857 \cdot 60.048 = 17.1557 \; g(L^{-1}) \tag{3.13}$$

The water amount for the synthesis can be calculated considering the same ratio of equation 3.8, as follows:

$$\frac{[H_2O]}{[Zr + Ce]} = 1 \;\Rightarrow\; n^\circ mol_{H_2O} = 0.14285 \; mol \tag{3.14}$$

which corresponds to the water mass:

$$mass_{H_2O} = n^{\circ}mol_{H_2O} \cdot Molecular\ Weight_{H_2O} = 0.14285 \cdot 18 = 2.5713\ g \quad (3.15)$$

However, it is necessary to consider that cerium nitrate is hydrated 6 times and for this reason the total water amount has to be re-calculated subtracting the cerium-water amount. The water amount bonded to cerium nitrate is equal to:

$$n^{\circ}mol_{H_2O\ cerium\ nitrate} = n^{\circ}mol_{Ce(NO_3)_3 \cdot 6H_2O} \cdot 6 = 0.04285 \cdot 6 = 0.2571\ mol \quad (3.16)$$

which corresponds to the water mass:

$$mass_{H_2O\ cerium\ nitrate} = n^{\circ}mol_{H_2O\ cerium\ nitrate} \cdot Molecular\ Weight_{H_2O} = 0.2571 \cdot 18 = 4.6278\ g \quad (3.17)$$

The water amount related to cerium nitrate (equation 3.17) is higher than the water amount calculated for hydrolysis reactions by equation 3.15. This means that the water amount bonded to cerium nitrate molecules is higher than the water amount necessary for the stoichiometric chemical reactions. For this reason, the sol synthesis performed in this work, was consequently carried out without the addition of the water amount calculated by equation 3.15 since conditions for hydrolysis reactions are guaranteed by the cerium nitrate coordinate water.
The synthesis procedure was therefore followed by the evaluation of the sols viscosity. A deeper investigation on viscosity measurements has been discussed in chapter 8 while in the present section the evolution of stable and non stable sols has been discussed. Viscosity measurements were performed by using a HAAKE, model RS 50 RheoStress. Viscosity measurements were performed immediately after the sol synthesis, every hour during the first day and every 24 hours for the first week. Figure 3.2 shows viscosity measurements carried out on stable and non stable systems. The solid curve corresponds to the sol with $\frac{[Zr]}{[Ce]} = \frac{90}{10}$ and $\frac{[AcH]}{[Zr]} = 1$ while the dash curve is related to a similar system with $\frac{[Zr]}{[Ce]} = \frac{90}{10}$ and a different zirconium/acetic acid molar ratio, equal to $\frac{[AcH]}{[Zr]} = 2$. The former system (not stable) evolves faster than the latter one (stable). This behaviour is most probably due to the different amount of chelating ligands added to the two

sols. In the case of the solution containing a higher amount of acetic acid, the nucleophilic attack of the metal oxide precursor is rendered more difficult and the hydrolysis reaction rate is reduced. Hence, for the stable system, a constant value of viscosity was measured for the entire first week. Otherwise, the non stable sol displays a rapid increase of the viscosity up to 9 $mPa \cdot s$ after one week. This behaviour is probably due to an insufficient amount of acetic acid which is not able to stabilize the strong reactivity of the precursor.

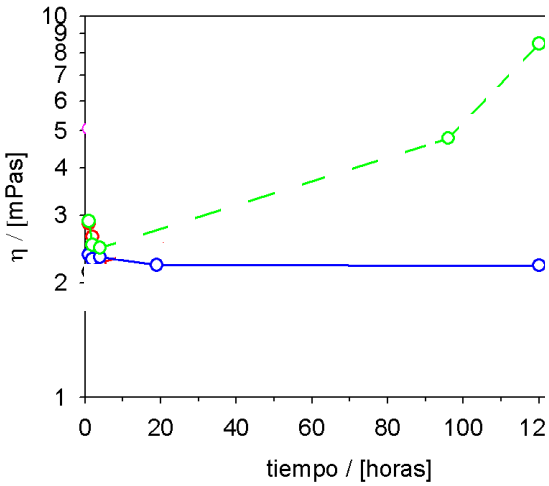

Figure 3.2: Sols viscosity as a function of immersion time

3.4 Coatings Characterization

The synthesis and the characterization of sols have been followed by the characterization of the sol-gel coatings structure. First of all, sol-gel coatings are thermally treated for the improvement of the structure densification and the elimination of the solvent (as explained in the Chapter 2). Since the temperature and time treatments are dependent on both the sol synthesis and the metal substrate (like other experimental parameters), in every chapter the information about the single treated topic is reminded. However, it is important to underline that aluminum alloys require low treatment temperatures because their microstructure is very often susceptible to overaging. Therefore, zirconia sol-gel coatings studied in this project were subjected to low thermal treatment temperatures which were not able to produce a crystalline oxide structure. Amorphous systems were therefore

obtained.
In order to evaluate the critical thickness of sol-gel coatings (i.e. corresponding to the maximum thickness of sol-gel coatings deposited without defects), several depositions were carried out by dipping with different withdraw rates on glass substrates. The results (not reported here) allowed to identify the withdraw rate of 22 cm/min as good compromise between the quality of the coating and the duration of the dip-coating process. Further depositions were carried out on SiO_2 substrates on which UV-visible spectra were recorded. Spectra were recorded in a range between 190 nm and 1000 nm by using an UV-PerkinElmer, Lambda 950 UV/VIS Spectrometer.

3.4.1 Scanning Electron Microscopy

The scanning electron microscope (SEM) is used to examine microscopic detail of solid specimens that may have initially been viewed in a light microscope but subsequently requiring SEM examination in order to provide information not available from the light microscope. The image is produced by scanning an extremely small focused beam of electrons (adjustable down to 1.5 nm in diameter) across the surface of a specimen in an array of picture points (pixels). High-energy electron bombardment of the specimen causes signals to be emitted at each pixel. These are collected and their intensities are used to produce images of the specimen by modulating the brightness of equivalent pixels on a monitor. Initial viewing of the specimen uses the secondary electron emission signal to provide an image very similar in shape to that seen in the light microscope. Unlike the light optical microscope that displays images in true color, the SEM presents intensity images where zero signal is displayed as black, intermediate signals as shades of grey and maximum signal as white.

Resolution The resolution limit of any microscope is defined as the minimal perceptible distance between two points and is partly dependent on the wavelength of the source. The wavelength of electrons is considerably smaller than that of light, hence the improvement in resolution. The better resolution of the SEM enables surface detail not normally visible in the light microscope to be viewed at high magnifications.

Depth of field The SEM has a considerably better depth of field than a light microscope (i.e. the ability to maintain sharp focus of detail as the specimen surface height changes). This facilitates the examination of specimens that have a very irregular topography.

Microanalysis The elemental composition of the specimen can be determined from the X-ray spectra excited by high-energy electron bombardment of the specimen. Each element has its own unique spectra that can be identified. Particles as small as 1 micrometer can be analysed. Detection and quantification of the spectra is achieved in one of two ways. An Energy Dispersive X-ray detector System (EDXS) is the more popular as this detector can display all the elements present in the specimen and enables their rapid identification. It enables the composition of the specimen to be determined to an overall accuracy of about 1% and detection sensitivity down to 0.1% by weight. Where resolution and sensitivity are of the utmost importance, particularly for elements of low atomic number, an additional detector called a Wavelength Dispersive X-ray Spectrometer (WDXS) would be required. This detector collects one discrete element at a time and hence is relatively slow in identifying elements in a specimen of unknown composition. However its detection sensitivity is in the order of 0.01 % by weight thus making trace analysis possible. Also, because its resolution is approximately 10 times better than that of an EDXS, it can clearly identify elements that are severely overlapped in the EDXS spectrum.
The morphology of ZrO_2 sol-gel layers was investigated by means of a Carl Zeiss Evo-40XVP Scanning Electron Microscope (SEM) with INCA Energy Dispersive X-ray Spectroscopy (EDXS) microanalysis equipment for chemical analysis [9].

3.4.2 Glow Discharge Optical Emission Spectroscopy

GD-OES technique is widely employed for the characterization of samples with low thickness, thin films, surfaces, interfaces and it can be also employed for bulk analysis. This technique enables to obtain results with high accuracy and reliability ranging from the first surface nanometers to a few micrometers in depth [1]. By using GD-OES technique, it is possible to acquire chemical composition profiles on both conductive and non conductive materials like metals, semi-conductors, organic coatings, powders or glass and ceramic materials [2, 3, 4]. Studies carried

out on oxide layers due to hot-working processes [1], anodized aluminum surfaces [5], hot-dip galvanized steels [6], hardened steel surfaces [7] are some examples of useful GD-OES investigations.

The working principle of GD-OES technique is based on two steps: the first is related to the photons emission provided by the material under investigation while the second step is based on the analysis of the characteristic electromagnetic waves associated to the emitted photons. The photons flow is generated by an high energy polarized plasma which is carried towards the surface of the sample to analyze. The plasma is generated in a low pressure chamber which is filled with argon. The chamber is made of a copper pipe sealed at one tip by a rubber gasket in contact with the sample. The other pipe tip is plugged by a Mg_2F window . A high potential difference is applied between the copper pipe and the sample. The copper pipe acts as the anode while the sample is connected as the cathode. The potential can be maintained constant (DC method) or can be modified by applying a high frequency variable signal (Radiofrequency method). The latter method is usually used for non conductive materials [2]. The intense electric field applied between the two electrodes (i.e. copper pipe and sample) promotes the formation of an electrons flow from the cathode to the anode. The high energy electrons hit argon molecules. From this impact, argon ions (Ar^+) plasma are formed. Argon cations are then attracted by the cathode (sample) and their impact on the surface sample enables to remove materials atom by atom (M)[8]. The material erosion is known as *sputtering process*. The collision between argon cations (Ar^+) and the sample surface produces the formation of secondary electrons which are attracted by the copper pipe (anode). The secondary electrons flow collides with argon atoms in the chamber producing new argon ions (Ar^+) which allow the plasma regeneration. On the other hand, far from the material surface, atoms subtracted to the sample (sputtered atoms, M) collide with argon plasma. Due to the ($M - Ar^+$) collision, material atoms (M) are excited to a higher energy level (M^*) which is not as stable as the low energy level. When excited atoms (M^*) return to the original lower energy state (M), they lose the extra-energy emitting electromagnetic waves with characteristic wavelength [2]. The photons flow constitutes the optical signal which can be consequently analyzed by optical spectrometers. The optical spectrometers are built following the ROWLAND CIRCLE architecture based on the reflection and the deflection of electromagnetic waves dependent on their wavelengths. Characteristic angles are associated

to every wavelength which are strictly correlated to each chemical element. All the chemical elements can be detected by GD-OES technique, hydrogen and helium included. The light intensity acquired by photomultipliers is converted into a electric signal proportional to the element concentration. The electric signal is amplified and digitalized for the software elaboration. GD-OES signals produce qualitative results which means that profiles are acquired as a function of sputtering time. By elaborating the signal acquired is however possible to convert qualitative results into quantitative results displaying the chemical element concentration as a function of sputtering depth. This is possible by performing a detailed calibration of each element detected. The calibration consists on the determination of the *calibration curve* measuring the sputtering rate as a function of sample composition. For each element, several samples with different chemical composition have to be used for the determination of the *calibration curve*. The conversion of qualitative profiles to quantitative profiles is allowed by using the calibration curves of the detected elements. Since during GD-OES measurements the sample region under analysis is defined by the gasket size, the area investigated by this technique is a macro-region (usually with a diameter equal to 4 mm). Therefore, GD-OES technique is not able to provide local information on sample composition profiles. Measurements carried out during the development of this thesis were performed with a RF-GDOES equipment supplied by Horiba Jobin Yvon.

3.4.3 Macro-Electrochemical Characterization

As briefly discussed in section 2.3, it is possible to use DC or AC electrochemical technique for the evaluation of electrode corrosion behaviour. In this work, electrochemical techniques were widely employed for different purposes. Electrochemical measurements were performed on sol-gel coated aluminum alloys and the results have been reported in chapter 4, 5 and 8. Electrochemical techniques were also employed for the evaluation of the inhibition effect on the corrosion behaviour of bare aluminum alloys. In chapter 6, it has been discussed how cerium nitrate affects the electrochemical behaviour of AA2024 aluminum alloy in chloride solutions. Chapter 9 is focused on EIS experimental approaches for the evaluation of the electrochemical behaviour of not stable systems.
Macro-electrochemical measurements were performed using an AUTOLAB/PG-

STAT30 potentiostat/galvanostat. This equipment enables to apply a current or a voltage input perturbation as detailedly described in chapter 9. The potentiostat/galvanostat is equipped with a FRA module ($FrequencyResponseAnalyzer$) for the electrochemical impedance spectroscopy measurements. A standard three electrode setup was employed for macro-electrochemical tests where the working electrode corresponded to the sample exposed area defined by the diameter size of the electrochemical cell. The electrochemical cell was made of a PVC pipe glued at one tip to the surface sample under investigation. The PVC pipe is sealed by a silicon gasket which avoids solution leakage. All the electrochemical measurements were performed by using a Faraday cage as electromagnetic fields shield. In this project, working electrode with areas ranging from 3 cm^2 (for measurements on sol-gel coated systems) to 15 cm^2 (for measurements carried out on bare samples immersed in inhibited solutions) were employed. The counter electrode was a platinum wire (diameter 1.5 mm) and the reference was an Ag/AgCl electrode. The chemical conditions inside the electrochemical cells can reproduce the environment where metals will be employed or they can be less aggressive in order to study the evolution of corrosion mechanisms. The former conditions are obtained using aggressive species with the same concentration found in the environment (i.e for marine studies aqueous solutions containing 3.5% NaCl are usually used since this concentration corresponds to that of water sea) while the latter ones are reached reducing the concentration of aggressive species down to a level which enables to promote a less intense corrosion attack. In this thesis, electrochemical measurements were performed in 0.05M NaCl or in diluted Harrison solution (containing 0.05%(wt) $NaCl$ and 0.35%(wt) $(NH_4)_2SO_4$). Both solution pHs is around 5.5. Measurements shown in chapter 6 were performed in sodium chloride solution containing cerium nitrate as inhibitor. In the experimental section of that chapter are described in more detail the procedures and the composition of the electrolytic solutions employed.

OCP potential measurements were performed in order to study the stability of the working electrode. This type of measurement was carried out for different lengths of time ranging from minutes to a couple of days. Potentiodynamic polarization curves were performed in order to obtain more information about corrosion behaviour. Polarization curves were acquired with a scan rate of 0.2 $mV \cdot s^{-1}$ starting near the OCP previously measured.

Electrochemical impedance spectroscopy measurements were performed under

voltage and current control. The experimental procedure employed for the current control approach is described in chapter 9. Impedance measurements carried out under voltage control, were performed at open circuit potential with ac voltage amplitude of 10 mV and frequency range from 10 mHz to 100 kHz (10 points were measured for each decade of frequency).

3.4.4 Micro-Electrochemical Characterization

Micro-electrochemical investigation were performed for the evaluation of the cerium inhibition on the aluminum alloys corrosion behaviour. As explained in chapter 2, by reducing the working electrode area, it is possible to obtain information on the local electrochemical behaviour of metals. In the micro-cell technique, the reduction of the working electrode area is obtained by using micro-glass capillaries. Hence, the working electrode area exposed to the electrolyte is defined by the mouth of the capillary used (see Figure 2.14). The preparation of glass capillaries consists of three stages: pulling of the capillary, grinding and sealing of the pulled tip. The micro-capillary is pulled using a pipette puller in order to reduce its inner diameter. After this stage, the inner capillary diameter is a few hundreds nanometers. The capillary tip is then ground by using grinding paper up to P2000. This stage enables to control the inner diameter of the glass capillary. In the following stage, the capillary tip is covered by a silicon gasket by dipping in a silicon rubber sealant. To measure the internal capillary diameter, it is possible to observe it by means of scanning electron microscopy. The micro-cell measurements shown in chapter 7 were performed by using a glass capillary with 50 μm internal diameter. Since this is significantly higher than the AA2024 intermetallics size, the characterization with the micro-cell technique was performed on regions consisting of intermetallics and a fraction of matrix.
The standard three electrode setup was used as shown in Figure 3.3. The working electrode was defined by the micro-capillary size (50 μm diameter). The counter electrode was a platinum wire positioned inside the micro-cell. As reference, a stable Ag/AgCl electrode was used. The reference was connected to the micro-cell through a small pipe link which enables to refresh the electrolyte in the capillary after every measurement. All electrodes were connected to a modified potentiostat/galvanostat able to measure currents in the range of fA.

Micro-cell measurements were carried out in 0.05M. Open circuit potential

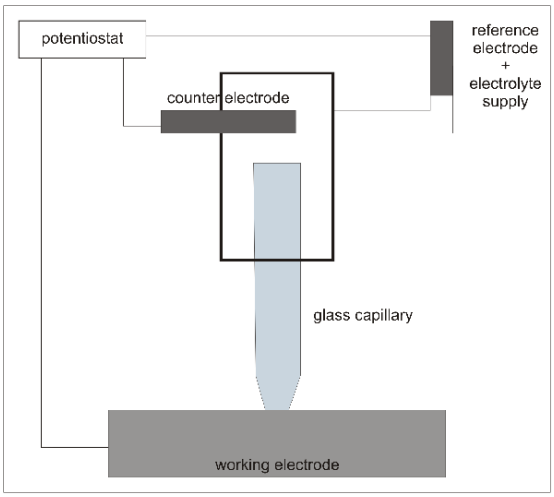

Figure 3.3: Micro-cell setup

measurements were carried out for 5 minutes followed by potentiodynamic polarization curves with a scan rate of 1 $mV \cdot s^{-1}$. Polarization curves started near the OCP previously measured. Micro-cell measurements were performed on bare AA2024 and on the same surface modified by the interaction with cerium species.

Bibliography

[1] ZEISS EVO ®Series Scanning Electron Microscopes User Guide, Cambridge, England, 2005

[2] G. Buytaert, Ph.D thesis Vrie Universiteit Brussel (VUB) (2005)

[3] R. Payling, D.G. Jones, A. Bengtson, Glow Discharge Optical Emission Spectrometry John Wiley & Sons Ltd, Chichester, UK (1997)

[4] R.K. Marcus, J.A.C. Broekaert, Glow Discharge Plasmas in Analytical Spectroscopy John Wiley & Sons Ltd, Chichester, UK (2003)

[5] T. Asam, M. Analytis, T. Nelis, U. Greb, Trans. IMF. 77 (5) (1999) B91

[6] K. Shimizu, G.M. Brown, H. Habazaki, K. Kobayashi, P. Skeldon, G.E. Thompson, G.C. Wood, Surf. Interface Anal 27 (1999) 24

[7] A. Bengtson, Spectrochim. Acta 49B (4) (1994) 411

[8] R. Payling, M. Aeberhard, D. Delfosse, J. Anal. Atomic Spectrom 16 (1) (2001) 50

[9] R. Payling, J. Michler, M. Aeberhard, Y. Popov, Surf. Interface Anal. 35 (2003) 583

Chapter 4

Zirconium Oxide from Metal-Organic Precursors

Thin ZrO_2 films applied with the sol-gel technique are a possible replacement of chromium based pre-treatments on aluminium alloys. These pre-treatments should promote coating adhesion and provide good barrier properties. Moreover, they should improve long term corrosion protection and possibly introduce self-healing ability. Thin ZrO_2 pre-treatments (100-200 nm) were applied by sol-gel technology on AA2024. ZrO_2 films from metal-organic precursors were initially deposited changing the dip number, the withdraw rate and the concentration of the precursor. The pre-treatments were subsequently produced from solution doped with 2-mercaptobenzothiazole and cerium nitrate.

4.1 Introduction

Aluminium alloys for aerospace applications are protected with a paint system consisting of conversion layers, primers and top coats. Cr-based pre-treatments are extensively employed as conversion coatings because they provide very good adhesion for primers and top coats associated with good barrier properties [1]. Moreover, chromate conversion coatings exhibit self-healing ability [1]. However, hexavalent chromium-containing compounds are regarded as toxic and not environmental friendly [1, 2, 3, 4]. Therefore, use of chromate conversion coatings is restricted and alternative pre-treatments should be employed for aluminium alloys. Coatings obtained with sol-gel technique are a possible replacement for chromate conversion coatings. This technique enables deposition of mixed metal oxides and metal oxide-organic composites on different metal substrates [1, 4, 5, 6, 7]. The thickness of coatings deposited with sol gel technology is generally in the micrometer range (1-20 μm). Corrosion protection of different types of sol-gel coatings have been extensively investigated in the past [1]. Oxide layers deposited by dip-coating and spin-coating from sol-gel systems improve the corrosion resistance of aluminium alloys [1, 8]. Silane based sol-gel coatings are reported to improve resistance of aluminium to general and localized corrosion [9, 10]. Moreover, mixed SiO_2 and ZrO_2 oxide layers deposited on AA2024 with sol-gel technique increased resistance to localized attack [11]. It was shown that Zr-based sol-gel coatings can be used as barrier layers in paint systems for AA2024 [12]. The sol-gel technology presents the possibility to introduce corrosion inhibitors in the oxide layer. Cr-free organic and inorganic inhibitors have been incorporated in different sol-gel coatings in order to improve corrosion resistance and provide self-healing ability. Triazole and thiazole compounds have been investigated by several authors [13, 14, 15]. Triazole compounds promote strong cathodic inhibition because they tend to be adsorbed on Cu-rich cathodic phases [13]. Moreover, they might also affect anodic processes on the alloy surface [15]. This behaviour is explained by the ability of triazole and thiazole compounds to rapidly form a protective film on the alloy surface. The introduction of active nanoparticles like ZrO_2 in sol-gel coatings is another interesting approach in order to improve corrosion resistance of AA2024 [16]. Ce-based conversion coatings exhibited promising self-healing ability in different studies [17]. Despite self-healing ability of Ce-based pre-treatments was not as good as for chromate

conversion coatings, inorganic Ce compounds like cerium nitrate might be considered for application as corrosion inhibitors in sol-gel systems. Introduction of cerium nitrate in ZrO_2 based sol-gel coatings might be difficult because it might affect reactions involved in the deposition of the sol-gel coating [18]. This might affect barrier properties of sol-gel layers doped with cerium nitrate [16]. Nevertheless, cerium nitrate was shown to have a positive effect on long term corrosion resistance of Si-based sol-gel coatings [16]. In the case of ZrO_2-based sol-gel coatings, it has not still been possible to determine a clear inhibition effect due to incorporation of cerium nitrate [18, 19]. The development of nonchromated coating systems for aerospace application has been previously targeted with the attempt to replace chromate conversion coating with a thin sol-gel layer (typically 50-200 nm) [20]. This approach is new because sol-gel coating systems are usually thick (in the micrometer range) and are generally regarded as complete coating systems. The superior adhesion behaviour of thin Zr and Si-based sol-gel films relative to chromate conversion coatings is the main advantage of developing thin coatings. Barrier properties and long term corrosion resistance need to be further improved in order to substitute chromate conversion coatings with thin sol-gel films. Moreover, introduction of inhibitors in thin sol-gel films is still a critical aspect [20]. In previous work, our research group followed the strategy of developing thin sol-gel coatings for different aluminium alloys [21, 22]. Thin ZrO_2 amorphous films (100-200 nm) were deposited on AA1050 with dip-coating technique [21]. These coatings promote adhesion of organic coatings to the ZrO_2 pre-treatment. Moreover, the electrochemical behaviour of AA1050 coated with ZrO_2 films is strongly dependent on deposition parameters, which affect film quality. ZrO_2 pre-treated AA6060 exhibits barrier properties similar to chromate conversion coated AA6060 when a continuous layer was deposited on the surface through successive dipping steps in the sol-gel solution [22]. The ZrO_2 pre-treatments on AA6060 do not exhibit self-healing ability as chromate conversion coated AA6060. However, a limited recovery of the barrier properties was observed for ZrO2 pre-treatments with a small number of defects. This was attributed to the formation of corrosion products that might plug the defects in the layer. The work presented in this chapter deals with the deposition of thin (100-200 nm) ZrO_2 sol-gel pre-treatments on AA2024 and the evaluation of their barrier properties. Due to the limited thickness of the layers deposited in our work (70-180 nm), it is very important to evaluate the ability of ZrO_2

sol-gel pre-treatments to provide a good barrier against corrosion. Moreover, introduction of corrosion inhibitors (2-mercaptobenzothiazole and cerium nitrate) is targeted in order to improve corrosion resistance.

4.2 Experimental Procedure

The substrate for the deposition of ZrO_2 films was AA2024 aluminium alloy. The alloy composition is given in Table 3.1. Prior deposition of sol-gel layers, the sample surface underwent surface preparation consisting of alkaline cleaning, alkaline etching and acid etching. The sol-gel solution was 0.1M and 0.6M $Zr(OBu^n)_4$ in anhydrous n-butanol. The deposition of the film was performed by dipping sol-gel technique. The samples were withdrawn with a controlled rate of 1 mm/s. The dipping step was repeated 2, 3 or 4 times in order to deposit overlapping layers on AA2024 samples. After each dip in the sol-gel solution, the samples were subjected to thermal treatment. The thermal treatment was performed at 120 ° C for 4 min. Thermal treatment was followed by drying at room temperature. Two corrosion inhibitors were selected for doping ZrO_2 pre-treatments deposited with sol-gel technology: 2-mercaptobenzothiazole and cerium nitrate. The introduction of inhibitors in sol-gel pre-treatments was carried out following two approaches. In the first approach, the inhibitor was added to the sol-gel solution leading to the formation of a sol-gel film doped with the inhibitor. In the second, the inhibitors were added with a final dip in a solution containing the inhibitor on a multilayer structure consisting of a first layer of ZrO_2 obtained with 0.1M sol-gel solution and a second layer deposited with 0.6M solution. The inhibitors were alternatively applied by spraying for the second approach. The morphology of ZrO_2 sol-gel layers was investigated by means of scanning electron microscope (SEM) equipped with energy dispersive X-ray spectroscopy (EDXS). Glow discharge Optical Emission Spectroscopy (GDOES) depth profiles were recorded with a Jobin Yvon GD profiler. Quantitative profiles were obtained with a calibration procedure using certified reference materials. The electrochemical behaviour of samples coated with ZrO_2 was investigated by means of potentiodynamic polarization measurements and Electrochemical Impedance Spectroscopy (EIS) in 0.05M NaCl solution. Potentiodynamic polarization measurements were recorded using a Pt counter electrode and Ag/AgCl reference electrode. The area of the working electrode was 3.6 cm^2. The scan rate was 0.2 $mV\ s^{-1}$. Impedance mea-

surements were carried out at open circuit potential with AC voltage amplitude of 10 mV and frequency range from 10 mHz to 100 kHz. The measurements were performed using an AUTOLAB PG-STAT 12 potentiostat equipped with a Frequency Response Analyser module. In order to compare the barrier properties of samples coated with ZrO_2, potentiodynamic polarization scans and impedance measurements were performed on chromate conversion coated AA2024.

4.3 Results and discussion

Figure 4.1(a) shows a SEM micrograph of the surface of as received AA2024. The rolling direction is clearly visible in the micrograph. Moreover, second phase particles appearing darker than the matrix can be seen in the same micrograph. These particles are Al-Cu-Fe-Mn- or Al-Cu-Mg intermetallics, which are typical constituent particles of AA2024 [23]. It is also possible that a number of dark spots are associated to holes generated by removal of intermetallics during hot and cold-rolling of the alloy. Before deposition of sol-gel film, the samples underwent surface preparation consisting of alkaline degreasing, alkaline etch and acid etch. The aim of surface preparation is to remove the intermetallics and the defected oxide layer resulting from cold-rolling. Figure 4.1(b) shows the surface of AA2024 after surface preparation. Alkaline etch leads to the formation of rather large cavities on the alloy surface. This is probably related to non uniform attack due to the inhomogeneous microstructure of AA2024 alloy. Moreover, it is likely that cavities are generated by removal of intermetallics during alkaline etch.

Figure 4.2(a) is a SEM micrograph of AA2024 coated with a ZrO_2 film deposited with sol-gel technique (4 layers). The ZrO_2 film could not be clearly distinguished in the micrograph since the deposited layer is thin (in the range of 100-200 nm). However, the SEM micrograph at higher magnification in Figure 4.2(b) reveals the existence of a ZrO_2 film, which appears uniform and well adherent on the substrate. Alkaline etch leads to the formation of rather large cavities on the alloy surface, which are still visible after deposition of ZrO_2 film. It is important to point out that cavities on the surface are covered by the film. Another important aspect is that film deposition is not affected by the existence of second phase particles like intermetallics in the alloy microstructure.This is further confirmed by TEM observation of cross-sections of samples coated with a ZrO_2 film. In contrast, these particles have a negative effect on deposition of

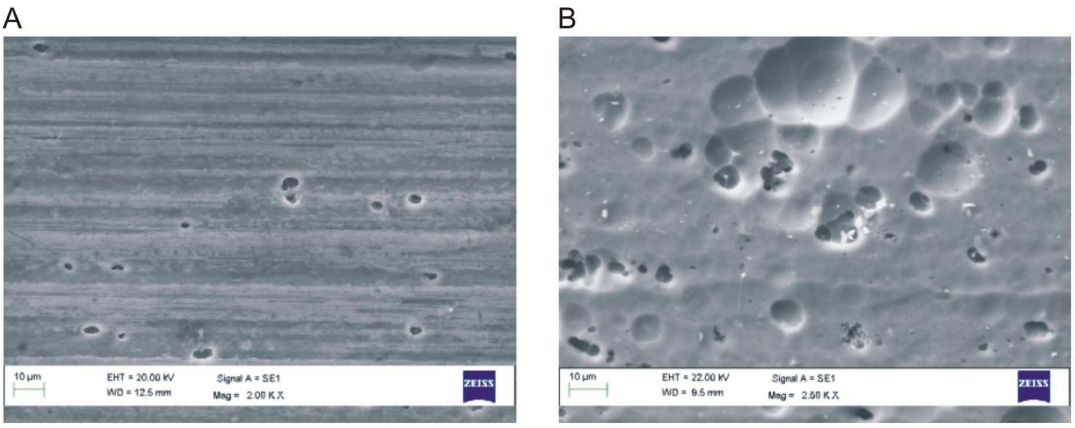

Figure 4.1: SEM micrographs of as received AA2024 (A) and of alloy surface after surface preparation (B)

conversion layers on aluminium alloys due to their cathodic or anodic behaviour relative to aluminium matrix [13]. This indicates that AA2024 is uniformly covered by deposition of a ZrO_2 film with sol-gel technique.

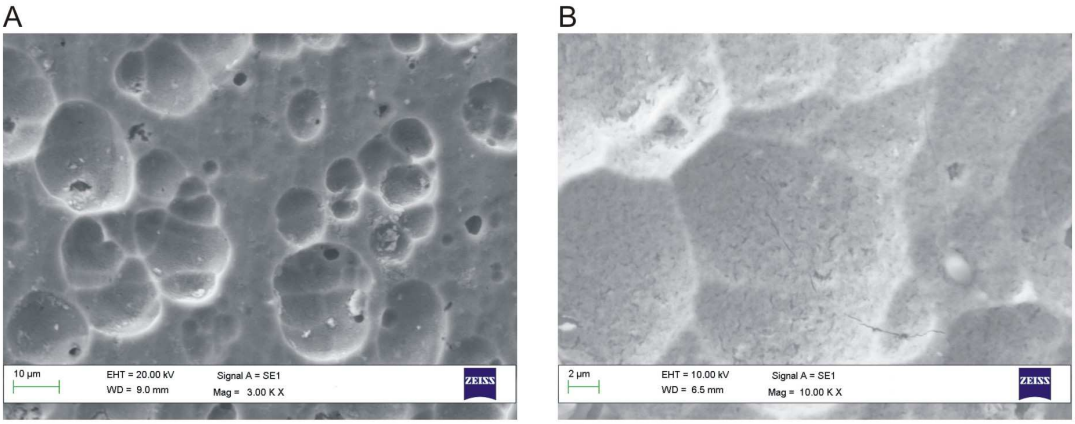

Figure 4.2: SEM micrographs of AA2024 samples pre-treated with ZrO2 layers deposited with sol-gel technique

Figure 4.3 displays a semi-quantitative GDOES composition profile for a sample coated with 2 layers of ZrO_2 deposited with sol-gel technique. The Zr and O signals reveal the existence of a layer of ZrO_2 on the substrate. The interface between sol-gel film and aluminium substrate is associated to decrease of Zr and O signals and to increase of Al signal. This is located at about 150 nm indicating that sol-gel technique can be employed for deposition of thin ZrO_2 layers

on AA2024. This result is in line with SEM micrographs reported in Figure 4.2. Moreover, the transition of Al, Zr and O across the interface is rather broad. This is probably related to surface roughness of coated samples (Figure 4.2(a) and (b), which might affect GDOES measurements. Moreover, the GDOES profile in Figure 4.3 exhibits a C signal that is relatively high in the ZrO_2 film and progressively decreases approaching the substrate. The existence of a C signal in the sol-gel layer indicates that a fraction of metal-organic precursor remains in the film. In addition, a C contamination is also possible on the sample surface. This is possibly related to thermal treatment of the layer, which is carried out at a rather low temperature and for a short time in order to avoid degradation of mechanical properties of the alloy.

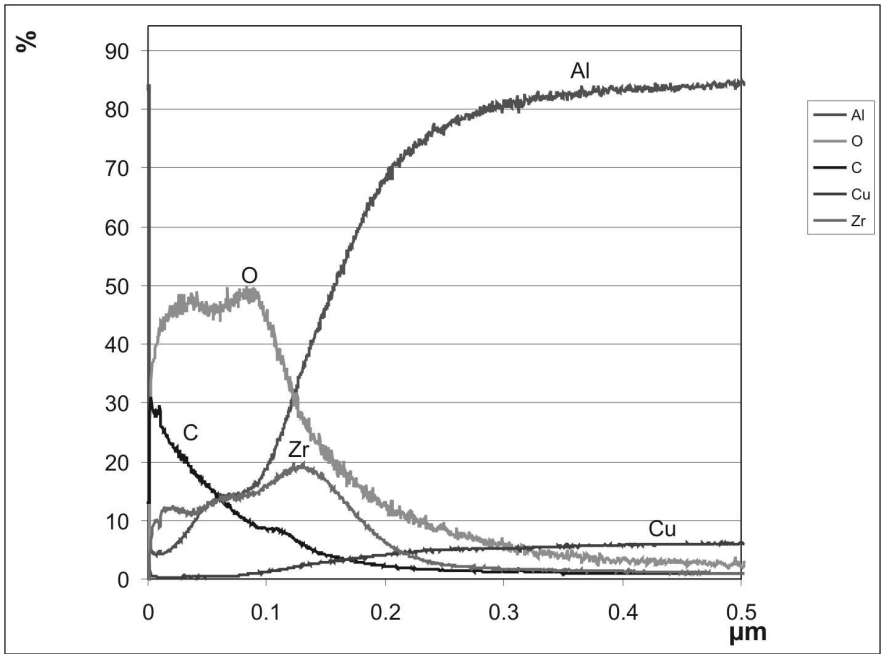

Figure 4.3: GDOES semi-quantitative composition profile for ZrO2 pre-treatment on AA2024

ZrO_2 films become thicker increasing the number of dips in the sol-gel solution reaching more than 200 nm after 4 dips in sol-gel solution. However, GDOES semi-quantitative profiles reveal that the increase of the film thickness is limited for depositions successive to the first one. The thickness of these sol-gel ZrO_2 films is in the same range as that of conventional chromate conversion coatings on AA2024, which generally are in the range of 100-300 nm. From this point of view,

these sol-gel layers might be an option for replacement of Cr-based conversion coatings, as also indicated by our previous works [21, 22]. Figure 4.4 exhibits typical defects that might be observed in thin ZrO_2 pre-treatments deposited with sol-gel technique. Figure 4.4(a) exhibits a rather deep hole in the sample. This layer discontinuity might expose the substrate and could be a problem concerning barrier properties of the film. It is likely that the hole was created during surface preparation and that it could not be covered in the following deposition of ZrO_2 film. Indeed, rather deep holes might be formed on the alloy surface during surface preparation due localized attack at locations of intermteallics in AA2024. This evidences that surface preparation of the substrate is a very important step in order to reduce the number of defects in the ZrO_2 layer and to obtain a well adherent film. It has been found that a relatively short alkaline etching step (2 min) can improve the quality of sol-gel films deposited on AA2024 but it was not able to completely remove dirt and greases from the entire surface.
Another fact was that the sol-gel solution could not penetrate inside smaller cavities leading to a defected film structure at these locations. Figure 4.4(b) reveals the existence of cracks in the ZrO_2 film. These cracks tend to be located at the bottom of relatively large cavities because a thicker film is formed in the cavities than outside, as confirmed by EDXS maps. Indeed, there is a larger amount of sol-gel solution at the bottom of large cavities than in the surrounding regions when samples are located in horizontal position in the oven for the thermal treatment of sol-gel layer. In general, it is observed that rather thick ZrO_2 films have a stronger tendency to form cracks than thin layers. Therefore, it is expected that crack formation is more probable inside cavities than on flat portions of the surface. Carrying out thermal treatment with AA2024 sheets placed vertically in the oven strongly reduces crack formation in the ZrO_2 layers.

Surface preparation prior film deposition with sol-gel technique is very important in order to obtain a uniform ZrO_2 layer on the substrate. The procedure for surface preparation of the substrate needed to be optimized in order to reduce the number of defects in the sol-gel layer. Indeed, film defects might impair barrier properties leading to poor corrosion resistance. However, it has to be pointed out that we tried to deposit thin layers in order to produce a pre-treatment for replacement of chromate conversion coatings. Thus, the ZrO_2 layer will be painted with a coating that will contribute to provide a barrier against corrosion. Therefore, paint adhesion to deposited film is another very important

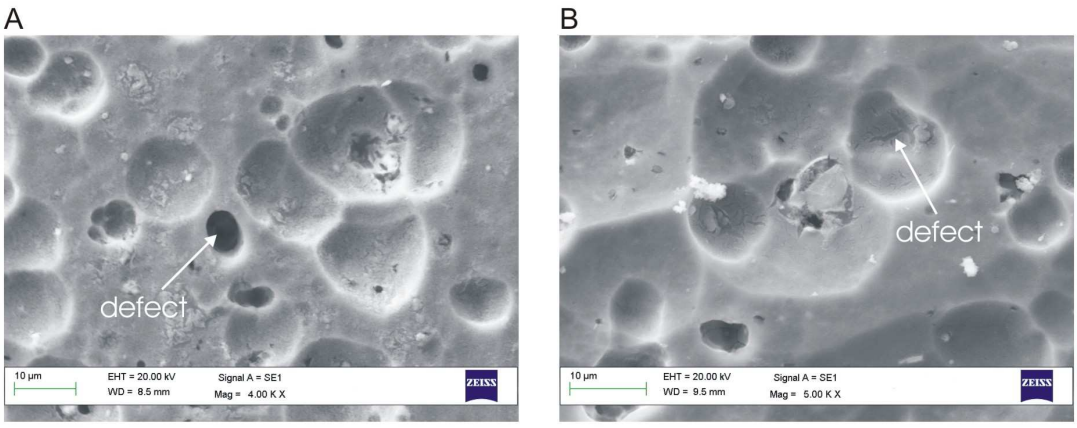

Figure 4.4: SEM micrographs showing typical defects on AA2024 samples pre-treated with ZrO2 layers deposited with sol-gel technique

aspect to be investigated. Although this aspect is not considered in this chapter but will be considered in Chapter 10, ZrO_2 films revealed very good paint adhesion on AA6060 [22] and AA2024. In order to assess barrier properties of ZrO_2 pre-treatments, potentiodynamic polarization scans were initially carried out for ZrO_2 layers on AA2024. Figure 4.5 displays potentiodynamic polarization curves carried out in 0.05 M NaCl solution on AA2024 coated with 2 and 4 layers of ZrO2 and on bare substrate.

The coated samples evidence a marked reduction of the cathodic and anodic current density with respect to bare substrate. This can be explained with reduction of area available for cathodic and anodic reactions due to the ZrO_2 film. Extrapolation of corrosion current density from Tafel slopes gives $1 \cdot \mu A\ cm^{-2}$ for AA2024 coated with 2 layers of ZrO_2 and $0.2 \cdot \mu A\ cm^{-2}$ for pre-treatment with 4 layers. In contrast, the corrosion current density is $10 \cdot \mu A\ cm^{-2}$ for the bare substrate. The strong reduction of corrosion current density of coated samples with respect to bare AA2024 indicates that deposition of ZrO_2 pre-treatment with sol-gel technique leads to a marked improvement of the corrosion resistance of AA2024. This is due to the barrier effect of the deposited film. This is evident from the value of anodic current density at -500 mV vs. Ag/AgCl (immediately after the corrosion potential), which is three orders of magnitude lower for pre-treatment with 4 layers of ZrO_2 ($0.55 \cdot \mu A\ cm^{-2}$) than for bare substrate ($550 \cdot \mu\ Acm^{-2}$). The very low anodic current density for the pre-treated sample is an indication of strong reduction of aluminium corrosion due to ZrO_2 film.

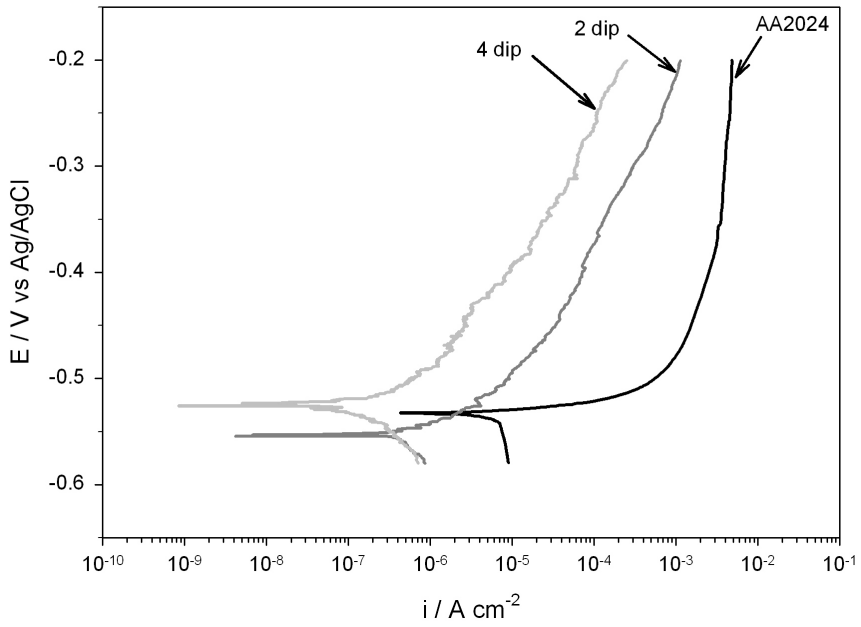

Figure 4.5: Potentiodynamic polarization curves in 0.05M NaCl solution for AA2024 samples pre-treated with ZrO2 layers deposited with sol-gel technique

Nevertheless, the potentiodynamic polarization curve for a sample coated with 4 layers of ZrO_2 does not exhibit a clear passive behaviour in the anodic branch. This behaviour might be related to a small number of defects that might be present in the ZrO_2 layer (Figure 4.4). Film defects might be preferential sites for localized attack. This is confirmed by the SEM micrograph reported in Figure 4.6 showing the surface of coated AA2024 after potentiodynamic polarization in 0.05 M NaCl. The micrograph exhibits a relatively large pit with a size of about 100 μm, while the surrounding area appears not attacked. In addition, the ZrO_2 film displays good adhesion to the substrate after potentiodynamic polarization. The corrosion attack most likely initiates at discontinuities similar to those reported in Figure 4.4. Moreover, the attack is localized at the locations of film defects leading to pitting of the surface.

Since defects in the ZrO_2 film deposited with sol-gel technique have a negative effect on the electrochemical behaviour, introduction of corrosion inhibitors in the pre-treatment was considered in order to improve corrosion resistance. In the current chapter, results on inhibited coatings have been discussed. How-

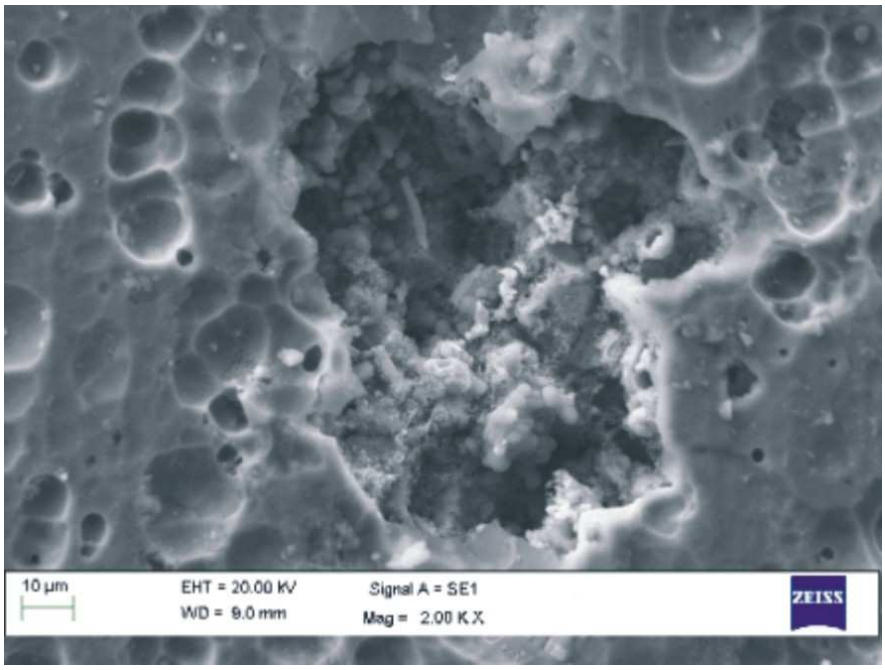

Figure 4.6: SEM micrograph of an AA2024 sample coated with ZrO2 deposited with sol-gel technique after potentiodynamic polarization in 0.05M NaCl solution

ever, in Chapter 8, a deeper evaluation on the inhibition effect of cerium nitrate directly added to the starting sol will be treated. In that case, the cerium nitrate salt was used as inhibitor species in multi-layer sol-gel coatings. Figure 4.7(a) shows a SEM micrograph of the surface of AA2024 coated with ZrO_2 pre-treatment doped with 2-mercaptobenzothiazole. The inhibitor was introduced in the sol-gel solution before deposition by dipping of the ZrO_2 layer. The sample in Figure 4.7(a) is coated with 2 layers of ZrO_2 doped with inhibitor. The film morphology is very similar to that shown by undoped ZrO_2 pre-treatment (Figure 4.2(a)). The alloy surface appears uniformly coated revealing cavities produced during pickling. As already considered above, these film defects might be related to the alloy morphology obtained after surface preparation. However, film discontinuities might be also generated by inhibitor addition in the sol-gel bath leading to a viscosity increase. This renders film cracking more probable relative to thin films obtained from a precursor solution with low viscosity. The SEM micrograph in Figure 4.7(b) exhibits the surface of a ZrO_2 pre-treatment consisting of two overlapping ZrO_2-based layers. The first layer is obtained with 0.1M precursor concentration in the sol-gel solution, as for the sample in Figure

4.7(a). The second is produced by dipping in 0.6 M sol-gel solution. The inhibitor is added to this multilayer system by a final dip in a solution containing 2-mercaptobenzothiazole or by spraying the same solution on the pre-treatment. In addition, samples doped with cerium nitrate were also produced with the same approach. The morphology of pre-treatments doped with cerium nitrate is similar to that shown in Figure 4.7(b). Otherwise, it can be recognized that the second layer of the pre-treatment (0.6M precursor concentration) is discontinuous and porous. It can be expected that the first layer is similar to that visible in Figure 4.2(a) since it is obtained according to the same procedure. The first layer should provide a barrier for corrosion protection, while the second layer should enhance adhesion of top coat and provide a microstructure that favours inhibitor storage in the ZrO_2 film.

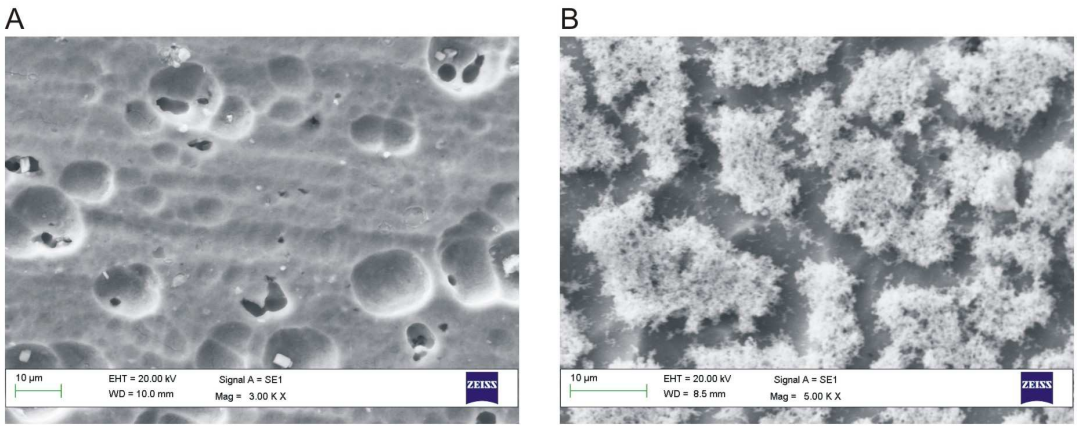

Figure 4.7: SEM micrographs of AA2024 coated with ZrO2 layers doped with 2-mercaptobenzothiazole: inhibitor introduced in the sol-gel solution before deposition with sol gel technique (A) and multilayer pre-treatment structured with a first ZrO2 layer obtained with 0.1M precursor concentration, a second layer deposited with 0.6 M concentration and final addition of inhibitor (B)

Figure 4.8 shows a GDOES semi-quantitative composition profile for a sample pre-treated with ZrO_2 film doped with 2-mercaptobenzothiazole. The pre-treatment consists of two overlapping layers of ZrO_2 containing inhibitor, as for the sample shown in Figure 4.7(a). It was not possible to carry out GDOES profiles on the multilayer pre-treatment shown in Figure 4.7(b) because surface roughness did not enable uniform sputtering disturbing signal acquisition. The semi-quantitave composition profile in Figure 4.8 shows similar trend for Zr, O

and Al signals to the profile for undoped pre-treatment. Film thickness is in the same range (150-200 nm) for doped and undoped pre-treatments. In general, the thickness of multilayer pre-treatment as in Figure 4.7(b) is slightly thicker than for the film in Figure 4.7(a). The S signal evidences a surface enrichment and a rather uniform concentration in the ZrO_2 layer. This signal can be related to incorporation of 2-mercaptobenzothiazole in the pre-treatment. This is supported by the observation that the S signal is below detection limits for undoped pre-treatments (Figure 4.3).

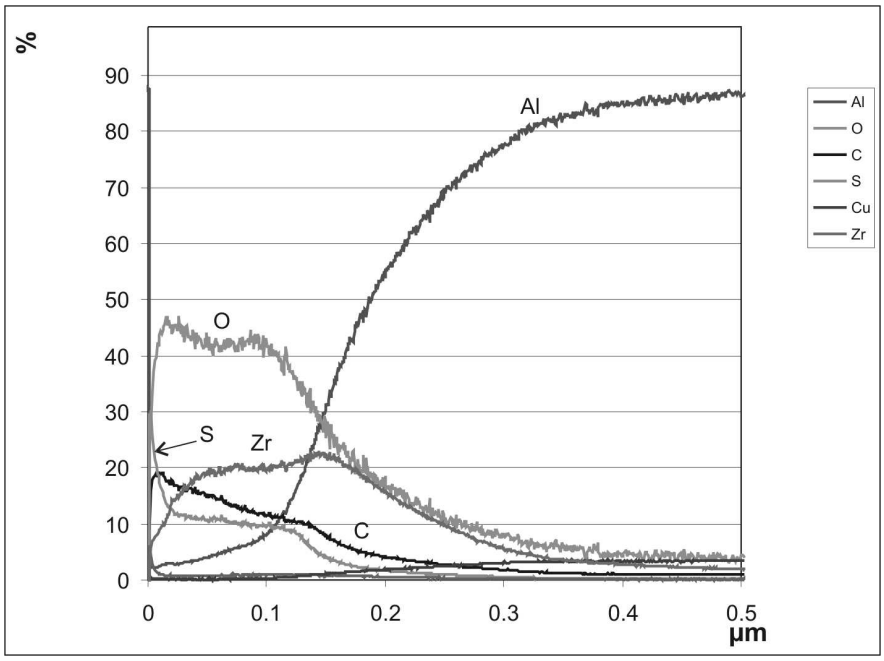

Figure 4.8: GDOES semi-quantitative composition profile for ZrO2 pre-treatment containing 2-mercaptobenzothiazole

Figure 4.9 reports potentiodynamic polarization curves for AA2024 coated with ZrO_2 films containing 2-mercaptobenzothiazole. The inhibitor was added to the system by spraying the inhibitor solution on the ZrO_2 films deposited by the procedure described for the system shown in Figure 4.7(b). In addition, the figure displays the potentiodynamic polarization curve for an undoped ZrO_2 pre-treatment (2 layer) and for the bare AA2024 substrate. The curve for the ZrO_2 pre-treatment doped with 2-mercaptobenzothiazole (applied by spraying) evidences a passive range (about 200 mV) and breakdown at -370 mV vs Ag/AgCl. Moreover, it displays a marked reduction of cathodic and anodic current density

with respect to the undoped pre-treatment and bare AA2024. The corrosion current density is 0.02 $\mu A\ cm^{-2}$ for the doped system. This is about two orders of magnitude lower than the corrosion current density shown by undoped ZrO_2 pre-treatment and about three orders of magnitude lower than that for bare substrate. The existence of a passive range associated to low anodic current density might be related to the deposition of a homogeneous barrier film (the inner layer, deposited with 0.1M precursor concentration). It is likely that this barrier layer is defect-free, in accordance with the low corrosion current density detected for this sample. The low cathodic current density for the same protection system is probably related to addition of 2-mercaptobenzothiazole, which is known to be an efficient inhibitor of cathodic reactions. The combination of an efficient barrier layer and inhibition due to 2-mercaptobenzothiazole leads to good corrosion protection of the substrate during potentiodynamic polarization. Results shown in Figure 4.9 indicate that discontinuities in the ZrO_2 pre-treatments deposited with sol-gel technique are a critical factor concerning corrosion protection. Moreover, this has a negative effect on reproducibility of potentiodynamic polarization curves. This is consistent with morphology observed for ZrO_2 films. The electrochemical behaviour of pre-treatments obtained with direct addition of inhibitor in sol-gel solution (morphology shown in Figure 4.7(a)) is similar or even worse than that for the undoped system. It is likely that addition of 2-mercaptobenzothiazole in the sol-gel solution negatively affects hydrolysis and condensation reactions involved with deposition of the sol-gel layer affecting film continuity. This might be reflected by the electrochemical behaviour.

Figure 4.10 shows the potentiodynamic polarization curve for ZrO_2 pre-treatment doped with cerium nitrate by spraying with the same procedure employed for the production of the inhibited coating shown in Figure 4.7(b). The figure reports the curves for pre-treatment without inhibitor and bare substrate. As reported above, cerium doped sol-gel systems will be further treated in the chapter 8 with a different sol synthesis approach. In that chapter, the cerium nitrate has been directly added to the starting solution where multi-layered sol-gel structures were produced alternating inhibited layers with non inhibited layers. In the current chapter cerium nitrate was instead used as inhibitor applied directly on the dried sol-gel film. By using this procedure, the cathodic and anodic current densities (Figure 4.10) are similar for pre-treatment with and without inhibitor. The same behaviour is observed for the corrosion current density. Moreover, there is a

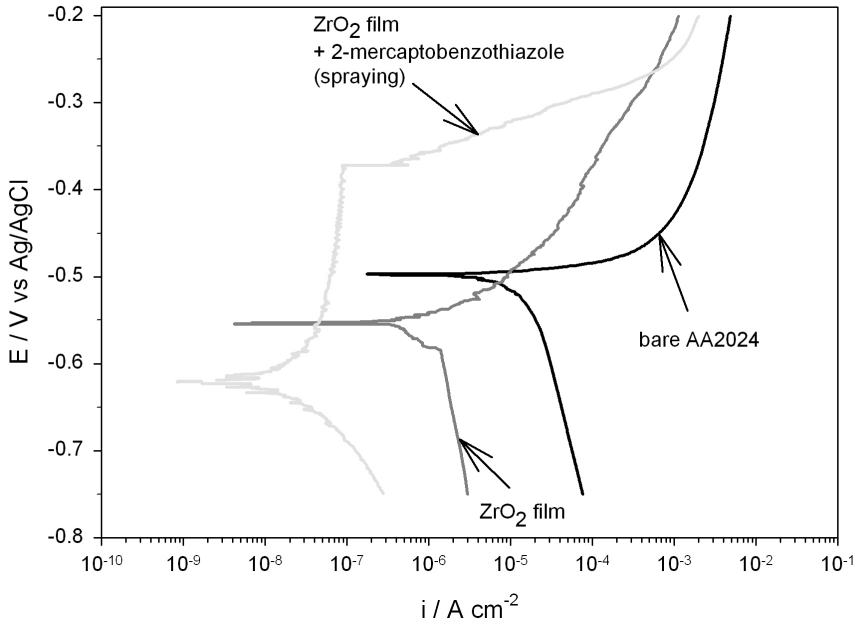

Figure 4.9: Potentiodynamic polarization curves in 0.05M NaCl solution for AA2024 samples pre-treated with ZrO2 layers deposited with sol-gel technique with and without 2-mercapotobenzothiazole

shift of the corrosion potential in the anodic direction for the pre-treatment with inhibitor suggesting a higher resistance with respect to passivity breakdown.

Electrochemical impedance measurements were carried out on ZrO_2 pre-treatments in order to evaluate corrosion protection for long immersion times in 0.05M NaCl solution. Figure 4.11 displays the modulus of electrochemical impedance at 0.01 Hz versus immersion time for ZrO_2 pre-treatment on AA2024 (2 layers and 4 layers). In addition, this figure shows the impedance modulus for a reference chromate conversion coating and for bare substrate. The impedance modulus measured at 0.01 Hz immediately after immersion in the electrolyte (0 h) is in the range of $10^6 \Omega \cdot cm^2$ for the sample coated with 4 layers of ZrO_2 and $3.7 \cdot 10^5$ Ωcm^2 for that with 2 layers. It is $4.4 \cdot 10^3$ Ωcm^2 for chromate conversion coated AA2024 and $4.6 \cdot 10^4$ Ωcm^2 for bare AA2024. Samples coated with ZrO_2 film exhibit a decrease of impedance modulus during the first 8 h in solution. In contrast, the impedance modulus of chromate conversion coated alloy progressively increases during the measurement. The impedance modulus is in the same range for the sample coated with ZrO_2 (4 layers) and chromate conversion coated

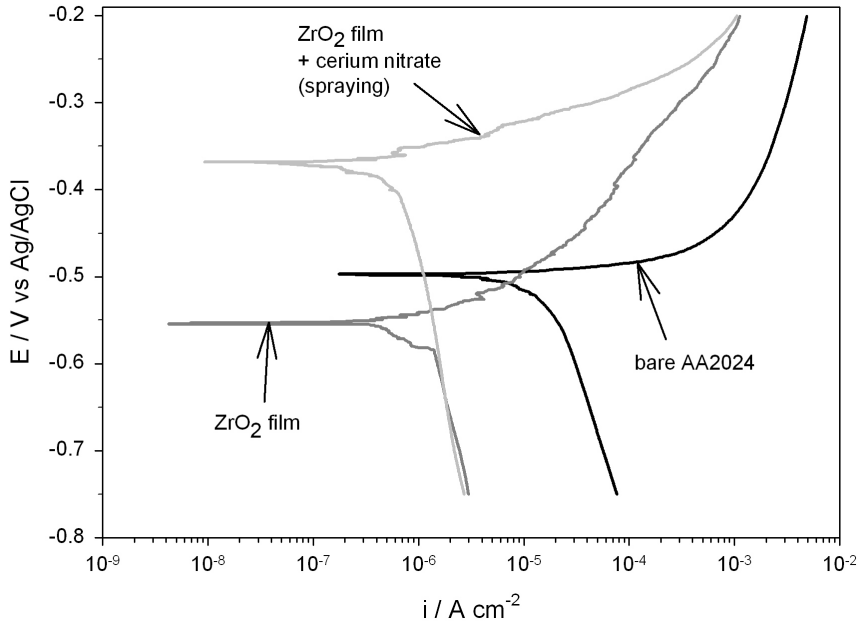

Figure 4.10: Potentiodynamic polarization curves in 0.05M NaCl solution for AA2024 samples pre-treated with ZrO2 layers deposited with sol-gel technique with and without cerium nitrate

sample in the time interval between 24 h and 72 h. The impedance modulus is $2.9 \cdot 10^5\ \Omega cm^2$ for chromate conversion coated AA2024 after 192 h in solution, while it is about one order of magnitude lower for samples coated with ZrO_2. The trend of impedance modulus as a function of immersion time evidences that barrier properties of ZrO_2 film are higher than those of chromate conversion coating for relatively short immersion times (about 24 h) in NaCl solution. As already seen from potentiodynamic polarization curves, the sample coated with 4 layers exhibits a better barrier than that with 2 layers due to the existence of a thicker layer on the former sample. The sample with 4 layers of ZrO_2 displays similar impedance values to chromate conversion coated one between 24 h and 72 h immersion time indicating that the barrier properties remain rather good. In contrast, the chromate conversion coated sample displays higher impedance modulus than other samples for long immersion times. This is most likely due to self-healing that is well known for this type of coating [1]. This behaviour is not observed for samples coated with ZrO_2 film.

Figure 4.12 reports electrochemical impedance modulus at 0.01 Hz versus

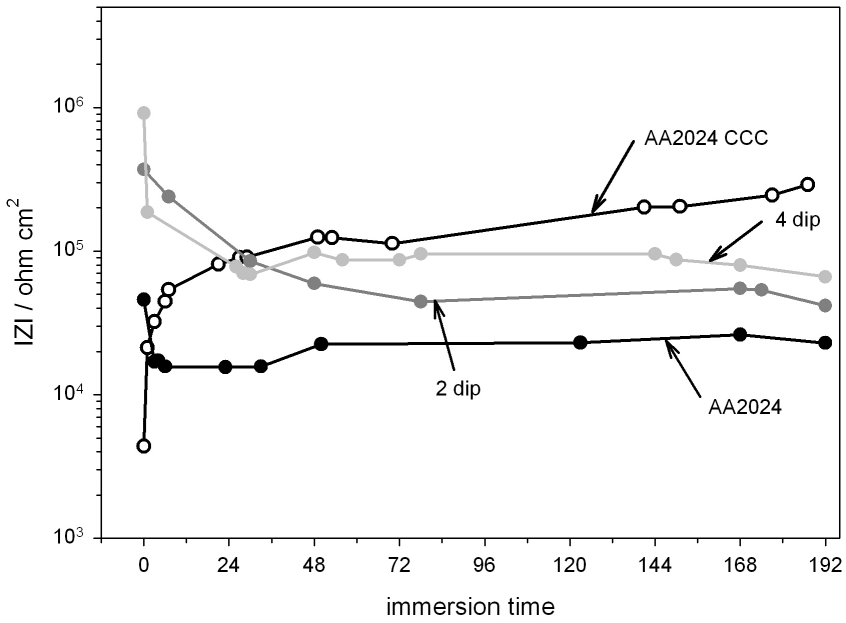

Figure 4.11: Electrochemical impedance modulus at 0.01 Hz as a function of immersion time in 0.05M NaCl solution for AA2024 samples pre-treated with ZrO2 layers deposited with sol-gel technique, chromate conversion coated AA2024 and bare AA2024

immersion time for ZrO_2 pre-treatments doped with 2-mercaptobenzothiazole. Chromate conversion coating and undoped ZrO_2 sol-gel coating are also reported in the figure. The impedance modulus measured at 0.01 Hz immediately after immersion in the electrolyte (0 h) is in the range of 10^7 Ωcm^2 for the sample coated with ZrO_2 containing 2-mercaptobenzothiazole. This sample is structured with two layers of ZrO_2 oxide and the inhibitor is deposited directly on the pre-treatment by spraying. It has to be reminded that the inner oxide layer is obtained with 0.1M precursor concentration and the outer with 0.6M, as described in the comment of Figure 4.7(b). The impedance modulus of this sample exhibits a rather fast decrease over 48 h in the electrolyte. However, the modulus of ZrO_2 pre-treatment doped with 2-mercaptobenzothiazole is significantly higher than that measured for chromate conversion coating. Moreover, this is higher than the modulus of undoped ZrO_2 film over 24 h in the electrolyte. The trend of impedance modulus visible in Figure 4.12 for ZrO_2 pre-treatment doped with mercaptobenzothiazole evidences a clear effect of the inhibitor on corrosion

resistance only over a relatively short immersion time in the electrolyte (about 24 h). The inhibition is most likely associated to deactivation of cathodic reactions, which is proven for this type of inhibitor [13]. This effect tends to disappear for longer immersion times. This might be related to complete release of the inhibitor over the first hours in the electrolyte. It is believed that release of inhibitor might be limited by deposition of a paint onto ZrO_2 pre-treatment. Indeed, the paint should favour retention of released inhibitor on the surface of the ZrO_2 film extending over longer times the positive effect of 2-mercaptobenzothiazole on electrochemical behaviour. In chapter 8, the development of a multi-layer structure consisting of inner doped layers and by outer undoped layers was carried out to limit the inhibitor release towards the electrolyte. Moreover, the samples containing 2-mercaptobenzothiazole do not exhibit signs of repassivation (self-healing ability) in contrast with the behaviour of chromate conversion coating. Nevertheless, long term corrosion resistance of ZrO_2 pre-treatment (with and without inhibitor) can be considered rather good taking into account that film thickness is in the range of 100-200 nm.

4.4 Conclusions

Thin ZrO_2 pre-treatments (100-200 nm) were applied by sol-gel technology on AA2024. The pre-treatments were also doped with 2-mercaptobenzothiazole and cerium nitrate. Film morphology and composition have been investigated by means of SEM-EDXS and GDOES. Electrochemical behaviour has been investigated by means of potentiodynamic polarization scans and electrochemical impedance spectroscopy in order to assess barrier properties and long term corrosion protection of pre-treatments. The ZrO_2 pre-treatment uniformly covers the substrate as confirmed by SEM micrograph and GDOES semi-quantitative composition profiles. Film morphology is strongly affected by surface preparation (alkaline cleaning, alkaline etching and acid etching) leading to formation of rather large cavities due to inhomogeneous attack of AA2024 substrate. This has a negative effect on quality of pre-treatment, which might exhibit defects like discontinuities or cracks. However, the number of defects in ZrO_2 pre-treatment can be minimized modifying deposition parameters. ZrO_2 pre-treatments applied with sol-gel technique improve corrosion resistance of AA2024. This can be attributed to a barrier effect of deposited pre-treatments. However,

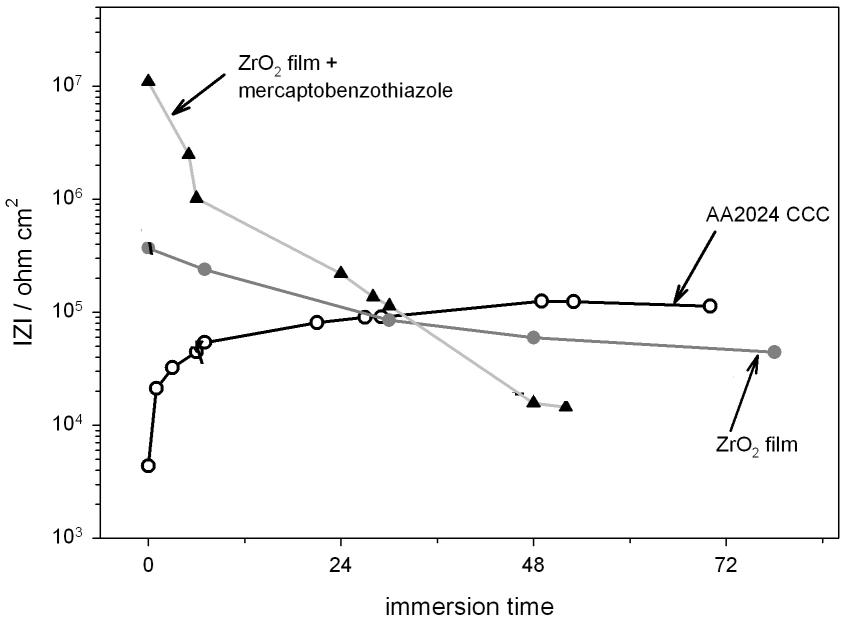

Figure 4.12: Electrochemical impedance modulus at 0.01 Hz as a function of immersion time in 0.05M NaCl solution for AA2024 samples pre-treated with ZrO2 layers deposited with sol-gel technique with and without 2-mercaptobenzothiazole and chromate conversion coated AA2024.

undoped pre-treatments do not show a passive range in potentiodynamic polarization scans. This might be related to the existence of defects in the ZrO_2 layer behaving as initiation sites for localized attack (pitting). Introduction of 2-mercaptobenzothiazole and cerium nitrate do not significantly affect morphology of sol-gel ZrO2 pre-treatments. However, it cannot be excluded that addition of inihibitor in the sol-gel solution contributes to formation of discontinuities in the pre-treatment. 2-mercaptobenzothiazole produces a marked reduction of cathodic current density in potentiodynamic polarization scans, in accordance to its well known ability to deactivate cathodic reactions. Moreover, the passive range exhibited by ZrO_2 pre-treatment doped with 2-mercaptobenzothiazole confirms good barrier properties. 2-mercaptobenzothiazole evidences clear inhibition effect over a relatively short immersion time in electrolyte (about 24 h). The inhibition effect vanishes for longer immersion times probably due to complete leaching of inhibitor. This effect might be limited by deposition of a paint onto ZrO_2 pre-treatment. Nevertheless, long term corrosion resistance of ZrO_2 pre-treatments

doped with this inhibitor should be considered good taking into account small thickness of the pre-treatment. Sol-gel systems doped with cerium nitrate deposited on the dried ZrO_2 coating does not clearly improve electrochemical behaviour of ZrO_2 pre-treatments.

Bibliography

[1] T.L.Metroke, R.L.Parkhill, E.T.Knobbe Progress in Organic Coatings 41 (2001) 233

[2] R.Di Maggio, L.Fedrizzi, S.Rossi J. Adhesion Sci. Technol. 15 (2001) 793

[3] M.Bethencourt, F.J.Botana, J.J.Calvino, M.Marcos, M.A.Rodriguez-Chacon Corrosion Science 11 (1998) 1803

[4] J.H.Osborn Progress in Organic Coatings 41 (2001) 280

[5] M.Guglielmi Journal of Sol-Gel Science and Technology 8 (1997) 443

[6] R.L.Ballard, J.P.Williams, J.M.Njus, B.R.Kiland and M.D.Soucek European Polymer Journal 37 (2001) 381

[7] T.L.Metroke, A. Apblett Progress in Organic Coatings 51 (2004) 36

[8] N.N.Voevodin, N.T.Grebasch, W.S.Soto, F.E.Arnold, M.S.Donley Surface and Coatings Technology 140 (2001) 24

[9] NA.M.Beccaria, G.Padeletti, G.Montesperelli, L.Chiaruttini Surface and Coatings Technology 111 (1999) 240

[10] A.M.Beccaria, L.Chiaruttini Corrosion Science 41 (1999) 885

[11] X.F.Yang, D.E.Tallman, V.J.Gelling, G.P.Bierwagen, L.S.Kasten, J.Berg Surface and Coatings Technology 140 (2001) 44

[12] N.N.Voevodin, V.N.Balbyshev, M.S.Donley Progress in Organic Coatings 52 (2005) 28

[13] H.Yang, W.J. van OOij Progress in Organic Coatings 50 (2004) 140

[14] M.L.Zheludkevich, K.A.Yasakau, S.K.Poznyak, M.G.S.Ferreira Corrosion Science 47 (2005) 3368

[15] A.N.Khramov, N.N.Voevodin, V.N.Balbyshev, M.S.Donley Thin Solid Films 447 (2004) 549

[16] M.L.Zheludkevich, R.Serra, M.F.Montemor, I.M.Miranda Salvado, M.G.S.Ferreira Electrochimica Acta 51 (2005) 208

[17] P.Campestrini, H.Terryn, A.Hovestad, J.H.W. de Wit Surface and Coatings Technology 176 (2004) 365

[18] N.N.Voevodin, N.T.Grebasch, W.S.Soto, F.E.Arnold, M.S.Donley Surface and Coatings Technology 140 (2001) 24

[19] V.Moutarlier, B.Neveu, M.P.Gigandet Surface and Coatings Technology 202 (2008) 2052

[20] J.H.Osborne, K.Y.Blohowiak, S.R.Taylor, C.Hunter, G.Bierwagen, B.Carlson, D.Bernard, M.S.Donley Progress in Organic Coatings 41 (2001) 217

[21] L.Fedrizzi, R.Di Maggio, S.Rossi, L.Leonardelli Benelux Metallurgie 43 (2003) 15

[22] F.Andreatta, P.Aldighieri, L.Paussa, R.Di Maggio, S.Rossi, L.Fedrizzi Electrochimica Acta 52 (2007) 7545

[23] P.Campestrini, E.P.M. van Westing, H.W. van Rooijen, J.H.W. de Wit Corrosion Science 42 (2000) 1853

Chapter 5

Zirconium Oxide from Inorganic Precursors

Design, development and scale-up of environmental friendly coatings are very important in order to replace chromate-based coatings for aluminum alloys. Sol-gel materials are candidates for use in protective coating applications, as it is possible to form highly adherent and chemically inert oxide films on metal substrates. ZrO_2 pretreatments were developed by means of sol-gel technology. An inorganic salt was employed as zirconium precursor in an aqueous solution. The deposition was initially carried out on AA2024 by means of dip and spray technology at laboratory scale. Corrosion inhibitors were introduced to improve corrosion behavior of the films. At a later stage, coating deposition was carried out with a robot-controlled air-pressure gun in spraying cabins in order to evaluate industrial production of the pretreatments.

5.1 Introduction

Research carried out in the field of environmental friendly coatings has considered several alternative technologies [1] including sol-gel coatings, physical vapour deposition (PVD) and chemical vapour deposition (CVD) technology,[2, 3] plasma deposition, self priming topcoats,[4, 5] electrodeposition,[1, 6] conducting polymers, self assembled monolayers and various inorganic and organic inhibitors. The sol-gel technique can be employed for the production of oxide films on different metal substrates [7]. A wide range of metal alkoxides or salts can be used as precursors for the oxide synthesis. The coating undergoes hydrolysis and condensation to form a continuous oxide structure during the deposition procedure. Sol-gel technology enables formation of highly adherent, chemically inert oxide films on metal substrates. Moreover, it is possible to deposit thin films of submicrometer thickness or thicker films through application of multiple layers by controlling deposition parameters like the withdraw rate in the case of dip-coating technology [7]. The wide variety of sol-gel precursor materials commercially available enables preparation of several combinations of high purity, single and multicomponent oxide materials. Incorporation of water and alcohol-soluble dopant ions is also possible increasing the versatility of the sol-gel method. In this chapter will be investigated ZrO_2 pretreatments produced using water-based precursor solutions by means of sol-gel technology for application on AA2024 aluminum alloy. The development targets the industrial application of the pretreatments by means of spraying technology.

5.2 Experimental

The substrate employed for deposition of ZrO_2 pretreatments was AA2024-T3 aluminum alloy. The alloy composition is given in Table 3.1. Prior deposition of sol-gel layers, the sample surface underwent surface preparation consisting of alkaline cleaning, alkaline and acid etch. Alkaline cleaning was carried out in 40 g/l solution of Metaclean 2001/4 VP2 for 10 min at 70 °C; alkaline etch was performed in 60 g/l solution of Turco Liquid Alluminetch for 30 s at 70 °C; acid etch was performed in 200 g/l solution of Turco Liquid Smutgo NC for 5 min at 25 °C. Sol-gel films of ZrO_2 were deposited on AA2024 employing a water-based solution containing the film precursor. This solution consisted of 0.4 M

$ZrO(NO_3)_2$ in water. This method eliminates organic compounds in the deposition process of ZrO_2 pretreatment. At a first stage, the deposition was carried out by dipping technology. AA2024 samples were immersed in the sol-gel solution and withdrawn with controlled rate of 4 mm/s. The dipping step was repeated one, two or three times in order to deposit overlapping ZrO_2 layers on the samples. After each dip in the sol-gel solution, the samples were subjected to thermal treatment at 120 °C for 4 min followed by drying at room temperature. At a second stage, ZrO_2 films were produced by means of spraying technology in order to assess viability of coating application of water-based pretreatments with this technology. Coating application was carried out in our laboratory using an air-pressure gun operated manually. Therefore, it was rather difficult to control deposition parameters in the case of application at laboratory scale. Introduction of corrosion inhibitors was also considered at this stage. The introduction of the corrosion inhibitors in the sol-gel films was carried out using a multilayer approach. Benzothiazole (BT) and 2-mercapto-benzothiazole (MBT) were applied by spraying on the alloy surface prior to deposition of ZrO_2 films by spraying. This approach is based on the consideration that the efficiency of the inhibitor is expected to be higher when the inhibitor is in contact with the aluminum substrate rather than when the inhibitor is trapped in the sol-gel film. Moreover, the introduction of organic inhibitors like BT and MBT in the coating solution might affect the long-term stability of the bath and alter the quality of the deposited film. At a third stage, production of water-based ZrO_2 pretreatments was carried out by means of a robot-controlled air pressure gun in a spraying cabin at Fraunhofer Gesellschaft - IPA (Stuttgart, Germany) in order to produce demonstrators for industrial scale-up of ZrO_2 films. In this stage, ZrO_2 films were initially produced without corrosion inhibitors. Optimization of deposition parameters was necessary in order to produce ZrO_2 films with thickness similar to that obtained for pretreatments produced at laboratory scale. In this work, ZrO_2 films with thickness in the range of 100-200 nm will be considered because quality of pretreatment is rather good in this range. The morphology of ZrO_2 sol-gel layers was investigated by means of scanning electron microscope (SEM) equipped with energy dispersive X-ray spectroscopy (EDXS). Glow discharge optical emission spectroscopy (GDOES) depth profiles were recorded with a Jobin Yvon GD profiler. Composition profiles were obtained with a calibration procedure using certified reference materials in order to estimate qualitatively film

thickness and composition. The electrochemical behavior of samples coated with ZrO_2 was investigated by means of potentiodynamic polarization in 0.05 M NaCl solution. Potentiodynamic polarization measurements were recorded using a Pt counter electrode and Ag/AgCl reference electrode. The area of the working electrode was 3.6 cm^2. The scan rate was 0.2 $mV\ s^{-1}$. The corrosion current density was estimated by means of extrapolation of the Tafel lines. In some case, this might be difficult due to the existence of a passive range for the samples. In that case, the corrosion current density was considered the value obtained by the intersection of the Tafel line of the cathodic branch with the vertical line defined by the corrosion potential. In addition, open circuit potential (OCP) was recorded for 24 h in the same electrolyte.

5.3 Results

Figure 5.1(a) and (b) shows the typical morphology of an AA2024 sample coated with a water-based ZrO_2 pretreatment deposited by dipping technology. The surface evidences several craters, which are generated during surface preparation (degreasing, alkaline and acid etching) before film deposition. This is most likely related to removal of intermetallics during alkaline etch. The alloy surface appears uniformly covered by the ZrO_2 film, as confirmed by the GDOES composition profile reported in Figure 5.1(c), which displays signals of Zr and O on the alloy surface. Moreover, the pretreatment is well adherent on the substrate. This was observed in transmission electron microscopic images (not shown here) obtained on cross sections of samples coated with sol-gel layer. In addition, the SEM image shown in Figure 5.1(b) does not exhibit film delamination at the locations of defects suggesting good adhesion between the sol-gel film and the metallic substrate. The existence of craters on the alloy surface leads to possible formation of cracks in the ZrO_2 pretreatment, as can be seen in the SEM micrograph in Figure 5.1(b). This micrograph shows that there is a more marked tendency to form cracks in the craters than in the surrounding flat regions, where the pretreatment is uniform and without defects. It can be expected that cracks in the craters are produced during thermal treatment carried out after film deposition in order to promote condensation reactions in the sol-gel film. It is possible that a higher amount of the precursor solution remains inside the craters leading to formation of a slightly thicker film than outside. This thick film in the craters is more sus-

ceptible to crack formation than the thin film outside the craters, in accordance with morphology observed in Figure 5.1(a) and (b). Although cracks are seldom observed in the pretreatments, it has to be mentioned that crack formation is more probable with deposition by dipping than with spraying technology. The GDOES profile in Figure 5.1(c) evidences signals of Zr and O in the surface region, which are attributed to the ZrO_2 pretreatment on the alloy surface. The film thickness can be arbitrarily estimated by the intersection of the Al and Zr signals. This is about 70 nm for the ZrO_2 pretreatment produced with dipping technique. This estimation is rather rough due to the broad ZrO_2 film/substrate interface. This is most likely related to the high surface roughness of the substrate. As can be seen in the profile, there is about 30 wt% of Zr in the film and the O signal ranges between 80 wt% on the surface and 30 wt% at the interface with the substrate. The high amount of oxygen in the pretreatment might be related to nitrate ions trapped in the film during film deposition. Moreover, there is C in the ZrO_2 layer. This is possibly related to contamination. The trend observed in Figure 5.1C indicates that the composition of the pretreatment is non stoichiometric.

A successive step in the development of the water-based films was production by means of spraying technology using the same precursor solution employed for deposition by dipping. This was initially carried out using laboratory equipment. Figure 5.2(a) and (b) shows the morphology of a ZrO_2 pretreatment produced using an air-pressure gun operated manually. The sample shown in Figure 5.2 was coated with a solution containing corrosion inhibitor (MBT) before application of the ZrO_2 film. This was done in order to evaluate the possible implementation of films containing inhibitors for industrial application. The SEM micrograph in Figure 5.2(a) shows that the AA2024 substrate is coated with a uniform film without evident defects. The adhesion of the pretreatment on the substrate appears very good. Similar morphology was observed for a sample containing BT instead of MBT. The morphology in Figure 5.2(a) is similar to that shown in Figure 5.1(a) evidencing that film deposition can be successfully performed by spraying technology. Moreover, the occurrence of cracks in films produced by spraying appears strongly reduced with respect to pretreatments made by dipping technology. This is confirmed by Figure 5.2(b) that shows a uniform film in craters due to surface preparation, in contrast with the morphology observed in Figure 5.1(b). This might be related to a better control of the amount of precur-

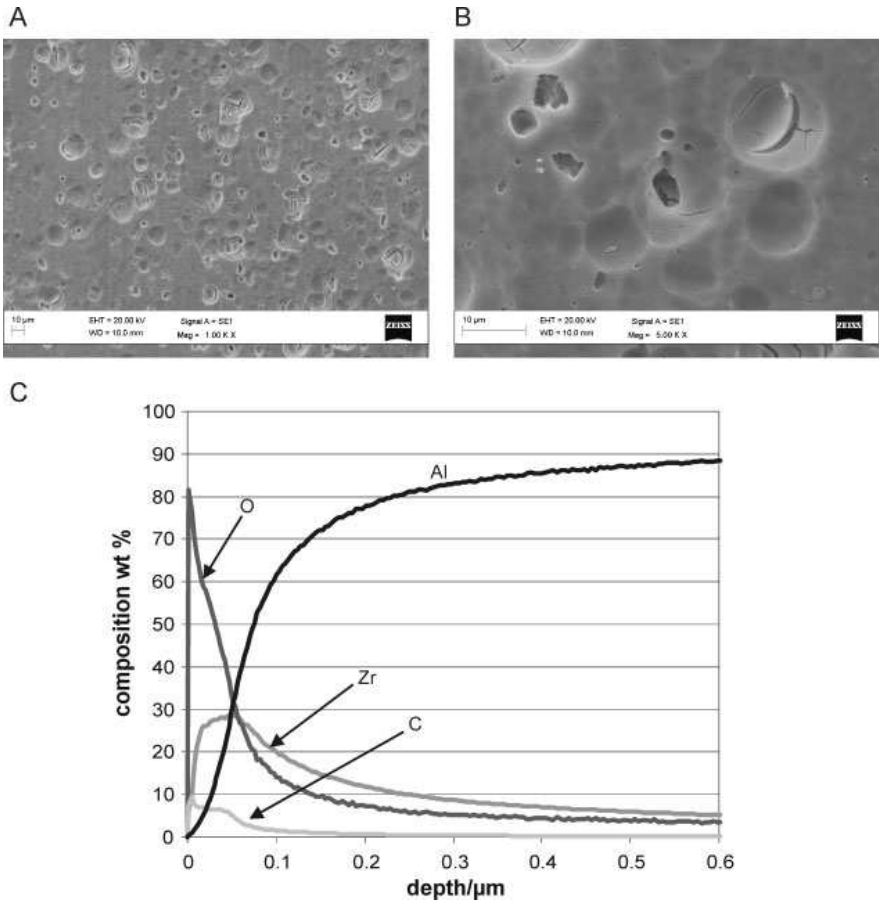

Figure 5.1: SEM micrographs (A and B) and GDOES composition profile (C) for AA2024 coated with one layer of ZrO2 deposited by dipping

sor solution deposited on the alloy surface by spraying than by dipping. However, the control of deposition parameters like spraying distance and deposition speed could not be accurate in our laboratory because the air-pressure gun was operated manually. This is reflected by film thickness estimated by the GDOES composition profile in Figure 5.2(c), which is about 170 nm. The profile exhibits a similar trend to that shown in Figure 5.1(c). The Zr content is about 30 wt% in line with the sample coated by dipping. The C content is higher in Figure 5.2(c) than in Figure 5.1(c) due to introduction of corrosion inhibitor (MBT) in the pretreatment procedure. This is strengthened by the detection of the signal of S, which is also related to the inhibitor.

A further step in development of water-based pretreatment for AA2024 is the evaluation of possible application using industrial equipment. This step was carried out in collaboration with Fraunhofer Gesellschaft - IPA (Stuttgart, Ger-

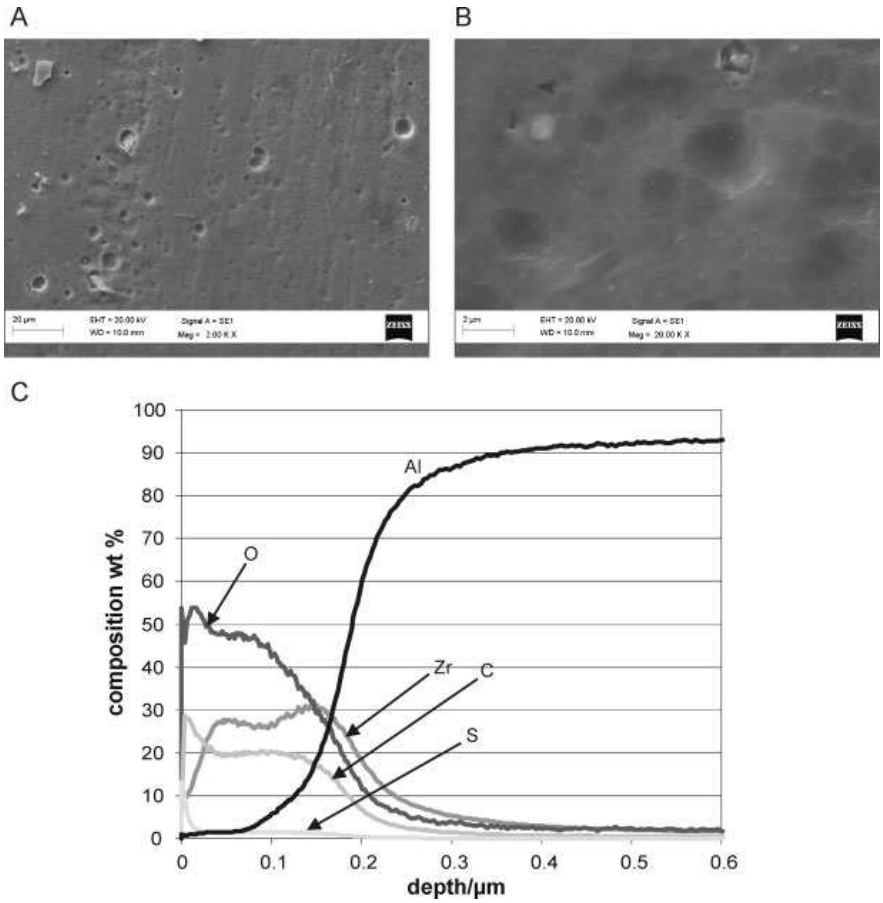

Figure 5.2: SEM micrographs (A and B) and GDOES composition profile (C) for AA2024 coated with one layer of ZrO2 deposited by dipping

many), which carried out the optimization procedure for deposition by spraying with a robot-controlled air-pressure gun. The SEM micrographs in Figure 5.3(a) and (b) show the morphology of a sample produced according to an optimized procedure. The surface appears uniformly coated and without defects even in craters generated by surface preparation. This is very similar to the morphology reported in Figure 5.2 for depositions carried out by spraying with a spraying gun operated manually. This is an indication that the precursor solution employed for deposition by dipping and spraying at laboratory scale can be also used for production of pretreatment using industrial equipment. The micrograph in Figure 5.3(a) evidences bright and dark areas. EDXS analysis evidences that the peak intensity of Zr is the same for these areas. Moreover, the GDOES composition profile in Figure 5.3(c) confirms the existence of a ZrO_2 film on the alloy surface, as can be seen by the trend of Zr and O signals. Film thickness is

about 70 nm, which is in the same range than that obtained by dipping (Figure 5.1(c)). Production of relatively thin films (100 nm) is considered very important as the optimization work carried out with the robot-controlled air-pressure gun indicated that film quality tends to become less good when the film thickness increases. In particular, there is a marked tendency to form cracks for films thicker than 200 nm. Besides, the C signal in the GDOES profile in Figure 5.3(c) is in the same range for the same signal in Figure 5.1(c). This strengthens the observation that the increase of C level in Figure 5.2(c) could be related to the introduction of inhibitor in the pretreatment. Film morphologies shown in Figure 5.1, Figure 5.2 and Figure 5.3 indicate that the 0.4 M zirconyl nitrate solution is suitable for application of water-based pretreatments on aluminum alloys by dipping and spraying technology.

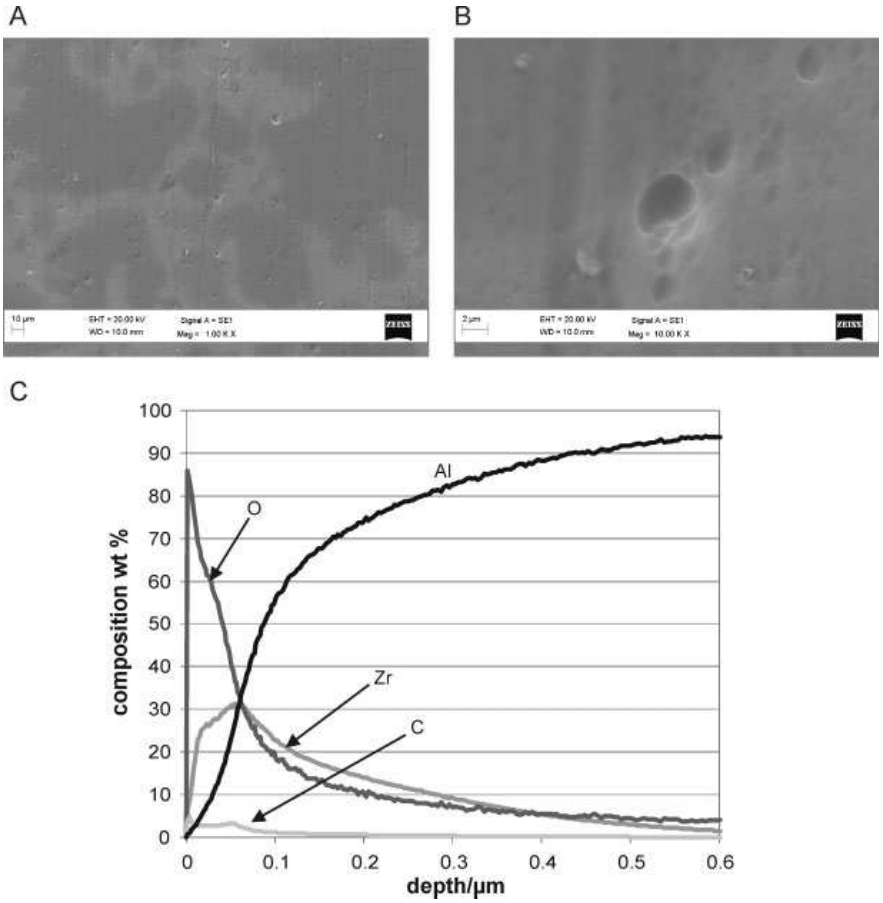

Figure 5.3: SEM micrographs (A and B) and GDOES composition profile (C) of AA2024 coated with ZrO2 deposited by spraying technology using a robot-controlled air-pressure gun.

Figure 5.4 shows potentiodynamic polarization curves carried out in 0.05 M NaCl solution for samples coated with water-based ZrO_2 pretreatments. In addition, the polarization curve for bare AA2024 is also reported. The curve for the ZrO_2 pretreatment applied by dipping exhibits a corrosion current density of about 0.6 $\mu A\ cm^{-2}$, which is more than 1 order of magnitude lower than for bare AA2024 (30 $\mu A cm^{-2}$). This is an indication that the ZrO_2 pretreatment improves the corrosion behavior of AA2024. This is further supported by the marked decrease of cathodic and anodic current density observed for the alloy coated with the ZrO_2 film deposited by dipping relative to the bare alloy. The breakdown potential is at -370 mV vs. Ag/AgCl, which is about 50 mV higher than the corrosion potential. The morphology of the sample with ZrO_2 film exhibited pitting attack mainly localized at few locations on the surface most likely associated with film defects like cracks. Nevertheless, it can be stated that the ZrO_2 pretreatment behaves like a barrier against corrosion. This effect is mainly due to the strong reduction of the area of active sites, as indicated by the marked reduction of corrosion current density for the sample coated with ZrO_2 pretreatment. Since the ZrO_2 oxide film could be assumed inert in the aggressive electrolyte, the active sites are mainly film defects related to application of the ZrO_2 film. Therefore, technologies for deposition of water-based ZrO_2 films should be optimized in order to minimize the risk of introducing defects in the pretreatment. The potentiodynamic curve relative to the sample with ZrO_2 pretreatment applied by spraying with laboratory equipment (air-pressure gun operated manually) exhibits a rather extended passive range associated by a relatively low current density. The breakdown potential is -410 mV vs. Ag/AgCl for this sample. This is about 180 mV higher than the corrosion potential. The corrosion current density is 0.3 $\mu A\ cm^{-2}$, which is slightly lower than for the same pretreatment applied by dipping. The existence of a passive range is in line with the strong reduction of the number of cracks observed on the alloy surface for the sample coated by spraying than for that coated by dipping (Figure 5.2(a) and (b)). Moreover, it should be considered that the sample coated by spraying technique contains BT, which was applied on the substrate before deposition of the ZrO_2 film. The corrosion inhibitor has a beneficial effect on the electrochemical behavior. In particular, this effect might be important at defects, which might still be present in the ZrO_2 pretreatment. The potentiodynamic polarization curve for the water-based ZrO_2 film deposited with a robot-controlled air-pressure gun

appears rather noisy. This is typically observed for this type of sample and should be attributed to the high quality of the ZrO_2 pretreatment obtained with this application technology. The deposition of a nearly defect free film renders current density detection rather difficult during potentiodynamic polarization. This is confirmed by the corrosion current density of 0.02 $\mu A\ cm^{-2}$ measured for the alloy coated with robot-controlled air-pressure gun. This is significantly lower than the corrosion current density measured for the pretreatments produced at laboratory scale by dipping and spraying techniques. The anodic current density progressively increases above the OCP and remains very low until a breakdown is observed at -480 mV vs. Ag/AgCl. The breakdown potential is 150 mV higher than the corrosion potential for this sample suggesting the existence of a very good barrier against corrosion. Several current spikes might be observed between the corrosion potential and the breakdown potential suggesting that metastable pitting takes place at weakest points of the ZrO_2 pretreatment.The potentiodynamic polarization curve for the sample coated by robot-controlled air-pressure gun exhibits similar barrier properties to chromate conversion coated AA2024 [8]. This is a further indication that the ZrO_2 pretreatments produced with industrial spraying equipment might be considered for the replacement of Cr-based pretreatments for AA2024.

Figure 5.5 shows OCP vs. immersion time for samples coated with ZrO_2 water-based films. These measurements were selected in order to evaluate the effect of introduction of inhibitors in the pretreatments. Figure 5.5 also exhibits the OCP of the sample coated with robot-controlled air-pressure gun. This sample is non inhibited because it was decided to initially optimize the procedure for industrial application before considering the introduction of inhibitors. The ZrO_2 films containing MBT and BT exhibit stationary open circuit. The pretreatment containing MBT evidences a decrease of the OCP after about 22 hours immersion. This decrease is probably associated to the onset of pitting. As compared to bare AA2024, pitting attack is strongly delayed for the sample containing MBT. This is probably due to a combined effect of the ZrO_2 pretreatment and of the corrosion inhibitor, as considered for the potentiodynamic polarization test. The sample coated with the pretreatment containing BT does not show the decrease of the OCP during 24 hours immersion in the electrolyte suggesting good corrosion resistance. The OCP of the sample coated with a pretreatment applied by spraying with a robot-controlled air-pressure gun exhibits significant poten-

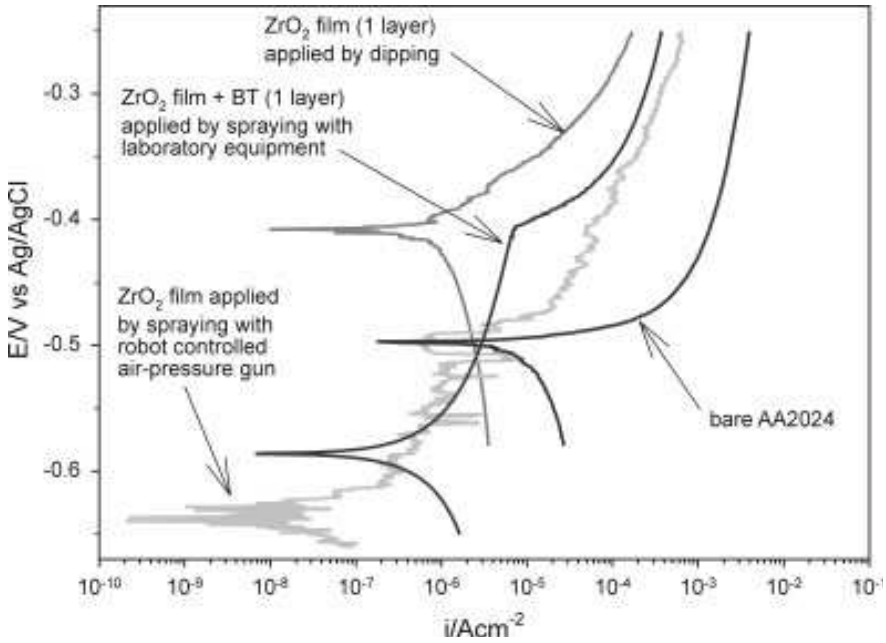

Figure 5.4: SEM micrographs (A and B) and GDOES composition profile (C) of AA2024 coated with ZrO2 deposited by spraying technology using a robot-controlled air-pressure gun.

tial oscillations during the measurement. This behavior is reproduced also for 72 hours immersion time. It is likely that these potential fluctuations are due to a nearly defect-free pretreatment, as considered for the anodic current density in the potentiodynamic polarization curve for the same sample. This sample does not show evidence of pitting corrosion even after 72 hours in the electrolyte. This is in line with good electrochemical behavior observed in potentiodynamic polarization curves. Moreover, results shown in Figure 5.5 indicate that the electrochemical behavior could be further improved by the introduction of corrosion inhibitors in pretreatments deposited with industrial equipment for application by spraying.

5.4 Conclusions

In this chapter, the morphology, composition and electrochemical behavior of water-based ZrO_2 pretreatments for AA2024 have been studied in the view of industrial scale-up by means of spraying technique. Thin and well-adherent ZrO_2 pretreatments can be deposited on AA2024 by means of sol-gel technique by

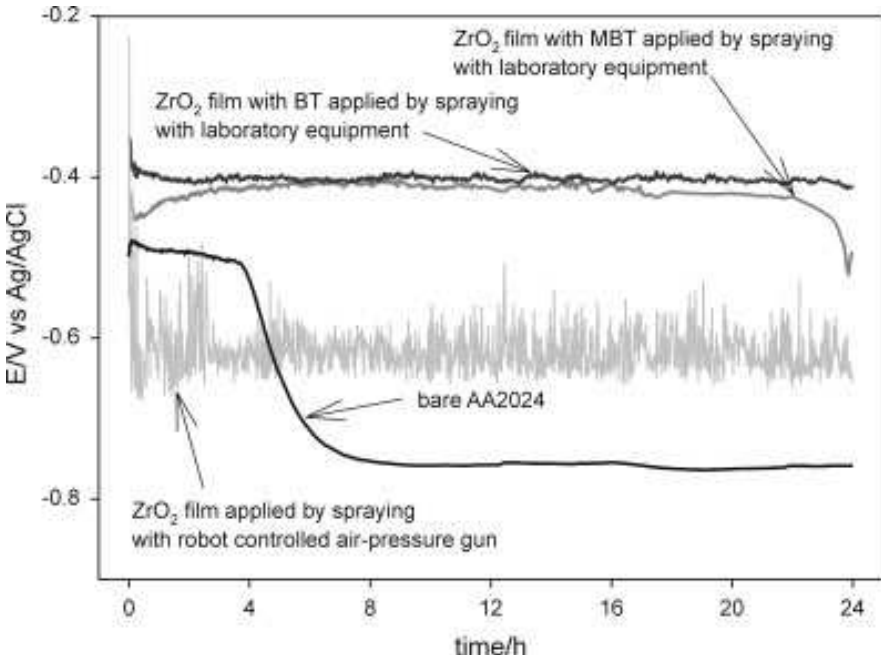

Figure 5.5: OCP vs. immersion time for AA2024 coated with ZrO2 film and for bare AA2024 (0.05 M NaCl solution)

either dipping or spraying at laboratory scale. In particular, characterization of film morphology and electrochemical behavior indicates that ZrO_2 pretreatment is suitable for application by spraying technology, which improves film quality. The barrier properties of water-based ZrO_2 films are rather good evidencing a marked reduction of corrosion current density in potentiodynamic polarization curves. Moreover, the electrochemical behavior can be improved by addition of corrosion inhibitors like MBT and BT in the ZrO_2 pretreatments. Application of ZrO_2 pretreatments has also been carried out by means of a robot-controlled air-pressure gun. The morphology and the electrochemical behavior of samples produced with this technique are further improved relative to samples obtained at laboratory scale. Results on samples produced with robot-controlled air pressure gun indicate that ZrO_2 pretreatments are suitable for industrial application.

Bibliography

[1] R.L. Twite, G.P. Bierwagen Prog. Org. Coat. 33 (1998) 91

[2] H. Yasuda, B.H. Chun, D.L. Cho, T.J. Lin, D.J. Yang, J.A. Antonelli Corrosion 52 (1996) 169

[3] N. Shirtcliffe, P. Thiemann, M. Stratmann, G. Grundmeier Surf. Coat. Technol. 1121 (2001) 142

[4] D.J. Hirst, A.T. Eng, W.J. Green US Patent 5043373 1991

[5] C.R. Hegedus, W.J. Green US Patent 4885324 1989

[6] L. Fedrizzi, F. Andreatta, L. Paussa, F. Deflorian, S.Maschio Prog. Org. Coat. 63 (2008) 299

[7] T.L. Metroke, R.L. Parkhill, E.T. Knobbe Prog. Org. Coat. 41 (2001) 233

[8] N. N. Voevodin, N. T. Grebasch, W. S. Soto, F. E. Arnold, M. S. Donley Surf. Coat. Technol. 24 (2001) 140

Chapter 6

Macro-Evaluation of Cerium Inhibition

Aluminum alloys like AA2024 are widely employed in aircraft industry due to combination of low weight and good mechanical properties. AA2024 is susceptible to severe localized attack and corrosion protection is a very important issue for application of this alloy. Corrosion resistance can be improved by means of coatings, which provide barrier effect to the metal substrate. Moreover, active protection systems against corrosion can be generated incorporating in the coating corrosion inhibitors or self-healing promoters. In this view, active protection systems could improve corrosion protection due to combination of barrier effect and additional protection mechanisms, which can be developed in the coating due to active species. In order to develop an active protection system, cerium nitrate was employed as source of species that could improve corrosion resistance of AA2024. The electrochemical behaviour of bare aluminum alloy was investigated in electrolytes with different content of cerium nitrate. Open circuit potential and potentiodynamic polarizations were carried out on AA2024 immersed in solution containing cerium nitrate and/or sodium chloride. In particular, effect of pH, concentration of cerium nitrate and chloride were studied by means of electrochemical measurements. Moreover, morphology and composition of AA2024 samples were investigated after immersion in solutions containing cerium nitrate by means of scanning electron microscopy and energy dispersive x-ray spectroscopy (S.E.M.-E.D.X.S.) in order to study the protection mechanism of cerium nitrate added to the aqueous solution. Open circuit potential measurements for AA2024 in different electrolytes exhibit a marked effect of cerium nitrate under free im-

mersion. Potentiodynamic polarization curves show that cerium nitrate improves corrosion resistance of AA2024. Moreover, corrosion inhibition is strongly dependent on cerium nitrate concentration. In particular, the inhibition effect becomes stronger increasing the concentration of cerium nitrate in the electrolyte. Moreover, S.E.M.-E.D.X.S. analysis evidence precipitation of compounds containing cerium on the metallic substrate suggesting that the protection mechanism is dependent on surface condition and microstructure of the aluminium alloy.

6.1 Introduction

AA2024 aluminium alloy is widely employed in aerospace applications due to its advantageous strength-to-weight ratio. In order to improve mechanical properties, AA2024 aluminum alloy undergoes thermal treatment to promote precipitation of nanometric second-phase particles which are able to strengthen the aluminum microstructure [1]. Unfortunately, large intermetallic particles generate a microstructure very susceptible to localized corrosion attack due to localized galvanic coupling with the aluminium matrix. Buchheit et al. [2] studied the distribution of intermetallic particles formed on polished AA2024-T3 aluminum alloy. They found that 61.3 % of the total amount of intermetallics was $CuMgAl_2$ (S-phase). $Al_6(Cu, Fe, Mn)$ represented 12.3 %, Al_7Cu_2Fe was 5.2 %, $(Al, Cu)_6Mn$ was 4.3 % while the remaining 16.7 % was not identified. $CuMgAl_2$ (which could be initially considered anodic relative to the matrix) promoted the development of severe local corrosion attack when aluminum alloys were exposed to chloride-containing solution [3, 4, 5]. Zhu et al. [6] studied polished AA2024-T3 immersed in 0.6M NaCl. They reported that in the first 3 hours immersion, pitting corrosion started at the S-phase particles due to magnesium dissolution. They observed that immediately after immersion, S-particles were anodic relative to the aluminium matrix. However, magnesium and aluminum content in the S-phase drastically decreased until the electrochemical behaviour of the S-particle turned from anodic to cathodic relative to the aluminum matrix. Therefore, as suggested by Buchheit et al. [12] a galvanic coupling between anodic matrix and cathodic modified S-particles is formed due to magnesium and aluminium dissolution promoting a localized aluminium dissolution at the matrix near S-particles. Another explanation of pitting corrosion development was given by Zhu et al. [6] who stated that the very fast magnesium dissolution occurring in the first 3 hours

immersion promoted a vigorous increase of reduction reactions rate at the matrix near the S-particles. They observed that OH^- ions produced were able to shift solution pH above 9, which represents the condition where aluminum oxide is not stable. Therefore, the natural oxide layer tended to dissolve and aluminum underneath started to re-oxidize. Aluminum dissolution that occurs under alkaline conditions is also known as aluminum cathodic corrosion. In addition to S-phase, intermetallics containing Al-Cu-Mn-Fe-Si are common in AA2024 aluminium alloy. These intermetallics act as cathodic sites relative to the matrix, as proved by several studies reported in literature [7, 8, 9, 10, 11]. In the case of Al-Cu-Mn-Fe-Si intermetallics, the cathodic-to-anodic ratio is not as unfavorable as in the case of $CuMgAl_2$ (S-phase) because aluminium matrix (larger area) behaves anodically while particles containing Al-Cu-Mn-Fe-Si (smaller area) act cathodically. Due to the existence of a large number of intermetallics in the microstructure, AA2024 aluminum alloy has to be protected in order to enhance its corrosion behaviour. Chromates have been widely used to improve corrosion protection of aluminium and its alloys [12, 13]. Although chromates are able to provide a very good protection against corrosion, they are toxics and carcinogenic [14]. Hinton et al., Arnott et al. and Ryan et al. [15, 26, 17, 18] proved that cerium and other rare-earth salts inhibited corrosion behaviour of aluminium alloys in aqueous solution containing chlorides. Inhibition effects obtained adding cerium ions as chloride compounds to the electrolytic solution were responsible of a strong improvement of corrosion resistance of AA2024 [19] promoting the formation of a compact film of cerium hydroxide and oxide on the metal surface [20]. Corrosion inhibition provided by cerium ions could be related to the decrease of the cathodic reaction kinetics [16]. This behaviour was observed for aluminium alloys rich in copper [17] and zinc [18]. In the case of zinc-containing alloys (AA7075) it was observed that cerium replaced the aluminium in the oxide layer [20]. It was also observed that oxygen reduction reaction was influenced by the nature of the electrode considered [21]. It was reported that oxygen reduction could follow two different paths. The first path follows a direct four-electrons reduction in which oxygen is completely reduced to hydroxide ion:

$$O_2 + 2H_2O + 4e^- \rightarrow 4OH^- \tag{6.1}$$

The second reaction-path for oxygen reduction involves a two-electrons mech-

anism in which oxygen is reduced to hydrogen peroxide and hydroxide ions:

$$O_2 + 2H_2O + 2e^- \rightarrow H_2O_2 + 2OH^- \tag{6.2}$$

Since cerium inhibition is influenced by oxygen reduction mechanism, the nature of the electrode is an important aspect to be considered. Several researchers investigated oxygen reduction mechanism on different electrodes like gold, iron and copper [22, 23, 24, 25, 26, 27]. It was shown that oxygen reduction mechanism occurring on gold substrate was dependent on electrode potential. Below -1V(SCE) oxygen reduction on gold electrode occurs according to the mechanism involving 4 electrons described by equation (1). Considering more noble potentials, the average number of electrons transferred tends to decrease and oxygen reduction mechanism involved at -0.7V(SCE) becomes controlled by equation (2). In the case of iron, it was shown that oxygen reduction mechanism was dependent on the potential applied rather than on the passive status of the electrode surface (controllare riferimento). For a copper substrate, oxygen reduction in neutral perchlorate solution took place under four-electrons mechanism at low potential [$<$ 0.8V(SCE)]. In the same electrolytic solution, it was also observed that near the peak of oxygen reduction rate at -0.5V(SCE) a small amount of oxygen peroxide was found. This was correlated to the formation of a catalytic surface film (copper hydroxide). However, it was shown that oxygen reduction always took place following the four-electrons mechanism in 1M NaCl solution unless the solution pH was increased to 10. Therefore, oxygen reduction reaction is able to control the precipitation of chemical species in solution. Aldykiewicz et al. [28] studied the film deposited on gold and copper substrates immersed in cerium chloride in aerated and deaerated solution. XANES spectra obtained on copper electrode showed that aerated solution promoted the formation of a thicker cerium-containing film than that formed in a deaerated solution. Moreover, the film precipitated employing the deaerated solution mainly contained cerium in the trivalent state. Otherwise, cerium in the tetravalent state was detected for films obtained in aerated solution. This aspect confirmed that oxygen reduction reaction influenced cerium precipitation mechanism on copper electrode. The work of Aldykiewicz et al. [28] took into account also the influence on cerium precipitation of oxygen reduction considering two or four-electrons mechanisms. It was observed that the two-electrons mechanism promoted the formation of

a more efficient/protective film than that obtained by means of the mechanism involving four electrons. In the case of the copper electrode, a rapid cerium deposition could be obtained when oxygen reduction was controlled by the two-electrons mechanism (producing hydrogen peroxide) or directly adding hydrogen peroxide to the cerium-containing solution. Indeed, hydrogen peroxide could be reduced causing an increase of solution pH, which favoured the precipitation of cerium compounds. The addition of hydrogen peroxide to the cerium chloride bath was patented by Wilson and Hinton [18] because this represented a method to obtain a protective cerium-based conversion coating with a fast process. After the first studies on the mechanism of cerium oxides/hydroxides precipitation [16, 17, 18, 19, 20], it was concluded that the process started on cathodic intermetallics where reduction reactions occurred. At these sites, solution pH tended to increase developing favourable chemical conditions to cerium precipitation. These works considering AA7075 aluminium alloy immersed in cerium chloride, suggested that cerium precipitation started at cathodic intermetallics (copper-rich intermetallics) and continued at a later stage in the surrounding regions via island growth. However, this mechanism is still not completely clarified. Hughes et al. [29] suggested that the residual surface could be covered by cerium compounds due to small active intermetallics not still involved in the process. Several investigations [30, 31, 32, 33, 34] confirmed that intermetallics with a cathodic behaviour relative to the matrix constituted the preferential sites for cerium precipitation. In the case of 2xxx and 7xxx aluminium alloys, the higher tendency to promote the deposition of cerium compounds has been correlated to the presence of copper-rich intermetallics on the surface. However, controversial results were obtained [35, 36] for cathodic intermetallics without copper like $(Fe, Cr)_3SiAl_{12}$ in AA6061. Several works [37, 38, 39, 40, 41, 42] have considered the deposition of a cerium-containing layer as an alternative conversion coating for the replacement of chromate based protective systems. In many cases, deposition processes of cerium-based conversion layers are not attractive for industrial applications because of either, the long time needed for the deposition or the formation of layers with extended cracks. For this reason, this paper considers cerium ions as corrosion inhibitors which can provide an additional form of protection when included in the bulk of a corrosion protective system. In our previous works [43, 44], interesting results were obtained adding cerium nitrate to organic-inorganic hybrid sol-gel systems deposited on AA2024 aluminum alloy. Coated AA2024 with hy-

brid cerium-containing system evidenced corrosion rates lower than those detected for the coating without cerium. Cerium ions entrapped in the coating structure were probably involved in the overall corrosion processes occurring at the metal surface providing additional protection. Besides, Hayes et al. [45, 46] proposed a revised E-pH diagram for cerium base systems using more actual thermodynamic data compared to those ones available for Pourbaix diagrams [47]. The revised E-pH diagram was subsequently employed in order to better understand the influence of cerium deposition parameters on processes involved in cerium-based conversion coating [48, 49, 50]. In the revised E-pH diagram, the theoretical pH at which trivalent cerium is oxidized to the tetravalent state is lower than that described by the Pourbaix E-pH diagram. Therefore, trivalent cerium can oxidize to tetravalent state by means of a sort of self-healing effect limiting corrosion process for local solution pH lower than those suggested by Pourbaix E-pH diagram. In this case, the protection is due to re-dox reactions (where cerium is oxidized rather than aluminum by cathodic reactions) promoting the formation of tetravalent cerium compounds instead of direct precipitation of trivalent cerium oxides/hydroxides. Based on previous results, the aim of this work is the evaluation of cerium inhibition mechanism on AA2024 rather than the study of a cerium-based conversion coating. The evaluation of AA2024 corrosion inhibition due to cerium ions in solution may be related to the behaviour of cerium ions during water diffusion into the coating containing free-cerium ions. Considering this important aspect, the electrochemical behaviour of AA2024 was investigated for several hours or some days in order to promote complete interaction between cerium ions and species involved in the corrosion processes.

6.2 Experimental Procedure

6.2.1 Materials and Surface Preparation

The substrate employed in this work was AA2024-T3 aluminium alloy. The alloy composition is given in Table 3.1. AA2024 aluminium alloy sheets (8 cm x 2.5 cm) were used as testing samples. Two different surface preparation procedures of AA2024 samples were employed: the first one consisting of an alkaline degreasing while in the second one alkaline degreasing is followed by an alkaline etching and by an acid etching. This second surface preparation procedure is referred as

pickling in this paper. Alkaline degreasing was carried out in 40 $g\ l^{-1}$ solution of Metaclean 2001-4 VP2 for 10 minutes at 70 $°C$. Alkaline etching was performed in 60 $g\ l^{-1}$ solution of Turco Liquid Alluminetch for 30 s at 70 $°C$ while acid etching was carried out in 200 $g\ l^{-1}$ solution of Turco Liquid Smutgo NC for 5 min at 25 $°C$. Degreasing procedure consists in an alkaline process which is able to remove oils and grease from the surface while no chemical modifications are expected. Pickling procedure employed to prepare AA2024 surface consists in an alkaline degreasing and in an alkaline etching followed by an acid etching. This procedure enables to remove the natural oxide layer and the intermetallic particles from the metal surface promoting a chemical modification of the surface.

6.2.2 Electrochemical Measurements

The electrochemical behaviour of AA2024 aluminium alloy was investigated by means of open circuit potential measurements (OCP) and potentiodynamic polarization. The measurements were carried out at room temperature in a standard electrochemical cell and the area exposed was 15 cm^2 (with 30 ml electrolyte). The counter electrode was a platinum wire (diameter 1.5 mm) and the reference electrode was Ag/AgCl for all measurements. Potentiodynamic polarization measurements were carried out at the end of open circuit potential measurements on the same area exposed to the electrolyte. The scan rate was 0.2 $mV\ s^{-1}$ for potentiodynamic polarization measurements. All measurements were performed using an AUTOLAB PG-STAT 12 potentiostat-galvanostat. The electrochemical behaviour of AA2024 aluminum alloy was evaluated employing different electrolytic solution. At the beginning, measurements were performed using 0.05M NaCl aqueous solution. Afterwards, in order to investigate the effect of compounds containing cerium species on AA2024 corrosion behaviour, cerium nitrate was added to the chloride solution. Two different cerium nitrate ($Ce(NO_3)_3 \cdot 6H_2O$) concentrations were employed: 0.001M or 0.01M. Besides, inhibited solutions were employed to carry out electrochemical measurements in combination with NaCl or alone. Open circuit potential measurements enable to evaluate possible surface modification and at the most enables to coarsely predict corrosion processes or inhibition mechanisms. However, this type of test is not able to provide quantitative results about electrochemical behaviour of corroding systems. Therefore, in order to make a deeper evaluation, potentiodynamic polarization

curves were performed as useful test to evaluate the cerium effect on AA2024 corrosion behaviour. Potentiodynamic polarization curves were carried out at the end of OCP measurements previously performed for 15 hours. The behaviour developing during the first 15 hours immersion has been discussed considering OCP measurements while the effect of surface modification due to immersion in cerium-containing solution has been evaluated by means of potentiodynamic polarization curves. In order to evaluate the inhibition ability of cerium nitrate as a function of solution pH, pickled AA2024 samples were immersed in alkaline and acid solutions containing cerium: in addition to cerium nitrate, sulphuric acid or sodium hydroxide were added. The acid solution was prepared adding to 0.01M $Ce(NO_3)_3 \cdot 6H_2O$ an amount of sulphuric acid until to reach the solution pH equal to 3 while alkaline solution was prepared adding sodium hydroxide until to reach the solution pH equal to 8. These values were selected because they correspond to the upper and the lower solution pH limits describing the aluminium passive region in Pourbaix diagram [47]

6.2.3 Morphology and Chemical Composition of AA2024-T3 Surface

After electrochemical measurements, surface morphology of AA2024 samples was investigated by means of Scanning Electron Microscopy (SEM) which was also used for the evaluation of the chemical composition of modified or unmodified AA2024 surface employing Energy Dispersive X-ray Spectroscopy (EDXS). A Carl Zeiss EVO 40XVP microscope equipped with INCA ENERGY 250 microanalysis equipment was used in this work. Glow Discharge Optical Emission Spectroscopy (GDOES) measurements were performed in order to obtain qualitative chemical composition profiles of AA2024 surface after the preparation procedure. GDOES analysis were carried out using a JY RF-GD PROFILER HR instrument, manufactured by Horiba Jobin-Yvonne. The instrument is equipped with standard 4 mm diameter anode, the polychromathor with 28 acquiring channels and the Quantum XP software.

6.2.4 Galvanic Coupling

In order to verify that the precipitation mechanism involving cerium is promoted on cathodic areas, immersion tests in the solution containing cerium nitrate were carried out for an AA8xxx aluminium alloy connected to a pure copper sheet in order to have galvanic coupling between the aluminium sheet and the copper sheet. In this configuration, the 8XXX aluminium alloy was the macro-anode while the pure copper was the macro-cathode. The galvanic couple was immersed in 0.05M NaCl aqueous solution containing 0.01M $Ce(NO_3)_3 \cdot 6H_2O$. After 6 hours immersion, aluminium and copper sheets were investigated by means of scanning electron microscopy in order to evaluate morphology and chemical composition. The experimental procedure described was used to separate macroscopically the anodic and the cathodic sites in order to evaluate cerium nitrate effect on both, the anode and the cathode.

6.3 Results and Discussion

6.3.1 Open Circuit Potential for AA2024 pickled samples

Figure 6.1 shows the open circuit potential (OCP) for pickled AA2024 as a function of immersion time in different electrolytic solutions. The measurements were performed in 0.05M NaCl (solid line) and in 0.05M NaCl solution containing 0.001M (long dash line) or 0.01M $Ce(NO_3)_3 \cdot 6H_2O$ (short dash line). Pickled AA2024 displays an OCP of about -600mV vs Ag/AgCl immediately after immersion in 0.05M NaCl solution. The OCP progressively increases during the first two hours in solution and reaches a stationary potential of -520mV vs Ag/AgCl, which may be considered as the steady corrosion potential (E_{corr}) for pickled AA2024 in 0.05M NaCl solution. OCP for pickled AA2024 immersed in a 0.05M NaCl solution containing 0.001M $Ce(NO_3)_3 \cdot 6H_2O$ (long dash line in Figure 6.1) shows similar behaviour to that observed for the same substrate immersed in a solution containing only chlorides (solid line in Figure 6.1). OCP for pickled AA2024 immersed in a 0.05M NaCl solution with 0.01M $Ce(NO_3)_3 \cdot 6H_2O$ is about -530 mV vs Ag/AgCl immediately after immersion and reaches a stationary potential of about -400 mV vs Ag/AgCl after 4-5 hours in the electrolyte. This is about 100 mV more positive than the OCP values observed for pickled

AA2024 immersed in 0.05M NaCl solution containing 0.001M $Ce(NO_3)_3 \cdot 6H_2O$ and for the same substrate immersed in 0.05M NaCl solution. The OCP increase detected during the first hours of immersion in 0.05M NaCl solution is probably associated to a transitory behaviour related to the dissolution of intermetallics on the metal surface. In particular, the increase of OCP can be due to the dissolution of magnesium, which could lead to the modification of chemical composition altering the electrochemical equilibrium at the metal/solution interface [38].

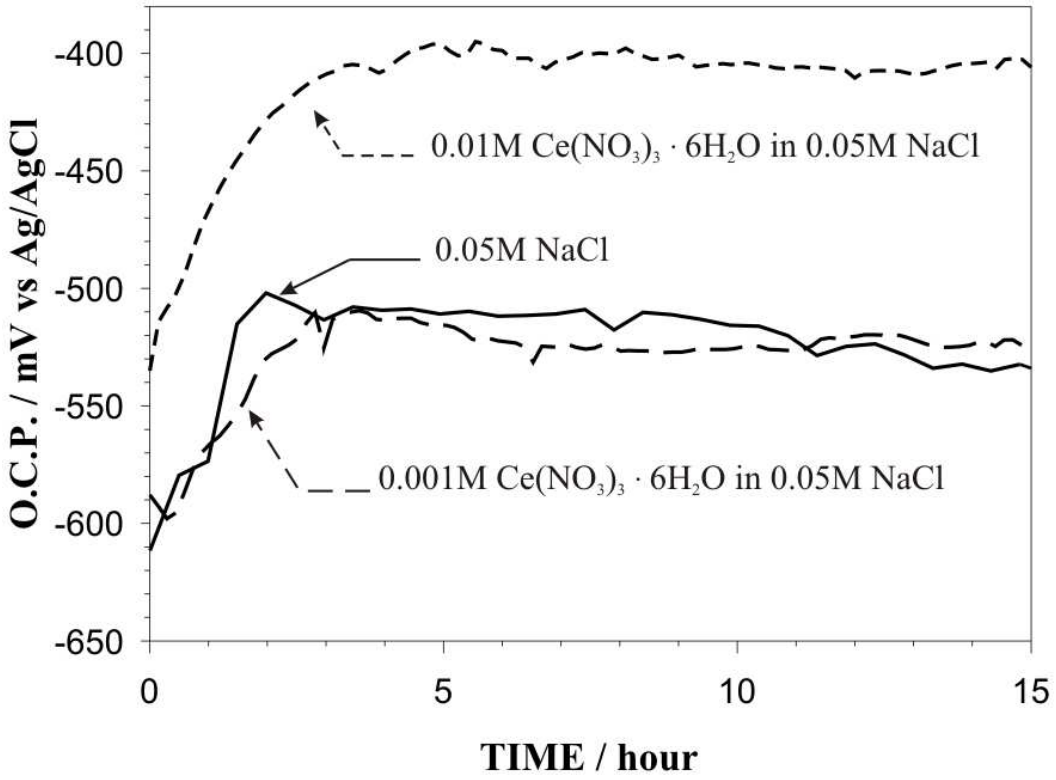

Figure 6.1: OCP potential in 0.05M NaCl with cerium nitrate

Figure 6.2 (a) shows an interpretation of the behaviour observed for pickled AA2024 immersed in a solution containing chlorides based on the mixed potential theory [1]. Based on the mixed potential theory, the open circuit potential is the point where the total rates of oxidation and reduction are equal. Immediately after immersion, it can be expected that the contribution of magnesium dissolution to the total oxidation rate is relevant since it is reported that magnesium undergoes very fast dissolution in AA2024 immersed in aggressive electrolytes [51].

Thus, the mixed corrosion potential corresponding to this condition is OCP_1. Due to progressive magnesium dissolution, it can be expected that the contribution of magnesium oxidation to the total oxidation rate becomes less important than that of aluminium oxidation for longer immersion times. During this stage, magnesium progressively dissolves and the curve for magnesium oxidation shifts to lower current because it is associated to the amount of magnesium available on the exposed substrate. When the substrate undergoes extensive magnesium oxidation after 2-3 hours in the electrolyte, it can be predicted that the total oxidation rate is mainly determined by aluminium oxidation. As a consequence, the mixed corrosion potential will be OCP_2. As it can be seen in Figure 6.2(a), OCP_2 is more positive than OCP_1. After reaching the mixed corrosion potential OCP_2, it can be expected that the mixed corrosion potential becomes stationary since the anodic reaction is mainly aluminium oxidation. The interpretation described in Figure 6.2(a) is in line with the behaviour observed in Figure 6.1 for pickled AA2024 immersed in a solution containing chlorides. The behaviour of pickled AA2024 in 0.05M NaCl solution containing 0.001M $Ce(NO_3)_3 \cdot 6H_2O$ (long dash line in Figure 6.1) is very similar to that observed in the solution containing only chlorides (solid line in Figure 6.1). Apparently, the amount of cerium nitrate added to the electrolyte (0.001M does not significantly modify the OCP trend for pickled AA2024. It is possible that cerium ions added to the solution might take part in the electrochemical processes at the metal substrate without providing an effective inhibition. The cerium mechanism reported in literature [[19, 20, 21, 22, 23, 24] suggests that a precipitation of cerium hydroxide-oxide occurs at the cathodic areas when corroding systems are considered. The cathodic inhibition due to cerium ions should reduce the current involved in the reduction processes causing a modification of measured OCP. In the case of the electrolyte containing 0.001M cerium nitrate, OCP trend for pickled AA2024 was similar to that in the solution without cerium because the amount of cerium added in the electrolyte is probably not enough to allow a remarkable inhibition. Indeed, cathodic areas involved in cerium precipitation may be only a fraction of those available on the aluminium surface. Therefore, it can be expected that the inhibition effect due to cerium precipitation is very limited. In order to further investigate this aspect, SEM-EDXS analysis was carried out on pickled AA2024 after 6 days immersion in a solution 0.05M NaCl containing 0.001M $Ce(NO_3)_3 \cdot 6H_2O$.

Figure 6.3 shows surface morphology and EDXS spectra detected on two dif-

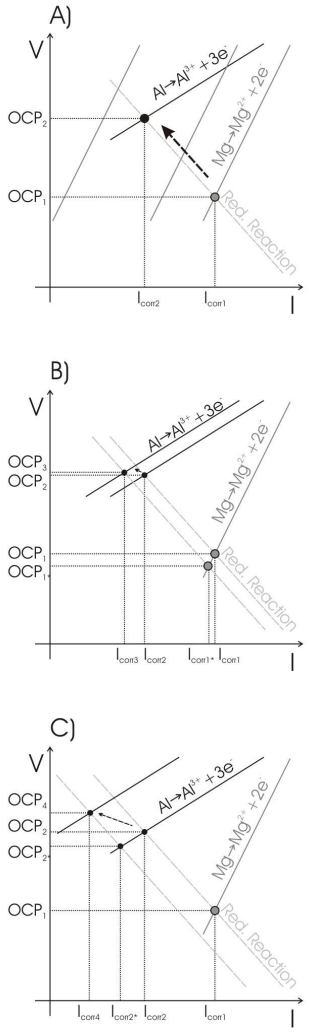

Figure 6.2: Mixed potential theory

ferent areas of the sample. In Figure 6.3(a), a cracked film can be recognized on the top-right of the micrograph while the remaining area appears uncovered. In Figure 6.3(a), the spectrum associated to the covered area (Spectrum 1) evidences the presence of a significant amount of cerium while the signal of cerium is below the detection limits for the spectrum acquired on the uncovered area (Spectrum 2). This experimental evidence suggests that only a small number of sites were strongly involved in the precipitation mechanism of cerium compounds when 0.05M NaCl with 0.001M cerium nitrate solution was used. A thin film can be observed on the substrate observing at higher magnification the region next to the boundary between covered and uncovered substrate (Figure 6.3(b)). In the EDXS spectra shown in Figure 6.3(b), the cerium content detected on the

area associated to Spectrum 1 is higher than that in the surrounding areas (Spectrum 3). The cerium precipitation occurred in the region where Spectrum 1 was recorded can be associated to the formation of cerium compounds, which could contain cerium chloride crystals. Indeed, the atomic ratio between chloride and cerium signals was roughly estimated around 3 corresponding to the stoichiometry of $CeCl_3$. It can be observed in Figure 6.3(b) that a very thin and continuous film covers the surrounding metal substrate. This is confirmed by the existence of a Ce signal above the detection limits in Spectrum 3. Although Spectrum 3 in Figure 6.3(b) shows a cerium signal lower than that in Spectrum 1, it can be supposed that a cerium hydroxide-oxide layer with a thickness in the range of few nanometers covers the substrate. However, in the regions far from areas where a strong cerium precipitation is involved, E.D.X.S. analysis are not able to clearly identify the presence of cerium on the metal substrate.

Figure 6.2(b) shows an interpretation of the behaviour observed for pickled AA2024 immersed in a solution 0.05M NaCl containing 0.001M $Ce(NO_3)_3 \cdot 6H_2O$. The reduction of cathodic current associated to cerium inhibition should shift the OCP to more negative values as indicated in the figure. In Figure 6.2(b), the initial value (OCP_1) tends to become more negative shifting to OCP_{1*} under the assumption that the magnesium oxidation reaction is the same as in Figure 6.2(a). In contrast, magnesium dissolution shifts the OCP in the direction of noble values (OCP_2). Moreover, the formation of a discontinuous layer containing cerium on the metal surface tends to reduce corrosion rate contributing to the increase of OCP value (OCP_3) [30]. As it can be clearly seen in the scheme of Figure 6.2(b), the combination of anodic and cathodic reactions influenced by cerium precipitation does not substantially modify OCP compared to that one shown by pickled AA2024 immersed in a solution without cerium. The different behaviour of pickled AA2024 in the 0.05M NaCl solution containing 0.01M $Ce(NO_3)_3 \cdot 6H_2O$ with respect to the 0.05M NaCl solution and to that with 0.001M $Ce(NO_3)_3 \cdot 6H_2O$ is most likely due to the introduction in the electrolyte of a higher amount of cerium species, which strongly influence the red-ox processes. The inhibition of cathodic areas associated to the decrease of their activity due to the precipitation of a cerium protective layer should reduce the cathodic current in the system improving AA2024 corrosion behaviour, as already reported in literature [15, 16, 17, 18]. However, the OCP shift from active to more noble values cannot be only explained with the inhibition mechanism associated

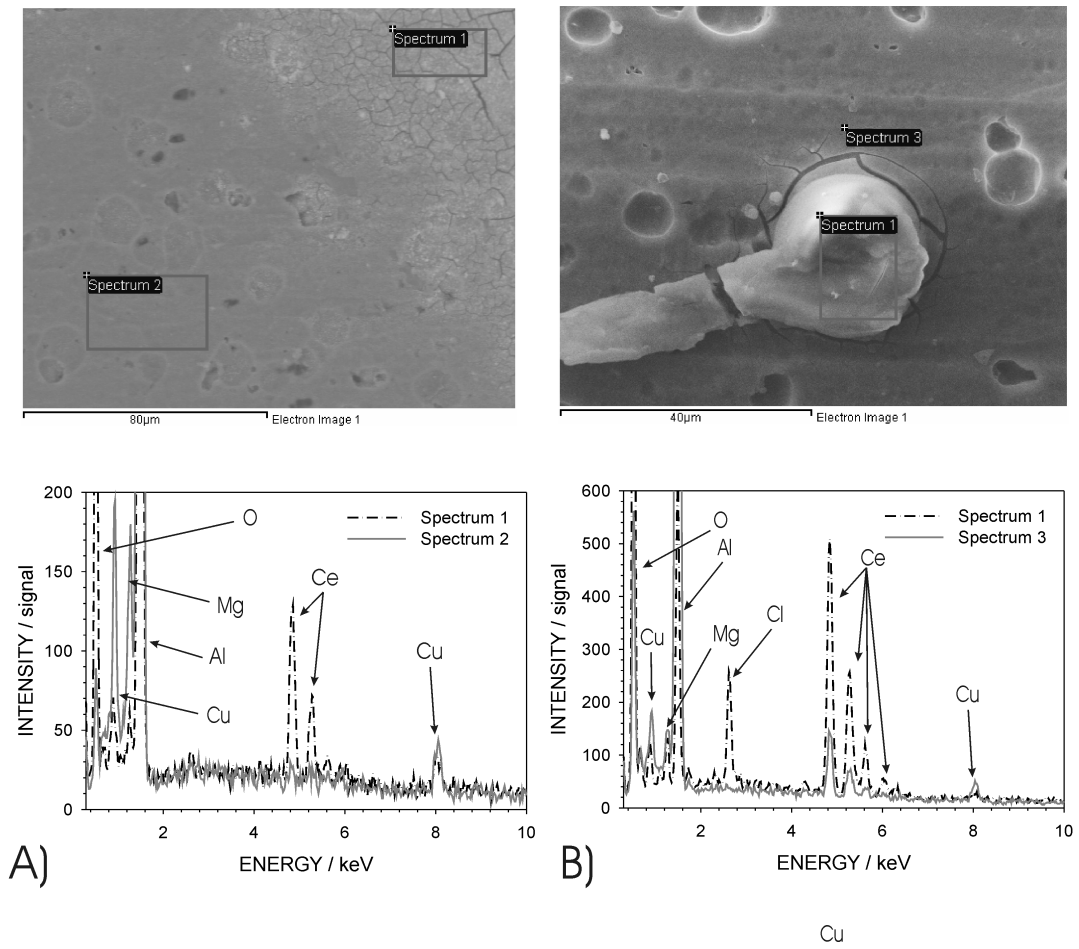

Figure 6.3: Surface morphology and EDXS analysis lower cerium concentration

to cerium precipitation on cathodic sites because cathodic inhibition mechanism would reduce the OCP value rather than increase it. Figure 6.2(c) shows an interpretation of the behaviour observed for pickled AA2024 immersed in 0.05M NaCl containing 0.01M cerium nitrate. It can be expected that the cathodic current is significantly reduced due to cerium precipitation on the substrate immersed in the solution containing an higher amount of cerium nitrate. To further explain the behaviours in solutions containing different amount of cerium nitrate, a surface morphology image of AA2024 immersed in 0.01M cerium nitrate solution has been also reported and discussed later in Figure 6.4.

As shown in Figure 6.2(c), considering the aluminium oxidation rate, the reduction of cathodic reaction rate should shift the OCP towards more negative values (from OCP_2 to OCP_{2*}). This is in contrast with the behaviour observed

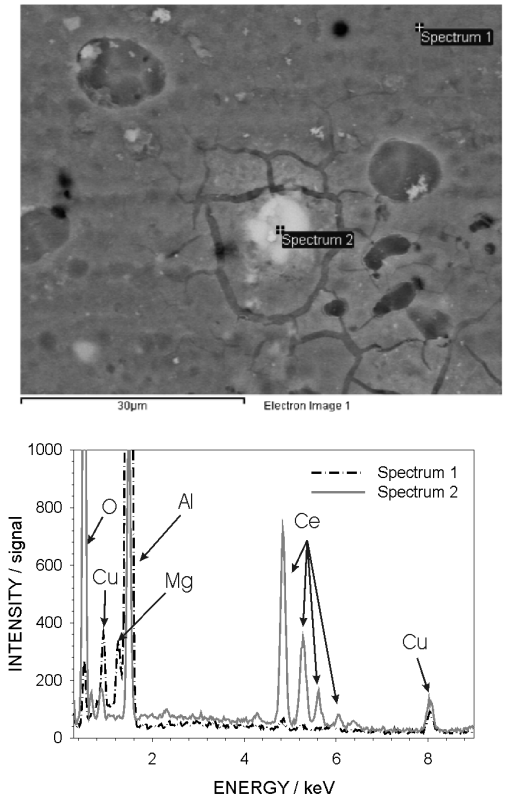

Figure 6.4: Surface morphology and EDXS analysis higher cerium concenration

in Figure 6.1, which clearly exhibited a shift of the OCP to more positive values for pickled AA2024 immersed in 0.05M NaCl solution with $Ce(NO_3)_3 \cdot 6H_2O$ with respect to the same substrate immersed in 0.05M NaCl solution 0.001M $Ce(NO_3)_3 \cdot 6H_2O$ and in 0.05M NaCl solution. This behaviour could be caused by decrease of oxidation reactions or by activation of reduction reactions. The activation of reduction reactions is not in line with the inhibition mechanism associated to cerium ions already proposed in literature [15, 16, 17, 18]. Therefore, it is likely that the inhibition of aluminum oxidation reactions is responsible for the noble OCP observed in Figure 6.1 for the substrate immersed in the solution with the higher content of cerium nitrate. As already seen in Figure 6.3(b), a protective thin film on aluminum surface was observed in some regions of the surface of pickled AA2024 immersed in the solution with lower concentration of cerium nitrate. Moreover, it is observed that this thin film is able to cover not only cathodic areas but even the aluminium matrix. Indeed, cerium precipitation probably starts at the cathodic sites and proceeds in the surrounding areas via

island growth, as reported in literature [30]. For a first rough estimation of the precipitation mechanism, the previous considerations do not take into account the cerium re-dox reactions which can occur at the metal substrate and influence the film structure. Therefore, in order to explain the behaviour of pickled AA2024 immersed in 0.01M cerium nitrate (the highest concentration used in this work), the film formed on the substrate should be able to reduce the oxidation rate of aluminium shifting OCP value from OCP_{2*} to OCP_4. Based on these considerations, the formation of a continuous film on aluminium alloy surface should be able to decrease both, cathodic and anodic reactions. In this work, cerium nitrate was employed as cerium source and nitrate ions may be also involved in the cerium-containing oxide layer formation. In literature, nitrates are considered as oxidant species and are often employed as oxidant agent in some electrochemical processes [51]. Nitrates can modify the metal surface promoting the formation of a passive aluminium hydroxide-oxide layer which could be able to improve AA2024 corrosion resistance in addition to the inhibition mechanism due to cerium precipitation via island growth. The effect of the counter ion was not further considered in this work because it will be investigated and discussed in another paper. Figure 6.4 shows the surface morphology of pickled AA2024 immersed for 11 days in a solution 0.05M NaCl with 0.01M $Ce(NO_3)_3 \cdot 6H_2O$. Holes and cavities formed during pickling procedure are visible in the image and it is possible to recognize the film on the substrate in the regions where cracks are formed. Indeed, the film is homogeneous in the regions where the pickling attack is less strong and the substrate morphology is not too much rough. Thus, it is very difficult to recognize the existence of this film in defect-free regions of the sample surface. Spectrum 1 detected in these areas evidences a low cerium signal indicating that a very thin film is formed. Spectrum 2 which was acquired on a cracked area, displays a higher amount of cerium compared to that one observed in Spectrum 2. However, Figure 6.4 indicates that a film containing cerium covers the entire sample surface. Indeed, cathodic or anodic areas are not identified by a preferential precipitation of cerium compounds according to the cerium precipitation via island growth suggested by Hinton et al. [15, 16, 17, 18]. Moreover, pickled AA2024 surface is not corroded and appears slightly yellow suggesting that a modification of cerium oxidation state occurs. Considering that cerium species were introduced as nitrates, it can be expected that initially the oxidation state of cerium ions was +3. Initially, the solution containing cerium

nitrate appears colourless. At the end of the immersion test (11 days) solution and AA2024 surface appeared yellowish, which is typical of compounds containing cerium with oxidation state +4. As stated by Hayes et al. [46, 47], Ce^{3+} ions can be oxidized to Ce^{4+} even in chemical conditions less oxidizing than that described by Pourbaix diagram. Therefore, Ce^{3+} ions added to the electrolytic solution could be oxidized during the immersion and involved in the corrosion mechanism of the substrate. By comparing the morphologies in Figure 6.3 and in Figure 6.4, it can be stated that the substrate is covered with a film containing cerium after immersion in the NaCl solution containing cerium nitrate with 0.001M and 0.01M concentrations. Nevertheless, SEM investigation indicates that the substrate is covered by a continuous and homogeneous film after immersion in the solution containing the higher concentration of cerium nitrate (0.01M). In contrast, it is likely that the amount of cerium available for the film deposition on the substrate is not enough to guarantee complete coverage of the substrate after immersion in the electrolyte containing a lower amount of cerium nitrate (0.001M). This is reflected by the trend of OCP that evidences a more noble behaviour for the substrate immersed in the solution containing the higher amount of cerium nitrate. Indeed, OCP measurements evidence that only the addition of 0.01M cerium nitrate to the electrolyte is able to significantly modify the electrochemical behaviour of the aluminium surface.

6.3.2 Potentiodynamic polarization for AA2024 pickled samples

Figure 6.5 shows anodic polarization curves performed on pickled AA2024 in the same electrolytes employed for OCP measurements. Polarization curves were carried out after 15 h immersion in the electrolyte. The polarization curve obtained on pickled AA2024 in 0.05M NaCl solution (solid line) does not evidence a passive region and the breakdown occurs immediately after the corrosion potential (E_{corr}) at -480 mV vs Ag/AgCl. The corrosion current density (i_{corr}) is $1\mu A \cdot cm^{-2}$. The potentiodynamic polarization curve carried out on pickled AA2024 immersed in 0.05M NaCl with 0.001M cerium nitrate (long dash line) exhibits a shift of the corrosion potential in the positive direction (about 20 mV) relative to the curve obtained in the solution containing only chlorides. No passive behaviour is visible for this curve and the breakdown takes place immediately after the corrosion

potential. However, the corrosion current density is about $0.4\mu A \cdot cm^{-2}$, which is lower than that observed for the sample immersed in NaCl solution without cerium nitrate. This evidences that immersion in the solution containing 0.001M cerium nitrate promotes only a slight improvement of the electrochemical behaviour of the substrate. These results strengthen the interpretation given in Figure 6.2(b) and is in line with scanning electron microscopy analysis discussed above. The potentiodynamic polarization curve for pickled AA2024 immersed in solution with 0.01M cerium nitrate (short dash line) shows a passive range extending for more than 50 mV above the corrosion potential localized at -385 mV vs Ag/AgCl. The current densities detected in this region are around $1\mu A \cdot cm^{-2}$ which can be considered in the range of passive behaviour for aluminium alloys. Chlorides are probably involved in the corrosion mechanism causing the failure and breakdown of the passive film at about -310 mV vs Ag/AgCl. However, it can be expected that corrosion rate for AA2024 immersed in a solution containing 0.01M $Ce(NO_3)_3 \cdot 6H_2O$ should be lower than that one for AA2024 immersed in a solution without cerium. Potentiodynamic polarization test confirms that corrosion resistance of AA2024 improves increasing the concentration of cerium nitrate in the electrolyte. These results are in line with the trend observed for the OCP in Figure 6.2.

Figure 6.6 displays a SEM micrograph of pickled AA2024 surface after potentiodynamic polarization test performed in 0.05M NaCl containing 0.001M $Ce(NO_3)_3 \cdot 6H_2O$. The surface appears less homogeneous compared to that observed in Figure 6.3 after open circuit potential measurement. The polarization test promoted the formation of large heterogeneous areas where there is precipitation of compounds on the oxide-hydroxide layer already detected after open circuit potential measurement. In addition, areas without evident precipitation are also visible in the SEM micrograph. Moreover, the sample surface often appears yellowish after potentiodynamic polarization test. Spectrum 2 performed on the area subjected to local precipitation during anodic polarization still evidences an intense cerium signal (cerium excitation lines are very intense and clear) confirming that a further precipitation of cerium-containing products occurred during potentiodynamic polarization. In contrast, Spectrum 4 performed on a region where local precipitation is not evident, displays a lower intensity of the cerium signal and a higher intensity of the aluminium signal than Spectrum 2. This indicates that films-precipitates with different thickness cover the substrate

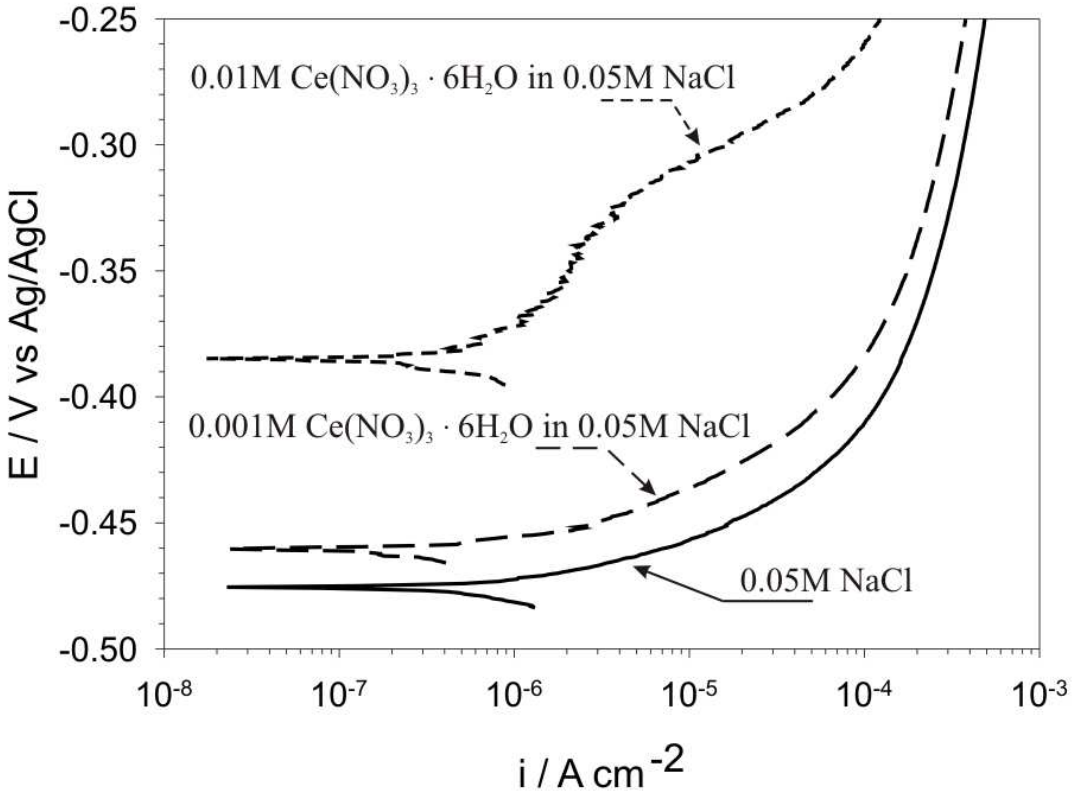

Figure 6.5: Potentiodynamic Polrization Curves in cerium nitrate solution

after potentiodynamic polarization. The precipitation promoted during potentiodynamic polarization is probably associated to a different mechanism compared to that occurring during free immersion conditions (OCP measurements). Indeed, the AA2024 substrate works as anode during anodic potentiodynamic polarization and undergoes oxidation reactions. Cathodic reactions take place at the Pt counter electrode. Therefore, it can be expected that precipitation occurring during anodic polarization tests is promoted by oxidation reactions rather than cathodic reactions. Accordingly, it is possible that cerium precipitation during potentiodynamic polarization is controlled by an initial oxidation in solution causing a change of the oxidation state of cerium from +3 to +4.

During anodic polarization tests carried out on AA2024 immersed in a solution containing 0.01M $Ce(NO_3)_3 \cdot 6H_2O$ and 0.05M NaCl, gas bubble generation was observed at the Pt cathode increasing the overpotential. This was accompanied by formation of a viscous gel compound at the platinum wire (cathode). This

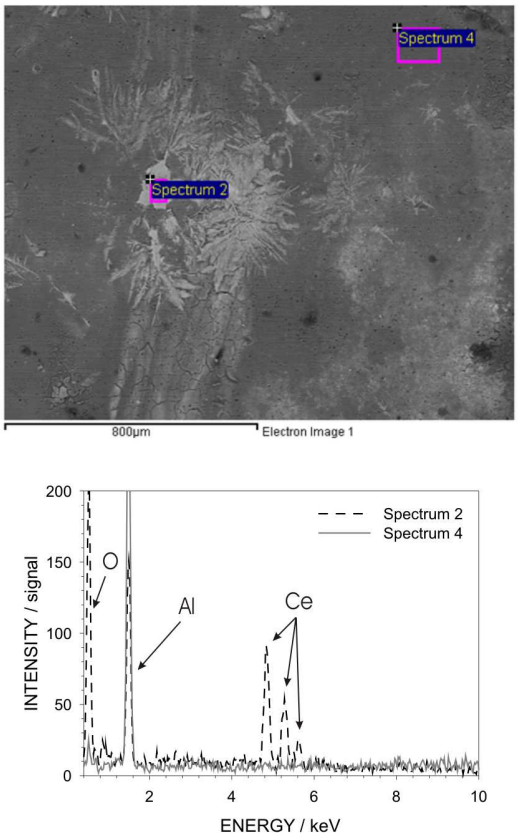

Figure 6.6: SEM micrograph after Potentiodynamic Polarization Curves

gel was collected after the measurement and dried in order to enable SEM-EDXS characterization. Figure 6.7 shows SEM micrograph and EDXS spectrum of the dried gel compound formed at the cathode. The SEM micrograph evidences a spongy structure for the gel with darker clusters. The spectrum 1 acquired on the spongy region of the gel evidences a high cerium content. Signals relative to silicon calcium and potassium should not be considered since they are generated by the glass substrate employed for the analysis of the product collected after potentiodynamic polarization. The spectrum 2 acquired on the dark cluster in the SEM micrograph evidences the presence of cerium, chloride and sodium suggesting that sodium chloride and cerium chloride crystals precipitated during drying step. Results of EDXS analysis on the gel formed at the cathode confirms that precipitation of cerium compounds occurs preferentially on sites where reduction reactions take place.

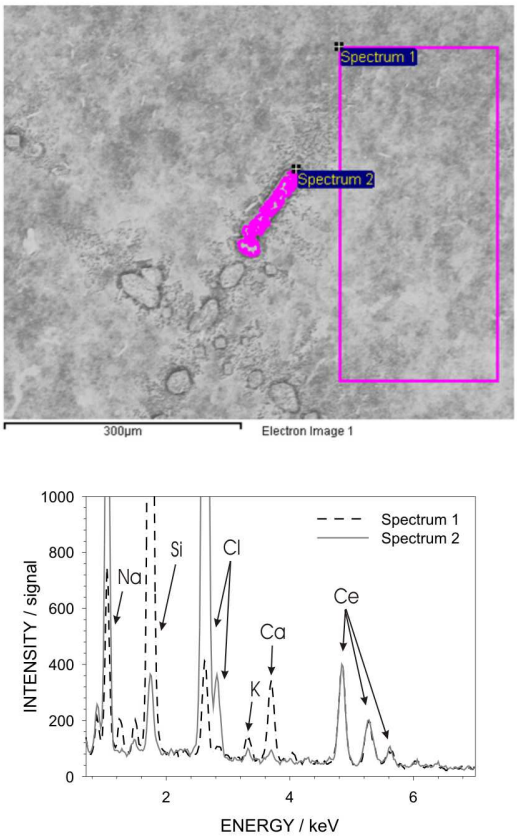

Figure 6.7: Dried gel morphology and Chemical Composition

6.3.3 Influence of chlorides in 0.01M cerium nitrate

In order to further evaluate the inhibition mechanism provided by cerium nitrate, electrochemical measurements have been performed employing aqueous solution without chlorides. Figure **??** shows the anodic polarization carried out on pickled AA2024 in a solution containing 0.01M $Ce(NO_3)_3 \cdot 6H_2O$ (long dash line). Potentiodynamic polarization curves carried out in 0.05M NaCl solution containing 0.01M $Ce(NO_3)_3 \cdot 6H_2O$ (short dash line) and in 0.05M NaCl solution have also been reported in the figure. Polarization curve carried out in cerium nitrate solution without chlorides shows an extended passive region with current density in the range of $1\mu A \cdot cm^{-2}$. By comparing the electrochemical behaviour exhibited by pickled AA2024 in 0.05M NaCl containing 0.01M $Ce(NO_3)_3 \cdot 6H_2O$ (short dash line) and in the solution without chlorides (long dash line), it can be seen that cerium nitrate is able to provide a sensible effect on the electrochemical of AA2024 aluminum alloy. The existence of chlorides in the electrolyte prevent the forma-

tion of a passive range leading to localized corrosion attack of the metal substrate. It is likely that the cerium-containing film is subjected to formation of defects or weak spots during immersion in chloride solutions, as confirmed by other works reported in literature [1]. Several yellow areas were observed on the AA2024 surface after the polarization to 1V vs Ag/AgCl in the solution without chlorides. According to the Pourbaix diagram for cerium [47], the cerium oxidation reaction is possible at the potentials reached during the potentiodynamic polarization. This oxidation reaction is associated to the modification of the oxidation state from Ce^{3+} to Ce^{4+} leading to the formation of compounds containing tetravalent cerium instead of trivalent one. As seen above, a similar behaviour was observed also for OCP measurements after 1 week immersion in the electrolyte containing cerium. Therefore, the behaviour observed in OCP measurements and potentiodynamic polarization test confirms that trivalent cerium progressively tends to change its oxidation state when high over-potential or longer immersion time in the electrolyte are considered [2].

6.3.4 Influence of surface preparation 0.01M cerium nitrate

Figure 6.9 shows open circuit potential measurements in 0.01M $Ce(NO_3)_3 \cdot 6H_2O$ carried out on AA2024 only degreased (short dash line) and pickled (long dash line line). The open circuit potential for degreased AA2024 shows an initial fast transient in the first 2-3 hours of immersion. A steady state value of about -230 mV vs Ag/AgCl is reached after about 5-7 hours of immersion. The OCP for pickled AA2024 shows a similar transient in the first hour immersion, but a value of about -320 mV vs Ag/AgCl is observed at the end of the measurement. This value is about 100 mV less noble than the value observed for degreased AA2024. OCP trends are in line with the scheme described in Figure 6.2. Since pickling produces a different surface condition than degreasing, it can be expected that the electrochemical equilibrium at the surface can affect the kinetics of reactions involving cerium. Moreover, these reactions are dependent on intermetallics present in AA2024, mainly Al-Cu-Mg and Al-Cu-Mn-Fe-Si intermetallics [1]. The former exhibit anodic behaviour relative to the aluminium matrix, while the latter display cathodic behaviour [2, 4, 7].

Figure **??** shows a qualitative GDOES profile (intensity versus sputtering

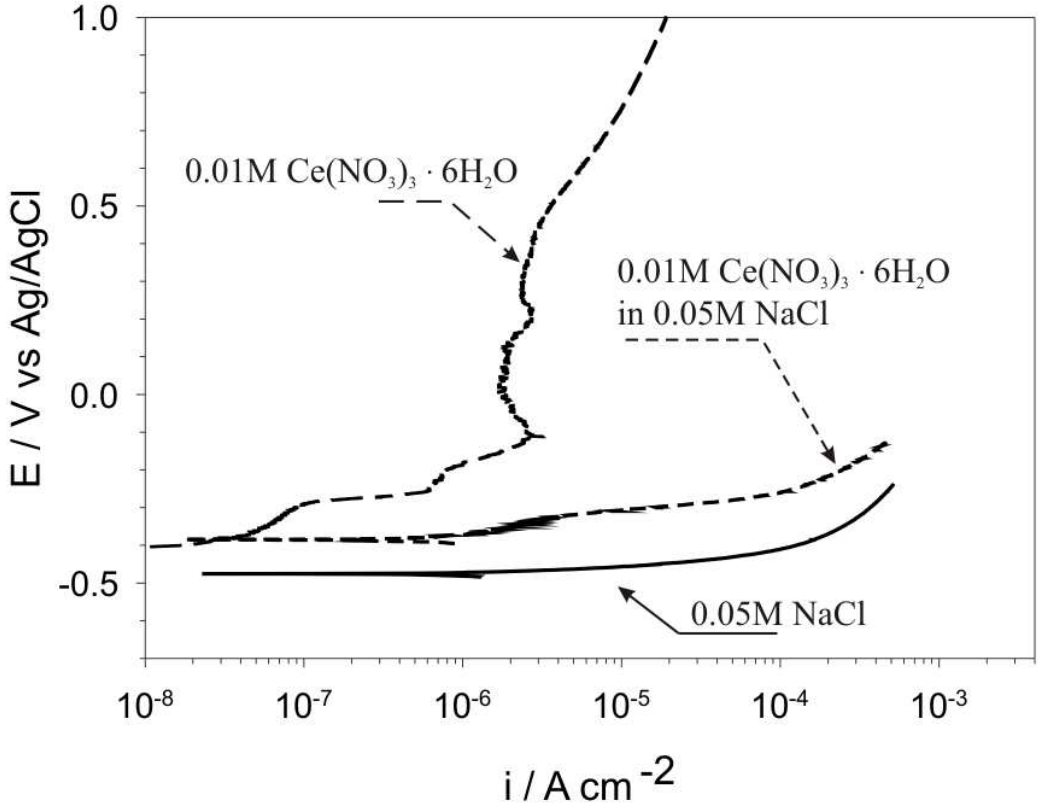

Figure 6.8: Chloride Influence

time) for only degreased and pickled AA2024 displaying signals relative to carbon, oxygen, silicon, copper, manganese and magnesium. The sputtering or erosion time is defined as the time during material is removed from the sample. The analysis were carried out for studying the chemical surface composition of AA2024 both, degreased and pickled. Measurements have evidenced that after 0.2 seconds of analysis the bulk was reached because no variation of chemical composition was detected. Since the investigated area by means of GD-OES was in the range of 10 mm2, the heterogeneity of the microstructure due to intermetallics did not affect the measurement. Indeed, measurements carried out on different regions of the same sample gave the same response. A relatively high amount of carbon is observed for degreased AA2024 while a very low carbon signal is detected for pickled one. The C signal is high for both samples at low sputtering time (0.01 sec) due to surface contamination of the samples. However, the trend of carbon signal clearly evidences that the degreasing procedure employed in this

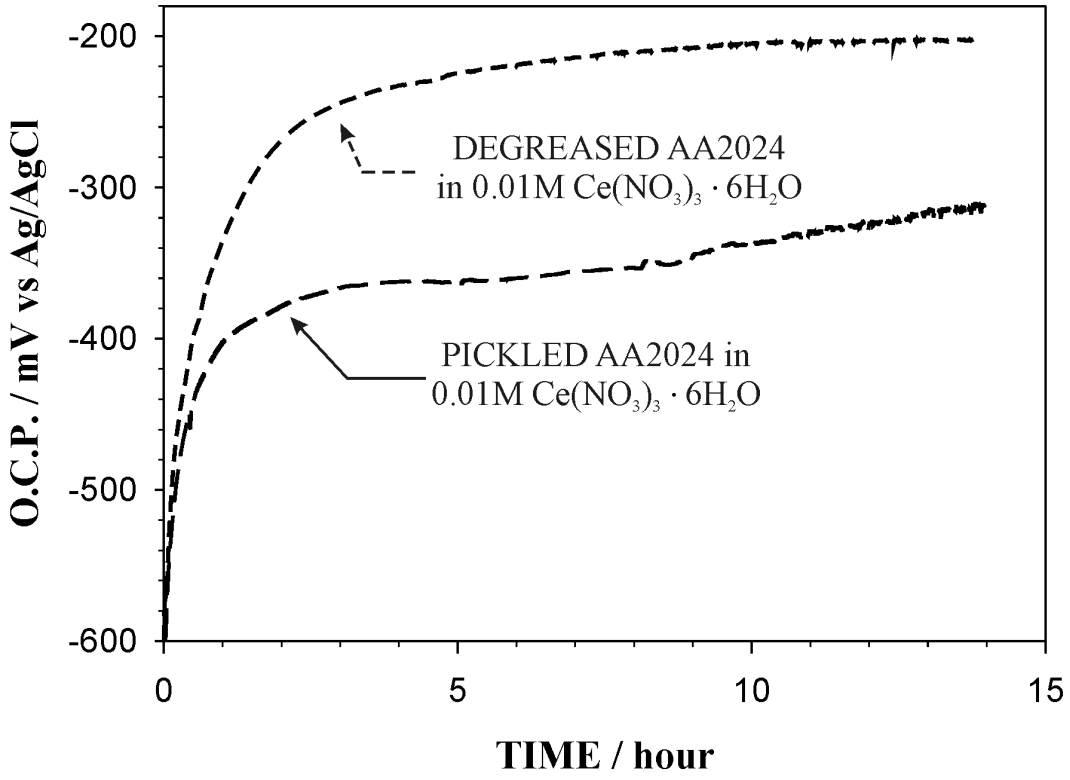

Figure 6.9: Surface Preparation Influence

work could not completely remove from the sample surface oil and organic residuals of rolling processes or hot and cold metal deformation. In contrast, pickling effectively removes oils and other residuals from the sample surface. The oxygen signal displays higher intensity for the degreased sample than for the pickled one. This indicates that the thickness of the oxide layer covering the degreased metal substrate is higher than that on the pickled one. Thus, pickling removes the natural oxide layer, which is successively reformed with lower thickness than on the only degreased sample. Copper and manganese signals evidence surface enrichment after pickling, while this is not observed after only degreasing. The surface enrichment of Si, Mn and Cu is most likely caused by dissolution and re-precipitation phenomena taking place during pickling and involving intermetallic particles and the solid solution (matrix), as already reported in literature [54]. In particular, the results in Figure 6.10 clearly indicate that there is a marked Cu enrichment on the pickled sample, in accordance with the work of P. Campestrini

et al. [54]. It can be expected that the surface enrichment of elements like Cu with a cathodic behaviour relative to the matrix affects the behaviour of cerium nitrate introduced in the electrolyte because cerium precipitation is favoured at cathodic sites. This aspect can be related to the OCP shift towards more noble values. The magnesium signal in Figure 6.10 exhibits a strong surface enrichment for the degreased sample, while this is not observed for the pickled sample. The different surface enrichment of magnesium observed for the two samples might be still mainly associated to the OCP curves reported in Figure 6.9. Indeed, it is likely that magnesium quickly starts to oxidize immediately after immersion in the electrolyte supplying a considerable amount of electrons for reduction reactions. Since oxidation and reduction reactions occur at the same rate in order to maintain the net current equal to zero under free immersion conditions, the strong magnesium dissolution occurring immediately after immersion in the electrolyte [38] can be considered as the source of electrons supporting reduction reactions. Since cerium precipitation kinetic is influenced by the rate of reduction reactions, it can be concluded that the magnesium dissolution promotes the formation of a layer containing cerium with a faster kinetic for the degreased sample than for the pickled one. Since magnesium amount present at the surface tends to be consumed by oxidation reactions, after the first hours of immersion, the surface becomes less reactive and the slope of OCP curves tend to diminish. On the other hand, the surface of pickled sample which is less rich in magnesium and more rich in copper tends to be less reactive than the degreased one (enriched in magnesium) supporting a slower kinetics of cerium precipitation.

6.3.5 Influence of pH

In order to evaluate the inhibition ability of cerium nitrate as a function of solution pH, pickled AA2024 samples were immersed in alkaline and acid solutions containing cerium. Figure 6.11 shows OCP measurements acquired for 5 hours on pickled AA2024 in the different solutions considered. In Figure 6.11, the OCP detected in acid solution (dash-dot line) immediately after immersion is about -400mV vs Ag/AgCl which is more noble than that acquired in the neutral solution (short dash line). The OCP value measured is quite constant during the first 5 hours of immersion meaning that a very fast activation of the metal surface which is in line with the behaviour described by Pourbaix diagram. The

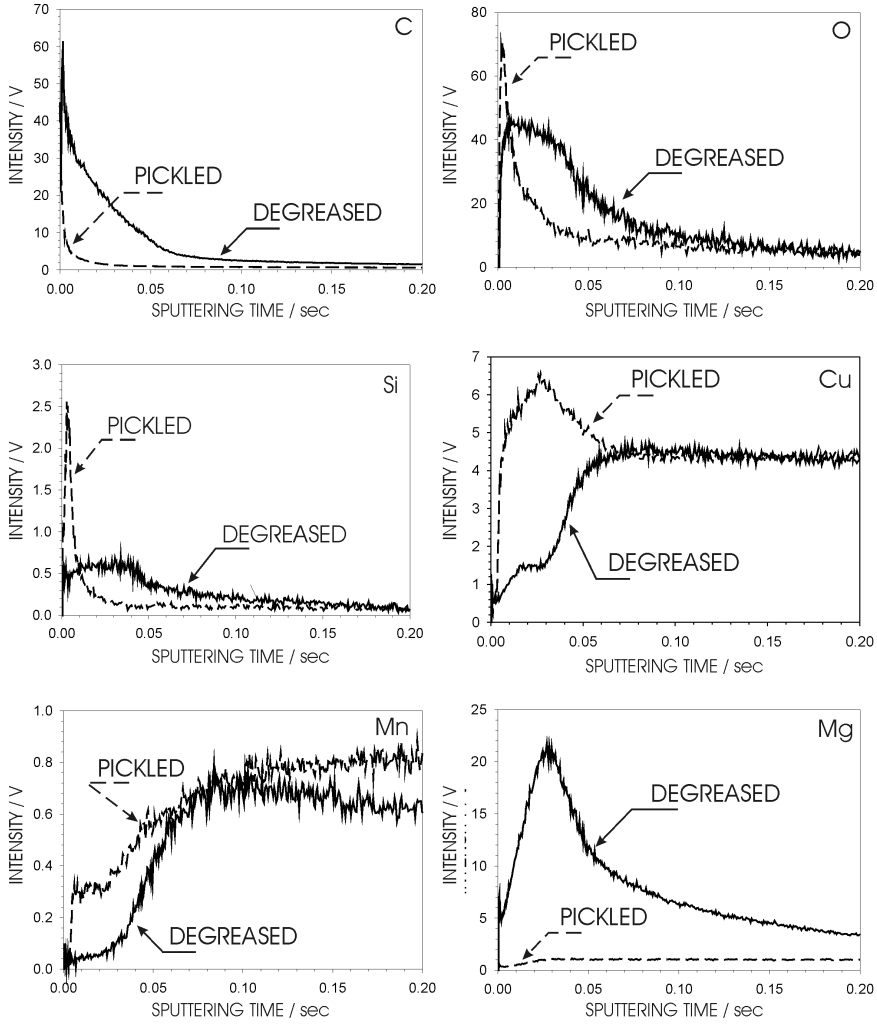

Figure 6.10: Qualitative GD-OES profiles

OCP measured immediately after immersion in alkaline solution is more active than that measured in acid solution suggesting that a lower amount of cerium compounds precipitate on the metal substarte. The OCP rapidly increases in the first hour of immersion, while the increase becomes less evident for longer immersion times. OCPs detected in acid or in alkaline solutions become very similar after 3 hours immersion reaching a value closed to -380mV vs Ag/AgCl. This suggests that a similar steady state condition involving cerium nitrate is established on the metal surface in acid and alkaline conditions. However, since the electrochemical behaviour detected during the first 3 hours immersion are not the same, the corrosion processes are most probably affected by solution pH in the

first hours of immersion. The different OCP trend in alkaline and acid solution might be explained considering the electrochemical behaviour of magnesium immersed in either, acid or alkaline solution. According to Pourbaix diagram [47], magnesium corrosion reactions can easily occur in acid solution, while in alkaline environment with solution pH equal to 8 or higher, magnesium tends to passivate forming magnesium hydroxide. The lower reactivity displayed by AA2024 in alkaline than in acid conditions can be due to a lower activity of magnesium in alkaline environment, which does not provide the electron flow necessary to promote reduction reactions with the same rate of those occurring in acid conditions. Since cerium precipitation is limited in tests carried out in alkaline condition, a longer immersion time is necessary to reach a steady OCP in this environment than in acid condition.

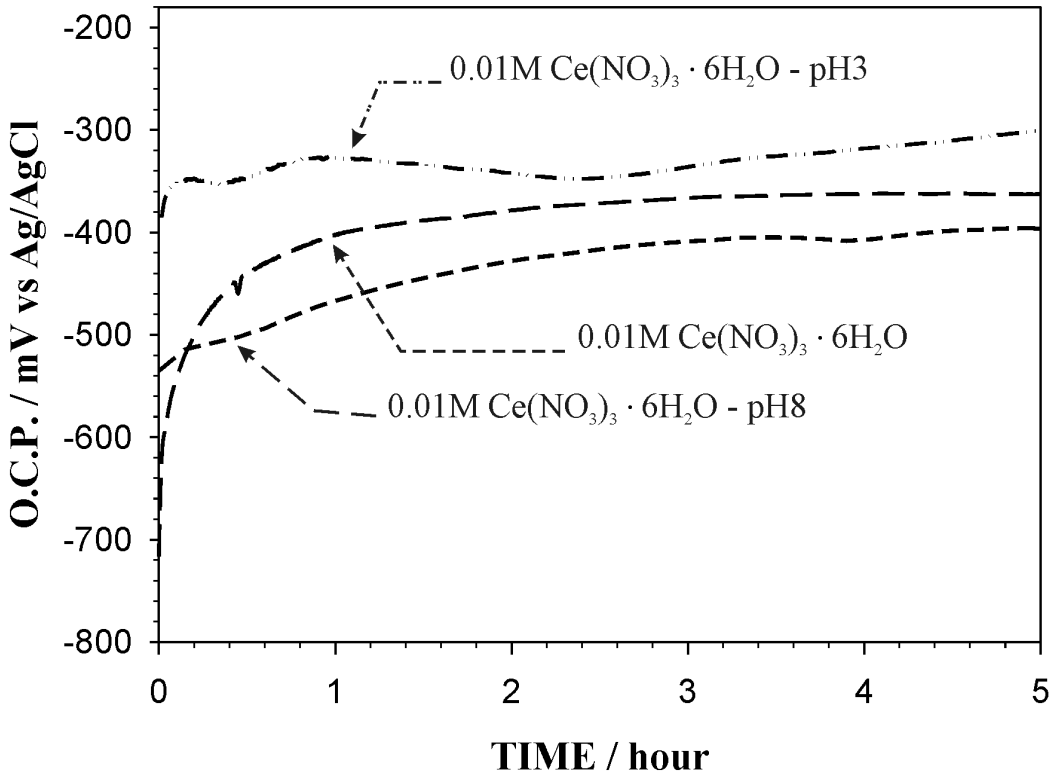

Figure 6.11: pH solution Influence on OCP

Figure 6.12 shows anodic polarization curves performed on pickled AA2024 samples in acid and alkaline solutions containing 0.01M $Ce(NO_3)_3 \cdot 6H_2O$. Po-

tentiodynamic polarization performed in neutral 0.01M $Ce(NO_3)_3 \cdot 6H_2O$ is reported as a reference. For overpotentials ranging from -0.2V to -0.1V vs Ag/AgCl potentiodynamic polarization curves carried out under acid, alkaline and neutral cerium-containing solutions shows a current peak near the Ecorr followed by a passive region, which is more extended in the neutral solution than in alkaline and acid ones. However, measurements performed under acid and alkaline solutions display current density higher than that acquired for AA2024 samples immersed in neutral solution. From results shown in Figure 6.12, it seems that corrosion reactions are however inhibited in the pH region ranging from 3 to 8 suggesting that localized corrosion attack at the metal surface can be reduced in solutions in the considered pH range by adding cerium nitrate at the electrolyte.

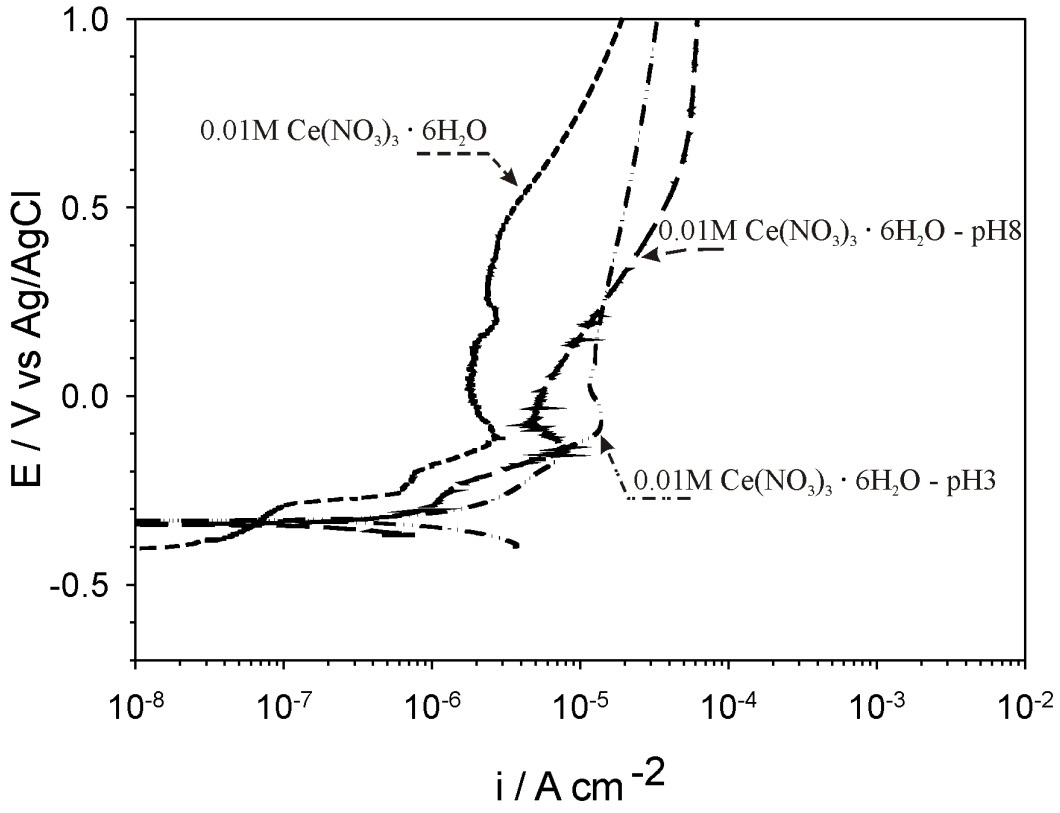

Figure 6.12: pH solution Influence on PPC

6.3.6 Galvanic coupling

In order to better understand AA2024 corrosion inhibition mechanisms provided by cerium nitrate in solution, a sheet of 8xxx series aluminium alloy (used as anode) was connected to a pure copper sheet (used as cathode) to have galvanic coupling between the two metals as shown in Figure 6.13(a). When the galvanic couple is immersed in 0.05M NaCl containing 0.01M $Ce(NO_3)_3 \cdot 6H_2O$ aqueous solution, the aluminium surface starts to corrode while reduction reactions occur on the copper electrode. Therefore, the copper surface should works as the preferential site for cerium precipitation while aluminium should be involved only as the anode in the electrochemical cell, as shown in Figure 6.13(b). The surface of pure aluminium underwent severe attack after immersion (SEM micrograph not shown). Analysis performed with EDXS equipment was not able to identify cerium on aluminium substrate indicating that its anodic behaviour does not promote cerium deposition.

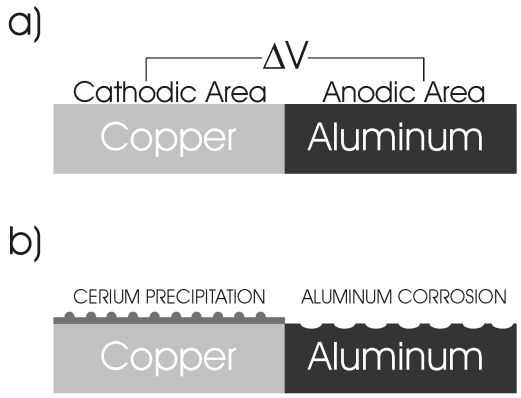

Figure 6.13: Galvanic couling Scheme

Figure **??**(a) and (b) shows the morphology of the copper sheet galvanically coupled to the aluminium sheet after 6 hours in 0.05M NaCl containing 0.01M $Ce(NO_3)_3 \cdot 6H_2O$. Relatively large crystals with size of 1-2 μm can be identified on the substrate. Moreover, the copper surface in Figure 14a), is uniformly covered by a thin cerium-containing film whereas cracks can be seen near the areas where a local precipitation of crystals took place. Crack formation is most probably due to high vacuum in the chamber and electron beam power settings in the scanning electron microscopy rather than to heterogeneous film formation

during immersion in the electrolyte. Indeed, at the beginning of SEM observation, the thin film was more continuous and crack formation was observed during the analysis. This evidence suggests that the thin layer is probably constituted of hydrated hydroxide, which releases water during S.E.M. observations producing extended cracking. However, the SEM images confirm that cathodic reactions occurring on copper surface are most probably related to an increasing of the solution pH near to the surface electrode which is able to promote cerium precipitation. In addition to the thin film layer formed on the pure copper surface, in Figure 6.14(a) crystal formation on the top of the film is observed. It seems that active sites promote the formation or the re-deposition of crystals involving chemical species present in the aqueous solution. EDXS analysis performed on crystal A) (not shown here) exhibits nitrogen, oxygen and cerium signals. This indicates that a crystal of cerium nitrate precipitates on copper surface where reduction reactions occur. Moreover, in Figure 6.14(a), it is possible to recognize a second type of crystal indicated with the mark B). EDXS analysis performed on this crystal, evidences oxygen and cerium signals. The morphology of crystal B) is not as smooth as in the case of crystal A). Figure 6.14(b) reports the cross-section of the copper surface showing that crystals of type B) grow forming a columnar structure which can be associated to cerium hydroxide/oxide]. Besides, Figure 6.14(b) evidences that film formation and local precipitation occur on the entire copper surface confirming that cathodic regions can be considered as preferential sites for the precipitation of compounds containing cerium. Based on results in Figure **??**, the precipitation mechanism of cerium compounds on cathodic sites can be divided in two different steps: in the first step, a thin oxide-hydroxide film is formed on the copper substrate. In the second step hydroxide crystals grow near active sites depending on copper grain orientation, reticular defects, impurity, defects of the first thin layer of oxide-hydroxide formed. The second step of the deposition can take place together with the first one or at a different stage.

Figure 6.15 shows a scheme of possible re-dox reactions occurring at the AA2024 surface, based on the simple model of the aluminium-copper galvanic couple behaviour previously discussed. Cathodic second phase particle and anodic aluminium matrix are represented in the figure. Following the mechanism proposed for galvanic coupling between pure copper and aluminium, cerium precipitation should occur only on cathodic sites. Therefore, second phase particles

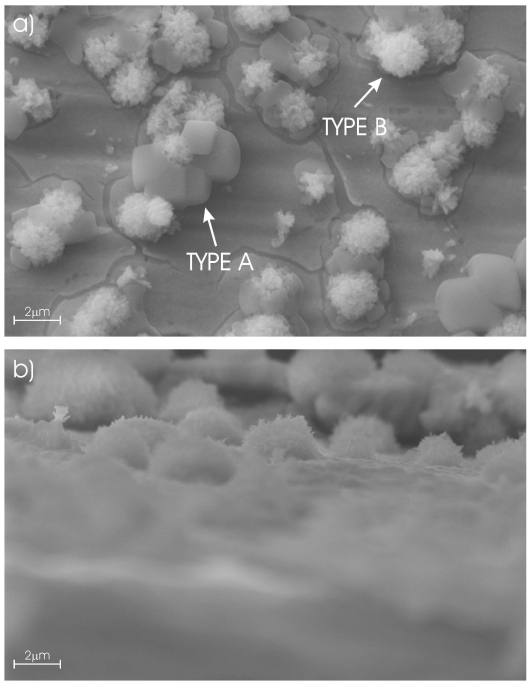

Figure 6.14: Surface morphology after immersion

with cathodic behaviour should be covered by cerium compounds. Aluminium matrix should not be involved, because cerium precipitation (depending on local solution pH) is promoted by the alkalinisation of the solution which is otherwise provided by reduction reactions at cathodic sites. On the contrary, Figure 6.4 enables to recognize an homogeneous layer formed on AA2024 after immersion in a solution containing cerium nitrate. However, it is not possible to identify areas with anodic or cathodic behaviour in Figure 6.4 because the entire surface is covered. Indeed, cathodic and anodic areas cannot be macroscopically separated in the case of AA2024 because the size of cathodic areas range from micrometers to nanometers. As stated by Wilson and Hinton [15, 16, 17, 18, 19], cerium precipitation starts from cathodic sites involving the surrounding areas via island growth. Hughes et al. [31] suggested that after the initial cerium precipitation on the larger cathodic areas, the residual surface could be covered by cerium compounds due to small active intermetallics not still involved in the process. Our results are in accordance with the island growth proposed by Hughes for the explanation of cerium precipitation mechanism. Cerium precipitation occurring on AA2024 progressively covers the entire surface because small cathodic sites

are homogeneously dispersed in the anodic matrix. Nevertheless, it seems that anodes and cathodes are both necessary for the formation of cerium hydroxide-oxide film. In order to validate this statement, another test was made: a sheet of aluminum alloy (8xxx series) was immersed in aqueous solution containing 0.01M $Ce(NO_3)_3 \cdot 6H_2O$ for several days. Scanning electron microscopy and EDXS analysis had not evidenced cerium precipitation at the metal surface as in the case of AA2024. Intermatallics present on the surface of 8xxx aluminium alloy are rich in iron and manganese and behave cathodically relative to the aluminum matrix. Cerium precipitation on 8xxx aluminum alloy does not occur or occurs very slowly because probably the driving force associated to the cathodic and the anodic reactions occurring on respectively, intermetallics and matrix, is not strong enough to provide an adequate cerium precipitation rate. This further confirms that cerium precipitation is promoted by the nature of the alloy microstructure, which is not able to provide the electrochemical conditions for an effective cerium precipitation in the case of less reactive system.

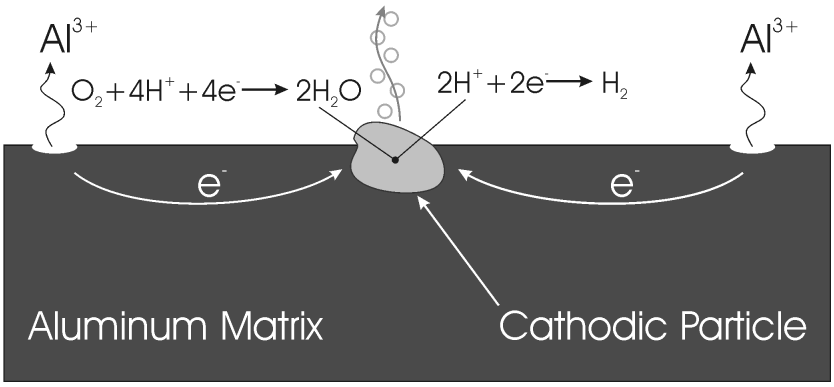

Figure 6.15: Mechanism of cerium precipitation

6.4 Conclusions

The inhibition effect of cerium nitrate on the electrochemical behaviour of AA2024-T3 aluminum alloy has been investigated by means of DC techniques like open circuit potential measurements and potentiodynamic polarizations. The evaluation of the effectiveness of two cerium nitrate concentrations (5 gL^{-1} and 0.5 gL^{-1}) was carried out.

Cerium compounds precipitate on AA2024-T3 aluminum alloy as hydroxides or hydrated oxides. The precipitation involves the entire surface producing a very thin film even if on small regions a very intense cerium precipitation has been detected. The solution containing 5 gL^{-1} of cerium nitrate strongly affects the electrochemical behaviour of AA2024-T3 aluminum alloy while a smaller effect has been observed for the less concentrated solution (0.5 gL^{-1}).

Chlorides significantly decrease the inhibition effect due to the presence of cerium nitrate ions in solution. Cerium salts are instead able to homogenize the electrochemical behaviour of AA2024-T3 aluminum alloy in a pH range between 3 and 8.

The cerium precipitation phenomenon occurs more fast on AA2024-T3 surfaces rich in magnesium. The precipitation is most probably promoted by the intense redox reactions correlated to the fast magnesium dissolution.

The observation of the AA2024-T3 surface morphologies of cerium precipitations, by means of scanning electron microscopy, evidences that cathodic sites are preferential sites for cerium precipitation. However, it is not still clear the mechanism of cerium deposition on the entire surface (consisting of micro-anodes and micro-cathodes). For cathodic inhibitors, the mixed-potential theory indicates that E_{corr} shifts to more active values. Since the results obtained are not in accordance with the theory, the cerium nitrate salt are most likely able to inhibit both the anodic and the cathodic behaviour.

Bibliography

[1] Handbook Committee, *"Metals Handbooks, manuals"* ASM International, Printed in the United States of America

[2] R.G. Buchheit, R.P. Grant, P.F. Halva, B. Mckenie, G.L. Zender, J. Electrochem. Soc. 144 (8) (1997) 2621

[3] G.S. Chen, M. Gao, R.P. Wei, Corrosion 52 (1) (1996) 8

[4] V. Guillaumin, G. Mankowski, 41 (1990) 421

[5] H.M. Obispo, L.E. Murr, M. Arrowood, E.A. Trillo, J. Mater. Sci. 35 (2000) 3479

[6] D. Zhu, W.J. van Ooij, Corros. Sci. 45 (2003) 2163

[7] C. Blanc, B. Lavelle, G. Mankowski, Corros. Sci. 39 (3) (1997) 495

[8] V. Guillaumin, G. Mankowski, Corros. Sci. 41 (1999) 421

[9] C.M. Liao, J.M. Olive, M. Gao, R.P. Wei, Corrosion 54 (6) (1998) 451

[10] P. Schmutz, G.S. Frankel, J. Electrochem. Soc. 145 (7) (1998) 2285

[11] P. Schmutz, G.S. Frankel, J. Electrochem. Soc. 145 (7) (1998) 2295

[12] J.J. MacMullen, M.J. Pryor, The Oxidation of Metals p. 52, Butterworths, London (1969)

[13] J. K. Hawkins, H. S. Isaacs, S. M. Heald, J. Tranquada, G. E. Thompson, and G. C. Wood, Corros. Sci. 27, 391 (1987)

[14] Toxicological Profile for Chromium, ATDSR/TP-88/10, Agency for Toxic Substances, U.S. Washington, DC (1989)

[15] B.R.W. Hinton, D.R. Arnott, N.E. Ryan, Met. Forum 7 (1984) 211

[16] B.R.W. Hinton, D.R. Arnott, N.E. Ryan, Mater. Forum 9 (1986) 162

[17] R. Arnott, B.R.W. Hinton, N.E. Ryan, Corrosion 45, 12 (1989)

[18] B.R.W. Hinton, J Proceedings of Corrosion 89́ Paper No. 170, NACE (1989)

[19] D.R. Arnott, B.R.W. Hinton, N.E. Ryan, Mater. Perform. 42 (1987) 47

[20] D.R. Arnott, N.E. Ryan, B.R.W. Hinton, B.A. Sexton, A.E. Hughes, Appl. Surf. Sci. 22/23 (1985) 236

[21] J. O'M. Bockris, S. U. M. Khan, Surface Electrochemistry p. 319, Plenum Press, New York (1993)

[22] S. Strbac, N. Anastasijevic, R. R. Adzic, J. Electroanal. Chem. 323, 179 (1992)

[23] V. Jovancicevic, J. O'M. Bockris, ibid. 133, 1797 (1986)

[24] S. Zecevic, D. M. Drazic, S. Gojkovic, J.Electroanal. Chem. 265, 179 (1989)

[25] E. R. Vago, F. J. Calvo, M. Stratmann, Electrochim. Acta 39, 1655 (1994)

[26] F. King, C. D. Litke, Y. Tang, J. Electroanal. Chem. 384, 105 (1995)

[27] F King, M. J. Quinn, C. D. Litke, ibid. 385, 45 (1995)

[28] A. J. Aldykiewicz, Jr., A. J. Davenport, H. S. Isaocs, J. Electrochem. Soc. 143 (1) (1996)

[29] A.E. Hughes, S.G. Hardin, T.G. Harvey, T. Nikpour, B. Hinton, A. Galassi, G. McAdam,A. Stonham, S.J. Harris, S. Church, C. Figgures, D. Dixon, C. Bowden, P. Morgan, S.K. Toh, D.D. McCulloch, J. DuPlessis, Proceedings of the Third International Symposium on Aluminium Surface Science and Technolog (Bonn, Germany, 2003, p. 264)

[30] L. Wilson, B.R.W. Hinton, A Method of Forming a Corrosion Resistant Coating Patent WO 88y06639, 1988

[31] A.E. Hughes, R.J. Taylor, B.R.W. Hinton, L. Wilson, Surf.Interface Anal. 23 (1995) 540

[32] A.E. Hughes, S.G. Hardin, K.W. Wittel, P.R. Miller, Proceedings of the NACE meeting: Corrosiony2000, Research topical Symposium: Surface Orlando, US, 2000

[33] A.J. Aldykewicz Jr, H.Ws. Isaacs, A.J. Davenport, J. Electrochem. Soc. 142 (1995) 3342

[34] A.E. Hughes, J.D. Gorman, P.J.K. Paterson, Corros. Sci. 38 (1996) 1957

[35] M. Dabala', L. Armelao, A. Buchberger, I. Calliari, Appl. Surf. Sci. 172 (2001) 312

[36] A.E. Hughes, J.D. Gorman, P.J.K. Paterson, Corros. Sci. 38 (1996) 1957

[37] S. You, Materials Letters 61 (2007) 3778

[38] L.E.M. Palomino, Electrochimica Acta 51 (2006) 5943

[39] B.Y. Johnson, Materials Characterization 54 (2005) 41

[40] A. de Frutos, Surface & Coatings Technology 202 (2008) 3797

[41] A. Decroly, J.P. Petitjean, Surface & Coatings Technology 194 (2005) 1

[42] A.E. Hughes, J.D. Gorman, P.R. Miller, B.A. Sexton, P.J.K. Paterson, R.J. Taylor, urf. Interface Anal. 36 (2004) 290

[43] N.C. Rosero-Navarro, S.A. Pellice, A. Duran, M. Aparicio, Corros. Sci. 50 (2008) 1283

[44] L. Paussa, N. C. Rosero-Navarro, F. Andreatta, Y. Castro, A. Duran, M. Aparicio, L. Fedrizzi, Surf. Interface Anal. 42 (2010) 299

[45] S.A. Hayes, P.Yu, T.J. O-Keefe, M.J. O-Keefe, J.O. Stoffer, J. Electrochem. Soc. 149 (12) (2002) C623

[46] W. G. Fahrenholtz, M. J. O-Keefe, H. Zhoua, J.T. Grant, Surface & Coatings Technology 155 (2002) 208

[47] POURBAIX ATLAS

[48] B.Y. Johnson, J. Edington, M.J. O-Keefe, Materials Science and Engineering A361 (2003) 225

[49] B.F. Rivera, B.Y. Johnson, M.J. O-Keefe, W.G. Fahrenholtz, Surface and Coatings Technology 176 (2004) 349

[50] W. Pinc, S. Geng, M. O-Keefe, W. Fahrenholtz, T. O-Keefe Applied Surface Science 255 (2009) 4061

[51] REF FONTANA REF FONTANA REF FONTANA

[52] Z. Szklarska-Smialowska Corros. Sci. 41 (1999) 1743

[53] Y. Xingwen, C. Chunan, Y. Zhiming, Z. Derui, Y. Zhongda Corros. Sci. 43 (2001) 1283

[54] P. Campestrini, E.P.M. van Westing, H.W. van Rooijen, J.H.W. de Wit Corros. Sci. 42 (2000) 1853

Chapter 7

Micro-Evaluation of Cerium Inhibition

Aluminium alloys like AA2024 are susceptible to severe corrosion attack in aggressive solutions (e.g. chlorides). Since the corrosion behaviour of aluminium alloys is strongly dependent on their microstructure, the evaluation of the behaviour in the micro-scale range enables to distinguish regions with different electrochemical activity. The micro-electrochemical technique using glass micro-capillary allows to investigate metal substrates with heterogeneous micro-electrochemical behaviour. Since it is well established that the precipitation of cerium species on corroding electrodes is activated by cathodic sites - like intermetallics -, the aim of this work is to investigate the electrochemical behaviour of AA2024-T3 in presence of cerium species. The investigation was carried out by means of a localized technique, the electrochemical micro-cell. Three different regions were considered: a first type containing a small amount of intermetallics (matrix region), a second type containing intermetallics rich in Al-Cu-Fe-Mn and a third type containing intermetallics rich in Al-Cu-Mg. The characterization was initially carried out evaluating open circuit potentials and potentiodynamic polarization measurements in sodium chloride solution. This step allowed to assess the behaviour of the three type of regions. Afterwards, measurements with the same approach were carried out on AA2024-T3 samples previously immersed in a solution containing cerium nitrate. This approach was employed in order to identify and clarify the role of intermetallics on cerium precipitation. SEM-EDXS analysis were furthermore performed to evaluate the composition of cerium compounds precipitated on both matrix and rich-intermetallics regions.

7.1 Introduction

AA2024 aluminium alloy is widely employed in aerospace applications due to its advantageous strength-to-weight ratio. In order to improve mechanical properties, AA2024 aluminum alloy undergoes thermal treatment to promote precipitation of nanometric second-phase particles which are able to strengthen the aluminum microstructure [1]. The heterogeneous microstructure of AA2024-T3 aluminum alloy strongly affects its corrosion behavior [2, 3, 4, 5]. Several electrochemical and metallurgical studies were carried out on the AA2024 microstructure in order to distinguish phases with different electrochemical behavior [6, 7, 8, 9]. Different kinds of coarse intermetallics have been identified for AA2024 aluminum alloy. Buchheit reported a compilation of corrosion potentials for aluminum-based intermetallics found in literature [10]. It has been found that corrosion potentials for intermetallics containing Al-Cu-Mg are more negative than those detected for intermetallics containing Al-Cu-Fe-Mn. For AA2024 aluminum alloy, Buchheit et al. [11] further evidenced that Al-Cu-Mg-based intermetallics are the most populated category while the second largest type is rich in Al-Cu-Fe-Mn. They found that immediately after immersion in a chloride solution, Al-Cu-Mg-based intermetallics act as anodic sites with respect to the aluminum matrix. However, magnesium and aluminum dissolution promotes the formation of Mg-Al-depleted intermetallics which can act cathodically for longer immersion times. Otherwise, Al-Cu-Fe-Mn intermetallics constantly act as cathodes with respect to the aluminum matrix [12, 13, 14]. It is well established that localized corrosion of aluminum alloys is affected by second phase particles which can promote the development of critical local conditions [10, 15, 16, 17, 18, 19, 20, 21]. Two different pitting growing mechanisms have been recognized: the preferential attack of aluminum matrix at the boundary with intermetallics or the selective dissolution of the intermetallics themselves. However, the electrochemical behavior of second phase particles is affected by the solution pH and it can become very complex [22]. As an example, Mg_2Si particle tends to be more noble in acid pHs but in acid conditions its dissolution rate tends to be increased if compared with that evidenced in neutral pH. This study [22] also suggests that the relationship between the electrochemical behavior of aluminum alloys and their microstructure depends on both the environment and the corrosion step considered. In particular, the corrosion step can locally affect the chemistry equilibrium of the corroding elec-

trode surface, where micro-anodes and micro-cathodes are involved. Guillaumin et al. [14], observed that anodic polarization curves preformed on AA2024-T3 show two breakdown potentials: the more active is related to both the local dissolution of the aluminum matrix surrounding Al-Cu-Mg-based intermetallics and the magnesium dissolution occurring at the bulk intermetallic. They found that Al-Cu-Mg-based intermetallics are surrounded by a copper-rich dispersoids free-zone. Therefore, the matrix surrounding intermetallics contains a lower copper amount than the rest of the matrix. In this area, dispersoids are therefore copper-lean and they behave anodically with respect to the matrix during the first period of immersion in chlorides. It was estimated that the first breakdown potential is mainly due to the intense magnesium dissolution occurring at Al-Cu-Mg-based intermetallics. The second breakdown potential is rather correlated to the further matrix dissolution occurring at the center grains and at grain boundaries, where anodic intermetallics have already been dissolved. The fast magnesium and aluminum dissolution from Al-Cu-Mg-based intermetallics leads to the formation of copper-rich spongy regions on which oxygen reaction can occur more easily promoting the further matrix dissolution [23, 24]. The micro-cell technique can be employed for the evaluation of the micro-electrochemical behaviour of metal microstructures. Indeed, the electrochemical micro-cell technique was initially employed by T. Suter et al. [25, 26, 27] to study the influence on pitting initiation of sulphide inclusions in stainless steels. In these works, the evaluation of the inclusions size, of the test-solution composition and of the working electrode area allowed to identify sulphide inclusions larger than 1 μm as very critical for pitting resistance. Moreover, Suter et al. proved that MnS-inclusions tend to dissolve in both chloride-free solutions and chloride-containing solutions. Suter el al. [28] employed the micro-cell technique to evaluate the AA2024-T3 electrochemical behavior in the micrometer range for the first time. In a following work with an experimental procedure similar to the that previously employed [25, 26, 27], the evaluation of the natural oxide stability of AA2024-T3 aluminum alloy was further carried out by using the electrochemical micro-cell technique [24]. Localized corrosion investigation can be performed by reducing the working area or by using a scanning micro-reference electrode. The working principle of the micro-electrochemical technique is based on the size reduction of the electrochemical cell [29]. The equipment basically consists of a glass micro-capillary sealed at the tip with a silicone gasket in order to avoid solution leakage at the electrode

surface. Since the micro-cell is mounted on the revolving nosepiece of a metallographic microscope, it is possible to center the region of interest shifting the revolving nosepiece from the objective to the micro-cell position. By reducing the glass micro-capillary size, measurements can be performed on very small regions, exactly in the micrometers range. In the paper [25] is discussed the influence of the glass micro-capillary size (corresponding to the working area exposed to the electrolyte) on the electrochemical behaviour of metals. Tt was found that by reducing the micro-capillary size, the pitting potential shifts to more noble values. This behavior was associated to the statistical reduction of the number of weak points like intermetallics, inclusions and grain boundaries. By employing micro-cell technique, Suter et al. found that the onset of pitting corrosion depends on the intermetallic category. In the case of Al-Cu-Mg-based intermetallics, it was observed that fast magnesium and aluminum dissolution preferentially starts at the edge rather than at the center grain. For longer immersion time, this intermetallic type can become cathodic with respect to the surrounding matrix. The preferential dissolution of iron and manganese was further detected at the edge of Al-Cu-Fe-Mn-based intermetallics. In that case, the chemical composition in the center part never changed. However, in addition to iron and manganese depletion at the intermetallic edge, dissolution even occurs in the surrounding aluminum matrix due to the galvanic coupling formed. The micro-cell technique was also employed for the study of the micro-electrochemical behaviour of AA7075 aluminum alloy [30]. The influence of cathodic intermetallics (Al_7Cu_2Fe) with respect to the matrix was detailedly investigated [31]. Al_7Cu_2Fe-based intermetallics promote the dissolution of the surrounding matrix inducing the formation of trenching corrosion morphologies. Furthermore, it was found that Mg_2Si intermetallics are anodic with respect to the matrix [32] and they constitute the preferential site for pitting corrosion initiation [33]. Indeed, magnesium-depleted Mg_2Si intermetallics tend to shrink provoking the formation of crevice corrosion at the interface with the matrix. Micro-cell investigations performed on AA7010 aluminum alloy have also allowed to detect the potential/current transient which can be related to the dissolution of both the equilibrium η-Mg_2Zn or the hardening $\eta^{'}$-Mg_2Zn phases [34].The electric charge associated to the current transient observed during a localized measurement (in that case with a glass capillary of 30 μm size) was calculated by the integration of the current vs. time diagram. This procedure was used in order to estimate the particle size associated to the

observed transient. It has been found that the potential/current transient can stem from the dissolution of both η and $\eta^{'}$ phases. It was stated that the dissolution of the equilibrium η phase is the responsible for intergranular and exfoliation attacks of Al-Zn-Mg-Cu alloys [35, 36]. Eckermann et al. [37] studied the micro-electrochemical reactivity of intermetallics present in Al-Mg-Si alloys. They found that an increasing of solution pH can be identified on MgSi intermetallic particles which should have an anodic behavior with respect to the matrix. Two different hypotheses have been formulated to explain that evidence. The first explanation is related to the development on MgSi particles of a strong hydrogen reduction associated to a fast magnesium dissolution [38]. The second mechanism takes its stand on the hypothesis that after magnesium dissolution, MgSi particles can change their behavior from anodic to cathodic. On modified MgSi particles, reduction reactions can occur producing the local increase in pH.

Corrosion behaviour can be improved by applying protective coatings or by employing corrosion inhibitors. By considering the second route, it has been found that salts of rare-earth elements are able to improve the corrosion behavior of aluminum alloys [39, 40, 41]. Hinton et al., Arnott et al. and Ryan et al. [42, 43, 44] proved that rare-earths and particularly cerium, inhibit redox reactions occurring on aluminum alloys. It has been evidenced that the improvement of the corrosion resistance is due to the precipitation of cerium compounds on cathodic regions promoting the inhibition of reduction reactions [45]. After the first studies on the mechanism of cerium compounds precipitation, it was proposed that the process starts on regions where solution pH tends to be increased by reduction reactions which produce favorable chemical conditions to cerium precipitation. It was proposed that the process continues in the surrounding regions via island growth involving small active regions not still covered [46]. Yasakau et al. [47] proved that cerium precipitation preferentially occurs on Al-Cu-Mg-based intermetallics modified by the local magnesium and aluminum dissolution which leads to the overall copper-enrichment of the intermetallic [34]. The inhibition effect of vanadates on AA2024 corrosion behavior was also evaluated by using the micro-cell technique [48]. It has been seen that vanadates promotes the decreasing of cathodic currents on both the matrix and the intermetallics. It has been proposed that the inhibition mechanism due to vanadates is related to their adsorption to the surface which prevents chloride ions attack [49]. Moreover, it was observed that vanadates are able to control the dealloying process occurring

at Al-Cu-Mg-based intermetallics stabilizing their electrochemical behavior and shifting the breakdown potential to more noble values. This is probably due to the suppression or the reduction of selective magnesium dissolution which avoids the formation of copper-enriched intermetallics able to support fast cathodic reactions. Nowadays, at our disposition there are several chemical compounds which are able to inhibit redox reactions limiting corrosion phenomenon. Cerium compounds represent one of the most interesting corrosion inhibitors for aluminum alloys. Despite the fact that many studies were focused on the comprehension of cerium precipitation mechanisms, there are some aspects which have to be still clarified. In this work, a detailed investigation on the effect of cerium precipitation on the micro-electrochemical behavior of AA2024-T3 aluminum alloy was carried out.

7.2 Materials and Experimental Procedure

Samples of commercial AA2024-T3 were ground with emery paper and polished with clothes of different resilience and abrasives. Polishing was carried out employing diamond suspensions diluted in ethanol with a grain size ranging from 6 μm to 1 μm. Ethanol was used instead of water in order to avoid or reduce the fast dissolution of the magnesium present on aluminum surfaces, especially as constituent element of Al-Cu-Mg intermetallics.
The micro-electrochemical investigation was carried out by means the micro-cell technique. The micro-cell apparatus basically consists of a glass micro capillary embedded in a micro-cell which is mounted on the revolving nosepiece of an optical microscope. This setup enables to point the measurements towards the region desired by observing the surface with the optical microscope. The sealing at the glass capillary tip is ensured by a silicone layer which enables to avoid solution leakage. A standard three electrode setup was employed for micro-electrochemical measurements where the working electrode corresponded to the exposed area defined by the diameter size of the glass micro capillary. In this work, micro capillaries of 50 μm size were employed. The counter electrode was a 1.5 mm platinum wire while a stable Ag/AgCl electrode was used as reference. All electrodes were connected to a modified potentiostat/galvanostat able to measure currents in the range of fA. Three different kind of regions were studied by means of micro-cell technique: regions containing a very limited number of inter-

metallics (indicated in the thesis as matrix), regions containing a higher number of Al-Cu-Mg-based intermetallics and regions containing a high number of Al-Cu-Fe-Mn-based intermetallics. Open circuit potential measurements (OCP) were performed for 5 minutes in order to evaluate the stability of the region identified by the micro capillary mouth. Potentiodynamic polarization curves were then acquired on the same area exposed during OCP measurements. A scan rate of $1mVs^{-1}$ was used to perform polarization curves. Anodic and cathodic branches were acquired separately starting near the OCP. All the micro-electrochemical measurements were performed in 0.05M NaCl aqueous solution. In order to evaluate the effect of cerium on the corrosion behaviour, OCP and polarization tests were performed on AA2024 samples previously immersed in 0.05M NaCl solution containing $5gL^{-1}$ $Ce(NO_3)_3 \cdot 6H_2O$. Polished samples were immersed for 12 hours in cerium solution in order to allow cerium precipitation. The modified AA2024 surface was therefore evaluated by means of electrochemical measurements carried out in 0.05M NaCl. Scanning electron microscopy (SEM) observations were combined with electrochemical measurements. The combination of the two techniques, allowed us to compare the electrochemical results with the surface morphologies observed with SEM. In order to enable the characterization of the same area of the sample before and after immersion in cerium-containing solution, the investigated areas were marked with a grid of indents prepared using a Vickers micro-indenter (Struers NAME INSTRUMENTATION). Square areas of 100 μm x 100 μm size were marked. This procedure enables to perform SEM and micro-cell characterizations on the same sample area. A Carl Zeiss EVO 40XVP microscope equipped with the INCA ENERGY 250 microanalysis apparatus was used.

7.3 Results and Discussion

7.3.1 AA2024-T3 Microstructure

Figure 7.1 shows the surface morphology of AA2024-T3 after polishing detected by means of scanning electron microscopy. The image was acquired by collecting back-scattered electrons signal emitted by the metal surface. From this picture is possible to recognize the heterogeneous microstructure of the alloy. The dark area corresponds to the aluminum matrix while the brighter regions are associated

to the second phase particles. Buchheit et al. [12] studied the distribution of second phase particles formed during casting process. They found that the most prevalent type of intermetallics correspond to that rich in Al-Cu-Mg. The second most prevalent group basically consists of Al-Cu-Fe-Mn. As explained in the experimental procedure (section 7.2), in this work three regions were considered as interesting areas for the evaluation of cerium precipitation mechanisms: regions rich in Al-Cu-Mg intermetallics (from now on called rich-Mg), regions rich in Al-Cu-Fe-Mn intermetallics (from now on called rich-Fe) and regions with a small amount of intermetallics (from now on called matrix). In Table 7.1 is reported the chemical composition of the regions identified by the three boxes in Figure 7.1: the matrix, the rich-iron intermetallic region and the rich-magnesium intermetallic region.

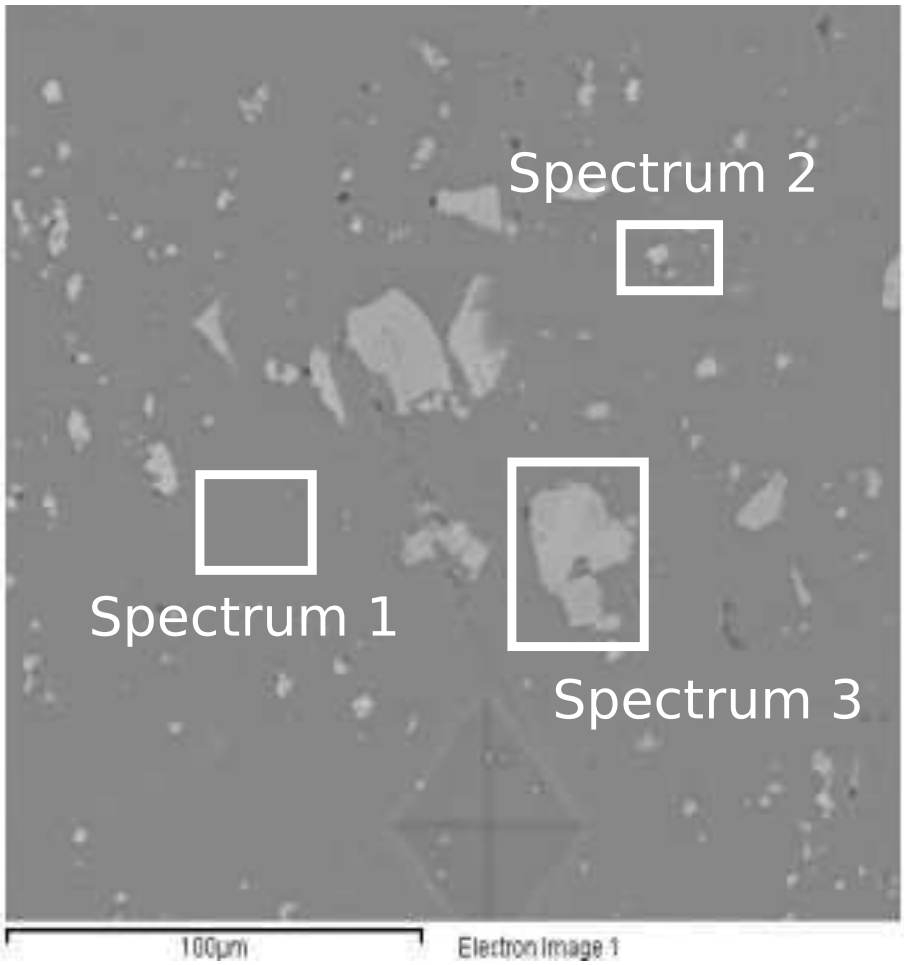

Figure 7.1: SEM image of polished AA2024-T3 surface

EDXS analysis (Table 7.1) performed on the matrix area (Spectrum 1) evidences a chemical composition in accordance with that of commercial AA2024-T3 aluminum alloys [1]. Spectrum 2 can be associated to an intermetallic rich in Al-Cu-Mg because the amount of magnesium and copper is rather higher than that detected in the matrix (Spectrum 1). In Spectrum 3, in addition to copper and aluminum signals, iron, manganese and silicon were detected. This chemical composition can be associated to the Al-Cu-Fe-Mn intermetallic type. It has been further seen and confirmed by a deeper investigation that intermetallics rich in iron are usually larger than those rich in magnesium as found by Buchheit el al. [12]. Whereas the maximum size of the rich-magnesium type is in the range of a few micrometers, the size of the rich-iron type can vary in a large range from a few micrometers up to 20 μm. Since in this work capillaries with an average diameter of 50 μm were used, the area directly exposed to the electrolyte necessarily includes both intermetallics and a fraction of matrix. It was not possible to perform measurements on regions including only intermetallics because of the very small size of these particles. This aspect has to be taken into account for the explanation of the results. It is also important to point out that it was easier to perform micro-electrochemical measurements on regions containing rich-iron intermetallics than on regions containing rich-magnesium intermetallics. Indeed, Al-Cu-Mg-based intermetallics are more reactive than those rich in iron because immediately after immersion, magnesium dissolution strongly affects the electrochemical behaviour. This aspect will be detailedly discussed in the following section 7.3.3.

Region	**Al**	**Cu**	**Mg**	**Fe**	**Mn**	**Si**
matrix (Spectrum 1)	**93.84**	**4.30**	**1.86**	/	/	/
Mg-rich INT (Spectrum 2)	**88.40**	**8.09**	**3.52**	/	/	/
Fe-rich INT (Spectrum 3)	**65.54**	**7.79**	/	**13.06**	**9.34**	**4.27**

Table 7.1: EDXS analysis on AA2024-T3

7.3.2 Open Circuit Potential Before Immersion in Cerium Nitrate

Figure 7.2 shows the open circuit potential in 0.05M NaCl for polished AA2024 samples measured on the three areas of interest defined in the section 7.2: the matrix region (solid line), the region containing rich-iron intermetallics (long-dash line) and the region containing rich-Mg intermetallics (dash-dot line). Matrix and rich-Fe intermetallics regions behave in a similar way. In the case of matrix (solid line), immediately after immersion OCP is -500mV vs. Ag/AgCl and after 300 seconds the value is very close to that detected at the beginning. However, some spikes were detected during the OCP measurement on the matrix. The first small OCP variation can be identified after 50 seconds while after 130 seconds, the OCP suddenly starts to decrease down to -600mV vs. Ag/AgCl. In the range between 130 and 200 seconds, the OCP for the matrix region appears noisy suggesting that corrosion attacks are taking place. This evidence can be likely associated to a localized corrosion attack which is typical of AA2024 aluminum alloy [10]. Immediately after immersion, OCP for the region containing rich-iron intermetallics (long-dash line) is equal to -510mV vs. Ag/AgCl and continuously tends to increase. It reaches -360mV vs. Ag/AgCl after 300 seconds immersion. The OCP shifting towards more noble values might be related to the activation of reduction reactions at the intermetallic surface which behaves cathodically with respect to the matrix [51]. The OCP trend for the region containing rich-magnesium intermetallics (dash-dot line) is not as constant as in the case of matrix and regions containing rich-iron intermetallics. Immediately after immersion, magnesium strongly affects the OCP which is -640mV vs. Ag/AgCl. For longer immersion time, the OCP shifts from very negative values (the minimum value is in the range of -1000mV vs. Ag/AgCl) to values typical of the aluminium matrix (close to -500mV vs. Ag/AgCl). For rich-magnesium intermetallics regions, the unstable OCP trend can be due to the high electrochemical activity of magnesium which quickly dissolves during the first period of immersion. In many cases, immediately after immersion, for rich-magnesium intermetallics regions the OCP was very active (down to -1100mV vs. Ag/AgCl) shifting to values typical of the matrix (close to -500mV vs. Ag-AgCl) before the end of the measurement (300 seconds). In these cases, the results of potentiodynamic polarization measurements, which will be discussed in the following

section (7.3.3), were very similar to those obtained on the matrix regions. In those cases, the magnesium content was totally dissolved during free immersion and the area underwent polarization was probably consisting of both the matrix and the intermetallics depleted in magnesium and rich in copper. This evidence was one of the most critical point to consider in the experimental approach for the evaluation of the micro-electrochemical behaviour of AA2024. From this point of view, polishing procedure has had an important role, because as explained in the experimental section 7.2, it was very important to prevent magnesium dissolution during samples preparation.

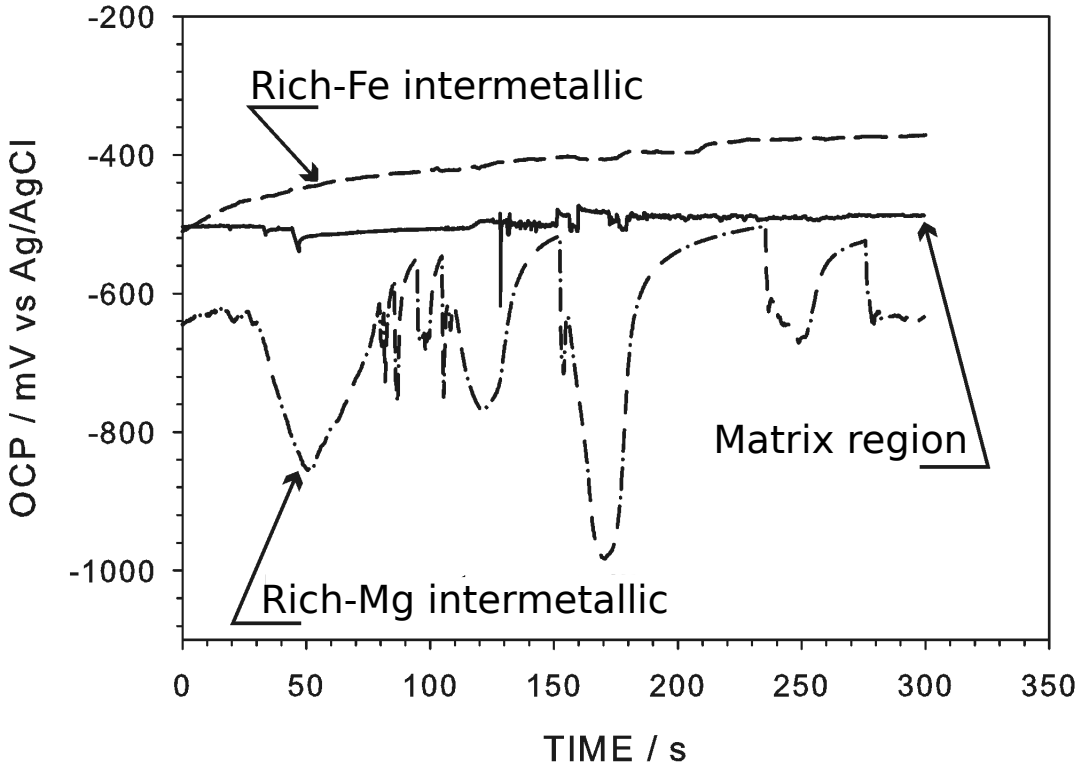

Figure 7.2: Open Circuit Potential for bare AA2024 in 0.05M NaCl

7.3.3 Potentiodynamic Polarization Curves Before Immersion in Cerium Nitrate

Figure 7.3 shows anodic and cathodic potentiodynamic polarization curves in 0.05M NaCl for polished AA2024 on the three areas of interest: the matrix re-

gion (solid line), the region containing rich-Fe intermetallics (long-dash line) and the region containing rich-Mg intermetallics (dash-dot line). Potentiodynamic polarization curves were performed on the same area exposed to the electrolyte during OCP measurements. Anodic behaviour shown in Figure 7.3(a), evidences that matrix and rich-iron intermetallics regions behave in a similar way. For rich-iron intermetallics regions, E_{corr} is more noble than that acquired for the matrix confirming the trend evidenced by OCP measurements. For regions containing rich-iron intermetallics, i_{corr} is around $1\mu A \cdot cm^{-2}$ which is almost one order of magnitude higher than that evaluated for the matrix region. This result can be explained considering that in the region containing rich-iron intermetallics, a fraction of the area exposed to the electrolyte is made of matrix. Since rich-iron intermetallics behave cathodically with respect to the matrix [11], the reduction reactions take place on intermetallics while the oxidation reactions occur on the matrix. Hence, aluminium matrix dissolution is promoted by the galvanic coupling with rich-iron intermetallic leading to higher corrosion rates.

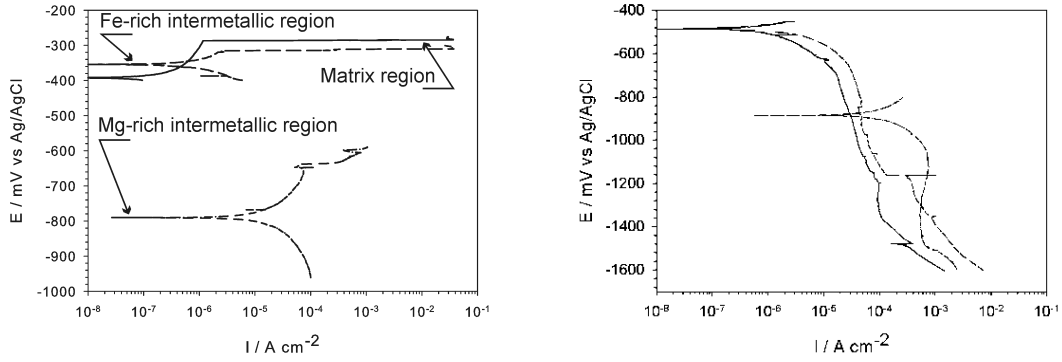

Figure 7.3: Potentiodynamic Polarization Curves in 0.05M NaCl

Figure 7.4 shows the corrosion morphology of a region containing Al-Cu-Fe-Mn intermetallics. The image was acquired after that the anodic polarization was carried out. A deep corrosion attack can be seen in the matrix where the aluminum dissolution occurs near the intermetallic boundary [49]. This evidence is related to the higher corrosion current density detected for rich-iron intermetallics regions with respect to that identified for regions containing only the matrix. This fact can be also associated to the different breakdown potentials exhibited by matrix and rich-iron intermetallics regions. Since the natural oxide layer grown at the interface between the matrix and the intermetallics tends to be weak, in these

points the oxide can be firstly dissolved by polarizing anodically the substrate. In Figure 7.3(a), it is possible to observe that for the matrix, the passive region is wider than for rich-iron intermetallics. The breakdown potential related to the localized corrosion attack can be identified at -290mV and -330mV vs. Ag/AgCl for the matrix and the rich-iron intermetallics regions, respectively. The anodic behaviour of regions containing rich-magnesium intermetallics (Figure 7.3(a)) is rather different compared to the anodic behaviour of both the matrix and the rich-iron intermetallics regions. For rich-magnesium intermetallics regions, E_{corr} is more active than those of other regions. This evidence confirms OCP measurements results. Magnesium strongly influences the electrochemical behaviour of every alloy and in the case of AA2024, second phase particles containing a high magnesium amount have a remarkable effect on E_{corr}. From Figure 7.3(a), for rich-magnesium intermetallics regions, i_{corr} is about $20\mu A \cdot cm^{-2}$ which is two order of magnitude higher than for the matrix. The breakdown potential can be identified at -640mV vs. Ag/AgCl which is very active with respect to those exhibited by the matrix and the rich-iron intermetallics. The magnesium effect on the electrochemical behaviour of AA2024 can be also evaluated in Figure 7.3(b) where cathodic potentiodynamic polarization curves are reported. Since the aim of this work is focused on the evaluation of cerium inhibition, it is essential to estimate the cathodic behaviour being strongly affected by the cerium precipitation compounds [39, 40, 41]. The matrix and the rich-iron intermetallics regions exhibit a similar cathodic behaviour near E_{corr} where the oxygen reduction and the hydrogen evolution reactions take place. At more negative potentials than E_{corr}, cathodic reactions taking place on both matrix and rich-iron intermetallics regions are strongly increased. The increase is most likely related to the water reduction reaction occurring at these potentials. The water reduction reaction seems to occur more easily on rich-iron intermetallic regions, than on the matrix. For example, at -1400mV vs. Ag/AgCl, the rich-iron intermetallic exhibits a higher cathodic current than that detected for the matrix. The cathodic current densities exhibited by the rich-magnesium intermetallics region are higher than those measured on the matrix. For rich-magnesium intermetallic regions, at potential around -1000mV vs. Ag/AgCl, the current densities are in the range of $400\mu A \cdot cm^{-2}$ which are two order of magnitude higher than those measured for the matrix region. At these potentials, on regions rich in magnesium intermetallics, a strong bubble evolution was observed which can be likely related to

intense hydrogen reduction reaction [50].
At the end of the micro-electrochemical investigation carried out on bare AA2024, it is possible to state that magnesium strongly affects the corrosion behaviour of the alloy. Anodic and cathodic reactions are heavily dependent on the amount of magnesium contained in the region under investigation. In the next section, the effect of cerium nitrate on the heterogeneous electrochemical behaviour of AA2024-T3 aluminum alloy will be discussed.

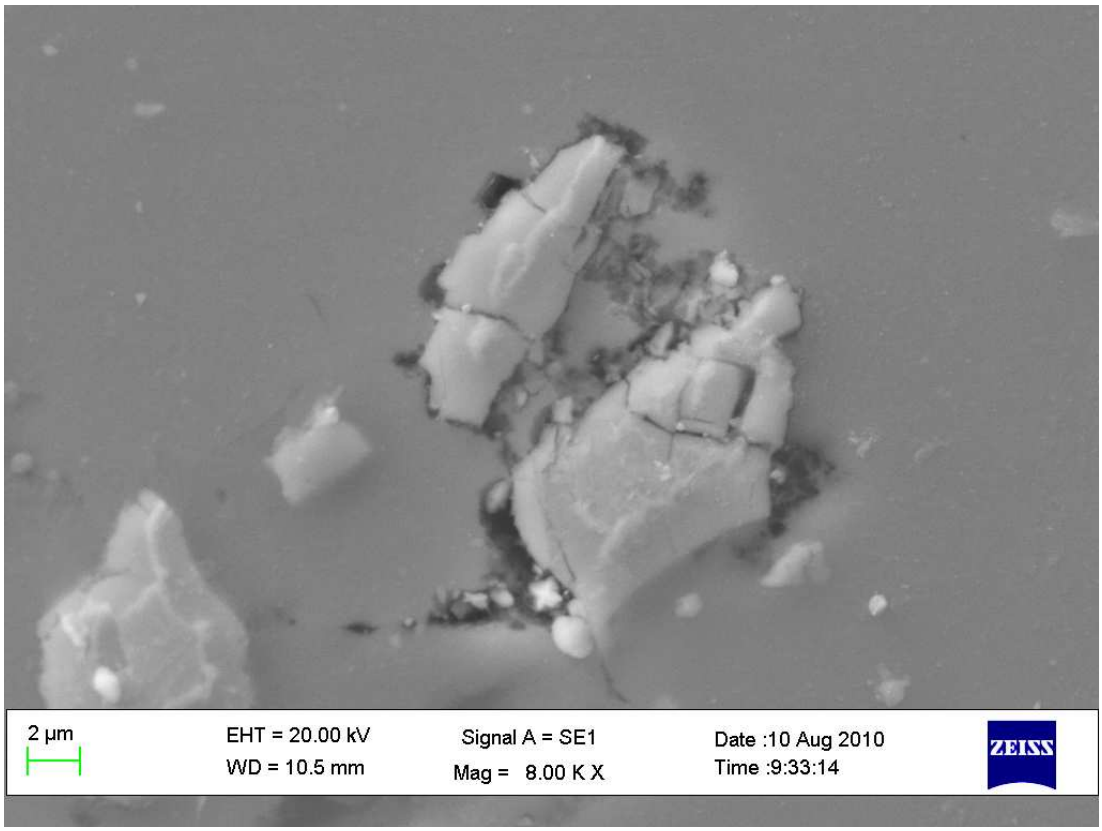

Figure 7.4: Al-Cu-Fe-Mn intermetallic corrosion morphology

7.3.4 Open Circuit Potential After Immersion in Cerium Nitrate

Figure 7.5 shows the open circuit potential for polished AA2024-T3 in 0.05M NaCl measured after 12 hours immersion in 0.05M NaCl containing $5gL^{-1}\ Ce(NO_3)_3 \cdot 6H_2O$. Measurements were performed on matrix regions (thick solid line), on regions containing rich-iron intermetallics (thick long-dash line) and on regions containing

rich-magnesium intermetallics (thick dash-dot line). OCP measurements acquired before immersion in the solution containing cerium are reported as reference (thinner lines). By comparing OCP measurements before and after immersion in cerium solution, it is possible to point out that a remarkable modification of the electrochemical behaviour can be observed for the entire surface. For matrix, rich-iron intermetallic and rich-magnesium intermetallic regions, OCP tends to be more noble than before immersion in cerium (thinner lines). For all the three regions, after 50 seconds in 0.05M NaCl, a steady state condition is reached and maintained until to the end of the measurement. In particular, for rich-magnesium intermetallics regions, characterized by a very unstable OCP before immersion, a stable OCP was detected after 12 hours immersion in cerium solution. The heterogeneous electrochemical behaviour of AA2024 was stabilized by the interaction with the cerium in solution.

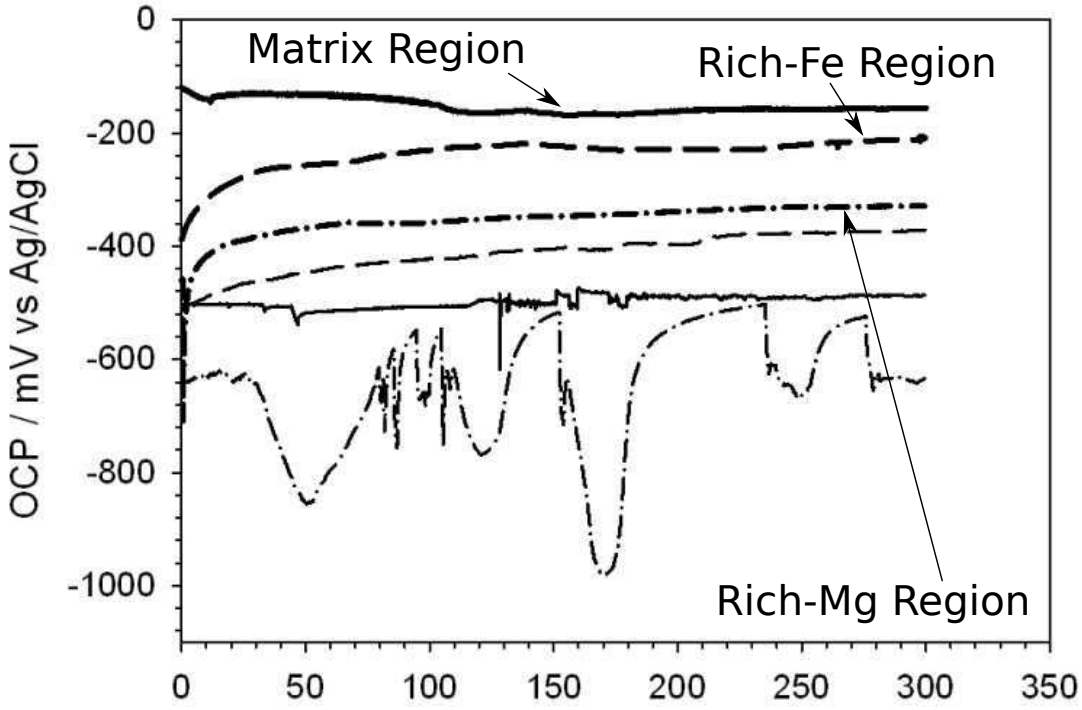

Figure 7.5: Open circuit potential in 0.05M NaCl after immersion in cerium nitrate

Figure 7.6 shows a detail of the AA2024 surface modified by the cerium in-

teraction. The Figure shows the surface morphology of a rich-iron intermetallics region (with cathodic behaviour) after 12 hours immersion in 0.05M NaCl containing $5gL^{-1}$ $Ce(NO_3)_3 \cdot 6H_2O$. From the picture, it is possible to recognize a very thin film on the intermetallic only because a crack is visible on it. On the surrounding matrix, it is not possible to recognize the film. This does not mean that the film is not present but it can mean that the film is only too thin to be observed. SEM-EDXS analysis performed on the region considered in Figure 7.6 are not able to identify the cerium signal because the penetration depth of the electron beam into the specimen is in the range of micrometers while the film thickness is probably in the range of a few nanometers. Hence, the contribution of the thin cerium film on the X-ray generation is not enough to guarantee a clear cerium signal. As well known in literature [5], cerium precipitation occurs on regions where cathodic reactions take place. As shown in Figure 7.7, cerium compounds were also observed on anodic intermetallics (Al-Cu-Mg-based) as intense precipitates. Figure 7.7 will be detailedly discussed in the next part of this section. In AA2024 aluminum alloy, immediately after immersion Al-Cu-Mg intermetallics behave anodically [8] but they can behave cathodically after magnesium dissolution. Since magnesium dissolution is very fast, it is possible that cerium precipitation occurs on the magnesium-depleted intermetallics which in the meantime might behave similar to a binary intermetallic rich in copper and aluminum. Binary Al-Cu intermetallic is more noble than both the ternary Al-Cu-Mg and the Al-Cu-Fe-Mn types [11]. It is reported [11] that in sodium chloride, the corrosion potential of the Al-Cu binary compound is -0.32 mV vs. SCE while that of the Al-Cu-Mg type is -0.92mV vs. SCE. The difference in corrosion potentials can explain the preferential cerium precipitation occurring on magnesium-depleted intermetallics. The fast magnesium dissolution is associated to a considerable electrons flow available in the surrounding areas for cathodic reactions. Since magnesium-depleted intermetallics are rich in copper, it is possible that cathodic reactions directly occur on magnesium-depleted intermetallics promoting the local pH variation needed for cerium compounds precipitation.

Figure 7.7 shows the surface of a marked AA2024 region before and after immersion in the solution containing cerium. Image reported in Figure 7.7(b) was acquired after the OCP measurement carried out on the surface modified by the immersion in the cerium solution. In Figure 7.7(a) and in Figure 7.7(b), the arrows indicate the same region containing a large number of rich-magnesium

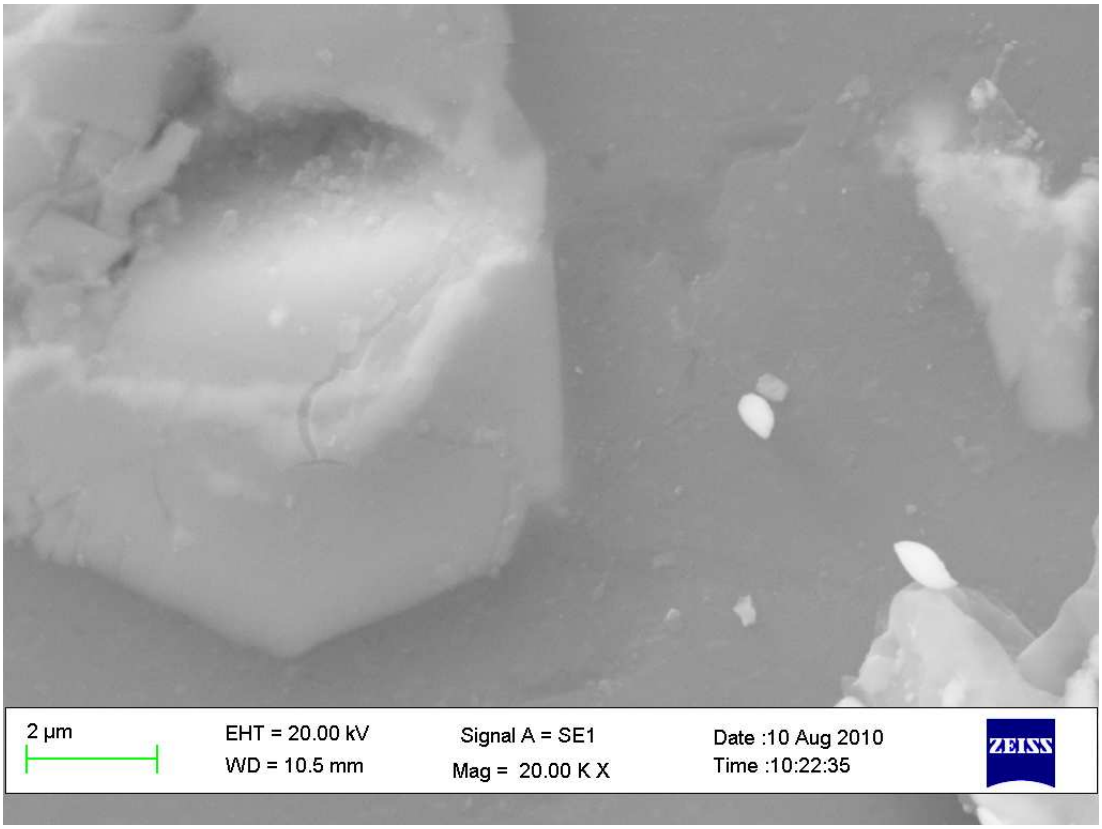

Figure 7.6: Surface morphology of rich-iron intermetallic after immersion

intermetallics before and after immersion in cerium nitrate solution. From Figure 7.7(b), it is possible to recognize that on the marked region a wide precipitation occurred covering the magnesium-rich intermetallics. The dark matrix region appears smoother than the bright rich-magnesium intermetallics, suggesting that the precipitation occurred on the matrix was not as strong as on rich-magnesium intermetallics.

Table 7.2 shows the EDXS micro-chemical composition of the region containing the magnesium-rich intermetallics which is indicated with the arrows in Figure 7.7(a) and (b). Before immersion, a high amount of magnesium was detected (7.46 %(wt)) which was not detected after immersion. On the other hand, an intense signal of cerium and oxygen was detected suggesting that a heavy cerium precipitation occurred in this region. Since after immersion the aluminum signal drastically decreases, the precipitate is probably thick enough to shield the metal substrate. EDXS analysis does not allow to acquire signals deeper than a couple of micrometers (depending on the material under investigation), and the low

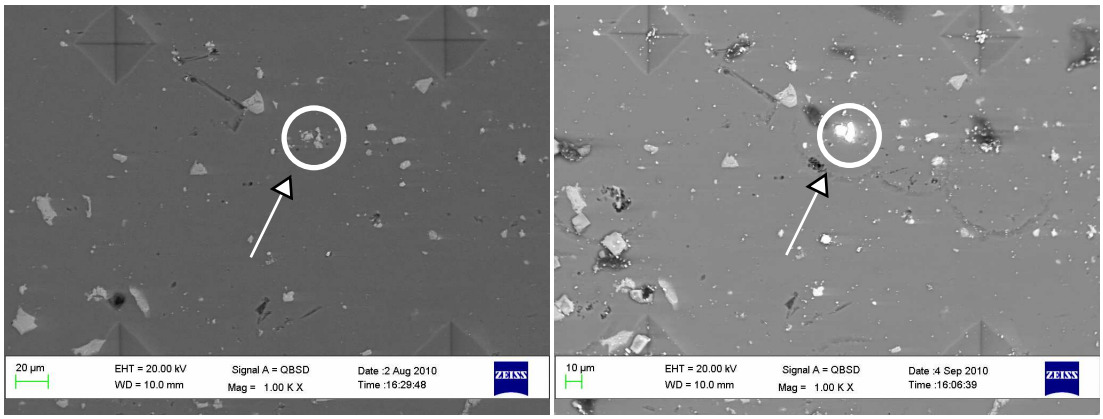

Figure 7.7: Surface morphology before and after immersion of a AA2024 marked region

aluminum signal acquired is a consequence of this limitation. On the contrary, EDXS measurements carried out on intermetallics rich in iron 7.6, were not able to recognize the cerium signal because the layer deposited in this region was not enough thick. This evidence enables to confirm that the preferential sites for cerium precipitation are those rich in magnesium.

	Al	**Cu**	**Mg**	**Ce**	**O**
Before immersion	**64.78**	**26.39**	**7.46**	/	**1.11**
After immersion	**4.81**	**2.12**	/	**55.45**	**37.26**

Table 7.2: EDXS chemical composition before and after immersion in cerium solution of the marked region of Figure 7.7

However, since cerium precipitation occurred on the entire AA2024 surface, the film growth can be explained by considering the island-growth mechanism proposed by Hughes et al. [48] for aluminum alloys. According to this mechanism, the island-growth considers the microstructure of metal substrates as a collection of micro-anodes and micro-cathodes where cerium precipitation can constantly occur. Cerium precipitation is stopped when all the entire surface is covered by the spontaneous film deposition. However, it is not still clear on what sites cerium precipitation starts and it has to be still clarified the role of the different intermetallic types.

7.3.5 Potentiodynamic Polarization Curves After Immersion in Cerium Nitrate

Figure 7.8 shows potentiodynamic polarization curves in 0.05M NaCl after immersion in the solution containing cerium for the three areas of interest: the matrix region (solid line), the region containing rich-iron intermetallics (long-dash line) and the region containing rich-magnesium intermetallics (dash-dot line). Potentiodynamic polarization curves were performed on the same area exposed to the electrolyte during OCP measurements (see Figure 7.5). After cerium immersion, for all the three regions, E_{corr} shifts towards more noble values confirming OCP results. By comparing E_{corr} values before and after immersion in cerium solution, it is possible to evaluate the variation due to the surface interaction with cerium. In the case of the matrix region, E_{corr} shifts from -400mV to -100mV vs. Ag/AgCl provoking a ΔE_{corr} equal to 300mV. For the region containing iron-rich intermetallics, E_{corr} shifts from -360mV to -200mV vs. Ag/AgCl while it changes from -800mV to -300mV vs. Ag/AgCl for the region rich in Al-Cu-Mg intermetallics. For the rich-iron intermetallics region, ΔE_{corr} is around 160mV while this Δ is in the range of 500mV for the magnesium-rich intermetallic region. Regions containing rich-magnesium intermetallics exhibit the largest ΔE_{corr}. Due to the immersion in cerium solution, i_{corrs} are also subjected to a strong reduction. In the case of matrix regions, i_{corr} changes from 0.2 $\mu A \cdot cm^{-2}$ (Figure 7.3) to $0.03\mu A \cdot cm^{-2}$ (Figure 7.8). For the region containing rich-iron intermetallics, before immersion, i_{corr} is $2\mu A \cdot cm^{-2}$ while it is reduced to $0.03\mu A \cdot cm^{-2}$ after immersion. Regions containing rich-magnesium intermetallics evidence the largest Δi_{corr}: before immersion i_{corr} is $20\mu A \cdot cm^{-2}$ while after immersion it decreases down to $0.06\mu A \cdot cm^{-2}$. It is important to point out this evidence because regions containing rich-magnesium intermetallics, before immersion in cerium solution, tend to corrode faster than both the matrix and the regions containing rich-iron intermetallics. After cerium precipitation, corrosion current densities measured on the entire surface are more close to a common value than before immersion. Moreover, areas containing rich-magnesium intermetallics display a very wide passive region (Figure 7.8) which is larger than that exhibited by both the matrix and the rich-iron intermetallics regions. The anodic behaviour of rich-magnesium intermetallics regions (Figure 7.8(a)) is considerably improved by the immersion in cerium solution. After immersion in cerium solution, the passive current

densities are two orders of magnitude lower than those before immersion. The breakdown potential is around +50mV vs. Ag/AgCl which is 100mV and 150mV more noble than for the matrix and the rich-iron intermetallics region, respectively. The effect of cerium precipitation can be also evaluated considering the cathodic behaviour (Figure 7.8(b)). Reduction reactions occurring on the entire substrate are strongly reduced by cerium precipitation. In particular, cathodic current densities measured on regions containing rich-magnesium intermetallics are strongly limited since they are reduced more than two order of magnitude. The strong current reduction observed for the rich-magnesium intermetallic region, can be related again to the high amount of cerium compounds precipitated on this region. However, the inhibition of cathodic reactions exhibited by the entire surface confirms that cerium precipitation involves all the microstructure.

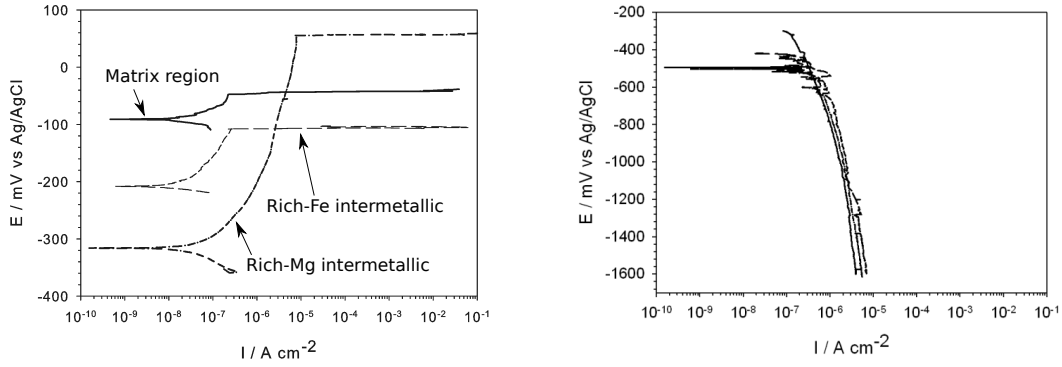

Figure 7.8: Potentiodynamic Polarization Curves in 0.05M NaCl after immersion in cerium nitrate

Figure 7.9 shows a region containing a large intermetallic with a very complex chemical composition. The three images ((a), (b) and (c)), were acquired after the anodic polarization carried out subsequently to the immersion in the solution containing 5 gL^{-1} cerium nitrate. Table 7.3 shows the average chemical composition acquired on the whole intermetallic before immersion in cerium. In Table 7.3 are also reported the chemical compositions of Region 1 and Region 2 after immersion in cerium nitrate. As can be seen in Table 7.3, Mg, Al, Cu, Fe, Mn and Si signals were detected in the average composition of the intermetallic before immersion in cerium. The latter three elements with Cu and Al, form intermetallics with cathodic behaviour [10] while intermetallic types containing Mg, Al and Cu behave anodically with respect to the matrix. Hence, the intermetallic

observed in Figure 7.9 is probably made of second phase particles with different micro-electrochemical behaviour. The intermetallic is probably formed by the combination of a part rich in Al-Cu-Mg (Region 1) and another part containing Al-Cu-Fe-Mn (Region 2).

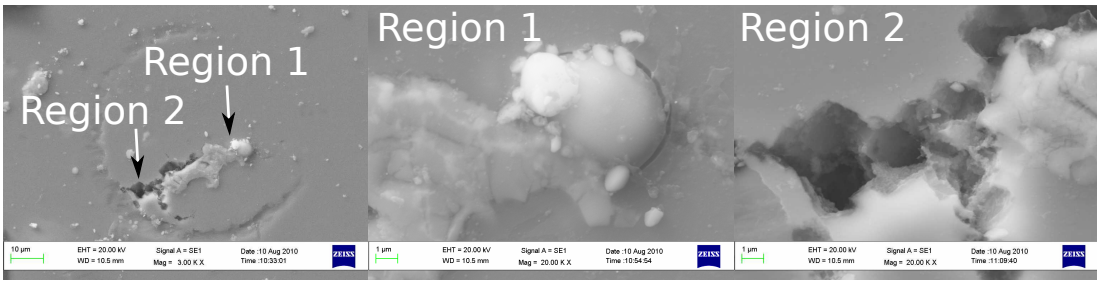

Figure 7.9: AA2024-T3 surface morphology after anodic polarization in 0.05M NaCl. Sample immersed in cerium solution for 12 hours

In Figure 7.9(a), the sign produced by the contact between the capillary mouth and the AA2024 surface defines the area exposed to the electrolyte during the measurement. It corresponds to a diameter mark in the range of 50-60 μm which corresponds to the glass capillary size. Figure 7.9(c) shows the localized corrosion attack at the matrix in correspondence to the interface with the intermetallic (Region 2). The corrosion attack occurred in correspondence with a restricted edge. In the opposite part of the intermetallic (Region 1), no evidences of corrosion are observed (Figure 7.9(b)). In Figure 7.9(b), it is also possible to recognize a strong cerium precipitation (see Table 7.3) which was most likely able to protect the metal substrate when the anodic polarization measurement was carried out.

	Al	**Cu**	**Mg**	**Fe**	**Mn**	**Si**	**Ce**	**O**
Average Composition Before immersion	**70.62**	**10.38**	**2.23**	**6.71**	**4.69**	**2.25**	/	**3.11**
Region 1 After immersion	**18.85**	**7.57**	/	/	/	/	**41.62**	**30.35**
Region 2 After immersion	**52.33**	**8.77**	/	**15.46**	**10.97**	/	**1.29**	**7.12**

Table 7.3: Chemical composition of the mixed intermetallic of Figure 7.9

The micro-chemical analysis carried out on the intermetallic region represented in Figure 7.9(c) exhibits a weak signal of cerium and oxygen while intense

peaks of iron and manganese were detected. Then, the pitting corrosion of the matrix visible in Figure 7.9(c), occurred in correspondence with the intermetallic interface rich in iron and manganese. The small amount of cerium detected and the morphology observed in Figure 7.9(c) indicate that a very thin film covers this part of the intermetallic and the surrounding matrix. The same evidence was observed for the rich-iron intermetallic of Figure 7.6. The corrosion attack identified at Region 2 is probably related to a limited protection provided by cerium compounds while the Region 1 is completely covered by a thick cerium precipitate. This aspect evidences one time more that on intermetallic regions rich in iron and manganese, cerium precipitation is less intense than on regions rich in magnesium-intermetallics. On the contrary, it is confirmed that regions containing an high amount of magnesium are preferential sites for cerium precipitation. Despite the fact that EDXS analyses performed after cerium precipitation on Region 1 and Region 2 were not able to recognize the magnesium signal, which was instead detected before immersion as an alloying element of the average composition of the entire intermetallic , it seems to be reasonable to hypothesize that the magnesium signal detected before immersion was mainly emitted by Region 1. This hypothesis is based on the considerations made on Figure 7.7.

The behaviour of the mixed intermetallic of Figure 7.9 should definitively confirm that regions containing magnesium tend to promote an intense cerium precipitation. Considering the results obtained, the cerium precipitation on rich-magnesium intermetallics could be related to two different precipitation mechanisms related to the magnesium dissolution kinetic proposed for MgSi intermetallics in Al-Mg-Si alloys [37]. The first deposition mechanism can be related to the fast magnesium dissolution which should be able to supply electrons for cathodic reactions occurring very close to the anodic region. This mechanism considers that magnesium dissolution and cathodic reactions occur together on intermetallics rich in magnesium which are immediately covered by cerium precipitation. The second mechanism proposed is based on a slower cerium precipitation kinetic. Measurements shown in Figure 7.2, evidence that the OCP for rich-magnesium intermetallics can shift from very negative potentials to potentials typical to the matrix in a very limited length of time. As already discussed, it is possible to suppose that the total amount of magnesium completely dissolves before that cerium precipitation strongly occurs. If this happens, intermetallics are depleted in magnesium (and aluminum) and become more rich in copper. The

modified intermetallics are probably more cathodic than the others [10] and they are able to promote a more intense cerium precipitation. It is very difficult to prove what mechanism is more probable. A combination of the two routes may be a reasonable hypothesis.

The results obtained by means of micro-electrochemical measurements have shown that regions containing rich-magnesium intermetallics are very reactive and cerium precipitation seems to be promoted on these regions. It was also found that cerium precipitates are not always able to cover homogeneously the metal substrate. As in the case observed in Figure 7.7, some cracks are observable on cerium precipitates. Hence, the corrosion protection provided is therefore affected by the compactness of cerium compounds . Some polarization measurements carried out on regions containing rich-magnesium intermetallics evidenced a complex electrochemical behaviour. Figure 7.10 shows one example of this. The Figure displays the cathodic branch of a polarization curves performed in 0.05M NaCl on a region containing rich-magnesium intermetallics. The sample was previously immersed in 0.05M NaCl containing $5gL^{-1}\ Ce(NO_3)_3 \cdot 6H_2O$ for 12 hours. Table 7.4 shows the partial data list of the measurement shown in Figure 7.10. The cathodic curve starts 50 mV more positive than the measured OCP. The first E_{corr} evidenced by Figure 7.10 can be identified in the data list shown in Table 7.4 as -375 mV vs. Ag/AgCl. This value is similar to those acquired for identical regions containing rich-magnesium intermetallics and modified by cerium action (Figure 7.5). By evaluating the values reported in Table 7.4, it is possible to point out that the current densities initially measured were positive. In corrosion studies, positive currents are associated to anodic reactions. Therefore the first branch corresponds to oxidation reactions occurring at the working electrode.

For potentials more negative than the first E_{corr}, the acquired current densities were rightly negative because reduction reactions occur at the surface electrode. By polarizing the substrate at more negative potentials, cathodic current densities continuously increase. At -497 mV vs. Ag/AgCl, the sign of the current changes from negative (cathodic) to positive (anodic) reaching $4000\mu A \cdot cm^{-2}$ in a very limited length of time. This behaviour seems to be correlated to the activation of the metal substrate due to the damage of the cerium film covering the exposed region. It is possible to suppose that the electrolyte reached the metal substrate through cerium film defects similar to those observable in Figure 7.7. Once this happens, the metal substrate is not protected and the electrochemical

V $[mV]$	**i** $[Acm^{-2}]$
-374.510	$7.78\cdot\ 10^{-9}$
-374.815	$6.22\cdot\ 10^{-9}$
-375.119	$1.56\cdot\ 10^{-9}$
-375.424	$-7.89\cdot\ 10^{-9}$
-497.010	$-1.00\cdot\ 10^{-9}$
-497.315	$-1.00\cdot\ 10^{-9}$
-497.924	$4.26\cdot\ 10^{-2}$
-498.229	$4.17\cdot\ 10^{-9}$
-498.534	$4.12\cdot\ 10^{-9}$
-936.732	$5.31\cdot\ 10^{-6}$
-936.036	$5.46\cdot\ 10^{-6}$
-937.341	$2.16\cdot\ 10^{-6}$
-937.646	$-1.62\cdot\ 10^{-7}$
-937.832	$-2.06\cdot\ 10^{-6}$
-937.951	$-1.51\cdot\ 10^{-6}$

Table 7.4: Partial data list of the V/I diagram of Figure 7.10

behaviour is then related to the underneath microstructure rather than to the cracked cerium layer. Therefore, anodic current densities are due to the metal substrate oxidation and probably to the activation of the amount of magnesium not still dissolved. For a further reduction of the applied potentials , a second E_{corr} can be identified at -937 mV vs. Ag/AgCl. This equilibrium point is most probably related to the reactions occurring on an electrode rich in magnesium. Indeed, rich-magnesium intermetallics exhibited similar E_{corr} values as observed in Figure 7.3. For potentials lower than -937mV vs. Ag/AgCl, current densities become negative again, suggesting that cathodic reactions occur on the uncovered metal substrate. At these potentials, cathodic current densities are very similar to those detected for rich-magnesium intermetallic regions displayed in Figure 7.3.

It seems reasonable to sink the hypotheses made. This example shows that cerium precipitates are not able to uniformly cover the metal substrate. There are some weak point where a corrosion attack can occur more easily than on other regions. The example of Figure 7.10 also shows that underneath cerium

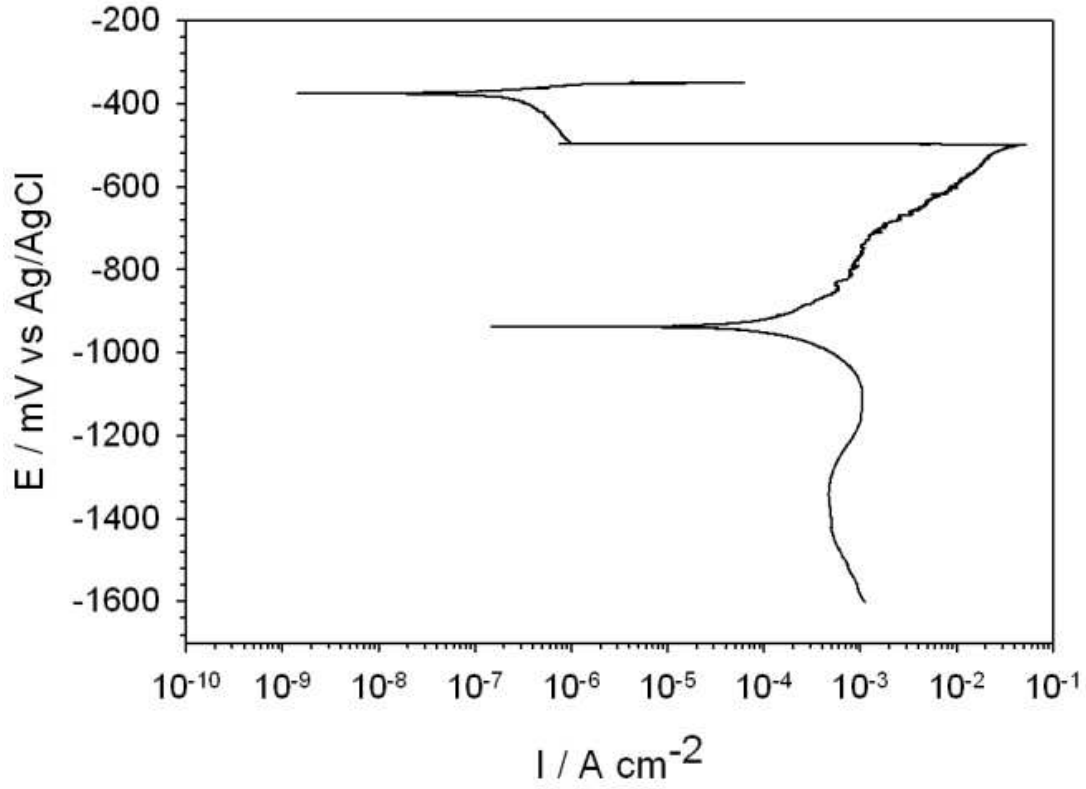

Figure 7.10: Cathodic polarization on cracked cerium film deposited on rich-magnesium regions

film, an amount of magnesium is still available. This means that on the region considered in Figure 7.10, the cerium precipitation cover the intermetallics rich in magnesium before that magnesium completely dissolves. This aspect has to be pointed out because it can be related to one of the mechanisms proposed for the explanation of the cerium deposition. Based on this evidence, further studies have to be performed to verify and confirm the hypotheses formulated on the inhibition mechanism associated to cerium precipitation on AA2024-T3 aluminum alloys.

7.4 Conclusions

The electrochemical micro-cell technique has been employed for the micro-evaluation of the effect of cerium nitrate on the corrosion behaviour of 2xxx aluminum alloys.

Magnesium-rich and iron-rich intermetallics have been considered as well as the matrix region.

The regions containing an high amount of magnesium-rich intermetallics are very reactive. The electrochemical activity is strongly affected by the fast magnesium dissolution coupled with the intense reduction reactions occurring.

The corrosion behaviour of AA2024-T3 samples immersed for 12 hours in the solution containing the cerium nitrate salt is significantly improved. The regions rich in magnesium tends to be more stable and the current flow related to Faradic processes is strongly decreased for the entire microstructure. The precipitation of a thin layer film improves both the anodic and the cathodic behaviour indicating that cerium can be considered as a general inhibitor. However, the regions rich in magnesium are sites on where a more intense cerium precipitation occurs. This behaviour is most likely related to the intense reduction reactions occurring on the intermetallics themselves which produce the pH increase necessary for cerium precipitation.

Bibliography

[1] Handbook Committee, *"Metals Handbooks, manuals"* ASM International, Printed in the United States of America

[2] A. Garner, D. Tromans, Corrosion 35 (1979) 55

[3] I.L. Mueller, J.R. Galvele, Corros. Sci. 17 (1977) 179

[4] R. Bakish, W.D. Robertson, This Journal 103 (1956) 320

[5] K. Urishino, K. Sugimoto, Corros. Sci. 19 (1979) 225

[6] Z. Szklarska-Smialowska, Corros. Sci. 41 (1999) 1743

[7] P. Campestrini, E.P.M. van Westing, H.W. van Rooijen, J.H.W. de Wit, Corros. Sci. 42 (2000) 1853

[8] N. Dimitrov, J.A. Mann, M, Vukmirovic, K.J. Sieradzki, J. Electrochem. Soc. 147 (2000) 3283

[9] I.T.E. Fonseca, N.E. Lima, J.A. Rodrigues, M.I.S. Pereira, J.C.S. Salvador, M.G.S. Ferreira, Electrochem. Commun. 4 (2002) 353

[10] R.G. Buchheit, J. Electrochem. Soc. 142 (11) (1995) 3994

[11] R.G. Buchheit, R.P. Grant, P.F. Halva, B. Mckenie, G.L. Zender, J. Electrochem. Soc. 144 (8) (1997) 2621

[12] T.J. Warner, M.P. Schmidt, F. Sommer, D. Bellot, Z. Metallk 86 (1995) 494

[13] V. Guillaumin, G. Mankowski, Corros. Sci. 41 (1999) 421

[14] C.M. Liao, R.P. Wei, Electrochim. Acta 45 (1999) 881

[15] N. Birbilis, R.G. Buchheit, J. Electrochem. Soc. 152 (2005) B140

[16] G.O. Ilevbare, O. Schneider, R.G. Kelly, J.R. Scully, J. Electrochem. Soc. 151 (2004) B453

[17] M. Buchler, T. Watari, W.H. Smyrl, Corros. Sci. 42 (2000) 1661

[18] O. Schneider, G.O. Ilevbare, R.G. Kelly, J.R. Scully, J. Electrochem. Soc. 151 (2004) B465

[19] G.O. Ilevbare, J.R. Scully, J. Electrochem. Soc. 148 (2001) B196

[20] J.R. Scully, T.O. Knight, R.G. Buchheit, D.E. Peebles, Corros. Sci. 35 (1993) 185

[21] R.P. Wei, C.M. Liao, M. Gao, Metall. Mater. Trans. A. 29 (1998) 1153

[22] N. Birbilis, R.G. Buchheit, J. Electrochem. Soc. 155 (3) (2008) C117

[23] C. Blanc, B. Lavelle, G. Mankowski, Corros. Sci. 39 (1997) 495

[24] R.G. Buchheit, L.P. Montes, M.A. Martinez, J. Michael, P.F. Hlava, J. Electrochem. Soc. 146 (1999) 4424

[25] T. Suter, H. Bohni, Electrochim. Acta 42 (1997) 3275

[26] T. Suter, T. Peter, H. Bohni, Materials Sci. Forum 25 (1995) 192

[27] H. Bohni, T. Suter, A. Schreyer, Electrochim. Acta 40 (1995) 1361

[28] T. Suter, R.C. Alkire, J. Electrochem. Soc. 148 (1) (2001) B36

[29] T. Suter, Ph.D Thesis No.11962, ETH Zurich (1997)

[30] J. Wloka, G. Burklin, S. Virtanen, Electrochim. Acta 53 (2007) 2055

[31] N. Birbilis, M.K. Cavanaugh, R.G. Buchheit, Corros. Sci. 48 (2006) 4202

[32] N. Birbilis, R.G. Buchheit, J. Electrochem. Soc. 152 (2005) B140

[33] F. Andreatta, M.M. Lohrengel, H. Terryn, J.H.W. de Wit, Electrochim. Acta 48 (2003) 3239

[34] J. Wloka, S. Virtanen, Surf. Interface Anal. 40 (2008) 1219

[35] T. Ramgopal, P.I. Gouma, G.S. Frankel, Corrosion 58 (2002) 687

[36] J. Wloka, T. Hack, S. Virtanen, Corros. Sci. 49 (2007) 1437

[37] F. Eckermann, T. Suter, P.J. Uggowitzer, A. Afseth, P. Schmutz, Electrochim. Acta 54 (2008) 844

[38] G.L. Song, A. Atrens, Adv. Eng. Mater. 1 (1999) 11

[39] M. Bethencourt, F.J. Botana, J.J. Calvino, M. Marcos, M.A. Rodriguez-Chacon, Corros. Sci. 40 (1998) 1803

[40] B. Davo, J.J. de Damborenea, Electrochem. Acta 49 (2004) 4957

[41] R.L. Twite, G.P. Bierwagen, Prog. Org. Coat. 33 (1998) 91

[42] B.R.W. Hinton, D.R. Arnott, N.E. Ryan, Met. Forum 7 (1984) 211

[43] B.R.W. Hinton, D.R. Arnott, N.E. Ryan, Mater. Forum 9 (1986) 162

[44] D.R. Arnott, B.R.W. Hinton, N.E. Ryan, Corrosion 45 (1989) 12

[45] D.R. Arnott, B.R.W. Hinton, N.E. Ryan, Mater. Perform. 42 (1987) 47

[46] A.E. Hughes, S.G. Hardin, T.G. Harvey, T. Nikpour, B. Hinton, A. Galassi, G. McAdam, A. Stonham, S.J. Harris, S. Church, C. Figgures, D. Dixon, C. Bowden, P. Morgan, S.K. Toh, D.D. McCulloch, J. DuPlesis, Proceedings of the Third International Symposium on Aluminum Surface Science and Tech
Bonn, Germany, 2003, p.264

[47] K.A. Yasakau, M.L. Zheludkevich, S.V. Lamaka, M.G.S. Ferreira, J. Phys. Chem. B. 110 (2006) 5515

[48] K.D. Ralston, T.L. Young, R.G. Buchheit, J. Electrochem. Soc. 156 (2009) C135

[49] M. Iannuzzi, G.S. Frankel, Corros. Sci. 49 (2007) 2371

[50] ASSISl
ASSIS ASSIS

Chapter 8

Zirconium Oxide from Metal-Organic Precursors containing Cerium Nitrate

Aluminum alloys are widely employed in many industrial and building applications due to the good combination of mechanical properties and low density. In particular, alloys of the 6xxx series like AA6060 are extensively employed in rolled and extruded products. Sol-gel coatings represent an alternative corrosion protection method to chromate based systems, which must be replaced. Recently, it was shown that ZrO_2 based sol-gel coatings deposited on AA6060 can provide good corrosion protection to AA6060. However, ZrO_2 based sol-gel systems cannot provide self-healing effect, which is a peculiar property of chromate conversion coatings. Indeed, the structure of the zirconium oxide does not contain species able to restore barrier properties when defects or damage impairs coating protection. In this chapter, ZrO_2 based sol-gel coatings doped with cerium nitrate were deposited in order to evaluate the inhibition effect of cerium ions on the corrosion behaviour of ZrO_2 sol-gel coated AA6060 aluminum alloy. The cerium nitrate was added to the solution containing the zirconium alkoxide precursor. Three types of samples were produced: a non-inhibited type consisting of 3 layers of ZrO_2, an inhibited system consisting of two layers of ZrO_2 with an intermediate layer doped with cerium nitrate and an inhibited system consisting of two layers containing cerium nitrate with a top layer of ZrO_2.

8.1 Introduction

Aluminium alloys are usually protected with a paint system consisting of a conversion layer, a primer and a top coat. Chromium-based pre-treatments are extensively employed as conversion coatings because they provide very good adhesion for primers and top coats associated with good barrier properties [1]. Chromate conversion coatings exhibit self-healing ability [1]. However, the use of chromate conversion coatings is restricted and alternative pre-treatments should be employed for the corrosion protection of aluminum alloys [1, 2, 3, 4]. Coatings obtained with sol-gel techniques are a possible replacement for chromate conversion coatings [5, 6]. In previous works, our research group followed the strategy of developing thin sol-gel coatings for different aluminium alloys [7, 8]. Thin ZrO_2 amorphous films (100-200 nm) were deposited on AA1050 with dip-coating technique [7]. These films promote the adhesion of organic coatings to the metal substrate. ZrO_2 sol-gel films were further deposited on AA6060. Barrier properties of sol-gel coated AA6060 were similar to those of chromate conversion coated AA6060 when a continuous layer was deposited on the surface through successive dipping steps in the sol-gel solution [8]. Moreover, ZrO_2 films deposited with sol-gel technique improved corrosion resistance of aluminium alloy AA2024 [5, 6]. It was proved that cerium and rare-earth salts inhibited corrosion behaviour of aluminium alloys in aqueous solutions containing chlorides [9, 10, 11]. The addition of cerium ions as chloride compounds to the electrolytic solution promoted the formation of a compact film of cerium hydroxide/oxide on the metal surface [12, 13]. Several works [14, 15, 16, 17, 18, 19] considered the deposition of cerium-containing layers for the replacement of chromate based conversion coatings. In our recent works [20, 21], interesting results were obtained adding cerium nitrate to organic-inorganic hybrid sol-gel systems deposited on AA2024 aluminum alloy. Coated AA2024 with hybrid coatings containing cerium evidenced corrosion rates lower than those detected for coatings without cerium. Cerium ions in the coating structure were probably involved in the overall corrosion processes occurring at the metal surface providing an additional protection. In this chapter, ZrO_2 sol-gel coatings containing cerium were deposited on AA6060 in order to combine barrier properties, previously observed for ZrO_2 based systems on the same substrate [8], with the additional protection guaranteed by cerium species introduced in the coating [21].

8.2 Experimental Procedures

The substrate for the deposition of ZrO_2 pre-treatments was AA6060 aluminum alloy. Prior deposition, the metal substrate underwent pickling procedure consisting of an alkaline etching followed by an acid etching. Sol-gel solutions were prepared using a metal-organic precursor of zirconium (0.1M $Zr(OPr^n)_4$) in anhydrous ethanol. Cerium species were introduced directly in the metal-organic solution precursor as cerium nitrate with an $\frac{[zirconium]}{[cerium]}$ molar ratio equal to $\frac{[70]}{[30]}$. Coatings were produced by means of dip-coating technique with 5 $cm\ min^{-1}$ and 22 $cm\ min^{-1}$ withdrawal rates. In this work, three different zirconia-based coatings have been considered. The coating systems were produced as the combination between layers deposited with solutions containing the zirconium precursor and solutions where, in addition to the zirconium precursors, cerium nitrate was added. Coatings were produced applying three layers by dipping. For the first sample, the three layers were deposited from the zirconium precursor solution non containing cerium nitrate (sample A). For the second sample, the two layers near the metal substrate were produced with the zirconium precursor solution containing cerium species, while the top layer was produced with the zirconium precursor solution non containing cerium nitrate. In the case of the third sample, the intermediate layer was deposited starting from the precursor solution containing cerium nitrate while the other two layers were produced from the undoped solution (sample B). The deposited sol-gel layers underwent thermal treatment in order to promote the formation of a cross-linking network. Thermal treatment was carried out at 250 $°C$ employing two different drying time. For a first group of samples, each layers was held at 250 $°C$ for 5 minutes (samples A, B, C). For the second group of samples, the drying time was increased to 10 minutes for the first two layers and to 20 minutes for the top layer (sample D). Table 8.1 shows the thermal treatment times and the names used in this chapter to recognize the systems. In order to evaluate the redox ratio Ce^{3+}/Ce^{4+} within zirconia based sol-gel films, Zr-Ce coatings were deposited on SiO_2 substrates on which UV-visible spectra were recorded. Spectra were recorded in a range between 190 nm and 1000 nm.

Samples produced in this work were characterized by means of SEM-EDXS in order to investigate the morphology of the sol-gel pre-treatment. Film thickness and composition were evaluated by means of glow discharge optical emission spec-

Sol-gel System	Thermal Treatment Time [min]	Sample name
ZrO2-ZrO2-ZrO2	5+5+5	A
ZrO2-ZrO2Ce-ZrO2Ce	5+5+5	B
ZrO2-ZrO2Ce-ZrO2	5+5+5	C
ZrO2-ZrO2Ce-ZrO2Ce	10+10+20	D

Table 8.1: Sol-gel systems deposited on AA6060

troscopy (GDOES). The electrochemical behaviour of the samples was studied by means of potentiodynamic polarization and electrochemical impedance spectroscopy in diluted Harrison solution (0.05 $wt\%NaCl$, 0.35 $wt\%(NH_4)_2SO_4$)). The scan rate used for polarization curves was 0.2 $mV\ s^{-1}$. Impedance measurements were carried out at open circuit potential with AC voltage amplitude of 10 mV and frequency range from 10 mHz to 100 kHz.

8.3 Results

Since the discussion on the procedure sol-gel synthesis has been already explained in detail in Chapter 3, it has not been further considered in this part. Figure 8.1 shows the viscosity curves obtained for both the zirconium sol (solid line) and the zirconium sol doped with cerium (dash line). Apart the behaviour at low shear stress, it is possible to observe that the viscosity for doped sol is almost 3 times higher than for the undoped. This behaviour is most likely due to the addition of cerium nitrate to the initial sol. Cerium nitrate promotes an increasing in the hydrolysis kinetics which are directly related to the viscosity of sols. From an industrial point of view, a low sol viscosity is preferred for spraying depositions because higher sol viscosity does not allow to easily perform coating depositions. However, the viscosity of the doped and the undoped zirconium sols is not much far from typical values of aqueous solutions (1 $mPa\cdot s$) and it remains stable for a length of time enough long to allow the deposition on the metal substrate.

The oxidation state of cerium in nitrate compounds is +3 but, as already explained in Chapter 6, during the sol-gel synthesis or the deposition of cerium based chemical conversion coatings, the cerium oxidation state can change. It is possible that Ce^{3+} oxidizes to Ce^{4+} during the synthesis of zirconia doped

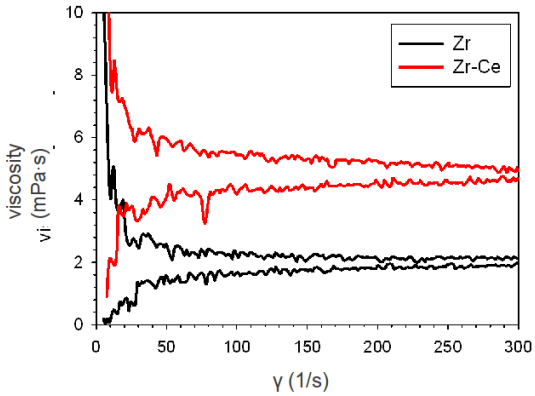

Figure 8.1: Sol viscosity of $Zr(OPr^n)_4$ sol and $Zr(OPr^n)_4$ sol doped with the $\frac{zirconium}{cerium}$ molar ratio equal to $\frac{70}{30}$)

coatings. Both oxidation states can be involved in the chemical precipitation of cerium oxide/hydroxide following the mechanisms described in literature and reported in Chapter 6. Another fact is that the oxidation reaction involving Ce^{3+} to form Ce^{4+} is a competitive reaction of aluminum dissolution. Therefore, Ce^{3+} added to zirconia sol-gel coatings can be oxidized to Ce^{4+} rather than the oxidation of the aluminum occurs. On the contrary, Ce^{4+} can not be further oxidized but it can be only reduced, being a non competitive reaction with the aluminum dissolution. This aspect has to be taken into account because Ce^{3+} oxidation can act as an additional protection of the metal substrate. The determination of the Ce^{3+}/Ce^{4+} ratio can be useful to understand how cerium can heal the metal substrate when corroded. As just observed, cerium ions can chemically precipitate without the change of the oxidation state (Ce^{3+}, Ce^{4+}) or can electrochemically precipitate changing the oxidation state (Ce^{3+}). In order to study the redox ratio Ce^{3+}/Ce^{4+}, UV-visible spectra were recorded between 190 and 1000 nm on Zr-Ce coatings deposited on SiO_2 substrates and treated in similar conditions than metals (AA6060, 10 minutes at 250 °C). These measurements and their evaluation were carried out at the Glass Ceramic Institute of Madrid as a part of a wider collaboration. Figure **??**(a) shows the absorption spectra of Zr-Ce thin coatings with a $\frac{[70]}{[30]}$ Zr/Ce molar ratio deposited on SiO_2 substrates, compared with the spectrum of pure ZrO_2 coatings. Two main bands appear in both spectra, one centred around 200 nm assigned to Ce^{4+} charge transfer, and another wider band around 260 nm. The latter can be resolved in two bands,

at 260 and 310 nm associated to Ce^{3+}. This evidence is most clear in the spectrum relative to the sol-gel coating deposited from the solution 0.4M (Zr) which contains an higher amount of cerium.

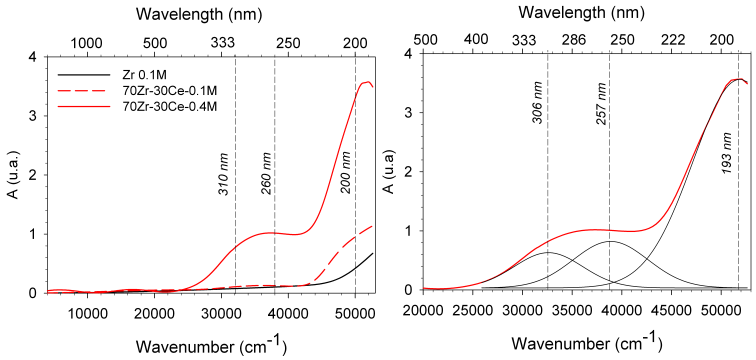

Figure 8.2: a) Absorption UV-vis spectra of Zr-Ce coatings deposited on SiO2 substrates. b) Deconvolution of Zr-Ce 0.4M spectra to determine the redox Ce4+/Ce3+ ratio

The deconvolution of the spectrum (0.4M zirconium precursor) confirm the visual approach exhibiting three bands centered at 193 nm 257 nm and 306 nm (Figure **??**(b)). For the calculation of the Ce^{4+}/Ce^{3+} redox ratio is required the molar absorptivity (ε) corresponding to the different transitions observed. The molar absorptivity (ε) can be derived from the combination of the absorption coefficient α (equation 8.1) and the extinction coefficient k (equation 8.2):

$$\alpha = \frac{4\pi k}{\lambda} \tag{8.1}$$

$$\varepsilon = \frac{4\pi k}{\lambda C} \tag{8.2}$$

where λ is the wavelength of the incident light and C is the ions concentration. Ce^{4+} is a $4f^0$ system and cannot present $f \rightarrow f$ transitions; the color of Ce^{4+} salts arises from the tail of a strong charge transfer band in the UV, centered on 200 nm. Although the wavelength of this electronic transition is near constant, the molar absorptivity changes depending on the nature of the complex and the electronegativity of the ligands, from 3800 $L\ mol^{-1}\ cm^{-1}$, in silicate glasses, up to 4000- 7000 $L\ mol^{-1}\ cm^{-1}$, in CeO_2 crystalline films deposited by different techniques or with different nanostructures. Ce^{3+} has a $4f^1$ ground electronic configuration with two free ion states separated by about 2000 cm^{-1}. The first

excited configuration is 5d and the optical spectra of Ce^{3+} consists of one $f \rightarrow f$ transition in the near IR ,that is Laporte forbidden, with very low molar absorptivity and two $f \rightarrow f$ transitions ($^2F_{5/2} \rightarrow^2 D_{3/2,5/2}$), that is Laporte allowed $nf \rightarrow n-1fd$ transitions in the UV. The maxima band corresponding to these transitions mainly depends on the neighbour ligands, being situated at 262 nm, 298 nm and 328 nm in ethanol solvent. Since cerium glass-like coatings are prepared from alcoholic sols, and the UV-visible absorption bands appear at similar wavelengths (267 nm and 310 nm), it is reasonable to assign the molar absorptivity corresponding to the bands 480 and 150 $L\ mol^{-1}\ cm^{-1}$. This assumption is needed for the semi-quantitative calculation of Ce^{3+} concentration. The band at 328 nm is not visible because ε is very low. From these data the redox ratio has been calculated leading to $Ce^{4+}/Ce^{3+} \approx \frac{10}{90}$. The Figure 8.2 shows the spectrum of a sodium-silicate glass containing cerium [22] where it is possible to observe the strong dependence of the redox ratio Ce^{4+}/Ce^{3+} on both the oxygen partial pressure during melting (Figure 8.2(a)) and the glass composition (Figure 8.2(b)). By comparing Figure **??** and Figure 8.2, it is possible to confirm that cerium in glass-like Zr-Ce coatings is present in ionic state (Ce^{4+} and Ce^{3+}) similar to that observed in silicate and other glasses. This is, cerium is present as Ce^{4+} and Ce^{3+} with similar geometry coordinations that in glasses. In the conditions applied to produce these coatings, the redox equilibrium is clearly shifted to reducing conditions with more than 90% of Ce^{3+}. Thus, the diffusion of Ce^{3+} ions will be much easier and faster than that occurring in the case of crystalline CeO_2, like in conversion coatings or CeO_2 nanoparticles added to the coatings.

The sol characterization was followed by the evaluation of the ZrO_2 sol-gel coatings deposited on AA6060 aluminum alloy. Figure 8.4 shows the morphology of zirconia-based sol-gel coating deposited on pickled AA6060 substrate. The image was acquired by means of scanning electron microscopy. The coating system shown in Figure 8.4 is composed of three layers of zirconia (sample A) deposited by the dipping in a solution containing the metal-organic precursor without cerium nitrate. In the image, it is not possible to clearly recognize the deposited sol-gel film. Otherwise, it is possible to observe the morphology of the metal substrate due to the pickling procedure carried out prior deposition. The pickling procedure employed enables to remove the oxide layer and the intermetallic particles from the metal substrate. It is possible to recognize a selective attack at the grain boundaries (which are electrochemically more reactive than the center of

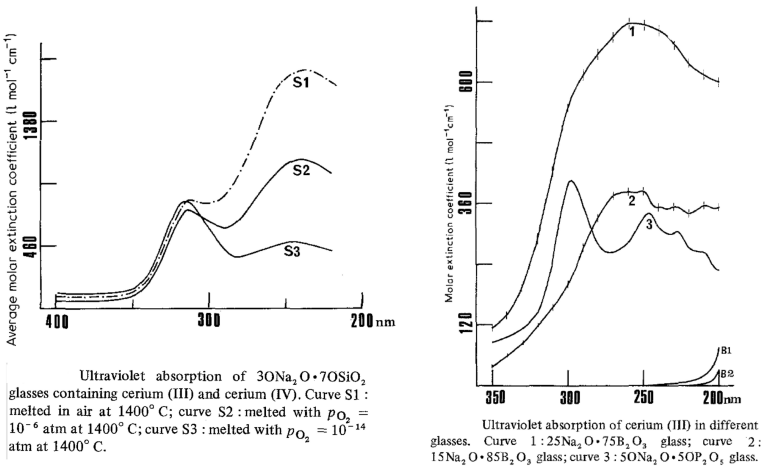

Ultraviolet absorption of $3ONa_2O \cdot 7OSiO_2$ glasses containing cerium (III) and cerium (IV). Curve S1 : melted in air at 1400° C; curve S2 : melted with $p_{O_2} = 10^{-6}$ atm at 1400° C; curve S3 : melted with $p_{O_2} = 10^{-14}$ atm at 1400° C.

Ultraviolet absorption of cerium (III) in different glasses. Curve 1 : $25Na_2O \cdot 75B_2O_3$ glass; curve 2 : $15Na_2O \cdot 85B_2O_3$ glass; curve 3 : $5ONa_2O \cdot 5OP_2O_5$ glass.

Figure 8.3: Cerium in glasses: a) at different condition of melting, b) with different composition glasses

the grains) producing a metallographic-like attack. The deep cavities are most probably generated by a localized attack due to presence of intermetallics. Since the zirconia-based sol-gel film deposited on the metal surface is very thin and defect-free, it is very difficult to recognize it on the pickled AA6060 surface. The morphology of sol-gel systems constituted by the combination between layers deposited from solutions containing cerium nitrate and layers without the inhibitor (sample B, sample C and sample D) appears very similar to that observed in Figure 8.4 for the sample A.

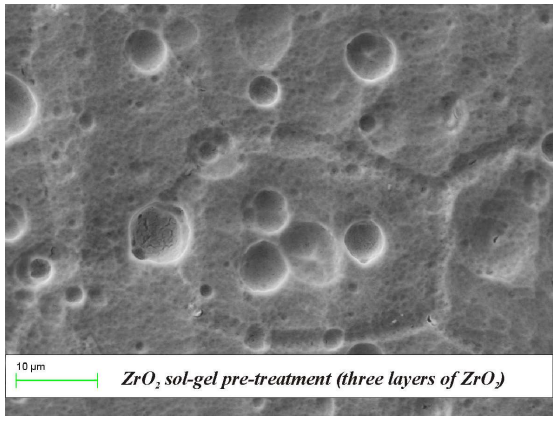

Figure 8.4: SEM micrograph for AA6060 coated with a ZrO2 sol-gel pre-treatment (three layers of ZrO2)

In order to evaluate the composition and the thickness of the coatings, chemi-

cal compositional profiles were acquired by means of glow discharge optical emission spectroscopy (GDOES). In particular, this technique was used to detect the profile of cerium contained in the inhibited system. Figure 8.5 shows the chemical composition profiles acquired by means of GDOES on coated systems listed in Table 8.1. Measurements were performed on coatings produced with 22 $cm\ min^{-1}$ withdrawal rate. The profile displayed in Figure 8.5(a) shows the composition in depth of the sol-gel coating non containing layers with cerium. In this profile, the signals of zirconium, oxygen, carbon and aluminum are visible. It can be observed that a not negligible amount of carbon was acquired. This is probably due to a fraction of organic compounds not eliminated during the thermal treatment. Indeed, the temperature of the drying step was 250 $°C$ which was probably not enough to allow the complete elimination of the organic fraction contained in the sol. Zirconium and oxygen signals are related to the presence of the ZrO_2 based coating which was not clearly visible in Figure 8.4. The thickness of the coating can be approximately evaluated where the aluminium signal tends to rapidly increase and zirconium signal starts to decrease. According with this procedure, the thickness of sample A can be identified in the range of 120 nm. Figure 8.5(b) shows the profile of the sol-gel system composed of two doped inner layers and a top layer without cerium. In this case, the cerium signal was also detected in addition to carbon, zirconium, oxygen and aluminium. The profile suggests that cerium is localized in the region at the interface with the metal substrate confirming that the top layer deposited using a cerium-free solution contains only zirconium, oxygen and carbon. The thickness of the sample B, is in the range of 160 nm which is 40 nm thicker than that of sample A. This is due to the different viscosity of the sols. Since the viscosity of the solution containing cerium is higher than the one non containing cerium, the inhibited layers are usually thicker than those produced without the inhibitor. Figure 8.5(c) shows the compositional profile for the sol-gel system with the intermediate layer containing cerium (sample C). It is possible to recognize a smaller cerium amount compared to that acquired for sample B which is instead composed of two inhibited layers. The thickness of sample C can be evaluated in the range of 140 nm which is lower than that measured for sample B while it is higher than the one evaluated for the sample A. These results confirm that systems containing inhibited layers are thicker than those non containing cerium. By comparing cerium profiles acquired, it is possible to evidence that the maximum of the cerium amount is localized in the

middle of the coating for the sample C while it is shifted towards the substrate for the sample B. As expected, in the sample B the cerium amount is located more close to the metal surface with respect to the sample C. Since inhibition mechanisms related to cerium ions depend on the diffusion path of cerium ions, the inhibition phenomenon should be more effective for the sample B rather than for the sample C. Figure 8.5(d) shows the compositional profile obtained on the sol-gel system with the same structure of the sample B but subjected to a longer thermal treatment (as listed in Table 8.1). It is possible to compare the profiles of the two systems evidencing that in the case of the system treated for a longer time (Figure 8.5(d)) the intensity of the zirconium signal starts to decrease at erosion depths lower than those observed for the system of Figure 8.5(b). The longer heat treatment employed enables to shrink the sol-gel structure reducing the coating thickness to about 60 nm. The thickness was therefore reduced more than 60% indicating that a significant amount of organic fraction is still contained into the coating subjected to the shorter thermal treatment.

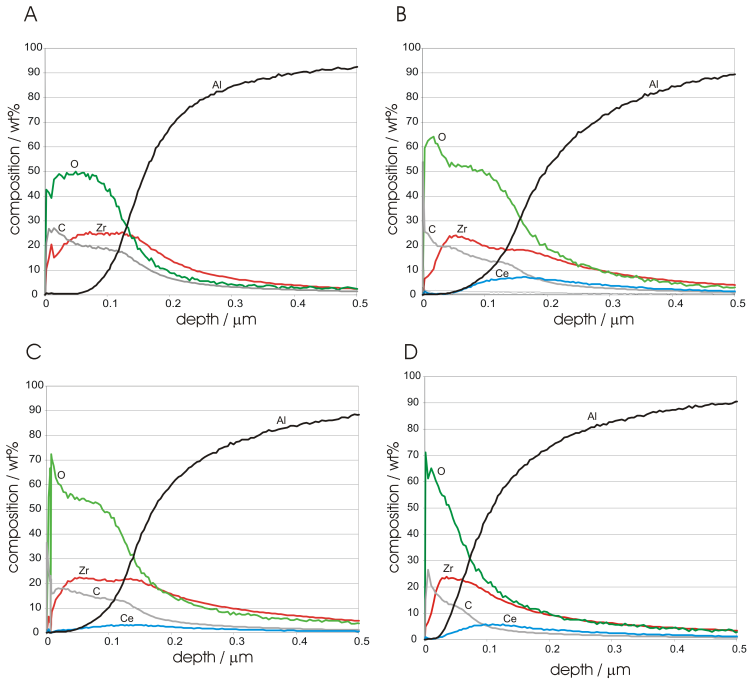

Figure 8.5: GDOES composition profile for AA6060 coated with a sol-gel pre-treatment composed of three layers of ZrO2 (A), two layers of ZrO2-Ce and a top layer of ZrO2 (B),two layers of ZrO2 and an intermediate layer of ZrO2-Ce (C) and two layers of ZrO2-Ce and a top layer of ZrO2 with a long thermal treatment (D)

Table 8.2 shows the film thickness of sol-gel systems produced by dipping with two different withdrawal rate: 5 $cm\ min^{-1}$ and 22 $cm\ min^{-1}$ (sample A, sample B, sample C). In the Table 8.2 is also reported the thickness of the sol-gel system containing two doped cerium layer treated at 250 °C for a longer time (sample D). In the Table is possible to observe that the film thickness increases as the number of doped layers increases. An higher sol viscosity (i.e. sol doped with cerium) strongly affects the thickness of sol-gel multi-layer systems. By considering a withdraw rate of 5 $cm\ min^{-1}$, the sample B, which consists of two layers containing cerium and the undoped top layer, is two times thicker than the undoped system (A). Moreover, it is possible to observe in Table 8.2 that there is a strong influence of the withdraw rate on the sol-gel thickness. The sample A produced with a withdrawal rate of 22 $cm\ min^{-1}$ is two times thicker than the same sample system produced with a withdrawal rate of 5 $cm\ min^{-1}$. This is due to the inertia related to the withdrawal of the aluminum sheet. The faster the withdraw rate is, the higher the sol-gel thickness is. For withdraw rates commonly used for the sol-gel deposition by dipping, shear stresses are directly dependent on the derivate of the withdraw rate. For this reason, sols can be considered a Newtonian fluids. In these conditions, the sol-gel thickness deposited by dip-coating technique can be approximately calculated by the $Landau-Levich$ equation 8.3, which considers also important parameters the sol viscosity, the force of gravity and the withdrawal angle [23, 24].

$$d = 0.94 \cdot (\frac{\eta \cdot v}{\gamma_{lv}})^{1/6} (\frac{\eta \cdot U}{\rho \cdot g})^{1/2} \tag{8.3}$$

where, d is the thickness, η is the sol viscosity, v the withdraw rate, ρ the sol density, γ_{lv} the surface tension and g the force of gravity. However, the withdraw rate is one of the most influent parameters on the sol-gel process. The maximum thickness which is possible to deposit by means of sol-gel processes is basically limited by the defect formation. Cracking phenomena is more probable to occur in thick coatings where the sol-gel system shrinkage, due to the solvent evaporation, is more critical. It was found that zirconia based coatings with thickness higher than 200 nm are widely defected [25]. It was further found that on sol-gel coatings ticker than 300 nm, delamination and cracking can occur together [25]. In order to minimize these drawbacks, in this work the deposition of the inhibited system was carried out limiting both the withdraw rate (22 $cm\ min^{-1}$) and the concentration

of the inhibitor ($\frac{[Zr]}{[Ce]} = \frac{[70]}{[30]}$). In this way, sol-gel multi-layer structures with a total thickness lower than 200 nm were produced, as already confirmed by GD-OES profiles shown in Figure 8.5.

System type	**Withdraw rate [cm/min]**	**Thickness [nm]**
Zr-Zr-Zr (A)	5	60
	22	120
Zr-ZrCe-ZrCe (B)	5	110
	22	160
Zr-ZrCe-Zr (C)	5	80
	22	130
Zr-ZrCe-ZrCe (D)	22	70

Table 8.2: AA6060 sol-gel film thickness

The thickness of sol-gel systems can give only a rough information about their corrosion behaviour because it does not take into account local defects and/or the physical barrier properties. It is possible that thick sol-gel coatings can be not as protective as thin systems. S.E.M. analysis showed that all the sol-gel coatings deposited on AA6060 (Table 8.1) are homogeneous and defects are seldom observed. In order to evaluate how the withdraw rate affects the sol-gel barrier property, potentiodynamic polarization curves were performed on systems produced with different withdraw rates. Figure 8.6 shows the potentiodynamic polarization curves in diluted Harrison solution for the undoped zirconia sol-gel system produced with 5 $cm\ min^{-1}$ (solid line) and 22 $cm\ min^{-1}$ (dash line). The potentiodynamic polarization curve for bare AA6060 is also reported as reference. By comparing the electrochemical behaviour of sol-gel coatings produced with 5 $cm\ min^{-1}$ withdraw rate with that of the bare AA6060, it is possible to point out that the sol-gel coating is able to reduce the corrosion current density more than one order of magnitude. For the system produced with 5 $cm\ min^{-1}$ withdraw rate, the anodic current densities are shifted to lower values with respect to the bare AA6060. Moreover, a passive behaviour (50 mV wide) is exhibited by the sol-gel system produced by using 5 $cm\ min^{-1}$ withdraw rate. The protection provided by this system is however not good because of the coating thickness is very limited (as seen in Table 8.2). The electrochemical behaviour of undoped sol-gel coatings produced by dipping with 22 $cm\ min^{-1}$ withdraw rate is better

than that of the sol-gel coatings produced with lower withdraw rate (Figure 8.6). The corrosion protection guaranteed by thick sol-gel coatings is due to the higher amount of sol deposited on the metal substrate which subsequently is dried to form the protective coating. By considering the sol-gel coating as the insulating material of parallel plate capacitors, it is possible to estimate the influence of the sol-gel thickness on the barrier properties provided. The equation correlating physical and electrical properties of parallel plate capacitors shows that the insulating ability is directly proportional to the coating thickness (eq. 8.4):

$$C_{coat} = \frac{\varepsilon_0 \varepsilon_r \Sigma}{d} \tag{8.4}$$

where C_{coat} is the sol-gel coating capacitance, ε_0 is the vacuum permittivity, ε_r is the relative permittivity, Σ is the capacitor plate area and d is the sol-gel thickness. The equation 8.4 indicates that the lower the sol-gel coating capacitance is, the higher the insulating ability is. Therefore, thicker sol-gel systems are able to provide better insulating properties against the attack of aggressive species.

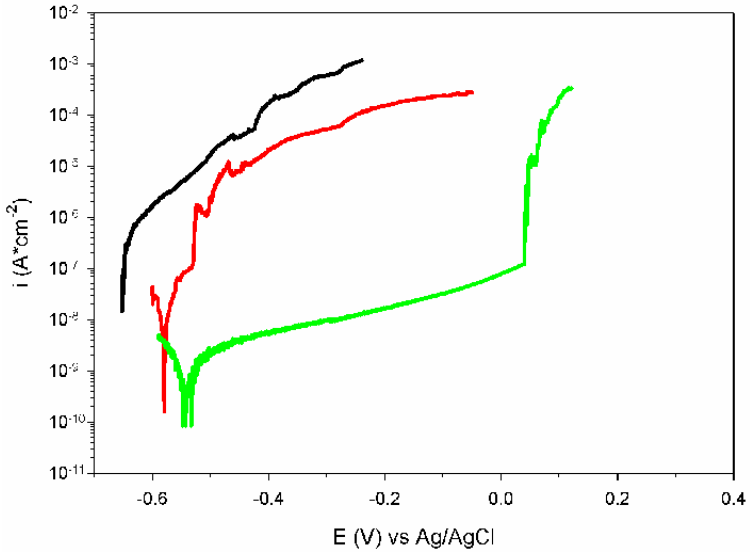

Figure 8.6: Influence on corrosion behaviour of withdraw rate

Figure 8.7 shows the potentiodynamic polarization curves in diluted Harrison solution for the sol-gel systems of Table 8.1 produced with 22 $cm\ min^{-1}$ withdraw rate. The potentiodynamic polarization curve for bare AA6060 is also reported

as reference. The barrier property provided by the sol-gel coatings is strongly influenced by the number of layers deposited with the solution containing cerium. Sample A (consisting of three layers without cerium) evidences a corrosion current density almost 3 order of magnitude lower than that observed for bare AA6060. It also displays a wide passive region ranging from the corrosion potential to 0V as Ag/AgCl. Sample C (one intermediate layer containing cerium) evidences lower barrier properties than those evidenced by sample A. Hence, the corrosion current density is higher than that for sample A. In addition, the passive current densities displayed by sample C are higher than those shown by sample A. In the case of sample C, the breakdown potential can be localized 100mV more negative than that observed for sample A. Furthermore, the barrier property evidenced by sample B (2 layers containing cerium and one top layer without cerium) is lower than that exhibited by sample C. The barrier property of the sol-gel systems is strongly influenced by the number of the inhibited layers. For the inhibited systems, the network developed during the heat treatment is most probably influenced by the presence of cerium ions which does not allow the formation of a dense cross-linked structure able to protect the metal substrate. In order to improve the cross-linking, sample D underwent thermal treatment for an extended time (see Table 8.1). A longer thermal treatment enables to obtain a more dense structure because the further elimination of organic compounds allows the formation of a more compact structure. Sample D evidences a better electrochemical behaviour than the one observed for the same system treated at 250 $^{\circ}C$ for a shorter time (sample B). Although sample D consists of 2 layers containing cerium and a top layer without cerium, its barrier properties are better than those evidenced by sample C which contains only one layer with cerium. The improvement of the barrier properties related to the densification of the sol-gel coating is therefore due to the formation of a more dense sol-gel structure.

Figure 8.8 shows the Nyquist plot representation of the electrochemical impedance measurements carried out in diluted Harrison solution on the undoped sol-gel system (sample A). During the first 7 hours of immersion, the evolution described by the spectra evidences that the barrier property tends to be reduced as a function of the immersion time. After 7 hours of immersion, the shape of the impedance spectrum is quite different if compared to the one related to the spectrum acquired immediately after immersion. For longer immersion time, the electrochemical behaviour is further modified. After 23 hours of immersion, the barrier property of

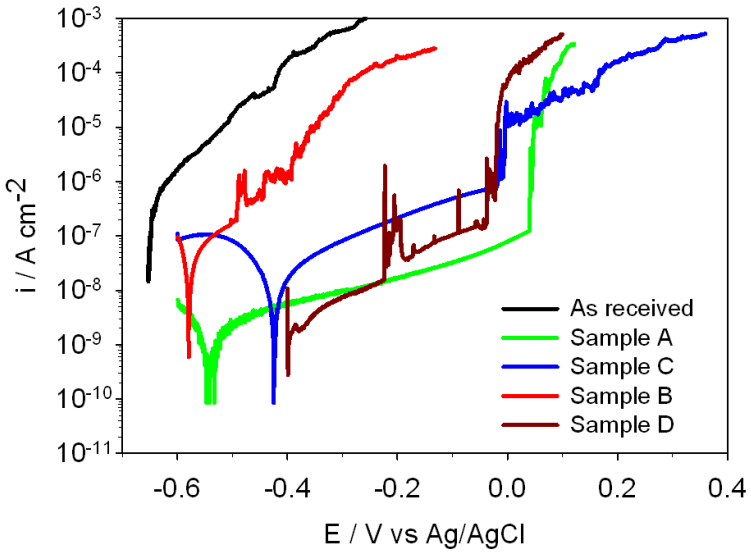

Figure 8.7: Potentiodynamic polarization curves in diluted Harrison solution for AA6060 coated with three layers of ZrO2, with two layers of ZrO2 and a layer of ZrO2 containing Ce (intermediate layer) and with two layers of ZrO2 containing Ce and a layer of ZrO2 (outermost layer). The potentiodynamic polarization curve for as received AA6060 is also reported in the figure.

the undoped coating is strongly reduced. By comparing the Nyquist plot acquired immediately after immersion and the one detected after 47 hours, is it possible to observe that the real part of the impedance (X-axis) at low frequency is strongly reduced. Since the real part of the impedance can be considered equal to the resistance correlated to the Faradic processes, its strong reduction suggests that corrosion processes occur at the metal substrate. Therefore, impedance measurements carried out on sol-gel systems without layers containing cerium evidence a gradual deterioration of the coating properties due to the progressive loss of the initial barrier.

Figure 8.9 shows the Nyquist plot representation of the electrochemical impedance measurements carried out in diluted Harrison solution on the sol-gel system composed of two layers with cerium and one top layer without cerium (sample D). In the first hours of immersion, the coating displays a gradual degradation due to water diffusion, as seen for sample A. The impedance data acquired immediately after immersion (0h) exhibits lower barrier property if compared to that evidenced by sample A. Immediately after immersion, sample D is not able to

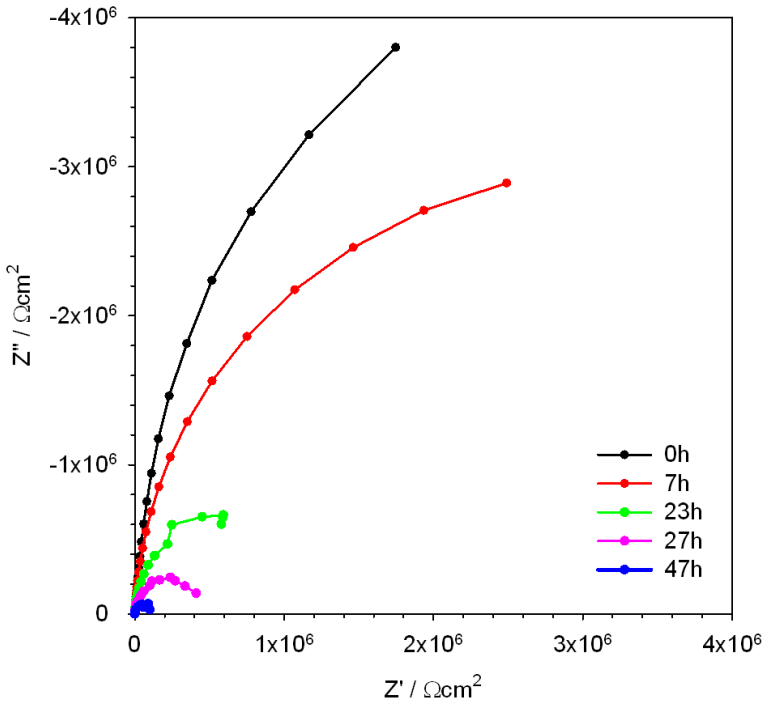

Figure 8.8: Nyquist plot of electrochemical impedance measured in diluted Harrison solution for AA6060 coated with three layers of ZrO2

guarantee the same protection of sample A, as it has been already shown by the polarization curves. After 2 hours of immersion, the impedance spectrum for sample D is very similar to that detected after 47 hours of immersion on sample A. The following measurements carried out on sample D evidence a different evolution. After 3 hours, the impedance modulus tends to increase rather than to decrease. Moreover, after 9 hours of immersion, the shape of the impedance spectrum is similar to that of the spectrum acquired immediately after immersion (0h). The corrosion resistance tends to be improved as a function of immersion time. The maximum of the impedance modulus is reached after 47 hours of immersion. This behaviour can be associated to the interaction between the metal substrate and cerium ions contained in the coating. The improvement of the corrosion behaviour of the system D can occur because cerium ions diffuse towards the metal substrate. The inhibition provided by cerium species can be supported by the comparison between the electrochemical impedance behaviour of the inhibited (D) and the non-inhibited samples (A). No recovery of the electrochemical

behaviour has been seen for the system without cerium which is in contrast with the trend observed for the inhibited system.

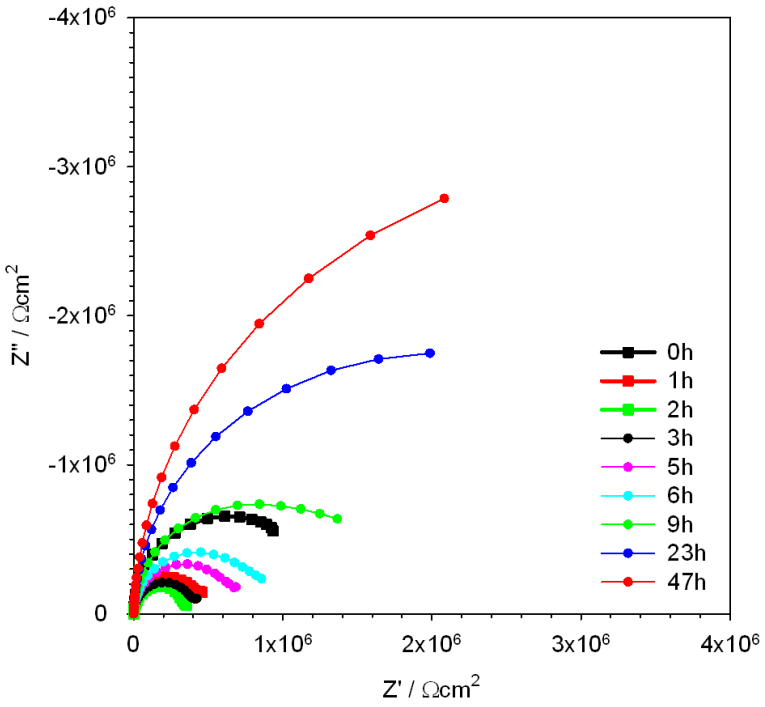

Figure 8.9: Nyquist plot of electrochemical impedance measured in diluted Harrison solution for AA6060 coated with two layers of ZrO2 containing Ce and a layer of ZrO2 (outermost layer).

The evaluation of the electrochemical behaviour of the inhibited and the non inhibited systems can be studied thoroughly by fitting EIS data. As already explained in Chapter 2, EIS data can be fitted using an equivalent electric model associated to the corroding system. The sol-gel coatings investigated in the present chapter was modeled with an equivalent circuit consisting of two RC meshes. In the equivalent circuit employed, the constant phase element (CPE) was used instead of an ideal capacitor to explain the deviations from the ideal behaviour. The circuit used is shown in Figure 8.10 where R_{sol} is the solution resistance, R_{coat} is the sol-gel coating resistance, R_{ct} is the charge transfer resistance, C_{coat} is the sol-gel coating capacitance and C_{dl} is the double layer capacitance.

Figure 8.11 reports the trends of the sol-gel coating resistance (R_{coat}), for the inhibited (sample D) and the non-inhibited (sample A) systems as a function of

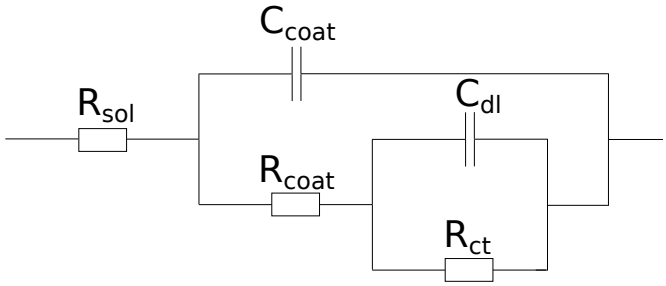

Figure 8.10: Equivalent circuit employed for data fitting.

immersion time. Immediately after immersion, for the inhibited and the non-inhibited systems, the R_{coat} does not take on the same value. The R_{coat} is higher for the inhibited system because it is thicker and denser than the non-inhibited one. After the first hours, for the non-inhibited system, the R_{coat} trend exhibits a fast decrease which is probably related to the progressive water diffusion into the coating. The R_{coat} trend for the inhibited system shows instead a uniform behaviour. Indeed, the initial value is held constantly for the entire test. This value is equal to the one observed for the non-inhibited system after 1 day. From these results, it might be possible to hypnotize that the inhibited sol-gel system is not able to provide an effective physical barrier. This was expected because the inhibited sol-gel coatings are not as denser as the non-inhibited ones. Dense sol-gel structures are required to provide good barrier properties but are not required for the development of porous systems where embedded chemical species have to be able to diffuse. This is exactly our case because the target of the work was to develop a thin ceramic layer as a primer providing self-healing ability.

The cerium inhibition effect on the corrosion behaviour of AA6060 can be therefore evaluated by considering the charge transfer resistance trends shown in Figure 8.12. Immediately after immersion, the non-inhibited system shows a R_{ct} which is almost 10 times higher than that exhibited by the inhibited sol-gel coating. Since the corrosion rate of AA6060 aluminum alloy is the same for both, in the case of the doped system, the area exposed to the electrolyte is 10 times larger. This is due to the addition of cerium to the initial sol which does not allow the formation of a linked sol-gel structure. The higher porosity of doped systems is also evidenced by the R_{coat} trend (Figure 8.11) which shows lower barrier properties for the inhibited coating. For longer immersion time, the trends of the charge transfer resistance R_{ct} are substantially different. In the case of the non-inhibited

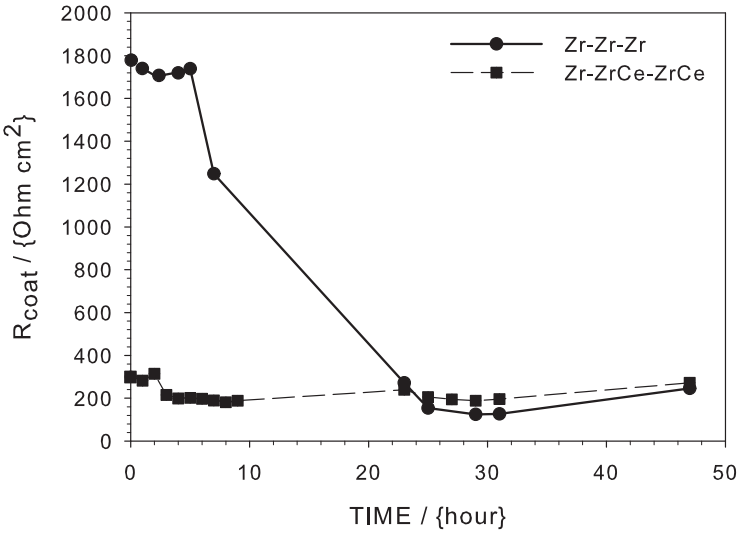

Figure 8.11: R_{coat} for the inhibited and the non-inhibited systems as a function of immersion time

system, the R_{ct} continuously tends to decrease due to the progressive increase of the substrate areas involving in the corrosion processes. After 2 days of immersion, the R_{ct} is very close to that of bare AA6060 aluminum alloy shown in our previous works [26]. The behaviour exhibited by the inhibited system follows a different evolution. Immediately after immersion, the R_{ct} values are very similar to that estimated for the non-inhibited system after 2 days. For longer immersion time, the R_{ct} starts to decrease down to a minimum corresponding to the impedance spectrum acquired after 2 hours (Figure 8.9). From this point, R_{ct} starts to increase exceeding, after 20 hours immersion, the R_{ct} value of the non-inhibited system. In correspondence with this point, the corrosion rates for the inhibited and the non-inhibited systems can be considered identical. For longer immersion time, the R_{ct} of the inhibited system continues to increase reaching $6 \cdot 10^6\ \Omega\ cm^2$ after 48 hours. This value is 3 times higher than the one estimated immediately after immersion. The improvement in the corrosion behaviour of AA6060 aluminum alloy depicted by the R_{ct} trend, can be likely related to the diffusion of cerium-free ions towards the substrate. Once cerium ions reach the metal, the corrosion inhibition is due to the cerium precipitation following the mechanisms proposed in Chapter 6 and Chapter 7. As it can be seen in Figure 8.12, the full additional protection related to cerium precipitation needs several

hours to occur due to the fact that the cerium diffusion is slow. The diffusion rate of cerium ions depends on the compactness of the sol-gel structure. Dense ZrO_2 sol-gel coatings developed in this work, did not show the increase of R_{ct} probably because a compact sol-gel structure hindered the cerium diffusion. However, dense sol-gel coatings are able to provide better physical barrier against the diffusion of water and aggressive ions. The additional protection provided by cerium precipitation is limited by the amount of inhibitors embedded in the coating. Since cerium leaching occurs towards the test solution, a not negligible amount of cerium ions can not diffuse towards the metal substrate for the improvement of the AA6060 corrosion behaviour. The deposition of the primer and the top coat on the inhibited sol-gel coated aluminum alloys should be able to limit the leaching towards the solution test.

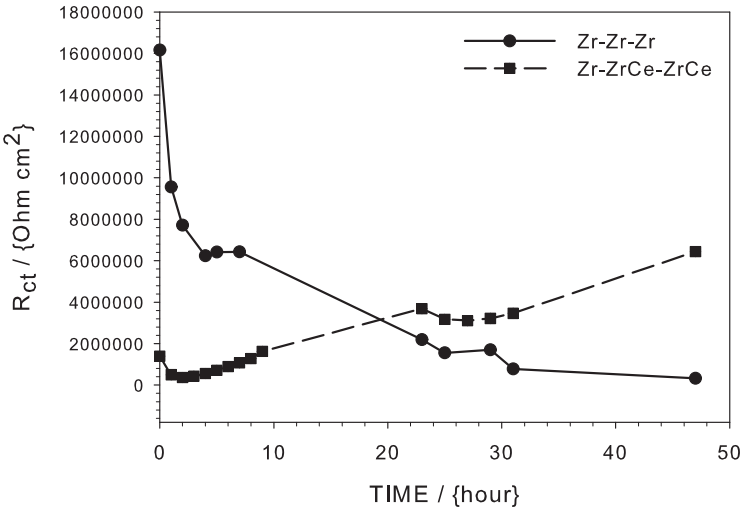

Figure 8.12: R_{ct} for the inhibited and the non-inhibited systems as a function of immersion time

8.4 Conclusions

Sol-gel coatings produced by dipping have been considered for the corrosion protection of aluminium alloy AA6060. ZrO_2 based sol-gel coatings were deposited from a solution containing metal-organic precursor of zirconium. In order to produce a protective system with self-healing ability, cerium nitrate was directly

added to the sol. Different coating systems were produced as the combination between layers deposited with solutions containing only the zirconium precursor and solutions in which cerium nitrate was added in addition to the zirconium precursor. Morphology of ZrO_2 coatings was investigated by means of SEM-EDXS. Film thickness and composition were studied by means of GDOES. Barrier properties were characterized by means of potentiodynamic polarization. The inhibition effect due to the interaction between cerium ions and the metal substrate was studied by means of the electrochemical impedance spectroscopy.

Sol-gel ZrO_2 based coatings deposited on AA6060 are uniform and defect-free. The film deposited appears colorless and covers the entire metal surface. Critical areas for the sol-gel deposition, like cavities produced by the pickling procedure, are also coated. The coating consisting of layers containing cerium shows a very similar surface morphology to that of the non-inhibited system. Since the addition of cerium nitrate to the starting solution increases the sol viscosity, the inhibited layers are thicker than the non-inhibited ones. The undoped systems display a strong barrier effect, as indicated by the passive behaviour of AA6060 aluminum alloy coated with three layers of ZrO_2. The barrier property associated to the sol-gel systems is strongly influenced by the inhibited layers. Inhibited systems are generally not able to guarantee the same protection evidenced by sol-gel systems without cerium. Electrochemical impedance measurements indicate that the gradual decrease of the corrosion behaviour of ZrO_2 coated aluminum alloys can be recovered only if cerium nitrate is added to the starting sol. The improvement of the corrosion behaviour of coated AA6060 is due to the beneficial action of cerium ions diffusing towards the metal substrate.

Bibliography

[1] T.L. Metroke, R.L. Parkhill, E.T. Knobbe, Progress in Organic Coatings, 41 (2001) 233

[2] R. Di Maggio, L. Fedrizzi, S. Rossi, Journal of Adhesion Science and Technology 15 (2001) 793

[3] M. Bethencourt, F.J. Botana, J.J. Calvino, M. Marcos, M.A. Rodriguez-Chacon, Corrosion Science 11 (1998) 1803

[4] J.H. Osborne, Progress in Organic Coatings 41 (2001) 280

[5] F. Andreatta, L. Paussa, P. Aldighieri, R. Di Maggio, L. Fedrizzi, Electrochemical behaviour of ZrO pre-treatments deposited with sol-gel technique on AA2
Proceedings EUROCORR 2007

[6] F. Andreatta, L. Paussa, P. Aldighieri, A. Lanzutti, D. Ondratschek, L. Fedrizzi, Surface and Interface Analysis 42 (2010) 293

[7] L. Fedrizzi, R. Di Maggio, S. Rossi, L. Leonardelli, Benelux Metallurgie 43 (2003) 15

[8] F. Andreatta, P. Aldighieri, L. Paussa, R. Di Maggio, S. Rossi, L. Fedrizzi, Electrochim. Acta 52 (2007) 7545

[9] B.R.W. Hinton, D.R. Arnott, N.E. Ryan, Metals Forum 7 (1984) 211

[10] B.R.W. Hinton, D.R. Arnott, N.E. Ryan, Materials Forum 9 (1986) 162

[11] R. Arnott, B.R.W. Hinton, N.E. Ryan, Corrosion 45 (1989) 12

[12] D.R. Arnott, B.R.W. Hinton, N.E. Ryan, Materials Performance 42 (1987) 47

[13] D.R. Arnott, N.E. Ryan, B.R.W. Hinton, B.A. Sexton, A.E. Hughes, Applied Surface Science 22 (1985) 236

[14] S. You, P. Jones, A. Padwal, P. Yu, M. O-Keefe, W. Fahrenholtz, T. O-Keefe, Materials Letters 61 (2007) 3778

[15] L.E.M. Palomino, I.V. Aoki, H.G. de Melo, Electrochimica Acta 51 (2006) 5943

[16] B.Y. Johnson, J. Edington, A. Williams, M.J. O-Keefe, Materials Characterization 54 (2005) 41

[17] A. de Frutos, M.A. Arenas, Y. Liu, P. Skeldon, G.E. Thompson, J. de Damborenea, A. Conde, Surface & Coatings Technology 202 (2008) 3797

[18] A. Decroly, J.P. Petitjean, Surface & Coatings Technology 194 (2005) 1

[19] A. E. Hughes, J. D. Gorman, P. R. Miller, B. A. Sexton, P. J. K. Paterson, R. J. Taylor, Surface & Interface Analysis 36 (2004) 290

[20] N.C. Rosero-Navarro, S.A. Pellice, A. Duran, M. Aparicio, Corrosion Science 50 (2008) 1283

[21] L. Paussa, N. C. Rosero-Navarro, F. Andreatta, Y. Castro, A. Duran, M. Aparicio, L. Fedrizzi, Surface & Interface Analysis 42 (2010) 299

[22] A. Paul, M. Mulholland, M. Zaman, Journal of Materials Science 11 (1976) 2082

[23] P. Aldighieri, Master Thesis University of Trento, 2004

[24] F. Girardi, Master Thesis University of Trento, 2004

[25] A. Mehner, W. Datchary, N. Bleil, H.W. Zoch, M.J. Klopfstein, D.A. Lucca, Journal of Sol-Gel Science and Technology 36 (2005) 25

[26] F. Andreatta, P. Aldighieri, L. Paussa, R. Di Maggio, S. Rossi, L. Fedrizzi, Electrochimica Acta 52 (2007) 7545

Chapter 9

Critical aspects in the electrochemical study of unstable coated metallic substrates

Electrochemical methods are largely employed for the study of coated metallic substrates. Electrochemical techniques are very useful for investigation of coating performances also in the field of corrosion protection of aluminum alloys where replacement of chromate based coatings is an important issue. Application of sol-gel technique has recently made available thin inorganic protective coatings that can be considered as an alternative to chromate systems. Therefore, it is important to evaluate the electrochemical behaviour of defect free inorganic films which can be considered an inert material. As a consequence, investigation of this inert material might generate critical aspects related to rapid fluctuations of its open circuit potential and current density during open circuit potential and potentiodynamic polarization measurements. Moreover, the unstable nature of the sol-gel very thin films is a critical issue also in electrochemical impedance measurements carried out under potential control because variation of the open circuit potential of the system during data acquisition might lead to sample damage. Impedance measurements under current control is an alternative method for data acquisition. This technique is considered in the present chapter for the investigation of AA2024 substrate coated with a thin sol-gel layer and for chromate conversion coated alloy.

9.1 Introduction

Aluminum alloys like AA2024 are widely employed in aerospace industry for the favourable weight/mechanical properties ratio. By alloying aluminum with other metals, physical and chemical properties are changed and mechanical properties can be improved [1]. The alloys of the 2xxx series undergo thermal treatments in order to precipitate hardening particles in the matrix. The hardening mechanism is related to alloying elements like copper and magnesium. However, alloying with copper and magnesium in combination with existence of intermetallics containing iron and silicon render AA2024 susceptible to localized corrosion [2, 3, 4]. In order to improve AA2024 corrosion behaviour it is necessary to protect this alloy with a coating. Nowadays, the protective system employed in aerospace industry consists of three different layers: the inner layer is deposited on the metallic substrate using a chemical conversion process or by anodizing. The intermediate layer is essentially an organic primer containing corrosion inhibitors and other compounds. The outer one is an organic topcoat. A conversion coating should provide three different properties: first of all, it should promote adhesion between the metallic substrate and organic coating. Moreover, the conversion layers should provide good barrier properties and possibly self-healing ability. Chromate based coatings are extensively employed in the aircraft industry because they guarantee a good combination of properties. The self-healing ability is due to the presence of a residual amount of Cr^{6+} in the conversion coating that is able to repair the oxide layer in case of damage. Unfortunately, conversion coatings containing Cr^{6+} are dangerous and not environmental friendly [5, 6, 7]. Therefore, industrial processes involving Cr^{6+} species are restricted for aircraft applications. Development of alternative technologies and chemical conversion processes is one of the most interesting topics in research about aluminum protection in order to replace chromium based systems. Different methods like plasma deposition, anodizing or sol-gel synthesis have been employed to produce alternative systems to chromate based conversion coatings [8, 9, 10]. In particular, sol-gel technology enables to obtain inorganic systems or hybrid inorganic-organic systems at low temperature [11, 12, 13, 14, 15]. In some cases, it is possible to produce thin homogeneous inorganic films for long time protection of metallic substrate by controlling deposition parameters and curing temperature for the densification of the sol-gel layer [16]. Electrochemical characterization of thin inorganic films deposited by sol-gel

technique is often problematic due to difficulty to reach a steady state condition. Moreover, properties of these systems are strongly dependent on deposition parameters. Therefore, surface reactivity of these systems might be affected by film defects, loss of adhesion and possible formation of nano-cracks during immersion in an aggressive solution [17, 18]. Electrochemical studies of corrosion behaviour of thin inorganic sol-gel films can employ two different methods: DC and AC techniques. Among AC techniques, electrochemical impedance spectroscopy (EIS) enables to obtain information about corrosion behaviour of the system investigated as a function of immersion time [19]. Moreover, it is necessary to validate impedance data in order to obtain reliable information. This can be done if the electrochemical system verifies three fundamental conditions: causality, linearity and stability [19]. The condition of causality imposes that system response must only be due to the input perturbation signal and noise. Moreover, the response must not contain signal components deriving from spurious source. The condition of linearity requires that the input perturbation and the output response must be described by a set of linear differential laws. This condition implies that the impedance, which represents the transfer function of the system, must be independent from the amplitude of the input signal perturbation. The condition of stability imposes that the system must return to its original condition when the input perturbation is removed. The three fundamental conditions mentioned above imply that a number of boundary requirements must be also satisfied. If the angular frequency ω tends to zero or to infinite, the impedance measured must be finite-valued. Finally, the impedance spectrum must be a continuous function in the range between $\omega = 0$ and $\omega = infinite$; that is, impedance spectrum does not contain singularity over all frequency range [19]. Many mathematical methods have been developed to verify the fundamental conditions for impedance spectra obtained experimentally, like Kramers-Kronig relations [19]. Orazem et al. suggested the use of these relations in order to verify the validity of impedance spectra carried out by means of stepped sine excitation [20, 21, 22]. An alternative approach for the validation has been proposed by Popkirov and Schindler [22, 23, 24, 25]. If an electrochemical system does not satisfy one of the fundamental conditions, impedance spectra are necessarily altered because the output response does not represent the real situation. Although a lot of electrochemical systems are not linear, EIS measurements can be equally performed applying an input perturbation of small amplitude. Indeed, the behaviour of an electrochem-

ical system can be approximated to a quasi-linear system reducing the amplitude of input perturbation. Theoretically, the amplitude of input perturbation should tend to zero in order to improve the approximation for a non-linear system. At the same time, the output signal/noise ratio leads to poor measurement accuracy when the input signal amplitude amplitude is too small [25]. Urquidi-Macdonald et al. have demonstrated that impedance spectra performed on corroding iron electrode in 1M H_2SO_4 with an amplitude of perturbation in the range from 5mV to 150mV lead to very different responses [26]. The quasilinear behaviour of this system becomes non-linear when a large amplitude perturbation is applied. As a consequence, different impedance spectra are detected with respect to the non-linear condition. Impedance spectra can be recorded for the electrochemical studies in the frequency and in the time domain. The frequency domain method is based on a voltage or current sinusoidal perturbation applied to the sample. The input signal is separately applied for each frequency. In this method, each impedance value is calculated at the end of every perturbation step [27, 28]. The time domain method (also known as white noise method) is based on Fast Fourier Transform (FTT). In this last case, a frequency-rich perturbation signal is applied on the sample at the same instant time [25, 29, 30, 31, 32]. Experimental activities described in this work have been developed in order to find an instrumentation set-up which is able to assure reliable and reproducible impedance results. Impedance measurements were performed with the frequency domain method (FRA) on a very complex electrochemical system. This system consist of a very thin ZrO_2 sol-gel film deposited on a reactive substrate like AA2024. The combination between an homogenous ceramic thin film and a reactive substrate constitutes a system which exhibits transient open circuit potential during impedance measurements. In particular, this chapter focuses on experimental aspects associated to the test conditions and to critical system features in order to improve accuracy of impedance measurements. It assesses the possibility of acquiring reliable electrochemical information using current control method on not completely stationary systems, which are usual studying corroding metals. The work is not focused on checking system linearity or system causality both under voltage control and under current control. Nevertheless, there is a common procedure to perform impedance measurements under voltage control to avoid linearity loss. Impedance measurements carried out under voltage control on conversion coatings are usually performed applying a perturbation with

10 mV amplitude which it is normally considered small enough to keep the system response in the linear behaviour. Considering the impedance measurements performed under current control in this work, the amplitude of the currents set in the experimental procedure has been chosen as the lowest values providing a reliable response possibly within a linear behaviour. However, the investigation does not propose a check validation of the impedance data but it considers an alternative method to acquire reliable impedance data when not stable systems are considered.

9.2 Experimental

AA2024-T3 was employed as substrate for deposition of ZrO_2 based film. Chemical conversion coatings and pre-treatments used to improve corrosion behaviour of metals require surface preparation of materials. Before deposition of sol-gel film, AA2024 sample underwent surface preparation consisting in an alkaline cleaning, an alkaline etching and an acid etching. ZrO_2 sol-gel films were deposited on AA2024 employing a water-based solution containing the precursor of the metal oxide. The solution used to produce inorganic films was 0.4M $ZrO(NO_3)_2$ in water. Film deposition was carried out by means of spraying technique controlling parameters like air pressure gun, distance between gun and sample and general set-up of the robot. Optimization of the spraying process enables to obtain very homogeneous ZrO_2 thin films, with limited crack formation and with good adhesion properties on AA2024. These films are nearly crack-free and exhibit very good adhesion to the substrate [33]. Procedure of sample preparation, optimization of deposition parameters and a film characterization are described in detail in the other chapters of the thesis. In addition chromate conversion coated AA2024 was also investigated as a reference. Corrosion behaviour of sol-gel ZrO_2 film deposited on AA2024 was investigated by means of different electrochemical techniques employing an AUTOLAB PG-STAT 30. DC and AC methods were employed for the analysis. In order to study the stability of the system, open circuit potential (OCP) was measured as a function of immersion time in an aggressive electrolyte. Barrier properties of ZrO_2 films were evaluated by means of potentiodynamic polarization. Potentiodynamic polarization measurements performed immediately after immersion in the electrolyte provide only limited information about the physical barrier associated to the pre-treatment. In order to check the

evolution of the barrier properties of the systems investigated in this work as a function of immersion time, electrochemical impedance spectroscopy technique (EIS) was employed. Moreover, it is possible to quantify adhesion properties, barrier properties and self-healing ability associated to any electrochemical system employing an electrical model correlated to the system investigated. Therefore, EIS technique provides very useful information about corrosion behaviour of electrochemical systems. DC and AC electrochemical measurements were performed in a solution containing 0.05M NaCl using a standard three electrode configuration (working, reference and counter electrode). The working electrode area was 3.6 cm^2. Ag/AgCl electrode was employed as reference and a platinum wire constituted the counter electrode. Open circuit potential was recorded for 15 h. Potentiodynamic polarization measurements were performed with a scan rate of 0.2 $mV\ s^{-1}$ starting at -100mV relative to OCP. EIS measurements were performed with two different approaches consisting of a voltage and a current method. With the first method the input perturbation of 10mV was applied at OCP and frequency range from 100mHz to 100 kHz while with the second one the input signal was applied at the zero current condition. The AUTOLAB PG-STAT 30 potentiostat/galvanostat equipped with FRA software version 4.9 and available in our laboratory does not enable to carry out impedance measurements under current control with an auto-setting configuration but a detailed experimental procedure has to be employed. The experimental procedure used to perform measurements under current control is carefully described and discussed in the following part of the chapter. The morphology of the pre-treatments was investigated by means of scanning electron microscopy (SEM) in order to provide information about the sample surface after deposition.

9.3 Results

Before considering electrochemical measurements carried out on AA2024 coated with sol-gel ZrO_2 thin film, it is important to consider some aspects related to the three fundamental conditions described in Chapter 2 for an electrochemical system. It can be assumed that the systems investigated in this work satisfy the conditions of linearity and causality. Therefore, the stability of the system is the only condition that can invalidate impedance spectra. A system is considered stable when stationary conditions are retained for the open circuit potential during

the time necessary for the acquisition of the impedance spectrum. In this work, an attempt is made to compare impedance measurements performed on a stable system with those on an unstable system. It is clear that non-stationary systems do not satisfy the stability requirement. Therefore, it might seem that it is not possible to perform impedance measurements on systems that are unstable. An alternative instrumental set-up approach to EIS measurements is considered in order to obtain helpful impedance results also in the case of systems that are not stationary during data acquisition. It is well known in literature [34], that chromate conversion coatings are auto-repair systems. Chromate based coatings can be considered stable systems because Cr^{6+} compounds in the layer can restore barrier properties after mild corrosion attack. Moreover, chromate based coatings can improve the barrier properties with the self-healing mechanism. Therefore, after an initial transient due to a passivation of the substrate, chromate conversion coatings provide continuous active protection when immersed in the electrolyte. The initial transient can be seen in Figure 9.1, which shows the open circuit potential for chromate conversion coating deposited on AA2024 in 0.05MNaCl (- - - short dash). Immediately after immersion in the electrolyte the OCP value exhibit a transient between -500mV and -440 mV vs. Ag/AgCl. This behaviour is most likely associated to auto-repair mechanism due to Cr^{6+} species leading to an improvement of barrier properties. However, a steady state condition is observed for longer immersion time. Therefore, we can assume that the chromate conversion coating becomes a stable system after 10 h immersion in 0.05M NaCl (Figure 9.1).

Figure 9.2 shows the anodic polarization curve in 0.05M NaCl after 15 h immersion for AA2024 coated with chromate conversion coating (- - - short dash). E_{corr} value identified by the potentiodynamic polarization curve is about -550mV vs. Ag/AgCl, in accordance with the open circuit potential showed in Figure 9.1.Moreover, the potentiodynamic polarization curve exhibits a very limited current noise.

Figure 9.3 shows a SEM micrograph of AA2024 coated with sol-gel ZrO_2 thin film. The sol-gel ZrO_2 film is very homogeneous and covers the entire substrate. This is confirmed by Glow Discharge Optical Emission Spectroscopy (GDOES) measurements reported in previous publications [33]. GDOES measurements shows that film thickness is less than 100nm for the coating considered in this work. This is in accordance with X-ray Photoelectron Spectroscopy anal-

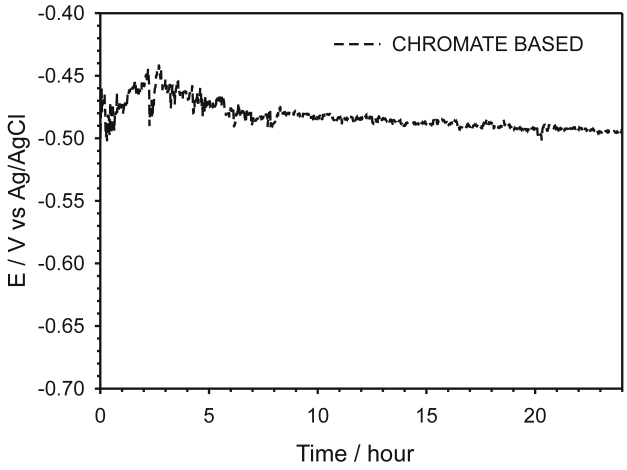

Figure 9.1: OCP for stable system

ysis (XPS) carried out on similar samples showing that film thickness ranges between 100 nm and 200 nm depending on deposition parameters [35, 36]. Energy dispersive X-ray spectroscopy confirms that the zirconium film is uniform on the substrate [33]. Therefore, AA2024 is coated with a very thin inorganic film which is nearly defect free. It can be expected that a significant variation of electrochemical behaviour occurs when defects in ZrO_2 film are formed. In contrast with chromate conversion coating that are auto-repair systems, sol-gel ZrO_2 thin film are not able to restore the initial uniform protective layer after damage or corrosion attack. This means that no self-healing ability is observed for sol-gel ZrO_2 films. Plugging phenomena can occur due to formation of corrosion products inside film defects leading to a partial stabilisation of the properties of ZrO_2 film. However, the protection provided in case of plugging phenomena is significantly lower relative to a defect free film. Therefore, electrochemical behaviour of ZrO_2 thin film is dependent on quality of the deposited coating. Hence, it can be stated that ZrO_2 thin film can easily become an unstable system.

Figure 9.4 shows open circuit potential in 0.05M NaCl for sol-gel ZrO_2 thin film deposited on AA2024 (-solid line). The open circuit potential is not stable and exhibits strong oscillations during the entire measurement. The OCP evidences very fast oscillations in the range of 150 mV. This behaviour can be associated to a complex system constituted by the deposition of a inert ZrO2 film on a very reactive substrate like AA2024. In addition, the solution containing

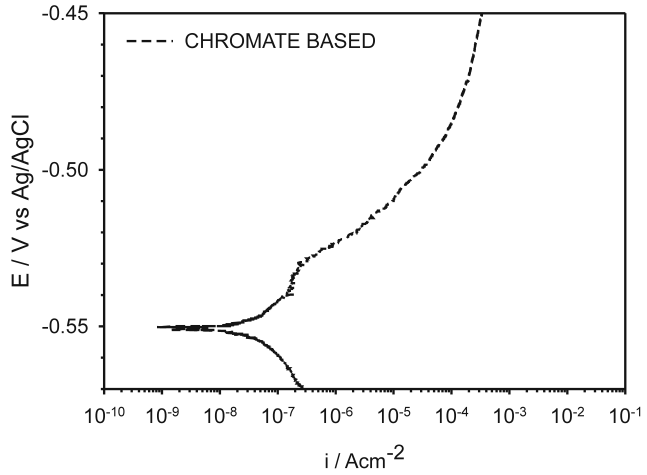

Figure 9.2: PPC for stable system

chlorides promotes meta-stable conditions, i.e. pitting corrosion. The equilibrium of the system is affected by the electrochemical reactions that can take place on the metal substrate. Open circuit potential oscillation visible in Figure 9.4 are a critical aspect for electrochemical impedance spectroscopy since it is clearly recognizable that the alloy coated with a very thin ZrO_2 film does not show stationary behaviour and can be considered as an unstable system.

Figure 9.5 shows the potentiodynamic polarization curve in 0.05M NaCl for sol-gel ZrO_2 thin film on AA2024 (-solid line). The curve acquired is very noisy suggesting unstable (non-stationary) conditions for the electrochemical system. In addition, the poten- tiodynamic curve shows significant scatter in the region of E_{corr}. This can be associated to incapability of the instrument to detect an unique value for this potential. Moreover, the anodic branch exhibits low anodic current density which is also characterized by significant scatter. This is due to excellent barrier properties related to the deposition of a defect free film. This result is in line with OCP measurements visible in Figure 9.4 and further strengthens the conclusion that on ZrO_2 films is very difficult to carry out accurate electrochemical measurements because are unstable systems. DC techniques provide information about stability and barrier properties of these systems while it is not possible to study the electrochemical behaviour of the system as a function of immersion time. This can be done with electrochemical impedance spectroscopy for systems that maintain stable conditions for the open circuit potential during

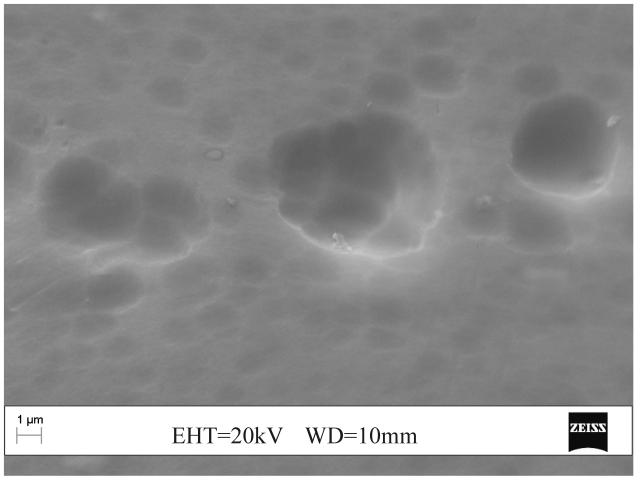

Figure 9.3: SEM micrograph for a sol-gel film on AA2024

the measurement.

Figure 9.6 shows the input signal acquired during an impedance measurement for AA2024 coated with chromate conversion coating after 24 h immersion in 0.05M NaCl. The impedance measurement is carried out under voltage control, also referred as potential approach. A schematic representation of input signal V_{in} for measurement under voltage control is represented in Figure 9.7(a). A voltage input perturbation with amplitude of 10mV is applied to the system at the open circuit potential (Figure 9.6). The OCP is measured for 60 s before acquisition of impedance data. The open circuit potential measured after 60 s represents the mean value of input sine wave voltage perturbation for the successive EIS measurement. The mean value of the OCP is -520mV vs. Ag/AgCl and remains stable during the impedance measurement, as can be seen by the trend of the input signal in Figure 9.6. In Figure 9.6 it can be clearly seen that a constant sine wave amplitude is applied during the frequency scan.

An alternative method to carry out electrochemical impedance measurement can be proposed based on a galvanostatic approach. The same was previously done for polarization resistance measurements (R_p). Jones [37] demonstrated the effectiveness of such an approach for the study of unstable electrodes. In order to measure R_p, a triangular sine is imposed and the system response is measured. R_p is equal to the ratio between voltage and current according to equation 9.1:

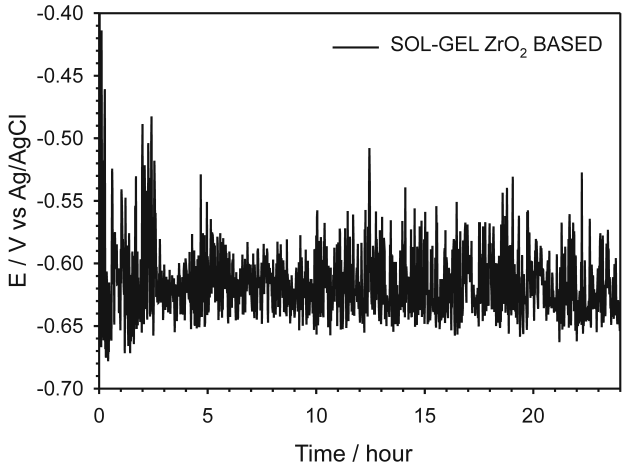

Figure 9.4: OCP for an unstable sol-gel system

$$R_p = \frac{\Delta V}{\Delta I} \tag{9.1}$$

The accuracy of results is better when the input signal is a current than when it is a voltage for R_p measurements performed on systems with unstable open circuit potential [37]. Moreover, Guyader et al. [38] compared R_p values obtained from electrochem- ical impedance spectroscopy and linear polarization resistance measurements under potentiostatic and galvanostatic control. In their studies, the galvanostatic method provided better results than the potentiostatic one when the corrosion potential was not constant as a function of immersion time.

Based on these results, a current control method is proposed in order to perform electrochemical impedance spectroscopy on unstable systems. Measurements under current control were initially carried out on AA2024 coated with chromate conversion coating, which can be considered as a stable system since it does not evidence significant potential fluctuations during the time necessary to carry out impedance measurements. These measurements are performed imposing a ΔI perturbation at a finite direct current value. The mean value of sine wave corresponds to a current that is equal to zero. This current is directly correlated to the open circuit potential of the system. Figure 9.7(b) shows a scheme of the input current perturbation I_{in} on a stable system. In Figure 9.7(b), the perturbation signal changes in amplitude because the impedance measurements

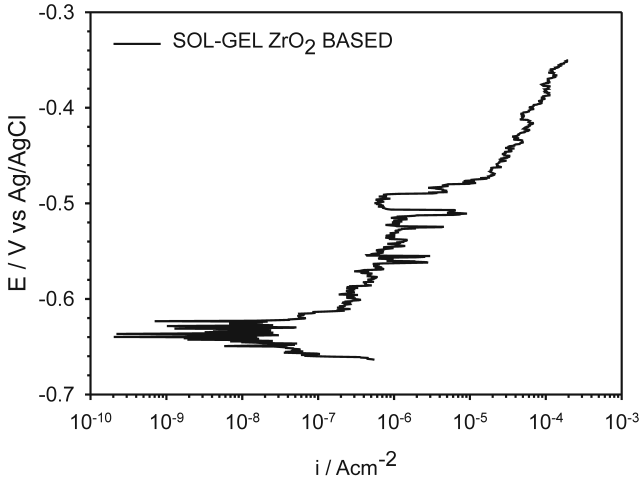

Figure 9.5: PPC for an unstable sol-gel system

carried out under current control have to be performed following the detailed procedure mentioned in the experimental section, which will be then explained for unstable systems. It is possible to observe in Figure 9.7 that the open circuit potential is the mean value for the sine wave under voltage control (Figure 9.7(a) while the zero current condition is the mean value under current control (Figure 9.7(b). Since the OCP is the value of the potential for which the net current of red-ox processes is equal to zero, measurements under current control must give the same response of those carried out under potential control. An example is given in Figure 9.8, which shows Bode module and phase angle plots for impedance measurement performed on AA2024 coated with chromate conversion coating in 0.05M NaCl under voltage and current control. These measurements have been carried out after 72 h immersion in order to have stationary conditions for the open circuit potential. In the case of a stable system, it can be seen that the plots of impedance modulus and phase angle overlap for the two systems. This indicates that measurements carried out under current and voltage control lead to the same system response in the case of stable sample. It is important to consider the behaviour under current and voltage control for an unstable system like the AA2024 coated with sol-gel ZrO_2 thin film investigated in this work.

Figure9.9 reports a scheme for impedance measurements associated to voltage and current control in the case of the unstable system. In Figure 9.9(a) it is possible to see the effect of a non-stationary open circuit potential on the impedance

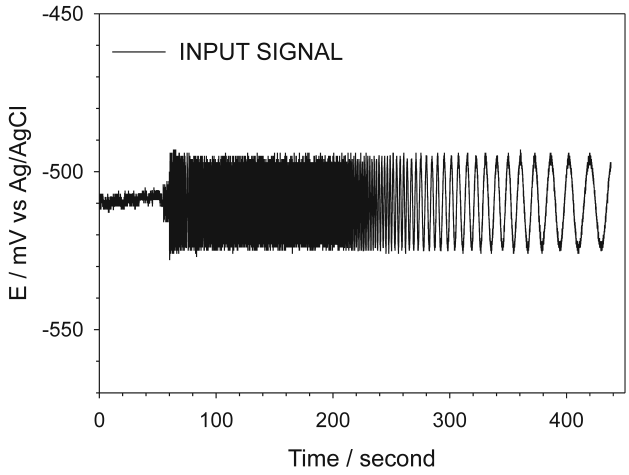

Figure 9.6: Input signal for a stable system

measurements under voltage control. In the example in Figure9.9(a) the open circuit potential becomes more negative during the impedance measurement. A mean value of sine wave corresponding to open circuit potential measured after 60 s immersion times is imposed under voltage control when the impedance measurement is started. This value is maintained constant during the entire measurement. Since the open circuit potential of the system is changing during the test, the sample is polarized at an anodic over-potential (η). In particular, the extent of the polarization becomes significant at low frequency because the potential shift might be rather large due to the duration of the measurement. Therefore, the instability of the system will impair the impedance measurement.

In addition, anodic polarization of the sample at low frequency might lead to extensive damage of the sample. As a consequence, it is not possible to obtain reliable information for impedance measurements carried out under voltage control on unstable systems. Indeed, these measurements cause accelerated degradation of the coating. An example is given in Figure9.10, which shows the input signal acquired during an impedance measurements under voltage control for AA2024 coated with sol-gel ZrO_2 thin film after 1 h immersion in 0.05MNaCl. The equipment performs the open circuit potential measurement during the first 60 s. The open circuit potential rapidly shifts from -580mV to -40mV vs. Ag/AgCl after about 10 s and from -40mV to -880mV vs. Ag/AgCl after about 15 s. This clearly represents a non-stationary condition for the open circuit potential. Dur-

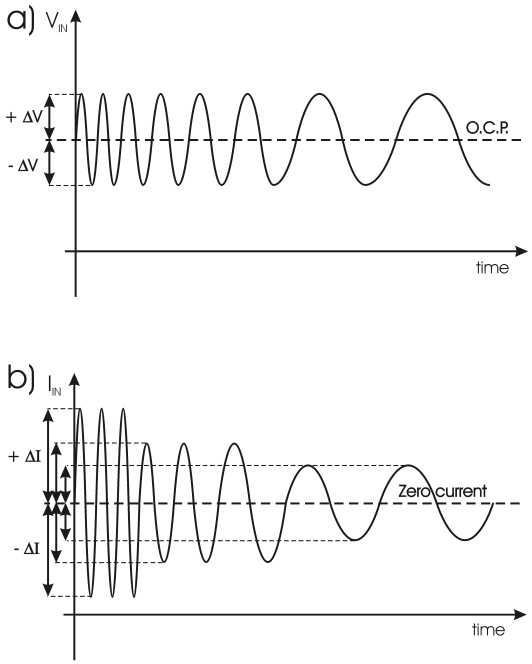

Figure 9.7: Schemes of Input signal for stable system

ing the impedance measurement a ΔV perturbation is superimposed to the value of OCP measured after 60 s. Constant potential oscillations are visible for the duration of the measurement in Figure 9.10. Due to the strong variation of the OCP it is likely that an over-potential is applied to the sample as considered in Figure9.9(a).

Figure 9.11 reports Bode module and phase angle plots for the system response corresponding to the input perturbation shown in Figure 9.10. The trend of impedance modulus and phase angle in Figure 9.11 clearly shows that for fre-

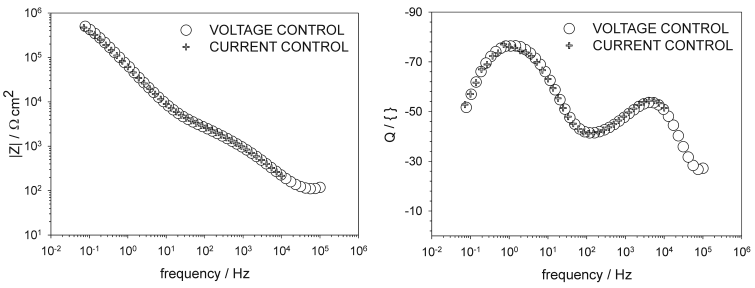

Figure 9.8: Comparison for stable system

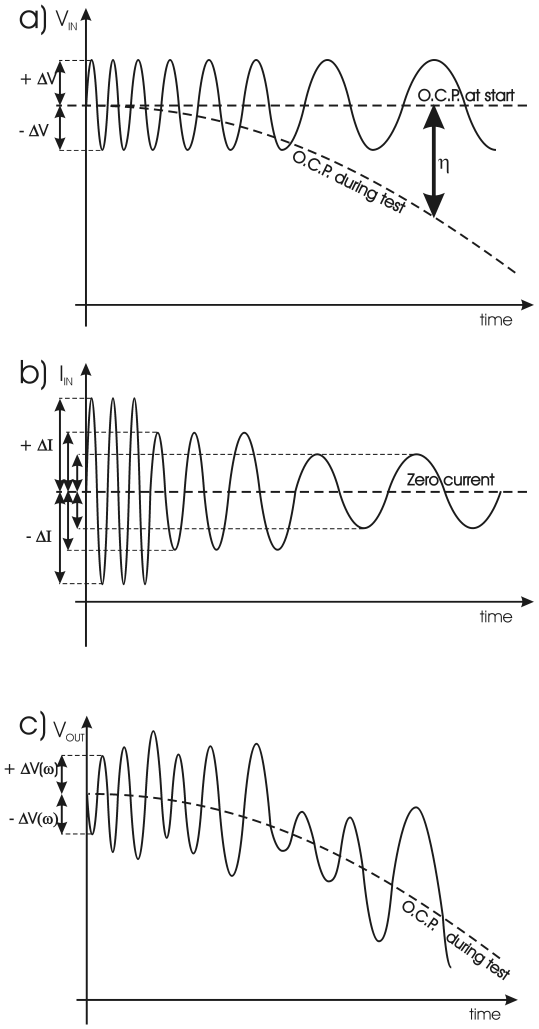

Figure 9.9: Schemes of Input signal for unstable system

quencies lower than 10 Hz the spectrum is not a continuous function resulting in an evident instability. The impedance measurement cannot be validated in this case and no reliable information can be obtained about the system under investigation. Figure 9.9(b) shows a scheme of the input signal for an impedance measurement under current control for the unstable system. The trend of the input signal is the same as for that shown in Figure 9.7(b) for the stable system. This is important because it confirms that current method is not dependent on variations of the open circuit potential. As it can be seen in Figure 9.9(b), the mean value of current perturbation corresponds to the condition of zero current.

However, the amplitude of the oscillations is not constant during the mea-

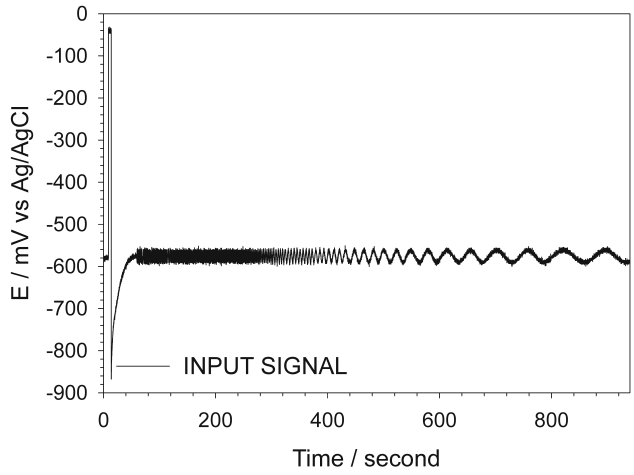

Figure 9.10: Input signal for unstable system

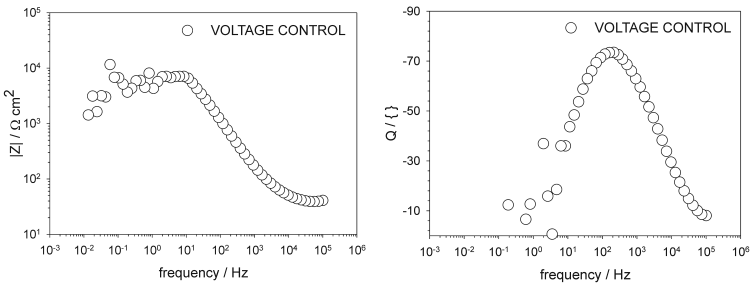

Figure 9.11: Impedance voltage control for unstable system

surements because the impedance response of the system is a function of the input signal frequency. This is the theoretical assumption for interpretation of impedance spectra by means of equivalent cir- cuit employed in literature for the study of systems like the ones investigated in this work. The impedance of the system is a transfer function that can be expressed in equation 9.2:

$$|Z(\omega)| = \frac{\overline{|V|}}{\overline{|I|}} \tag{9.2}$$

where I is the applied current (input signal) while V is the response of the system (output signal). Under current control, equation 9.2 implies that the output signal (V) tends to increase at low frequency if the input signal (I) is constant in the entire frequency range. This is due to the increase of the impedance of the electrochemical system, as can be seen in the example reported in Figure 9.8 for

a chromate conversion coated. The increase of $|Z(\omega)|$ might determine conditions for which the linearity of the system is not retained. Therefore, the amplitude of the input signal must be carefully selected for measurement under current control in order to obey to the linearity condition for the complete scanned frequency range. In particular, linearity issues might be avoided selecting the input current as a function of the frequency. The equipment employed for impedance measurements shown in this work enables to apply a specific current amplitude for different frequency ranges. Accordingly, a current amplitude which satisfies the linearity condition can be selected for a specific frequency range. This is shown in Figure 9.12 where four distinct input currents are applied for different frequency ranges. This approach enables to apply a relatively high current perturbation at high frequency (ΔI_1) between $10^4 - 10^2$ Hz and a small current (ΔI_4) between $10^0 - 10^{-1}$ Hz in order to maintain the linearity of the system.Moreover, intermediate current perturbation amplitudes ((ΔI_2, (ΔI_3) are imposed to the system between $10^2 - 10^0$ Hz in order to guarantee the continuity of impedance function. The variation of the input signal during measurements under current control is an important difference relative to those under voltage control, which have constant input signal. The application of different values of amplitude perturbation is an important issue concerning signal amplification during impedance measurements under current control. The signal amplification is controlled by an operational amplifier (OA) which determines optimum values of gain and resolution at each frequency of the impedance scan [39]. Since the equipment employed for impedance measurements under current control in this work enables to select only one current range (current auto-range function is available in voltage control set-up), it is important to define the input perturbations ((ΔI_i) in order to have optimal gain and resolution for the operational amplifier. Gain and resolution are defined automatically by the equipment as a function of the applied current. From an experimental point of view, it is important to ensure a smooth transition for the different input ΔI_i perturbations in order to obtain a continuous spectrum. This condition is generally verified when the operational amplifier works with a resolution gain between 40% and 70%.

The use of a single current range might affect accuracy of measurement carried out under current control. It is desirable to select a low current range in order to have a very high resolution for the zero current during the measurement. As an example, it is not possible to measure with good resolution a current of 0.01 μA

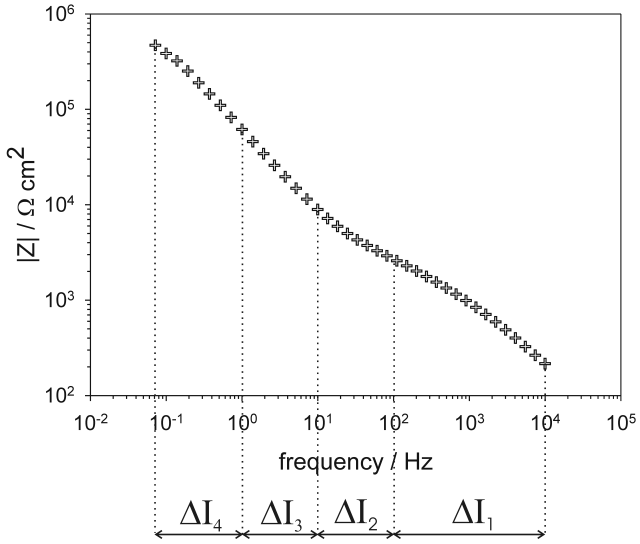

Figure 9.12: Variation of the input current perturbation

with a current range of 1A. With reference to the measurement shown in Figure 9.12 the use of a small current range is desirable at low frequency. In contrast, this is not the case for measurements at high frequency, for which the input current should be high enough to determine a favourable signal/noise ratio for the output. The reduction of available frequencies is a drawback related to the selection of a small current range. In particular, this is a limitation for high frequencies. As an example, the maximum available frequency is 10^4 Hz with a current range of 100μ A. The maximum frequency is reduced to 10^3 Hz with a current range of 10μ A. This is an intrinsic aspect related to the limits of the equipment for data acquisition at high frequency with small current ranges. It is important to point out that the drawbacks discussed above about measurements carried out under current control are not encountered for those under voltage control. Indeed, the gain and resolution of the operational amplifier and the current range are automatically selected for each frequency in the case of measurements under voltage control.

The main advantage of measurements under current control is that the output signal follows the variation of the open circuit potential, as shown in Figure 9.8(c). This guarantees the stability condition during the entire impedance scan. In the case of unstable systems, this approach preserves the sample from degradation due to the possible over-potentials which can be applied in the case of

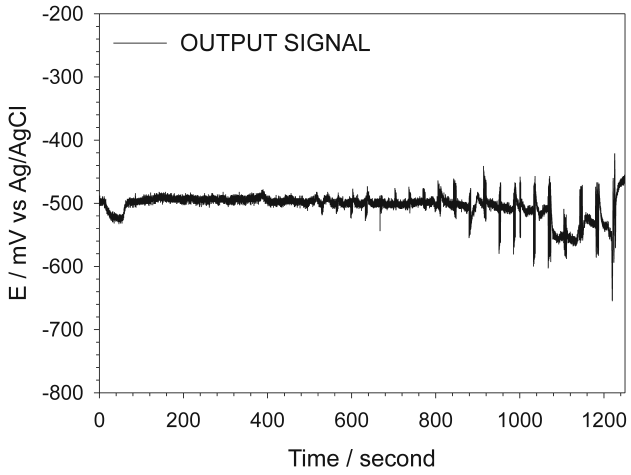

Figure 9.13: Output Signal for unstable system current controlled

measurements under voltage control. Figure 9.13 shows the output voltage signal detected during an impedance measurement carried out after 24 h immersion in 0.05M NaCl on AA2024 coated with a sol-gel ZrO_2 thin film. The mean value of the output signal corresponds to the open circuit potential of the system during impedance data acquisition. It can be seen that the open circuit potential significantly changes during the measurement confirming that the sample under investigation is an unstable system. Moreover, it can be seen that the oscillation of the output signal follows the trend of the open circuit potential during the measurement. It can be also seen that the amplitude of the output signal increases during the measurement due to the increase of the impedance $|Z(\omega)|$ of the system. This measurement was performed with a current range of 100 μA. Table 9.1 reports the parameters selected for the impedance measurement. Four sine wave amplitude were applied in four distinct frequency ranges. The sine wave amplitude ranges from 5 μA to 1.1 μA. It is important to point out that the input parameters should be defined for each electrochemical system under investigation.

Frequency Range [Hz]	$10^4 - 10^1$	$10^1 - 10^0$	$10^0 - 10^{-1}$	$10^{-1} - 10^{-2}$
Input Sine Wave Amplitude [μA]	5	2.5	1.2	1.1

Table 9.1: Input Parameters

Figure 9.14 shows in more detail the trend of voltage output signal at high (a) and low frequencies (b). The trend of the mean value evidences that the variation of the open circuit potential is tracked at high (Figure 9.14(a) and low (Figure 9.14(b)) frequencies. Moreover, the oscillations of the output signal effectively follow the open circuit potential in accordance with the theoretical scheme shown in Figure 9.9(c). This is a very important aspect related to validation of impedance measurements.

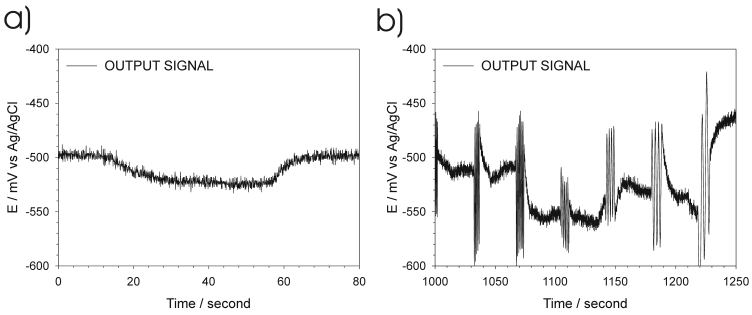

Figure 9.14: Output signal zoom for current and unstable system

In order to improve accuracy of impedance measurements carried out under current control, a zero current condition can be imposed before each frequency scan for 20 s. This is shown in Figure 9.15, which reports the output signal during an impedance measurement carried out after 24 h immersion in 0.05M NaCl on AA2024 coated with a sol-gel ZrO_2 thin film. The imposition of the zero current condition favours the achievement of a steady state after each frequency scan. This improves data acquisition for unstable systems. The approach of applying a zero current condition before each frequency scan is an important advantage of measurements under current control relative to those under voltage control. Indeed, the equipment employed in this work does not enable to apply a similar procedure to reach a steady state for data acquisition under voltage control.

Figure 9.16 displays the Bode module and phase angle plots after 24 h immersion in 0.05M NaCl on AA2024 coated with a sol-gel ZrO_2 thin film. This measurement was carried out under current control imposing a zero current condition for 20 s before each frequency scan. Input parameters were selected according to Table 9.1. The Bode plot for impedance module does not show singularities meaning that the impedance is a continuous function of the frequency. However, the Bode phase angle plot evidences a very small discontinuity probably

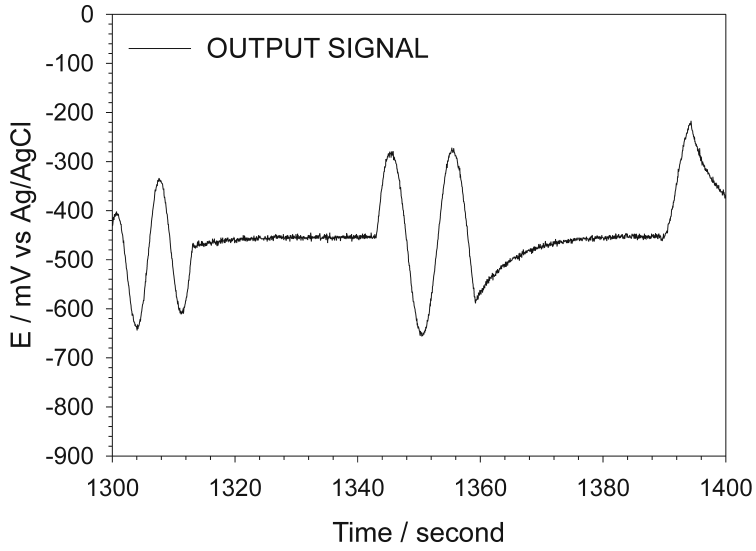

Figure 9.15: Steady condition under current control

due to a change of the parameters of the operational amplifier in correspondence of the variation of the input current amplitude at 10^{-1} Hz. In general, it can be stated that accuracy of the measurement is very good and that the linearity of the system is preserved during the measurement.

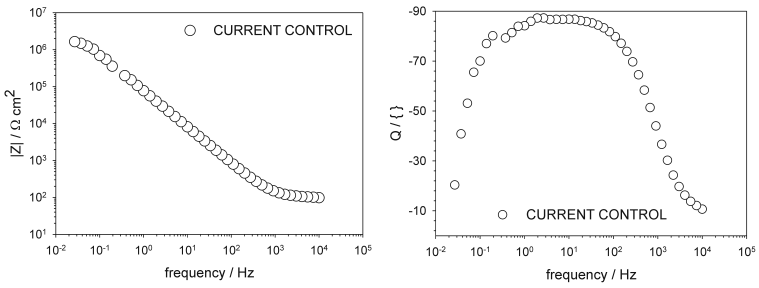

Figure 9.16: Impedance plot for unstable under current control

Figure 9.17 reports Nyquist plots for impedance measurement carried out under voltage and current control after 1 h immersion in 0.05M NaCl on AA2024 coated with a sol-gel ZrO_2 thin film. Figure 9.17(a) shows that impedance data for this unstable system can be acquired only under current control without damage of the sample during the measurement. In contrast, the Nyquist plot shown in Figure 9.17(b) with higher magnification evidences that data acquisition is not

successful under voltage control due to polarization of the sample. The absence of sample damage guaranteed under current control enables to study the evolution of the system as a function of immersion time in the solution. This information is not accessible by means of impedance measurements under voltage control on these unstable systems.

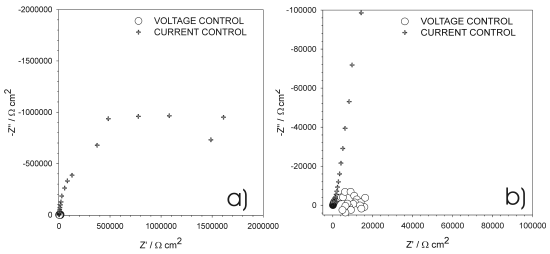

Figure 9.17: Comparison between under and voltage control

9.4 Conclusions

In this work, critical aspects related to electrochemical study of non-stationary coated metallic substrates are considered with particular attention to electrochemical impedance measurements. Impedance measurements were carried out on two different systems. The first is a chromate conversion coated AA2024, which is characterized by high stability in terms of open circuit potential during acquisition of impedance spectra. The second system is the same substrate coated with a sol-gel ZrO_2 thin film. This system evidences a marked instability in open circuit potential and potentiodynamic polarization measurements. This paper discusses experimental aspects related to impedance measurements carried out under voltage and current control. Experimental results evidences that impedance measurements under voltage control are successful only for the stationary system while quality of results is strongly impaired in the case of AA2024 coated with a sol-gel film. In order to obtain reliable data for such system, measurements under current control were performed. The main advantage of measurements under current control is that it is possible to avoid sample damage due to system polarization that might occur when the open circuit potential significantly changes during the measurement. This is the typical case of unstable systems like AA2024 coated with a sol-gel film. This enables to follow

the evolution of the system as a function of the immersion time without significant damage of the sample due to the method employed for the measurement. Moreover, the current control approach guarantees the stability of the system during the impedance measurement. Therefore, impedance measurements under current control performed on non-stationary systems can be validated. Nevertheless, some drawbacks are related to data acquisition under current control. The frequency range available for the measurements is reduced for measurements under current control due to the intrinsic operation mode of the equipment employed in this work. In addition, the output signal/noise ratio can be altered for measurements at high frequency due to the possibility to select only one current range for the entire frequency scan under current control. Finally, it is important to consider that input parameters must be carefully selected depending on the system investigated for measurements under current control.

Bibliography

[1] E.A. Starke Jr., J.T. Staley, Prog. Aerospace Sci. 32 (1996) 131

[2] Z. Szklarska-Smialowska, Corros. Sci. 41 (1999) 1743

[3] C. Blanc, B. Lavelle, G. Mankowski, Corros. Sci. 39 (1997) 495

[4] P. Campestrini, E.P.M. van Westing, H.W. van Rooijen, J.H.W. de Wit, Corros. Sci. 42 (2000) 1853

[5] M. Bethencourt, F.J. Botana, J.J. Calvino, M. Marcos, M.A. Rodriguez-Chacon, Corros. Sci. 11 (1998) (1803)

[6] J.H. Osborn, Prog. Org. Coat. 41 (2001) 280

[7] M.J. Tsapakos, T.H. Hampton, P.R. Sinclair, J.F. Sinclair, W.J. Bement, K.E. Wetterhahn, Carcinogenesis 4 (1983) 959

[8] C. Srividya, M. Sunkara, S. Babu, J. Mater. Eng. Perform. 6 (1997) 586

[9] V. Moutalier, M.P. Gigandet, J. Pagetti, L. Ricq, Surf. Coat. Technol. 173 (2003) 87

[10] D. Bakul, H. Xiankui, D. Yogeeswari, D. Shirshak, J. Sol-Gel Sci. Technol. 32 (2004) 143

[11] M. Guglielmi, J. Sol-Gel Sci. Technol. 8 (1997) 443

[12] R.L. Ballard, J.P. Williams, J.M. Nius, B.R. Kiland, M.D. Soucek, Eur. Polym. J. 37 (2001) 381

[13] A. Conde, A. Duran, J.J. de Damborenea, Prog. Org. Coat. 46 (2003) 288

[14] W.J.V. Ooij, D. Zhu, V. Palanivel, J.A. Lamar, M. Stacy, Silicon Chem. 3 (2006) 11

[15] S. Pellice, P. Galliano, Y. Castro, A. Duran, J. Sol-Gel Sci. Technol. 28 (2003) 81

[16] F. Andreatta, P. Aldighieri, L. Paussa, R. Di Maggio, S. Rossi, L. Fedrizzi, Electrochim. Acta 52 (2007) 7545

[17] L. Fedrizzi, F.J. Rodriguez, S. Rossi, F. Deflorian, R. Di Maggio, Electrochim. Acta 46 (2001) 3715

[18] H. Wang, R. Akid, Corros. Sci. 49 (2007) 4491

[19] J.R. Macdonald, E. Barsoukov, Impedance Spectroscopy, Second edition Wiley, New York, 2005

[20] P. Agarwal, M.E. Orazem, L.H. Garcia-Rubio, J. Electrochem. Soc. 139 (1992) (1917)

[21] P. Agarwal, O.D. Crisalle, M.E. Orazem, L.H. Garcia-Rubio, J. Electrochem. Soc. 142 (1995) 4149

[22] P. Agarwal, M.E. Orazem, L.H. Garcia-Rubio, J. Electrochem. Soc. 142 (1995) 4159

[23] G.S. Popkirov, R.N. Schindler, Electrochim. Acta 38 (1993) 861

[24] G.S. Popkirov, R.N. Schindler, Electrochim. Acta 39 (1994) 2025

[25] G.S. Popkirov, R.N. Schindler, Electrochim. Acta 40 (1995) 2511

[26] M. Urquidi-Macdonald, S. Real, D.D. Macdonald, Electrochim. Acta 35 (1990) 1559

[27] D.D. Macdonald, Electrochim. Acta 51 (2006) 1376

[28] G.K. Darowicki, Electrochim. Acta 42 (1997) (1781)

[29] Y. Van Ingelgem, E. TourwÃ¨, J. Vereecken, A. Hubin, Electrochim. Acta 53 (2008) 7523

[30] E. Van Gheem, J. Vereecken, J. Schoukens, R. Pintelon, P. Guillaume, P. Verboven, L. Pauwels, Electrochim. Acta 49 (2004) 2919

[31] E. Van Gheem, R. Pintelon, J. Vereecken, J. Schoukens, A. Hubin, P. Verboven, O. Blajiev, Electrochim. Acta 49 (2004) 4753

[32] E. Van Gheem, R. Pintelon, A. Hubin, J. Schoukens, P. Verboven, O. Blajiev, J. Vereecken, Electrochim. Acta 51 (2006) 1443

[33] F. Andreatta, L. Paussa, P. Aldighieri, A. Lanzutti, D. Ondratschek, L. Fedrizzi, Surf. Interface Anal. 42 (2010) 293

[34] T.L. Metroke, R.L. Parkhill, E.T. Knobbe, Prog. Org. Coat. 41 (2001) 233

[35] R. Di Maggio, P. Aldighieri, S. Rossi, L. Fedrizzi, Proceedings of the European Corrosion Congress EUROCORR2005, Lisbon, Portugal September 4-8, 2005

[36] L. Fedrizzi, R. Di Maggio, P. Aldighieri, F. Andreatta, F. Girardi, Proceedings of the 4th International Symposium on Aluminium Surface Science and Techn Beaune, France, May 14-18, 2006

[37] D.A. Jones, Corrosion 39 (1983) 444

[38] A. Guyader, F. Huet, R.P. Nogueira, Corrosion 65 (2) (2008) 136-144 (NACE)

[39] A.J. Bard, M. Stratmann, Instrumentation and Electroanalytical Chemistry vol.3, Wiley-VCH, 2003

Chapter 10

Industrial Scale-up

Development of chromium-free coatings is an important issue for replacement of chromate conversion coatings in aerospace and automotive industry. This aspect was targeted in the development of this thesis in which the research approach considers the production of thin ZrO_2 coatings (100-200 nm) by means of sol-gel technology for several types of aluminum alloys. ZrO_2 films were deposited employing solutions of Zr precursors. Two preparation routes were followed: the first employed a metal-organic precursor in an alcoholic solution; the second one used a water-based solution of a Zr salt. Coating application was carried out by dipping and spraying technology at a laboratory scale. Corrosion inhibitors like cerium nitrate and mercaptobenzothiazole were introduced in the films in order to improve corrosion behaviour of the sol-gel coatings. In addition, substrates pre-treated with ZrO_2 films were painted with an organic primer and top coat in order to evaluate paint adhesion and electrochemical behaviour of painted systems. At a later stage of the project, coating deposition was carried out with a robot-controlled air pressure gun in spraying cabins in order to evaluate industrial production of the ZrO_2 films.

10.1 Introduction

Aluminum alloys are usually protected with a paint system consisting of conversion layer, primer and top coat. Chromium-based pre-treatments are extensively employed as conversion coatings because they provide very good adhesion for primer and top coat associated with good barrier properties [1]. Moreover, chromate conversion coatings exhibit self-healing ability [1]. However, use of

chromate conversion coatings is restricted and alternative pre-treatments should be employed for aluminium alloys [1, 2, 3, 4]. Activities carried out in the thesis showed that coatings obtained with sol-gel technique are a possible replacement for chromate conversion coatings for aluminium and magnesium substrates [5, 6, 7]. Moreover, sol-gel coatings were also applied to steel substrates. The development of Cr-free coating systems has been previously targeted with the attempt to replace chromate conversion coatings with a thin sol-gel layer (typically 50-200 nm) [8]. This approach is new because sol-gel coating systems are usually thick (in the micrometer range) and are generally regarded as complete coating systems. The good adhesion behaviour of thin Zr and Si-based sol-gel films relative to chromate conversion coatings is the main advantage of developing thin coatings. In previous work, our research group followed the strategy of developing thin sol-gel coatings for different aluminium alloys [9, 10]. Thin ZrO_2 amorphous films (100-200 nm) were deposited on AA1050 with dip-coating technique [9]. These coatings promote adhesion of organic coatings to the ZrO_2 pre-treatment. Moreover, the electrochemical behaviour of AA1050 coated with ZrO_2 films is strongly dependent on deposition parameters, which affect film quality. ZrO_2 pre-treated AA6060 exhibits barrier properties similar to chromate conversion coated AA6060 when a continuous layer was deposited on the surface through successive dipping steps in the sol-gel solution [10]. Moreover, ZrO_2 films deposited with sol-gel technique improve corrosion resistance of aluminium alloy AA2024 and magnesium alloy AZ31 [5, 6, 7]. The development of thin ZrO_2 sol-gel pre-treatments targeted the industrial scale up of the coatings by means of spraying technology. This lead to production of demonstrators for application in different fields like aerospace, automotive and domestic appliances. The work presented in this part of the thesis targets the characterization of demonstrators coated with ZrO_2 films focusing on adhesion behaviour of paints applied on sol-gel pre-treatments. Demonstrators were coated with a corrosion protection system consisting of a ZrO_2 pre-treatment, a primer and a top coat. The ZrO_2 films were developed and optimized for deposition by spraying at the University of Udine while they were applied on demonstrators by means of spraying technology using a robot controlled air pressure gun at Fraunhofer Gesellschaft IPA. Three types of demonstrator were produced: AA6013 panel with AA6061 stringers for application in the aerospace industry (EADS Deutschland GmbH); AA7075 skin with holes for rivets for application in the aircraft industry (Hellenic

Aerospace Industry S.A.) and AA3105 sheets for coil-coating application in the field of domestic appliances industry (Plalam SpA).

10.2 Experimental Procedure

The substrate for development and optimization of ZrO_2 pre-treatments by means of sol-gel technology was mainly AA2024 in the framework of MULTIPROTECT project. In addition, ZrO_2 films were applied to other aluminium alloys like AA3105 and AA6060. The ZrO_2 sol-gel films were produced starting from metal-organic (0.1M $Zr(OBu^n)_4$ in anhydrous n-butanol) and inorganic (0.4M $ZrO(NO_3)_2$ in water) zirconium precursors. The inorganic precursor eliminates organic compounds in the deposition process of ZrO_2 pre-treatment. The water-based solution of the inorganic precursor was selected for the production of demonstrators. Three types of demonstrator were produced: AA6013 panel with AA6061 stringers for application in the aerospace industry; AA7075 skin with holes for rivets for application in the aircraft industry and AA3105 sheets for coil-coating application in the field of domestic appliances industry. The chemical composition of the aluminum alloys is given in Table 3.1. The application of the ZrO_2 pre-treatment was performed by means of spraying technology using robot controlled air pressure gun at Fraunhofer Gesellschaft IPA. After deposition of the sol-gel film, the demonstrators were subjected to thermal treatment, which was performed at 120 °C for 4 min. Thermal treatment was followed by drying at room temperature. The demonstrators were successively coated with a primer and a top coat. The AA6013 panel with AA6061 stringers and the AA7075 aircraft skin were coated with a water-based two component epoxy primer and top coat (Mankiewicz Seevenax 313-02 and 311-03). These demonstrators are shown in Figure 10.1 and Figure 10.2. The AA3105 sheets were coated with a polyester primer and top coat (Basf CP22-0422 and C124-0095 P S). Primer and top coat did not contain corrosion inhibitors.

Samples produced in the development and optimization phase were characterized by means of SEM-EDXS in order to investigate the morphology of the ZrO_2 pre-treatment. Moreover, film thickness and composition were evaluated by means of glow discharge optical emission spectroscopy (GDOES). Barrier properties were studied by means of potentiodynamic polarization curves and electrochemical impedance spectroscopy. The demonstrators produced were character-

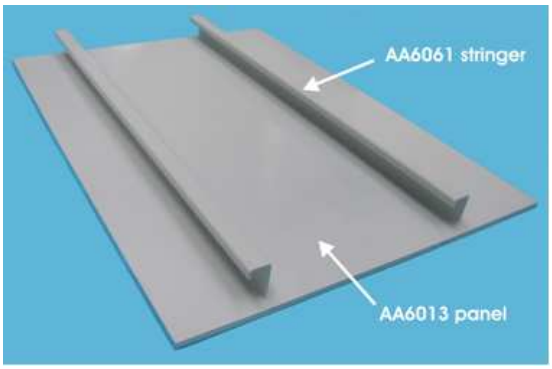

Figure 10.1: Demonstrator (AA6013 and AA6061) produced at EADS Deutschland GmbH in the framework of MULTIPROTECT project. The substrate was coated at Fraunhofer Gesellschaft IPA with a ZrO2 sol-gel film prior to application of an epoxy based non inhibited primer and top coat

ized by the end users. The AA6013 panels with AA6061 stringers were subjected to salt spray test (ISO 9227), filiform corrosion test (EN ISO 3665) and alternate immersion emersion test (DIN EN 3212) at EADS Deutschland GmbH. The AA7075 aircraft skin demonstrator were characterized at Hellenic Aerospace Industry S.A. by means of cross cut test in dry and wet conditions according to ISO 2409 and impact resistance test (ISO 6272). The AA3105 demonstrator underwent adhesion on embossing and on T-bend tests and salt spray test at Plalam SpA.

10.3 Results

Figure 10.3(a) shows a SEM micrograph of AA2024 coated with a ZrO_2 film deposited by spraying technology with a robot controlled air pressure gun. This is the typical morphology observed for samples coated with a thin (less than 100 nm) film deposited with sol-gel technology. The GDOES semi-quantitative composition profile in Figure 10.3(b) displays signals relative to Zr, O and Al. The trend of Zr and O signal can be associated to the deposition of the ZrO_2 sol-gel film on the substrate. The thickness of the film can be arbitrarily estimated by the marked decrease of Zr and O signals and by the increase of the Al signal related to the metal substrate. Film thickness is about 70 nm for the profile in Figure 10.3(b). This was confirmed by SEM measurements carried out on cross

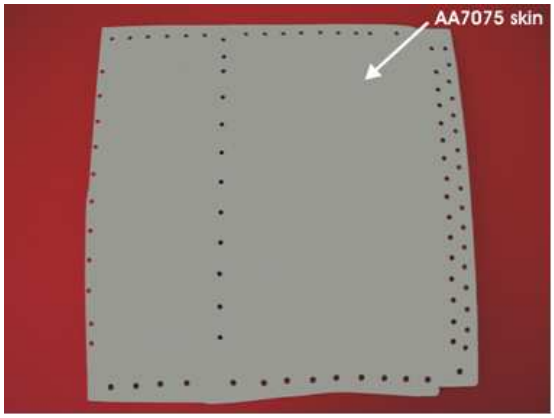

Figure 10.2: Demonstrator (AA7075) produced at Hellenic Aerospace Industry S.A. in the framework of MULTIPROTECT project. The substrate was coated at Fraunhofer Gesellschaft IPA with a ZrO2 sol-gel film prior to application of an epoxy based non inhibited primer and top coat

sections of coated samples.

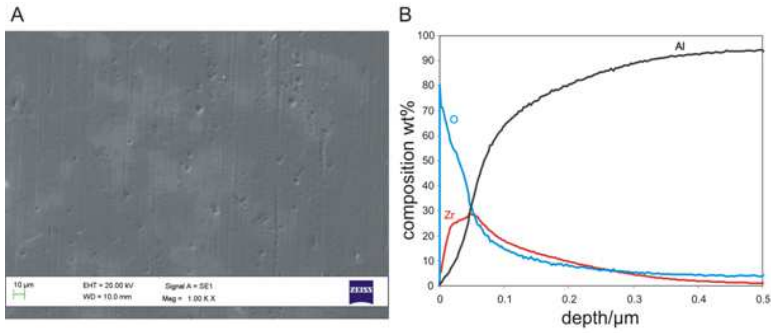

Figure 10.3: SEM micrograph (A) and GDOES semi-quantitative composition profile (B) for AA2024 coated with a ZrO2 sol-gel pre-treatment applied by spraying technology at Fraunhofer Gesellschaft IPA (Stuttgart, Germany)

It has been shown that the adhesion of the ZrO_2 film to the substrate is very good. In general, ZrO_2 pre-treatments deposited with a robot controlled air pressure gun are uniform and defect free provided that film thickness remains below 100 nm. Coating quality tends to be reduced by deposition of rather thick films due to a marked susceptibility of sol-gel films to form cracks during thermal treatment. Thin ZrO_2 films evidence a barrier effect in potentiodynamic polarization curves carried out on AA2024 and AA6060 alloys [5, 6, 10]. In the view of industrial application of ZrO_2 films applied with sol-gel technology, it is

very important to study the behaviour of painted systems because the ZrO_2 films are developed as a pre-treatment for aluminium substrates. In particular, barrier properties and paint adhesion are critical in order to provide corrosion protection to the substrate. Therefore, demonstrators were subjected to industrial tests in order to evaluate corrosion resistance and paint adhesion for different application fields.

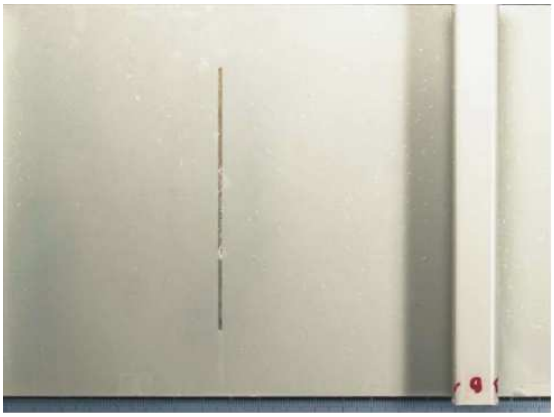

Figure 10.4: Demonstrator (AA6013 and AA6061) produced at EADS Deutschland GmbH after 1000h salt spray test according to ISO 9227

Figure 10.4 shows a demonstrator produced at EADS Deutschland GmbH after 1000h salt spray test. The panel is made of AA6013, while AA6061 is used for the stringers. The substrate was coated at Fraunhofer Gesellschaft IPA with a ZrO_2 sol-gel film before application of epoxy based non inhibited primer and top coat. The area of the scratch evidences tarnishing (visible also in Figure 10.5(a)) interesting the entire exposed area in the scratch. The corrosion occurring in the cut area is expected since the ZrO_2 pre-treatment does not contain corrosion inhibitors. Moreover, the primer and the top coat applied on the sol-gel film are not inhibited. Paint creepage form the scratch is very limited during salt spray test. This is only 1 mm or lower after 1000h salt spray test. No filaments are visible at the edges of the scratch. This indicates that the adhesion of the paint on the sol-gel film is very good, as can be seen in Figure 10.5(a).

The surface of the panel (AA6013) does not exhibit blistering or filiform corrosion in the salt spray test suggesting good corrosion resistance. The ZrO_2 pre-treatment is uniform on the panel surface because this is the area with the best accessibility in the application process. This leads to very good adhesion of

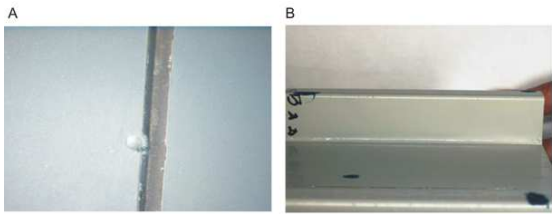

Figure 10.5: Demonstrator (AA6013 and AA6061) produced at EADS Deutschland GmbH after 1000h salt spray test according to ISO 9227: scratch (A) and stringer (B)

the paint and good corrosion protection of the substrate in the test. In contrast, the stringers are critical parts to be coated by spraying due to limited accessibility to the inner surfaces of the component as can be seen in Figure 10.1 and in Figure 10.5(b). As a result, the inner surfaces of the stringers often exhibit reduced paint thickness relative to areas with easy access. The inner surfaces of the stringers are susceptible to pitting, while the outer ones show higher resistance. As an example, Figure 10.5(b) shows no or very limited attack in the outer surface of the stringer. Moreover, the outer edges of the stringers exhibit good resistance in the salt spray test. This confirms that the ZrO_2 pre-treatment provides good barrier effect in the regions where it is possible to deposit a thin and uniform film by spraying technology. The inner edges of the stringers show higher susceptibility to pitting and creepage than other areas of the demonstrator because film defects might be present at the edges due to the limited accessibility in the spraying process. Figure 10.6 reports an image of the demonstrator produced at EADS Deutschland GmbH after 960h filiform corrosion test. The surface of the panel far from the scratch does not show blisters or delamination after 960h test indicating a very good corrosion resistance. This can be related to a barrier effect of the ZrO_2 pre-treatment, which strongly reduces corrosion of the aluminum substrate. This has a positive effect on the resistance to anodic undermining, which determines the filaments growth. In addition, delamination phenomena are most likely reduced due to the good adhesion of the paint on the ZrO_2 sol-gel film. In the region of the scratch, the AA6013 substrate is directly exposed to the electrolyte. Therefore, filament formation can be expected in this region. However, only 2 filaments could be detected in the scratch area after 500h filiform corrosion test. The maximum length of the filaments is less than 2 mm, which can be considered an indication of very good corrosion resistance in

the scratch area. Moreover, the number of filaments does not increase after 960h test. The maximum filament length becomes longer than 2 mm (respectively 2.2 mm and 3.6 mm for the two samples tested) for this exposure time. This is still an indication of good corrosion resistance in the scratch area. Since the barrier effect of the pre-treatment is not present in the scratch area, the low number of filaments and their limited growth can be related to good adhesion between ZrO_2 film and the substrate and between paint and ZrO_2 film. The edge of the AA6013 panel is a critical point in the filiform corrosion test. The edge of the panel exhibits a higher number of filaments than the scratch, as can be seen in Figure 10.6. Most importantly, the growth of the filaments is very limited after 960h. This emphasizes the good corrosion resistance provided by sol-gel film and paint. The stringers made of AA6061 show susceptibility to blistering in the region of the edges. In addition, the inner edges of the stringers are initiation sites for filaments. However, these filaments exhibit limited growth, as observed for the scratch area. As considered above, the inner edges of the stringers display higher susceptibility than other regions of the panel due to poor quality of the coating related to low accessibility during coating application by spraying.

Figure 10.6: Demonstrator (AA6013 and AA6061) produced at EADS Deutschland GmbH after 960h filiform corrosion test according to EN ISO 3665

Figure 10.7 shows the demonstrator produced at EADS Deutschland GmbH

after 1000h alternate immersion-emersion test. The scratch area evidences relevant corrosion, as seen for the salt spray test. The susceptibility to corrosion of the exposed substrate is due to the absence of inhibitors in the ZrO_2 film and in the paint, as already considered above. The amount of creepage from the scratch is very low in alternate immersion-emersion test. This is in line with the behaviour observed in salt spray and filiform corrosion tests. Hence, the good barrier effect of the coating (ZrO_2 pre-treatment and paint) is further evidenced. The inner surfaces and edges of the stringer are critical zones also in the alternate immersion-emersion test. Blistering is observed in these areas of the stringer (an example is evidenced with a blue marker on the external surface of the stringer). Moreover, pitting is often observed along the edges, where the coating is not uniform or even absent due to limited accessibility during coating application. This behaviour indicates that it is extremely important to improve coating quality in the inner surfaces of the stringer in order to provide corrosion resistance as good as for the panel surface, which is uniformly coated. In general, it can be stated that the ZrO_2 pre-treatment provides good barrier properties in combination with non inhibited epoxy primer and top coat. The strong adhesion of the paint to the sol-gel film contributes to the barrier behaviour. Results obtained for samples pre-treated with sol-gel film are in line with those observed for chromate conversion coated samples. In addition, it can be expected that the corrosion resistance of the demonstrators might be further improved by addition of inhibitors. This could be done in the sol-gel layer or in the primer and top-coat.

Figure 10.8 shows the AA7075 aircraft skin produced at Hellenic Aerospace Industry S.A. after dry and wet cross cut test. The AA7075 skin coated with the ZrO_2 pre-treatment, primer and top coat (same paint as for demonstrators produced at EADS Deutschland GmbH) passed the cross cut test in dry and wet conditions according to the standard employed by Hellenic Aerospace Industry S.A. (ISO2409). Moreover, the demonstrator coated with a sol-gel film evidences similar behaviour to chromate conversion coated reference sample.

The pictures of the skin after the cross cut test shown in Figure 10.8 indicate that the adhesion of the paint to the substrate is very good. This result is in accordance with the behaviour of the demonstrators produced at EADS Deutschland GmbH. The sol-gel films investigated in this work promote adhesion of primer and top coat. This can be associated to the ceramic nature of the film deposited. However, brittle behaviour of sol-gel films might be a possible drawback. Indeed,

Figure 10.7: Demonstrator (AA6013 and AA6061) produced at EADS Deutschland GmbH after 1000h alternate immersion emersion test according to DIN EN 3212.

the demonstrator coated with ZrO_2 pre-treatment, primer and top coat did not pass the impact resistance test (ISO 6272), as can be observed in Figure 10.9. It is likely that this result might be strongly influenced by the paint applied on the ZrO_2 pre-treatment because it can be expected that the contribution of the sol-gel film to impact resistance is very small. Nevertheless, the impact test might evidence a critical aspect for application of ZrO_2 films in aircraft skins.

Figure 10.10 displays demonstrators produced at Plalam SpA after adhesion on embossing and T-bend tests. Figure 10.10(a) shows that paint adhesion in the embossing test is limited for the AA3105 sample pre-treated with a ZrO_2 sol-gel layer. This result was considered not acceptable according to evaluation standards employed by Plalam SpA for characterization of coatings to be applied in the coil coating industry. However, it should be considered that the embossing test is a demanding condition for thin ZrO_2 pre-treatments applied on the demonstrators. The paint adhesion was considered acceptable in the T-bend test, which evidence crack formation after 4 bends. As considered above, the adhesion behaviour in embossing and T-bend tests is mainly determined by the paint thickness with a little influence of the sol-gel layer.

Demonstrators produced at Plalam SpA evidenced good corrosion resistance

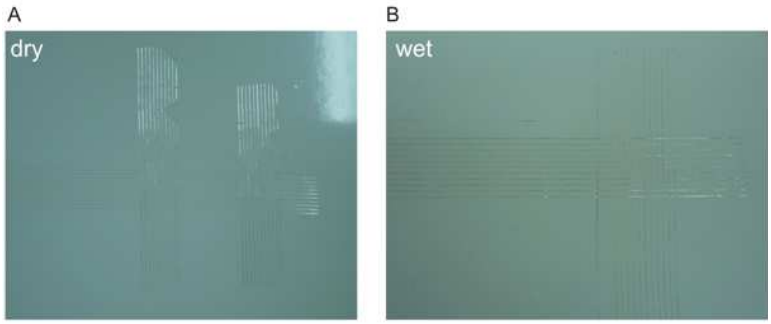

Figure 10.8: Demonstrator (AA7075) produced at Hellenic Aerospace Industry S.A. after dry (A) and wet (B) cross cut test according to ISO 2409

Figure 10.9: Demonstrator (AA7075) produced at Hellenic Aerospace Industry S.A. after impact resistance test according to ISO 6272

as compared to reference samples (with Cr free conversion layer) in the salt spray test. The scratch area visible in Figure 10.11 exhibits limited blistering and little or no creepage. The blisters are located within 1 mm from the scratch. Therefore, corrosion penetration from scratch can be considered very low. In addition, the ZrO_2 pre-treatment and the paint did non contain corrosion inhibitors. This strengthens the observation that the ZrO_2 sol-gel film can provide an efficient barrier against corrosion.

10.4 Conclusions

Aluminium alloys of the 2xxx, 3xxx, 6xxx and 7xxx series with application in different fields have been coated with a ZrO_2 film deposited by sol-gel technology

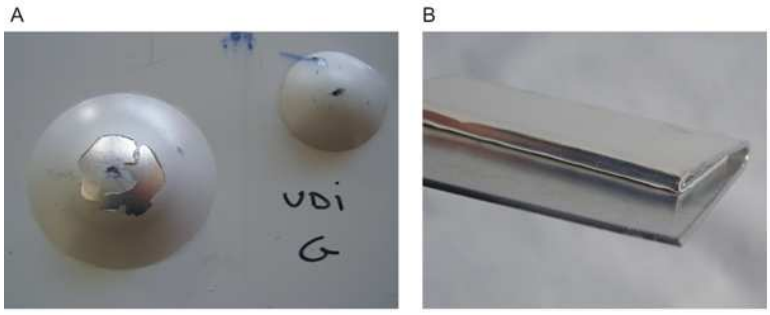

Figure 10.10: Demonstrator (AA3105) produced at Plalam SpA after adhesion on embossing and T-bend tests according to ISO 6272

Figure 10.11: Demonstrator (AA3105) produced at Plalam SpA after salt spray test

as an alternative to chromate based coatings. Demonstrators coated with a ZrO_2 pre-treatment and primer and top-coat have been produced in the framework of the research project. These demonstrators have been subjected to industrial tests like salt spray, filiform corrosion and alternate immersion-emersion tests in order to evaluate their corrosion resistance. The paint adhesion has also been investigated by means of industrial tests. The sol-gel technology enables deposition of thin ZrO_2 layers on different aluminium substrates by means of spraying technology. A ZrO_2 film could be successfully deposited on different components with this application technique. In general, the ZrO_2 pre-treatment is uniform on the demonstrators investigated in this work with the exception of zones with difficult accessibility like the inner areas of aircraft stringers. Demonstrators coated with

a primer and top coat (specific for each demonstrator) in addition to the sol-gel layer evidence efficient corrosion resistance in industrial tests due to the marked barrier effect provided by the sol-gel layer. Moreover, the sol-gel layer promotes paint adhesion limiting creepage and blister formation in the scratch area in salt spray, filiform corrosion and alternate immersion emersion tests. Paint adhesion is good in cross cut tests performed under dry and wet conditions. However, specific tests for the coil coating industry (adhesion on embossing and T-bend tests) reveal that the ceramic nature of the ZrO_2 pre-treatment might be a drawback when the demonstrators undergo strong deformations. Similar behaviour is shown in impact tests. It can be concluded that ZrO_2 sol-gel films applied by spraying technology can be considered as an alternative to chromate based pre-treatments for aluminium alloys due to combination of barrier behaviour and paint adhesion promotion.

Bibliography

[1] T.L. Metroke, R.L. Parkhill, E.T. Knobbe Prog. Org. Coat. 41 (2001) 233

[2] R. Di Maggio, L. Fedrizzi, S. Rossi Journal of Adhesion Science and Technology 15 (2001) 793

[3] M. Bethencourt, F.J. Botana, J.J. Calvino, M. Marcos, M.A. Rodriguez-Chacon Corrosion Science 11 (1998) 1803

[4] J.H. Osborne Prog. Org. Coat. 41 (2001) 280

[5] F. Andreatta, L. Paussa, P. Aldighieri, R. Di Maggio, L. Fedrizzi Proceedings EUROCORR 2007

[6] F. Andreatta, L. Paussa, P. Aldighieri, A. Lanzutti, D. Ondratschek, L. Fedrizzi Surf. Interface Anal. 42 (2010) 293

[7] F. Andreatta, L. Paussa, P. Aldighieri, A. Lanzutti, L. Fedrizzi Proceedings EUROCORR 2008

[8] J.H. Osborne, K.Y. Blohowiak, S.R. Taylor, C. Hunter, G. Bierwagen, B. Carlson, D. Bernard, M.S. Donley Prog. Org. Coat. 41 (2001) 217

[9] L. Fedrizzi, R. Di Maggio, S. Rossi, L. Leonardelli Benelux Metallurgie 43 (2003) 15

[10] F. Andreatta, P. Aldighieri, L. Paussa, R. Di Maggio, S. Rossi, L. Fedrizzi Electrochimica Acta 52 (2007) 7545

Chapter 11

Conclusions

Zirconium Oxide from Metal-Organic Precursors Thin ZrO_2 coatings (100-200 nm) were applied by sol-gel technology on AA2024. The ZrO_2 pretreatment uniformly covers the substrate as confirmed by SEM micrograph and GDOES semi-quantitative composition profiles. The film morphology is strongly affected by surface preparation (alkaline cleaning, alkaline etching and acid etching) leading to the formation of rather large cavities due to the inhomogeneous attack of AA2024 substrate. This has a negative effect on the quality of pretreatments, which might exhibit defects like discontinuities or cracks. However, the number of defects in ZrO_2 pre-treatment can be minimized modifying deposition parameters. ZrO_2 pre-treatments applied with sol-gel technique improve corrosion resistance of AA2024. This can be attributed to a barrier effect of deposited pre-treatments. However, ZrO_2 sol-gel coatings do not show a passive range in potentiodynamic polarization scans. This might be related to the existence of defects in the ZrO_2 layer behaving as initiation sites for localized corrosion attacks.

Zirconium Oxide from Inrganic Precursors Thin and well-adherent ZrO_2 pretreatments from water-based precursors can be deposited on AA2024 by means of the sol-gel technique by either dipping or spraying at laboratory scale. In particular, characterization of film morphology and electrochemical behavior indicates that ZrO_2 pretreatment is suitable for application by spraying technology, which improves film quality. The barrier properties of water-based ZrO_2 films are good evidence of a marked reduction of the corrosion current density in potentiodynamic polarization curves. The electrochemical behavior can be improved by

the addition of corrosion inhibitors like MBT and BT in the ZrO_2 pretreatment structure.

Zirconium Oxide from Metal-Organic Precursors containing Cerium Nitrate Sol-gel coatings produced by dipping have been considered for the corrosion protection of aluminium alloy AA6060. ZrO_2 based sol-gel coatings were deposited from a solution containing metal-organic precursors of zirconium. In order to produce a protective system with self-healing ability, cerium nitrate was directly added to the sol. Different coating systems were produced as the combination between layers deposited with a solution containing only the zirconia-precursor and another solution where, in addition to the precursor, cerium nitrate was added. Sol-gel ZrO_2 based coatings deposited on AA6060 are uniform and defect-free. The deposited film appears colorless and it is able to cover the metal surface. Critical areas for the sol-gel deposition, like cavities produced by the pickling procedure, are also protected. The coating composed of layers containing cerium shows a very similar morphology to the one observed for the system without cerium. Since the addition of cerium nitrate to the starting solution increases the sol viscosity, the layers deposited with the solution containing cerium are thicker than the ones without cerium. Potentiodynamic polarization measurements display a strong barrier effect for the non containing cerium systems, as indicated by passive behaviour of AA6060 aluminum alloy coated with three layers of ZrO_2. The barrier property associated to the sol-gel systems is strongly influenced by the presence of cerium in the sol. Layers deposited with solutions containing cerium are generally not able to guarantee the same protection evidenced by sol-gel systems without cerium. Electrochemical impedance measurements indicate that the gradual decrease of the electrochemical behaviour of ZrO_2 based coatings can be recovered only if cerium nitrate is added to the starting solution for the deposition. Indeed, coatings containing cerium can lead to an improvement of AA6060 corrosion behaviour due to the action of cerium ions diffusing towards the metal substrate.

Macro-Evaluation of Cerium Inhibition The inhibition effect of cerium nitrate on the electrochemical behaviour of AA2024-T3 aluminum alloy has been investigated by means of DC techniques like open circuit potential measurements and potentiodynamic polarizations. The evaluation of the effectiveness of two

cerium nitrate concentrations (5 gL^{-1} and 0.5 gL^{-1}) was carried out.
Cerium compounds precipitate on AA2024-T3 aluminum alloy as hydroxides or hydrated oxides. The precipitation involves the entire surface producing a very thin film even if local intense cerium precipitations have been detected. The solution containing 5 gL^{-1} of cerium nitrate strongly affects the electrochemical behaviour of AA2024-T3 aluminum alloy while a smaller effect has been observed for the less concentrated solution (0.5 gL^{-1}).
Chlorides significantly decrease the inhibition effect due to the presence of cerium nitrate ions in solution. Instead, cerium salts are able to homogenize the electrochemical behaviour of AA2024-T3 aluminum alloy in a pH range between 3 and 8.
The cerium precipitation phenomenon occurs faster on AA2024-T3 surfaces rich in magnesium. The precipitation is most probably promoted by the intense redox reactions correlated to the fast magnesium dissolution.
The observation of the surfaces of macro-anodes (aluminum sheet) and macro-cathodes (pure copper sheet) connected together in a solution containing cerium nitrate, evidences that cathodic sites are preferential sites for cerium precipitation. However, the mechanism of cerium deposition on AA2024-T3 (consisting of micro-anodes and micro-cathodes) is not clear yet. For cathodic inhibitors, the mixed-potential theory indicates that E_{corr} shifts to more active values. Since the results obtained are not in accordance with the theory, the cerium nitrate salts are most likely able to inhibit both the anodic and the cathodic behaviours.

Micro-Evaluation of Cerium Inhibition The electrochemical micro-cell technique has been employed for the micro-evaluation of the effect of cerium nitrate on the corrosion behaviour of 2xxx aluminum alloys. Magnesium-rich and iron-rich intermetallics have been considered as well as the matrix region.
The regions containing a high amount of magnesium-rich intermetallics are very reactive. The electrochemical activity is strongly affected by the fast magnesium dissolution coupled with the intense reduction reactions occurring.
The corrosion behaviour of AA2024-T3 samples immersed for 12 hours in solutions containing the cerium nitrate salt is significantly improved. The regions rich in magnesium tend to be more stable and the current flow related to the Faradic processes is strongly decreased for the entire microstructure. The precipitation of a thin layer film improves both the anodic and the cathodic behaviour indicating

that cerium can be considered as a general inhibitor. However, the regions rich in magnesium are sites on which a more intense cerium precipitation occurs. This behaviour is most likely related to the intense reduction reactions occurring on the intermetallics themselves which produce the pH increase necessary for cerium precipitation.

Industrial Scale-up Demonstrators coated with a ZrO_2 pre-treatment, a primer and a top-coat have been produced by using an industrial process. In general, the ZrO_2 pre-treatment is uniform on the demonstrators investigated in this work with the exception of zones with difficult accessibility like the inner areas of aircraft stringers. Demonstrators coated with a primer and top coat in addition to the sol-gel layer highlight efficient corrosion resistance in industrial tests due to the marked barrier effect provided by the sol-gel layer. Moreover, the sol-gel layer promotes a good paint adhesion limiting creepage and blister formation in the scratch area in salt spray, filiform corrosion and alternate immersion-emersion tests. Paint adhesion is good in cross cut tests performed under dry and wet conditions. However, specific tests for the coil coating industry reveal that the ceramic nature of the ZrO_2 pre-treatment might be a drawback when the demonstrators undergo strong deformations. Similar behaviour is shown in impact tests. It can be concluded that ZrO_2 sol-gel films applied by spraying technology can be considered as an alternative to chromate based pre-treatments for aluminium alloys due to combination of barrier behaviour and paint adhesion promotion.

Critical aspects in the electrochemical study of unstable coated metallic substrates Impedance measurements were carried out on two different systems. The first is a chromate conversion coated AA2024, which is characterized by high stability in terms of open circuit potential during acquisition of impedance spectra. The second system is the same substrate coated with a sol-gel ZrO_2 thin film. This system evidences a marked instability in open circuit potential and potentiodynamic polarization measurements. EIS results underline that impedance measurements under voltage control are successful only for a stationary system while quality of results is strongly impaired in the case of AA2024 coated with a sol-gel film. In order to obtain reliable data for such system, measurements under current control were performed. The main advantage of measurements under current control is that it is possible to avoid sample damage due to system po-

larization that might occur when the open circuit potential significantly changes during the measurement. This is the typical case of unstable systems like AA2024 coated with a sol-gel film. This enables to follow the evolution of the system as a function of the immersion time without significant damage of the sample due to the method employed for the measurement. Moreover, the current control approach guarantees the stability of the system during the impedance measurement. Therefore, impedance measurements under current control performed on non-stationary systems can be validated.